ALMA MATER STUDIORUM
UNIVERSITÀ DI BOLOGNA
Facoltà di Ingegneria

Corso di Dottorato di Ricerca in Ingegneria Chimica,
dell'Ambiente e della Sicurezza

(XIX CICLO)
Settore Scientifico-Disciplinare ING-IND/24

Supercritical Fluid Polymer processing:

Anomalous Sorption and Dilation Behavior

Candidato:
Vito Carlà

Relatore:
Prof. Ferruccio Doghieri

Co-relatori:
Prof. Ruben G. Carbonell
Prof. Giulio C. Sarti

Coordinatore del Corso di Dottorato:
Prof. Giulio C. Sarti

To my loving wife Elena & myself:

"Only someone who sees the invisibile
can do the impossibile"
(North Carolinian Saying)

Acknowledgments

First of all, I would like to express my gratitude to both my academic advisors, Prof. Ferruccio Doghieri, at University of Bologna, and Prof. Ruben G. Carbonell, at Kenan Center for Utilization of Carbon Dioxide located in Raleigh, North Carolina, who believed in my capacities to accomplish mostly everything conceivable by human mind. Thank you for your constant encouragement and unconditional faith in my visions and for being always patient and friendly. Special thanks go to Prof. Giulio C. Sarti and to Prof. Harold Hoffenberg for precious insights on polymer physics and thermodynamics.

I also thank my co-workers at Kenan Center, Ke Wang and Yazan Hussain, for helping me to carry out the experimental work and with whom I have spent many good times when my wife and I were in Raleigh. I would like to give special thanks to my extended research 'family', especially the 'CO_2-lab folks' in Raleigh and the Department of Chemical Engineering in Bologna. To all people with whom I have shared the rigors of graduate school, I extend my best wishes.

To my friends with whom I spend my social time, thank you for keeping my spirit up in the times when research progress was slow. I especially thank my American friends Laura and Pankaj with whom I had so many good dinners and talks. Last but not least, I must thank my wife Elena for her constant support and unconditional love. We have shared so much over the past few years and fought very hard to be where we are now. Thank you for always keeping a smile on my face and a joy in my heart.

Table of Contents

List of Tables

List of Figures

Foreword

I would like to spend a few words to introduce the reader to the general scopes of the present dissertation which sprung from the collaboration between Prof. Doghieri's research group at the University of Bologna and the Kenan Institute of Technology, Engineering and Science at NC state in Raleigh, North Carolina, US, where I have happily spent half of my Ph.D. period and where all the experiments have been carried out under the supervision of Prof. Ruben G. Carbonell.

This work was initially aimed at developing a fundamental understanding of the process of microphotolithography, through which millions of microchips are manufactured every year around the world, in order to try and enhance it. However, as it happens often while doing research, the project has taken a rather different path which eventually has lead to very interesting findings in a recent field of research that combines surface thermodynamics, critical fluid phenomena and thin film phenomena, and that give the title to the present effort.

The subdivision in three different parts of this dissertation reflects the original blueprint. An introductory part (chapters I to III) is aimed at introducing the unfamiliar reader to the process of microlithography (chapter I), the properties and general application of supercritical carbon dioxide (chapter II) and the experimental techniques adopted for this study (chapter III).

As we shall see in the first chapter, Microphotolithography consists of using a 'sacrificial' photoresist polymer film spun onto a silicon wafer which is then selectively exposed to a given wavelength (currently 193 nm) in order to render some regions more (positive) or less (negative) soluble in the development solvent (usually an aqueous solution of TMAH). The polymer film function, as the name itself says, is twofold. In fact aside from being able to photochemically react it also must be able to resist the successive etching procedure (plasma) that allows transferring the patterns developed onto the film down to the underlying silicon substrate. The residual polymer is then finally stripped with a much stronger organic solvent.

In the many different stages of the process a lot of aqueous and organic solvents are required, which aside from being not environmentally-friendly, can lead to damages to the features such as *Image Collapse* or *Line Edge Roughness*.

Many authors have pointed out over the years the need for a breakthrough technology in order to solve all the aforementioned issues altogether. We believed that supercritical carbon dioxide could be the answer. CO_2 has many peculiar properties, above all the capacity of tuning its solvent power with small changes of pressure or temperature, that make it ideal for replacing all the traditional microphotographic solvents, achieving *in theory* a fully-dry process. However only highly-fluorinated polymers and siloxanes are readily soluble in CO_2 and this means that either new photoresists or new strategies must be conceived in order to obtain an economically feasible process.

The main aim of the present thesis is to achieve a fundamental understanding of the sorption and dilation behavior of a typical photoresist polymer, *i.e.* PMMA, at two temperatures of industrial interest, 35°C and 50°C, and over a wide range of pressures, from atmospheric up to *ca* 140 bar (well into the supercritical region).

The experimental research has been carried out utilizing two different setups, High-Pressure Ellipsometry (HPE) and Quartz-Crystal Microbalance (QCM), which will be extensively discussed in the introductory part of the present effort.

Most of the results presented, to which part two is entirely devoted, are of paramount importance for a thorough comprehension of the mechanisms behind sorption and swelling of supported polymeric films in carbon dioxide but are not specific to microphotolithographic applications.

A new theoretical approach based on the NET-GP model coupled with a robust mean for predicting glass to rubber transition upon sorption of small molecules (plasticization), such as Chow's theory, has been developed to study sorption and swelling isotherms data obtained with HPE and QCM. Accidentally, as byproduct, an improved Chow's theory has been obtained by re-applying Gibbs-DiMarzio criterion for glass transition temperature depression upon sorption to a more complex partition function (Guggenheim's result).

Another important contribution of the present thesis has been the development of a new transport model, obtained combining our thermodynamic model with a free volume theory for predicting diffusion coefficients and with a simple rheological model for polymer relaxation.

Indeed a great limitation of modern lithographic techniques is represented by the long times required to batch process a wafer, linked to the diffusion times of water solutions within the polymeric film. $ScCO_2$ with its gas-like diffusivity and liquid-like density allows obtaining faster process times, as discussed in the following chapters.

Finally, a great emphasis has been posed on the last part which discusses the physics of thin films brought in contact with supercritical carbon dioxide and which contains the major novelty of the present thesis with respect to existing results in the published literature. The main finding that thin films in supercritical fluids do not behave like their bulk counterparts but present anomalies in the swelling isotherms is worth the title of the present dissertation.

Being born in the US, the present dissertation follows the praxis for American Ph.D. thesis in the sense that its core consists of self-sustaining pieces slightly modified from four manuscripts, rose from this research endeavor, that have been submitted for publications to major journals of polymer chemistry and chemical engineering.

PART I

Introduction

"The real voyage of discovery consists not in seeking new landscapes, but in having new eyes"
Marcel Proust

CHAPTER I

Semiconductor Microphotolithography: Standard process and open challenges

§ 1.1 Optical lithography for microelectronic devices manufacturing

Over the past 30 years, the semiconductor industry has made tremendous improvements in device manufacturing, and device cost reduction. The benefits to industry and society are numerous, including portable computing and communications, information technology, the advent of the World Wide Web, *etc*.

To create even greater processor speed and/or storage capacity, the size of the individual features on devices (and the distance between these features) must be reduced. This reduction in size will also reduce the cost of each device because more devices can be created per wafer, and the cost of batch producing a wafer is (nearly) constant. There is a simultaneous push to reduce the resolution of printed features while increasing the size of the wafers that are used in manufacturing.[1-3]

The trend that the number of devices per wafer doubles every 2 years is known as Moore's law, shown in Figure 1.1.[4] A central goal of the semiconductor industry is to continue the pace of Moore's law for as long as long as possible.

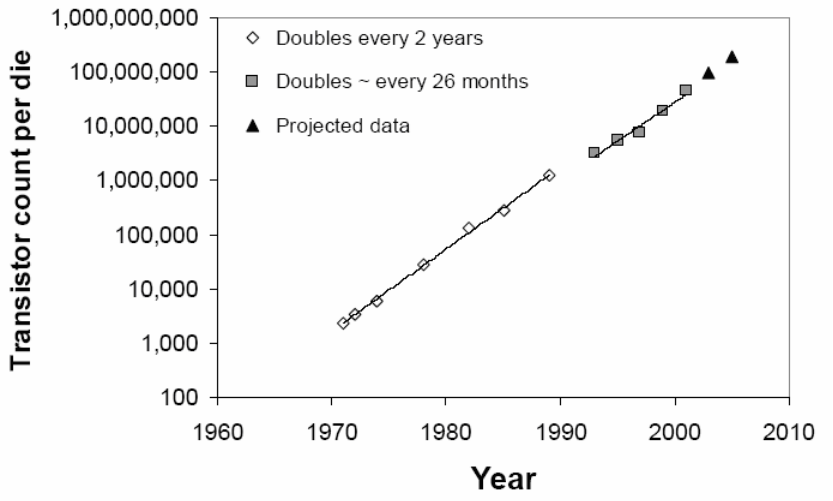

Figure 1.1 Moore's law is the trend that the number of transistors per chip doubles approximately every 2 years.

A simple example of device fabrication process flow is shown in Figure 1.2 in which two resistors in series are fabricated on a silicon substrate.[5]

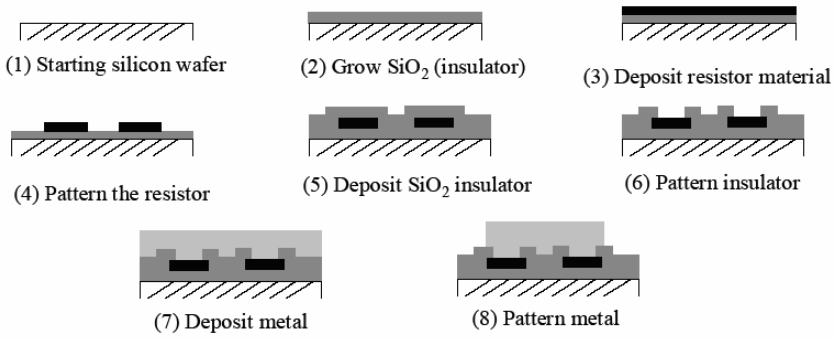

Figure 1.2 A simple example of device fabrication: two resistors in series.

This process involves several steps. First, an oxide insulator is deposited followed by resistor material deposition. The resistor material is patterned and then an insulating layer is deposited. Another patterning step is performed on the

insulating layer and then a metal layer is deposited. Finally, the metal is patterned to form the wire connecting the two resistors. The advantage of this approach is that many devices can be fabricated simultaneously on one wafer, yet the batch cost does not increase with additional devices. More complicated devices, such as transistors and memory devices, require more sophisticated processes, but the principles of batch production are the same. The only limiting factor to the number of devices that can be created is the patterning technology, which makes the patterning step one of the most important to improve in the entire process.

The patterning technology that is responsible for the ultimate feature size on a device is call microphotolithography. Currently, the technology exists to fabricate semiconductor devices with minimum dimensions less than 130 nm in width. A diagram of the lithographic process is shown in Figure 1.3. The primary material used for this process is a sacrificial polymer solution called a photoresist.

The photoresist formulation consists of a polymer resin in an organic casting solvent with a small quantity of a photoactive component, and possibly other performance improving additives. The purpose of the resist is twofold. First, it must be sensitive to exposure by light ("photo"). Second, it must act as a barrier to an etch transfer process, or an ion implantation process ("resist").[1-3]

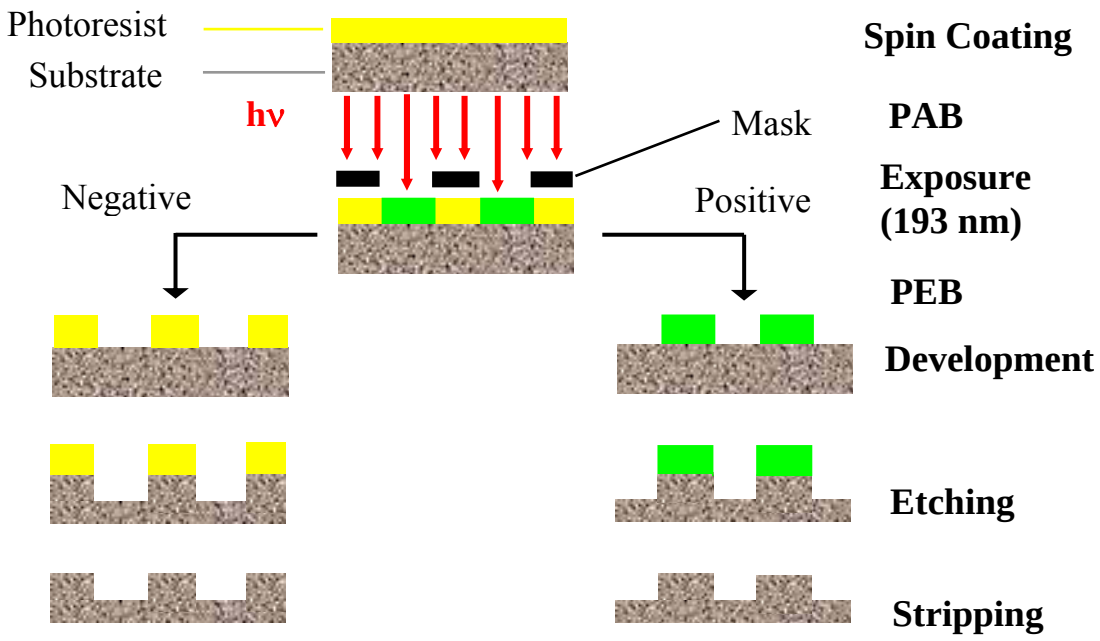

Figure 1.3 Primary steps of a photolithographic process.

The first step in the lithographic process is spin coating the photoresist solution onto the patterning layer. Next, Post-Apply Bake, a bake step, is performed to drive off residual solvent and anneal the film. The wafer is then placed in a "stepper", the purpose of which is to selectively expose the photoresist to monochromatic light through a photomask (a predetermined pattern of chrome on glass). The exposure step, combined with a Post Exposure Bake (PEB) causes a chemical change in regions of the photoresist film. In the case of a positive tone photoresist, the exposed areas are rendered soluble to a particular solvent, usually aqueous base. The aqueous base of choice for the semiconductor industry is 0.26N tetramethyl-ammonium hydroxide, TMAH, primarily because it does not contain metal ions that may contaminate the underlying device.

Likewise, a negative tone renders the exposed areas insoluble to a given solvent. An etch step is then used to transfer the pattern into the underlying layer, and finally the photoresist is removed (stripped) with an organic solvent. The primary advantages of this process are that many relief patterns can be produced simultaneously on a given layer with high throughput. Although the purpose of the resist was stated to be twofold, the number of material requirements is actually quite numerous. For example, adhesion, thermal stability, and good mechanical properties are required.[1-3]

The resolution of the smallest features is given by the Rayleigh criterion:

$$R = k\frac{\lambda}{NA} \tag{1.1}$$

where R is the minimum feature size, λ is the wavelength of light, NA is the numerical aperture of the optical elements in the stepper, and k is a process dependent parameter.[5] In order to reduce the resolution and "print" smaller device features, the wavelength of light must be decreased and/or the numerical aperture must be increased. The wavelength of light used for photoresist exposure has systematically decreased from 436 to 365 to 248 to 193 nm, and now 157 nm[6] is being considered for manufacturing devices with sub 70 nm features. Each downward shift results in several challenges, both in redesigning the exposure source and lens elements as well as the photoresist.

The main challenge in producing new photoresists is to develop a new polymer resin that is transparent at a given wavelength, yet possesses all of the other

necessary features of a photoresist (i.e. etch resistance, solubility switching upon exposure, sensitivity, adhesion, strippability, *etc*.) The synthesis of new photoresist materials is not a direct topic of this work but a little introduction about its historic developments will be given in the following paragraph.

§ 1.2 Brief history of photoresists development

One of the first successful photoresists was a mixture of cyclized poly(cis-isoprene) rubber and a *bis*(arylazide) photoactive sensitizer (shown in Figure 1.4), and was discovered by Hepher and Wagner at Kodak. This was known as the Kodak Thin Film Resist (KTFR), and is a two component, negative-tone resist.[1,3]

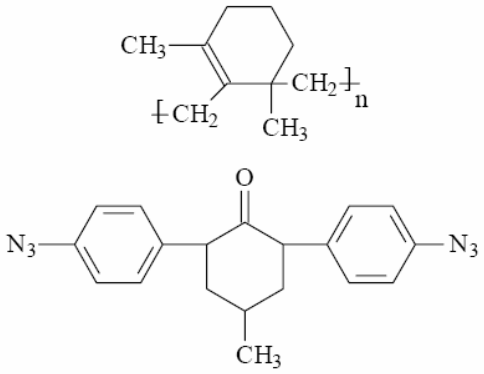

Figure 1.4 The component structure of Kodak thin film resist (KTFR).

In the exposed areas, the photoactive sensitizer decomposes into a highly reactive nitrene compound. This photoproduct is bi-functional, and crosslinks with two polymer chains, greatly increasing the molecular weight of the resin in the exposed areas. The dissolution rate of photoresists is a strong function of molecular weight; therefore, the exposed regions of this resist are rendered insoluble and it is

possible to create a negative tone relief image. The main problem with this resist is that it swells upon dissolution (due also to the high MW).

However, the KTFR was the mainstay of the semiconductor industry from 1957 until the early 1970s, at which point the resist could no longer resolve the micron size features in production at that time.

The next successful class of photoresists were borrowed from the printing plate industry and are known as DNQ/novolac resists.[1-3,7] These 436 and 365 nm photoresists, which were introduced in the early 1970's, are still used in manufacturing for non-critical device layers. This class of photoresist is a two component, positive-tone photoresist. The basic structures of these two components are shown in Figure 1.5. The main advantages of these resists are high contrast, good etch resistance, and limited swelling in aqueous base developer, which allows fabrication of high-aspect-ratio, high-resolution images.[7]

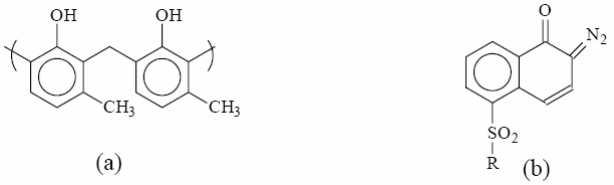

Figure 1.5 Structures of (a) novolac resin and (b) diazonapthoquinone (DNQ)

Novolac is a phenolic polymer with the interesting structural property that the aromatic ring is included in the backbone of the polymer. For nearly all photoresist applications the novolac molecular weight is kept very low, usually between 8-20 repeat units. Perhaps the most important property is that novolac resins are

transparent to 365 nm light (and above), which is a requirement in order to produce resist features from a single layer optical process.[7]

The photoactive component (PAC) of these types of resists is diazonapthoquinone (DNQ). Many different structures can be used for the PAC in novolac/DNQ resists, but they are all derivatives of the basic DNQ molecule.

Many PACs are multifunctional and have more than one photoactive component attached to the same molecule. Upon exposure to 365 nm light (in the presence of water) the DNQ forms an indene carboxylic acid photoproduct and nitrogen evolves from the film as a side product, shown in Figure 1.6. Some side reactions may occur. The photoproduct is much more transparent than the DNQ, a process known as bleaching that is very beneficial in obtaining high-resolution images.[3,7]

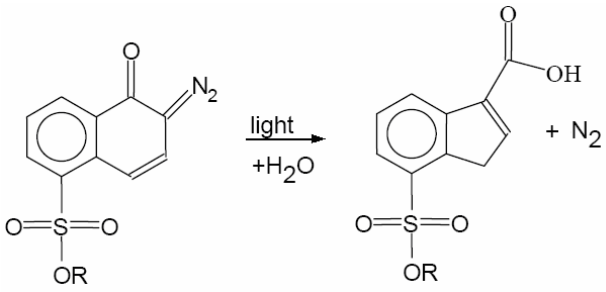

Figure 1.6 Conversion of 2-diazo-1(2H)-naphthalenone-5-sulfonate (left) to an indiene carboxylic acid (right)

Both the DNQ and the photoproduct have significant interactions with the matrix novolac polymer, making the exposure induced reaction (shown in Figure

1.6) a solubility switching reaction. The dissolution rate of the resin is also a strong function of the concentration of DNQ and photoproduct.

In 0.26N TMAH, typical novolac resins dissolve quite rapidly. However, the dissolution rate can be inhibited by 2-3 orders of magnitude by addition of 5-15 wt % DNQ. Upon exposure, the dissolution rate increases slightly above that of the pure novolac resin. This fortuitous interaction allows these photoresists to be successful as 365 nm imaging materials.[3,8-10]

DNQ/Novolac resists have been used successfully in commercial processes at 436 nm and 365 nm exposure. Features as small as 0.25 μm can be produced with these photoresists. However, at lower wavelengths in which powerful exposure sources are available (i.e. 248 nm), novolac resins absorb too much light. It is imperative that the photoresist resin is transparent so that light will penetrate to the bottom of the film. Thinner films could be used, but in that case the etch resistance of the film becomes a significant issue. The trade off between transparency and etch resistance presents a constant challenge in the synthesis of new photoresist resins.[1]

It became clear to researchers that a different polymer would have to be used in order to create smaller features with 248 nm light. A similar phenolic resin, polyhydroxystyrene (PHOST), shown in Figure 1.7, is transparent at 248 nm.

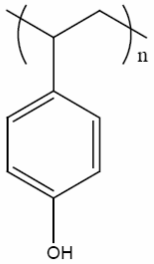

Figure 1.7 Structure of poly(p-hydroxystyrene), PHOST

However, the fortuitous DNQ/novolac interactions are not observed when typical PACs are added to PHOST formulations, despite the fact that the resins are so similar.[11] To date, materials have not been found that inhibit the dissolution of pure PHOST in the same manner as novolac. Since the exposure tool (the "stepper") is the bottleneck of any lithography process due to its large capital cost, 248 nm photoresists needed to be at least as sensitive as traditional novolac/DNQ resist systems so that the exposure time (and throughput) could remain constant.

All of these problems were solved by the advent of a class of photoresists that functioned by a completely different mechanism than traditional DNQ/novolac resists.[11-13]

The novolac/DNQ resists discussed above, as well as other photoresists used for 365 nm or longer wavelength imaging, can all be classified as non-chemically amplified (NCA) resists. Chemically amplified (CA) photoresists can be defined as photoresists in which the photoactive component, upon exposure, becomes a catalyst for further solubility switching reactions. The photoreaction itself does not directly provide the solubility switch as in the case of the novolac/DNQ system. Rather, the photoactive component reacts with light to form a catalyst (usually an acid catalyst).

During a subsequent bake step called a post exposure bake (PEB), the catalyst diffuses and reacts throughout the polymer matrix causing many reactive sites on the polymer to switch from insoluble to soluble monomer units.

A conceptual diagram of this scheme is shown in Figure 1.8. While this design is slightly more complicated and involves an extra reaction step, it is actually advantageous because it minimizes the exposure dose necessary to obtain images, which increases throughput in the bottleneck step of the process. Additionally, some low activation energy CA resists do not require a PEB, because the subsequent reaction occurs at room temperature.

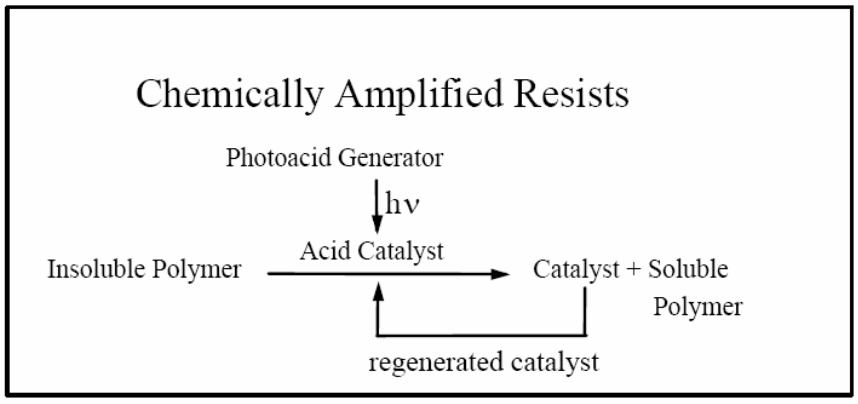

Figure 1.8 Conceptual diagram of chemically amplified photoresists

The successful demonstration of CA resists[11-13] provided viable solutions to the problems stated above, and have been used as the photoresist platform for 248, 193, and now 157 nm lithography.[14]

§ 1.3 Chemically Amplified Resists

Examples of a chemically amplified photoresist are shown in Figure 1.9a-b. The base resin is either poly(*p*-*t*-butyloxycarbonyloxystryrene) (also called *t*-BOCstyrene, or simply tBOC) which consists of a t-butyl blocking group placed on a PHOST resin or poly(methyl methacrylate) (simply PMMA), but other possibilities are viable options as well.

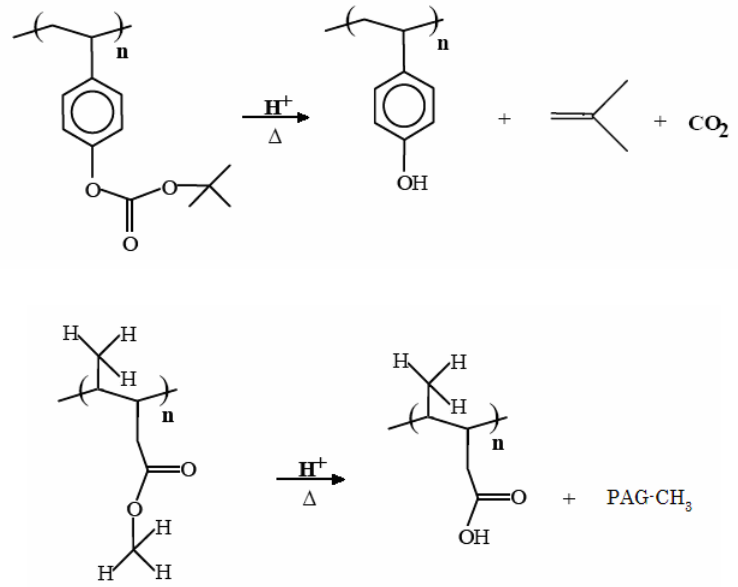

Figure 1.9 Examples of CA resists: (a) tBOC deprotects to form PHOST in the presence of acid and moderate heat and (b) PMMA reduces to PMA with the same mechanism.

These polymers are nearly transparent at 248 nm. In the presence of acid and moderate heat (~90°C), they undergo an acid catalyzed deprotection reaction in which chemicals are evolved from the photoresist as side products (carbon dioxide and isobutylene in the case of tBOC and a PAG-methylate in the case of PMMA). The initial material (tBOC or PMMA) is insoluble to base developer, whereas the final material (PHOST or PMA) is very soluble in base developer due to its acidic

nature. This solubility switch in the exposed areas provides the imaging mechanism. PMMA is the photoresist investigated extensively throughout this dissertation.

A typical photoacid generator (PAG) is shown in Figure 1.10. This molecule, bis,t-butyl phenol iodonium perfluorobutane sulfonate salt, reacts with light to produce perfluorobutane sulfonate acid and by-products. A typical PAG loading for a photoresist is 2.5 wt %, which corresponds to approximately one acid molecule for every 160 blocked sites (for a completely blocked polymer). In order for the deprotection reaction to continue to completion, the catalytic chain length of the acid must be at least 160. This number may be higher due to the efficiency of the exposure reaction and the fact that low exposure areas must also be rendered insoluble.[1] McKean *et al* estimate the catalytic chain length to be ~ 1000.

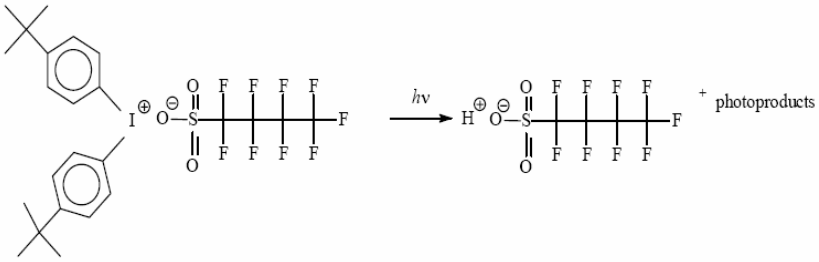

Figure 1.10 Photolysis reaction of a typical photoacidgenerator (PAG)

The high catalytic chain length provides sensitivity; low exposure doses can be used, resulting in large throughput during the bottleneck exposure step of the process. However, the large catalytic chain length also suggests that acid may migrate into areas that are unexposed, a detrimental effect that is known as acid diffusion.

§ 1.4 Current challenges in Microphotolitography (MPLG)

Before CA resists were introduced, it was thought that acid diffusion may cause complete image blur, rendering the entire film insoluble (fig. 1.11). However, it was determined that resist images could be resolved, albeit with a small degree of image blur.[13]

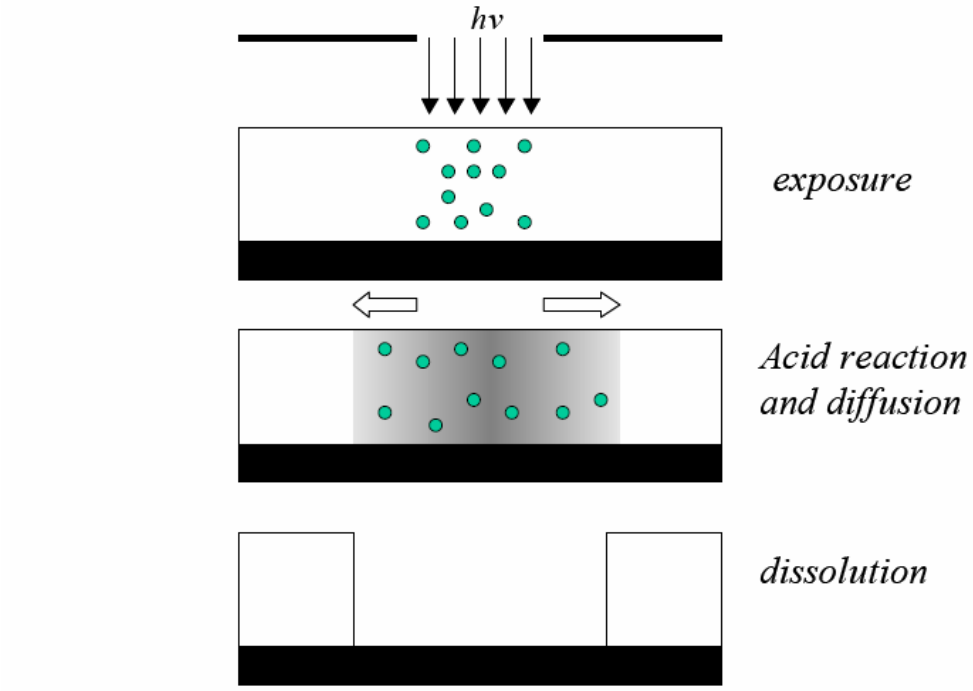

Figure 1.11 Diagram of line-width spread due to acid reaction and transport

This blurring effect becomes increasingly significant as feature and sizes are reduced. An experiment by Willson *et al.* with a thin (~ 2 nm) electron beam exposure resulted in a ~40 nm feature with tBOC.[15] However, it has been shown that (for a PEB of given temperature and time) diffusion is reduced in cases where the blocking fraction has been reduced.[16] Results of this nature indicate that acid

diffusion may not be an immediately prohibitive issue in the continued use of CA photoresists, but it provides serious engineering challenges.

Another related problem, caused in part by acid catalyzed deprotection and diffusion, is line edge roughness (LER), an example of which is shown in Figure 1.12.

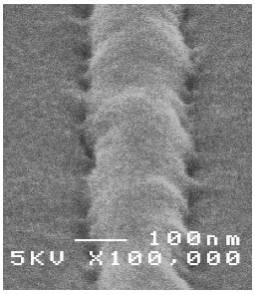

Figure 1.12 Line edge roughness on a feature seen with SEM.

As the miniaturization of electronic devices continues, line edge roughness (LER) is becoming an increasingly important problem to understand and control.

LER is defined as the variation in CD (critical dimension) along a feature edge. There are generally two types of line edge roughness encountered: low frequency and high frequency roughness depicted in Figure 1.13 (b) and (c). In this case the labels are obvious, but there are no strict definitions for these two cases. Currently, processes exist in semiconductor manufacturing that use 193 nm light to produce 130 nm structures with ~7 nm of line edge roughness (LER).

The International Roadmap for Semiconductors (2001) states that by 2005, 90 nm features with 4 nm of LER will be required. By 2016, 25 nm features with 1 nm of LER will be needed.[1] There are currently no known solutions for reducing LER, and a

large amount of research has recently been invested into determining the fundamental causes of LER and potential solutions.[2-10] Note that the future LER requirement (1nm) is *smaller* than the characteristic polymer size (3-7 nm) in the photoresist film!

It's important to note that LER of the resist image does not directly affect any property of the final device; rather, it is the LER of the etch-transferred feature that matters. If an etch process could be developed to "smooth out" LER of the resist during the etch transfer, then it would not be necessary to significantly minimize (nor to understand) LER formation in the resist image.

However, it is expected that etch transfer processes will not be capable of smoothing large amounts of LER, and that all efforts must be made to minimize LER during initial lithography imaging, that is why a lot of research into etch transferred LER is ongoing.[11,17]

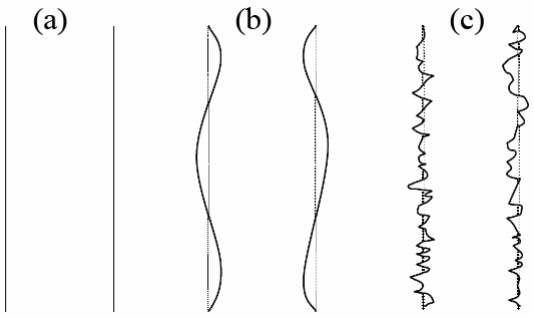

Figure 1.13 Top down diagram of line edge roughness (LER). (a) smooth feature, (b) low frequency LER, (c) high frequency LER

Even if LER represents a clear shortcoming of present lithographic technologies, perhaps the most relevant and stringent issue for microelectronic industries today is represented by a different phenomenon, known as *image collapse* or simply *IC*.[17-21]

IC could occur at any stage of the process but is mostly associated with the final operation of drying water out of the already developed features. Water has a very high surface tension which combined with the high aspect ratio of the features gives rise to strong bending forces that tend to fold and eventually lead to breaking and peeling off of the wanted patterns, as Figures 1.14 and 1.15 illustrate.

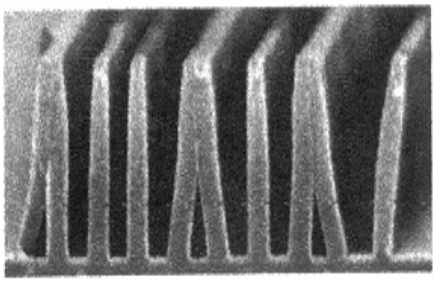

Figure 1.14 Image collapse seen with SEM, features developed on a silicon wafer collapse during drying because of the high surface energy of water.

While many procedures have been developed over time to try and repair the damages due to IC, it has always been highly desirable to achieve a process that will enable to get rid of IC altogether.

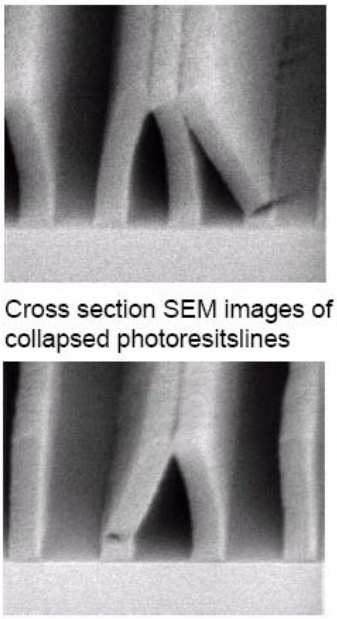

Figure 1.15 SEM images of IC, notice the lower aspect ratio compared to the previous picture.

Considering in more details the *bending beam problem* can help provide some insights to better understand the dynamics of this phenomenon and lead to possible solutions. Figures 1.16 and 1.17 depict a schematic representation of the physical situation leading to *IC*.

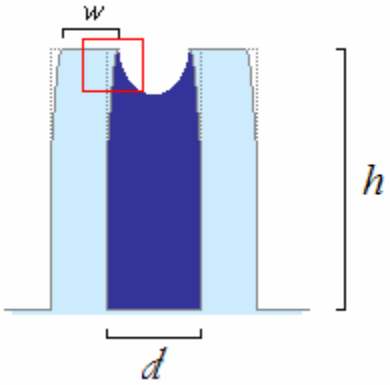

Figure 1.16 Schematic representation of the bending beam problem.

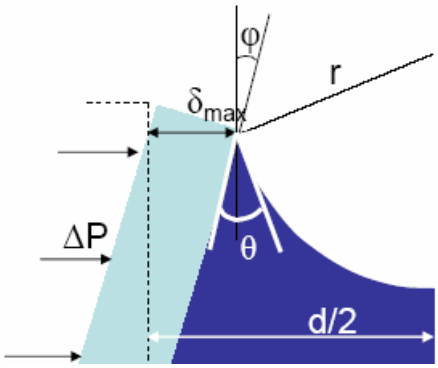

Figure 1.17 Enlargement of the inset from the above picture.

The surface tension of water γ, applied in the region highlighted in Figure 1.17, can be converted in a difference of pressure between the two sides of the feature and imagined diffused throughout the film height as follows[22]:

$$\Delta P = \frac{\gamma \cos(\theta - \varphi)}{\left(d/2 - \delta_{\max}\right)} \qquad (1.2)$$

with clear meaning of the symbols. ΔP is considered as bending force in a force balance together with the material reaction which holds against the surface tension and tends to restore the original shape of the feature.

As first approximation[22-25], assuming linear elasticity for the polymer one has:

$$A_c = \left(\frac{h}{w}\right) = \sqrt[3]{\frac{E}{4\left(1-\mu^2\right)}\frac{\delta_{\max}}{\Delta P}} \qquad (1.3)$$

where A_c stands for critical Aspect ratio, which is the aspect ratio after which breaking according to the bending beam theory occurs. Clearly reducing the bending force, or else the surface tension, will help prevent IC.

A further aspect that could be improved upon is the time required to process a batch, which for a 100 μm thick Novolac film is longer than 45 minutes. Long processing times mean usually added costs and more risks for damages.

Given that the limiting time step is the transport of water within the polymer which in turns is dependent upon the low diffusion coefficients of water a different choice of solvent could help speed up the process and reduce the time needed.

Last but not least there are growing concerns about environmental and heath safety issues related to the heavy consumption of toxic solvents during the many stages of the standard process, according to a recent report on the state-of-the-art for microelectronic industries (Williams rep. 2002) in order to produce 2 kg of microchips, 1.7 kg of chemicals and fossil fuels, 32 kg of water and 0.7 kg of noble gases are needed.

§ 1.5 Next generation technology: Is Dry-Microphotolithography really the answer?

In order to tackle all the issues raised in the previous paragraph many researchers[26-30] have pointed out that a brand new approach is necessary. This could be provided by what has been called *Dry-Microphotolithography*.

Dry-MPLG is based on the idea that carbon dioxide (CO_2) alone could successfully replace all the existing solvents in an economic-effective way. As it

will be discussed further in the following chapter, carbon dioxide possesses many unique properties, such as its tunable solvent power, that could allow it to be used as solvent in MPLG. However, whereas CO_2 absorbs and swells many polymers to a certain degree, only highly-fluorinated polymers and siloxanes are known to fully dissolve in CO_2.

This evidence would point to the need of designing and synthesizing a new kind of photoresist for Dry-MPLG or else of combining the properties of carbon dioxide with those of traditional solvents in a process that cannot be defined as truly *'fully dry'* but that surely represents and improvement upon the existing process and could help solve many of the aforementioned issues.

This dissertation aims at providing insights into the latter idea through a series of cunning tests and theoretical studies conceived to ascertain the feasibility of such a 'pseudo-dry' MPLG as suitable alternative to standard Microphotolithography.

The fundamental idea behind this project consists in the recent discovery that nearly every un-crosslinked polymer can be dissolved in $scCO_2$ if a small amount of its monomer (or else any other solvent compatible with CO_2) is added, forming a three-component system (four if we include the PAG). CO_2 role is twofold it acts as a plasticizer opening-up the entangled network of chains and as a carrier enhancing the solvent power of the third component, which given its affinity with the polymer is eventually able to dissolve it.

Even though the mechanism behind polymer dissolution in $scCO_2$ is not completely understood, it is believed to be rather different than classic dissolution with liquid solvents. Due to the fluctuating nature of the supercritical fluid, polymer

chains are forced to move of an oscillation movement, much like the way shoestrings untie from a loose knot while walking.

Given the fact that the third component (real solvent) is usually a very small volume fraction of the mixture, as first approximation and through the rest of this endeavor a two-component system will always be considered (PMMA- CO_2).

The *key questions* that will take us throughout this work are then formulated in terms of a photoresist film made of exposed and un-exposed region:

- *How fast will the exposed regions dissolve in $scCO_2$?*
- *How much will the unexposed regions swell and is this swelling reversible?*
- *Is the quality of the final product superior to that achieved with the standard technology, in particular can IC be overcome?*
- *How will ultra-thin films (below 100nm) behave in contact with $scCO_2$?*

In an attempt to answer these questions the present thesis has been divided into three parts. Part I is meant to be an introductive part and it comprises this chapter that introduces the whole argument, along with chapter II, which is an introduction to supercritical fluids and SCFs polymer processing, and chapter III that introduces the reader to both experimental techniques HPE and QCM widely adopted in this dissertation as means of investigation for the properties of our system, PMMA-CO_2, chosen because of the abundant literature data to which compare our own for reference.

The second part (chapters IV to VI), the core of this effort, consists mainly of reprints from manuscripts by the author, either already published or submitted for publication. Each one of these chapters is about a different aspect and is meant to tackle one of the key questions raised before.

Chapter IV contains the basic development of the sorption and dilation isotherms of PMMA in carbon dioxide, along with the thermodynamic model developed by the author to analyze such isotherms. This contribution helps explaining how PMMA swells in carbon dioxide and what the extent of dilation is once the pressure returns to atmospheric conditions.

In Chapter V a well-established theory, Chow's expression for glass temperature depression upon plasticizer sorption, will be revisited and interesting new aspects pointed out to the reader.

A transport model aimed at studying dynamics of our system is developed in Chapter VI, from a combination of the thermodynamic model discussed earlier with a rheological simple expression for the key variable considered in the system, the polymer density. The development of such a model is a prerequisite for obtaining information about polymer dissolution.

Finally in part III, which comprises chapter VII and the conclusions, a new interesting phenomenon, an anomalous behavior consisting in a maximum in the swelling isotherm, that occurs when operating with a very thin film (below 100nm) at high pressures (around the critical pressure) will be discussed in details and explained in the light of surface thermodynamics and supercritical adsorption phenomena.

§ 1.6 References

(1) Thompson, L. F.; Willson, C. G.; Bowden, M. J. *Introduction to Microlithography*; 2nd ed.; American Chemical Society: Washington D.C., 1994.

(2) Moreau, W. M. *Semiconductor Lithography: Principles, Practices, andMaterials*; Plenum Publishing: New York, 1988.

(3) Reiser, A. *Photoreactive Polymers*; John Wiley & Sons: New York, 1989.

(4) <*http://www.intel.com/pressroom/kits/quickrefyr.htm*>; *2003-05-International Technology Roadmap for Semiconductors, available at* <*http://public.itrs.net/Files/2000/UpdateFinal/ORTC2000final.pdf*>. **2002**.

(5) Campbell, S. A. *The Science and Engineering of Microelectronic Fabrication*; Oxford University Press: New York, 2001.

(6) Patterson, K.; Somervell, M.; Willson, C. G. *Solid State Technol.* **2000**, *43*, 41.

(7) Dammel, R. *Diazonapthoquinone-based Resists*; SPIE Optical Engineering Press: Bellingham, Washington, 1993.

(8) Mack, C. A. *Inside Prolith: A Comprehensive Guide to Optical Lithography simulation*; FINLE Technologies: Austin, TX, 1997.

(9) Burns, S. D.; Gardiner, A.; Krukonis, V.; Wetmore, P.; Schmid, G. M.; Lutkenhaus, J.; Flanagin, L. W.; Willson, C. G. *Proc. SPIE* **2001**, *4345*,37-49.

(10) Pol, V.; Bennewitz, J. H.; Escher, G. C.; Feldman, M.; Firtion, V.; Jewell, T. E.; Wilcomb, B. E.; Clemens, J. T. *Proc. SPIE* **1986**, *633*, 6.

(11) Ito, H.; Willson, C. G. *Polym. Eng. Sci.* **1983**, *23*, 1012-1018.

(12) Frechet, J. M. J.; Eichler, E.; Ito, H.; Willson, C. G. *Polymer* **1983**, *24*,995-1000.

(13) Willson, C. G. *Acs Symposium Series* **1983**, *219*, 87-159.

(14) Stewart, M. D.; Patterson, K.; Somervell, M.; Willson, C. G. *J. PhysicalOrganic Chemistry* **2000**, *13*, 767-764.

(15) Umbach, C. P.; Broers, A. N.; Willson, C. G.; Koch, R.; Laibowitz, R. B. *J. Vac. Sci. Technol. B* **1988**, *6*, 319-322.

(16) Stewart, M. D.; Schmid, G. M.; Postnikov, S.; Willson, C. G. *Proc. SPIE* **2001**, *4345*, 10-18.

(17) Houle, F. A.; Hinsberg, W. D.; Morrison, M.; Sanchez, M. I.; Wallraff, G. M.; Larson, C. E.; Hoffnagle, J. *J. Vac. Sci. & Tech. B* **2000**, *18*, 1874.

(18) Postnikov, S.; Stewart, M. D.; Tran, H. V.; Nierode, M.; Medeiros, D.; Cao, T.; Byers, J.; Webber, S.; Willson, C. G. *J. Vac. Sci. & Tech. B* **1999**, *17*, 2965-2969.

(19) Burns, S. D.; Stewart, M. D.; Hilfiker, J. N.; Synowicki, R. A.; Schmid, G.M.; Brodsky, C.; Willson, C. G. *Forefront of Lithographic Materials Research, Proc. of the 12th International Conference on Photopolymers* **2000**, 232-334.

(20) Hinsberg, W. D.; Houle, F. A.; Poliskie, G. M.; Pearson, D.; Sanchez, M. I.; Ito, H. *Journal of Physical Chemistry A* **2002**, *106*, 9776-9787.

(21) Lin, E. K.; Soles, C. L.; Goldfarb, D. L.; Trinque, B.; Burns, S. D.; Jones, R. L.; Lenhart, J. L.; Angelopoulos, M.; Willson, C. G.; Satija, S. K.; Wu, W.-l. *Science* **2002**, *297*, 372.

(22) Stewart, M. D.; Tran, H. V.; Schmid, G. M.; Stachowiak, T.; Becker, D. J.; Willson, C. G. *J. Vac. Sci. & Tech. B* **2002**, *20*, 2946.

(23) Hinsberg, W. D.; Houle, F. A.; Sanchez, M. I.; Wallraff, G. M. *Ibm Journal of Research and Development* **2001**, *45*, 667-682.

(24) Kunz, R. R.; Allen, R. D.; Hinsberg, W. D.; Wallraff, G. M. *Proc. SPIE* **1993**, *1672*, 66.

(25) Allen, R. D.; Wallraff, G. M.; Hinsberg, W. D.; Conley, W. E.; Kunz, R. R. *J. Photopolymer Sci. Tech.* **1993**, *6*, 575.

(26) Goken, H.; Esho, S.; Ohnishi, Y. *J. Electrochem. Soc.* **1983**, *130*, 143.

(27) Kaimoto, Y.; Nozaki, K.; Takechi, S.; Abe, N. *Proc. SPIE* **1992**, *1672*.

(28) Allen, R. D.; Wallraff, G. M.; Hofer, D. C.; Kunz, R. R. *IBM J. Res. Dev.***1997**, *41*, 95.

(29) Houlihan, F. M. J.; TI, W.; Nalamasu, O.; Reichmanis, E. *Macromolecules* **1997**, *30*, 6517.

(30) Okoroanyanwu, U.; Shimokawa, T.; Medeiros, D.; Willson, C. G.; Frechet, J. M. J.; J.Q., N.; Byers, J.; Allen, R. D. *Proc. SPIE* **1997**, *3049*.

CHAPTER II

Polymer processing in Supercritical carbon dioxide

Prior to discuss in further detail SCFs polymer processing for microelectronic device manufacturing, it is essential to review the properties of SCFs and their interactions with polymers. In this chapter, without the ambition of being completely exhaustive of the vast literature, we present an overview of the properties of SCFs and more specifically $scCO_2$. Given their importance, the interaction of $scCO_2$ with thin films, to which chapter VII is entirely dedicated, will also be briefly outlined here.

§ 2.1 Properties of Supercritical Fluids

A supercritical fluid, SCF, is a substance elevated above both its critical temperature and pressure.[1] The supercritical state is a distinct phase of matter, separate from the liquid and gas phases. SCFs have properties that often lie between those of liquids and gases. To illustrate this point, consider the compression of a gas to a liquid following two different pathways, as shown in Figure 2.1.

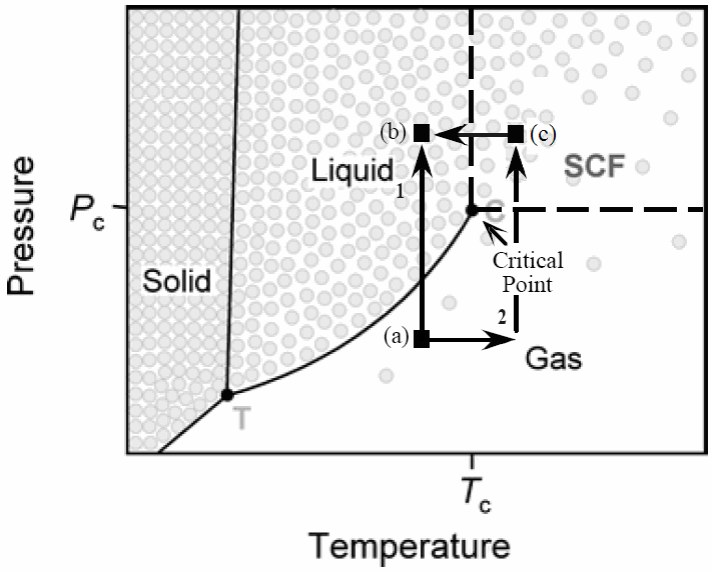

Figure 2.1 Pressure-temperature diagram for a pure fluid phase change from (a) to (b) by two paths, across the liquid-vapor equilibrium line and through the supercritical region.[2]

The first pathway, (1), consists of an isothermal compression of the gas, beginning from point (a) as seen in the figure. When the compression reaches the vapor-liquid equilibrium line, two phases coexist, *i.e.* liquid and gas. As a result of the first order phase change and the discontinuity it creates, the physical properties of these two phases are significantly different. The continued compression of the fluid results in a pure liquid phase, point (b). The same compression can proceed through the supercritical region by a separate three-step pathway, (2). In this case, the first step is isobaric heating above the critical temperature, followed by isothermal compression above the critical pressure, resulting in a SCF, (c). After isobaric cooling the same final liquid, point (b), is obtained.

During the second process, no distinct phase boundaries are crossed, implying no first order phase transition. Thus, the properties of the fluid must vary smoothly,

resulting in a continuum of properties between those of the gas and the liquid. The ability of a SCF to achieve this continuum of fluid properties makes them attractive in many applications, because advantage can be taken of properties not found in either the gas or liquid states.

Because of the direct relationship between density and pressure for a SCF, a continuum of densities ranging from vapor-like to liquid-like can be obtained by varying the pressure of the fluid at constant temperature, while maintaining a one phase system. Near infinite compressibilities at the critical point are possible.

Because minimal pressure changes result in significant density variations, this behavior produces large deviations in the Hildebrand solubility parameter, δ, which can be tailored to creating a situation where chemicals can be pulled into or dropped out of solution by selectively changing system pressure. This "tunability" with pressure is not limited to density. Other properties like viscosity, dielectric constant and thermal conductivity are also tunable with pressure and temperature.

§ 2.2 Supercritical CO_2

In recent years, supercritical and liquid CO_2 have emerged as leading alternatives to toxic organic solvents[1,3,4]. Annually, billions of kilograms of organic and halogenated solvents are used in industrial processes. Environmental concerns over the use of these toxic solvents have spurred the search for viable alternatives. Carbon dioxide is an attractive alternative because it is abundant, nontoxic, and nonflammable.

A phase diagram of CO_2 is presented in Figure 2.2.[3] By examination of Figure 2.2, the critical point of CO_2 can be found to occur at a temperature of 31.1°C and a pressure of 7.38 MPa (73.8 bar). This critical temperature is relatively low as compared to the critical temperatures of water (374.2°C), propane (96.7°C), or methanol (239.5°C), and makes the supercritical region of CO_2 easily accessible to thermally unstable solutes, including many polymeric materials.[4] The critical pressure of CO_2 is regularly achieved in some common industrial processes, making some applications ideal candidates for SCF adaptation.

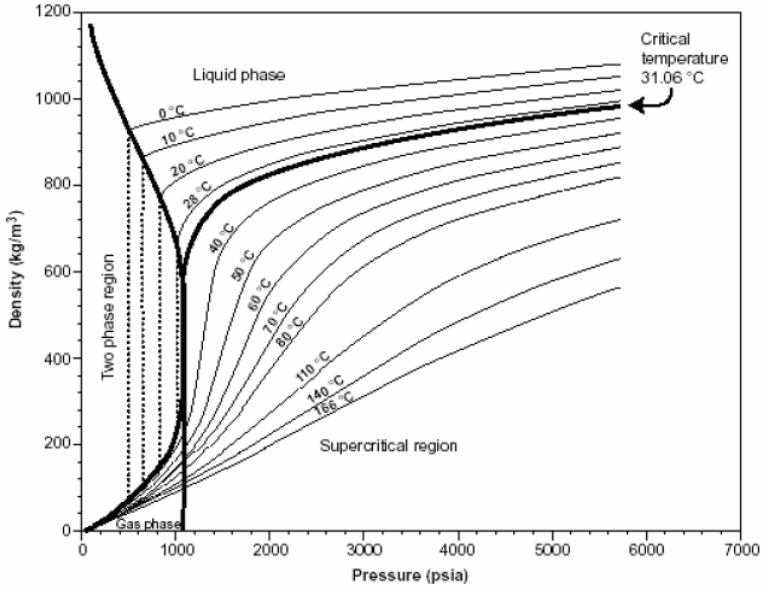

Figure 2.2 Carbon dioxide phase diagram

The unique physical properties of $scCO_2$ have been exploited in a number of both laboratory and industrial scale applications. Some examples include SCF extractions[4], homogeneous and heterogeneous polymerizations[6-8], enhanced oil recovery[9], and as a solvent medium for fluoropolymer coatings[10]. In addition, CO_2 is

non-corrosive, inexpensive and environmentally benign. Instead other commonly studied SCFs, such as scH_2O or sc-pentane are either extremely corrosive, or flammable[2].

In addition to environmental benefits, CO_2 offers other advantages in materials processing due to its low surface tension and its ability to swell, plasticize, and selectively dissolve compounds. The unique properties of CO_2 have been used advantageously in the modification of polymeric films through extractions and impregnations[2,4], plasticization[5], foaming[6], as well as the coating[4], developing[7], drying, and stripping of photoresist films in lithography[1,8,9].

Furthermore, many novel colloidal phenomena have been undertaken using CO_2 as the solvent, including the synthesis and stabilization of emulsions, microemulsions[10,11], nanocrystals[12], and latexes formed by dispersion polymerization[13] as well as the production of nanoparticles for drug formulation[14].

In order to use CO_2 in environmentally responsible processes, surfactants and polymers have to be developed to transport and stabilize insoluble dispersions. Designing effective stabilizers is a difficult challenge since CO_2 has no permanent dipole moment and has a low polarizability per volume (*i.e.*, weak van der Waals interactions) causing many nonvolatile compounds to be insoluble.

It has been found that polymers with low surface tension, and hence low cohesive energy densities, are most compatible as CO_2 stabilizers. This class of "CO_2-philic" stabilizers includes fluoroacrylates, fluoroethers, siloxanes, propylene oxides, polycarbonate copolymers, acetylated sugars, and some hydrocarbons[15-20].

While many small molecules are soluble in $scCO_2$, most polymeric materials have been found insoluble. Since 1992, DeSimone et al. have shown that many high molecular-weight fluorinated polymers are readily soluble and synthesized in $scCO_2$[8,11]. This has lead to the development of block co-polymer surfactants, which increase the utility of $scCO_2$ as a solvent for common hydrocarbon-based polymers[12]. While most polymeric materials themselves are not readily soluble in $scCO_2$, $scCO_2$ itself is soluble to moderately high weight fractions in a number of engineering polymers under elevated pressures. Examples of these are PDMS[13], PEEK[15], PC[16], PET[17], PMMA[18,19], PS[20] and polyurethane[21].

An understanding of the relationship between pressure and the solvent quality of $scCO_2$ can be gained by examining the Hildebrand solubility parameter, δ[22]. From thermo-chemical studies on polymer-solvent interactions, it is expected that when δ values of the polymer and solvent are similar, maximum solubility will occur[22]. As the values of δ diverge from one another, interaction is minimized, and eventually the polymer will become immiscible in the solvent. The solubility parameter for gaseous, liquid, and supercritical CO_2 is shown in Figure 2.3[23]. Below the critical point (–30 °C) a jump occurs in δ at the vapor pressure, corresponding to the phase change between liquid and gas. The solubility parameter for gaseous carbon dioxide is essentially zero whereas the value for liquid CO_2 is more comparable with a typical hydrocarbon value, near 9 $(cal/cc)^{(1/2)}$. However, at temperatures at or above the critical point (31°C, 70°C) it is possible to vary δ between gaseous and liquid-like values[23]. Similar "tunability" of $scCO_2$ viscosity can be seen in Figure 2.4[24]. The wide range of achievable values for the solubility parameter, the viscosity and density

allow the solvent quality of $scCO_2$ with respect to a specific solute to vary from good to poor with small changes in pressure and could help to solve many of the issues raised in the previous chapter.

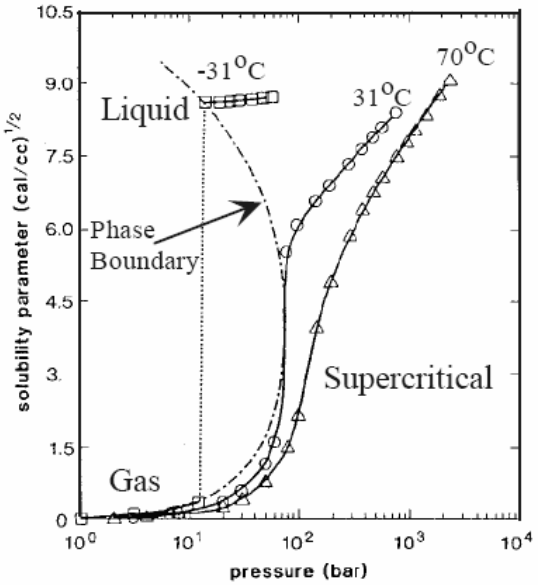

Figure 2.3 Solubility parameter, δ, of CO_2: at -31°C the fluid undergoes a first-order phase transition, resulting in a step change in δ from liquid to gas. Above the critical point, (31°C, 73bar) a continuum of properties exists, allowing previously unstable values to be achieved.

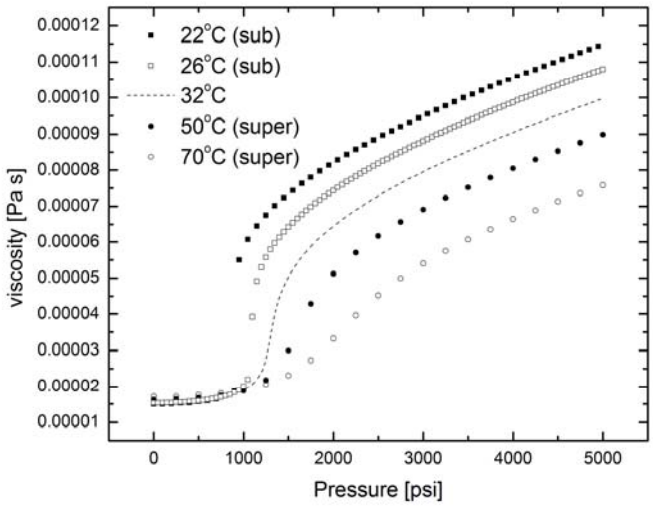

Figure 2.4 Viscosity continuum for supercritical CO_2: at the subcritical conditions there is a viscosity gap due to the first-order phase transition.

§ 2.3 Polymers in CO_2

§ 2.3.1 Plasticization of Polymers

According to the 1951 Council of the International Union of Pure and Applied Chemistry[25]:

> "A plasticizer or softener is a substance or material incorporated in a material to increase its flexibility, workability or distensibility. A plasticizer may reduce the melt viscosity, lower the temperature of second order transitions or lower the elastic modulus of the product."

In general, there are two types of plasticizers, internal and external. When a polymer undergoes a chemical modification or a copolymerization reaction is used to alter the chemical structure of a base polymer to improve flexibility or low temperature properties, it is referred to as internal plasticization. External plasticization is accomplished by addition of a discrete material into the polymer matrix, which brings about the same result of enhanced flexibility and low temperature properties. Our discussion will be limited to external plasticizers only, as this is an important part of this research endeavor to which chapter V will be entirely devoted.

External plasticizers are most often used either to modify the mechanical properties of end-of-the-line products, such as PVC tubing, or during processing to reduce the large energy costs associated with mixing highly viscous materials[26]. These plasticizers are typically small molecules that are compatible with a host polymer allowing them to penetrate much like a solvent[27].

Compressed fluids like supercritical CO_2, N_2O, propane, and C_2H_4, can dissolve to appreciably high levels in polymers at elevated pressures, as previously discussed[28]. The absorption of these fluids modifies the polymer by swelling the matrix and increasing free-volume and chain mobility. Free-volume is defined as the unoccupied space inside of a polymer matrix, into which polymer chains can move[29].

§ 2.3.2 Interaction of CO_2 with Polymers

Carbon dioxide exhibits significant specific interactions with many polymers, mainly due to its large quadruple moment[29]. These interactions often result in high sorption levels of CO_2 in polymers and can also greatly affect the solubility of many polymers and surfactants in CO_2.

$ScCO_2$ is also an efficient plasticizing agent because of its unique fluid properties. Its liquid-like density, high diffusivity, and low molecular weight make it soluble up to high weight fractions of 10-20% in a variety of different polymers[35-37].

$ScCO_2$ behaves much like a typical low molecular weight plasticizer but its concentration can be selectively tailored by controlling the pressure. This phenomenon is referred to as *gas-induced plasticization*. Gas-induced plasticization allows an initially glassy polymer to demonstrate the flexible properties associated with a rubbery or liquid-like state. By lowering the T_g and reducing viscosity, new processing windows may be available for the plasticized polymer melts that not only reduce energy costs, but also improve the efficiency of the process[34].

The specific effects of the high solubility of CO_2 on the plasticization of polymers are shown in Figure 2.5 and 2.6 for PS[29] and in Figure 2.7[38] for PMMA.

In general the plasticization of an amorphous polymer by $scCO_2$ has three distinct regions as shown by Figure 2.5. In region I, the swelling of the polymer matrix by the dissolved gas dramatically lowers T_g. This drop in T_g can occur even with small concentrations of CO_2 in the matrix (1-5 wt%)[20]. In region II, a constant T_g is observed at significantly lower temperatures than that of the pure substance, T_g^o. The large hydrostatic pressures generated to increase the solubility of the CO_2 dominate in region III.

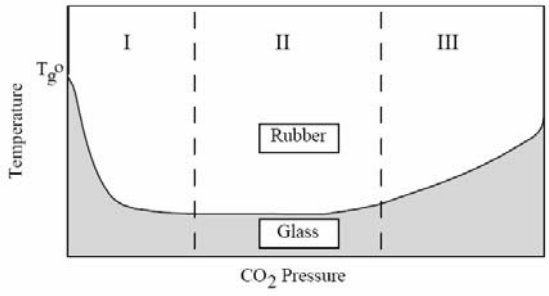

Figure 2.5 Example of glass-rubber transition for a generic polymer in CO_2

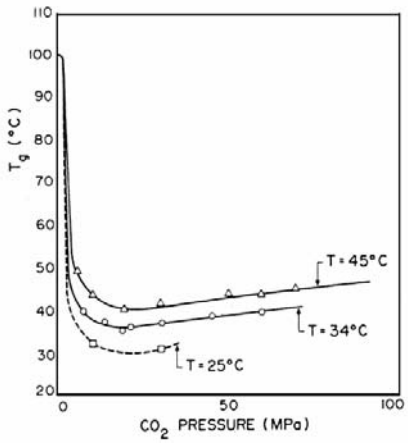

Figure 2.6 T_g of polystyrene as a function of CO_2 pressure.

Loss of free volume observed by the compression of the matrix by hydrostatic pressure results ultimately in a T_g increase. The size of each region and the amount of plasticization depends on the degree of swelling of the matrix, the polymer compressibility, and the solubility of CO_2 in the polymer. Similar behavior has been observed for the phase behavior of polymer blends plasticized by CO_2[38,39].

Condo and Johnston observed reductions of up to 100°C in the CO_2-induced glass transition of poly(methyl methacrylate) (PMMA) as shown in Figure 2.7[38].

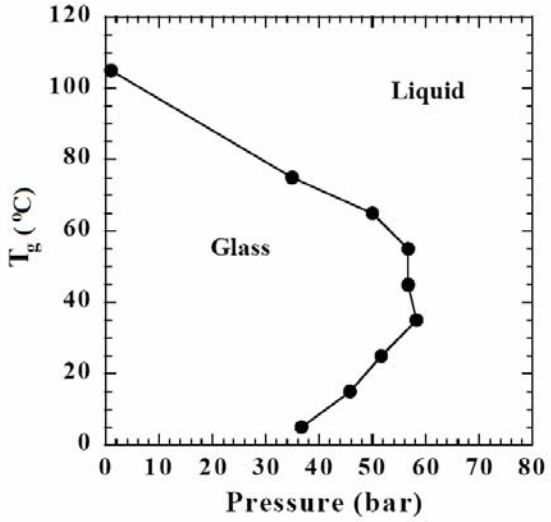

Figure 2.7 Glass transition temperature of PMMA as a function of CO_2 pressure as measured by creep compliance[22].

In addition, the phenomenon of *retrograde vitrification* has been observed for the PMMA/CO_2 system. Retrograde vitrification occurs when a liquid to glass transition takes place with an *increase* in T and it arises from the complex behavior of T and P on the sorption of CO_2 in the polymer[14,23].

Others have also reported large reductions in the coexistence T of polymer blends with sorbed CO_2[40]. RamachandraRao and Watkins observed reductions of up to 90 °C

in the lower critical solution temperature (LCST) phase boundary of polystyrene-poly(vinyl methyl ether) blends[40]. This CO_2-induced phase separation occurs with the sorption of very small amounts of CO_2 (~3.5 wt. %). This marked reduction in the phase separation *T* arises from the increasing difference in free volume of the polymer components in the blend facilitated by the sorption of CO_2. This disparity in free volume is entropically unfavorable and results in phase separation[40].

Carbon dioxide has tremendous potential in modifying polymeric materials. The ability of CO_2 to adsorb into and subsequently plasticize many polymers, while at the same time remaining a poor solvent for these materials, allows for the opportunity to alter polymer morphologies. For example, researchers have demonstrated the use of CO_2 as an effective foaming agent[6,41] for producing microcellular foams in PMMA.

Liquid and supercritical CO_2 also contribute to materials modification through the ability to extract and impregnate compounds into and/or from polymeric matrices. Extracting impurities, additives, or unreacted species from polymers with compressed CO_2 can be advantageous because of the high diffusivities, low surface tension, and large swelling and plasticization of the polymeric matrices[42]. These same properties can also be used advantageously for impregnating polymers. Supercritical CO_2 impregnation of polymers with dyes[43], organo-metallic complexes[43], and other monomers[26] have been demonstrated.

Furthermore, CO_2 high volatility offers the advantage of not leaving any residues in these materials, a property that has important implications for biomaterials applications.

§ 2.3.3 Polymeric Gas Separation Membranes

In order to make CO_2 an economically viable solvent, novel separation methods will have to be developed. High pressure CO_2 separations are attractive for avoiding high raw material and recompression costs resulting from the expensive nature of most "CO_2-phillic" stabilizers along with the high pressures involved in supercritical applications. Polymeric membranes are strong candidates for these types of separations.

Polyimide membranes have excellent gas separation properties especially for streams in which the permeated species has a larger diffusion coefficient than other components in the feed. Removing CO_2 from natural gas streams or from surfactant solutions would be an example of this type of separation. However, the same properties of CO_2 that make it effective at dilating and plasticizing polymers are detrimental to membrane performance. In membrane applications, swelling and plasticization compromise the selectivity of the membrane. Thus, designing membranes for high pressure CO_2-based separations presents a difficult engineering challenge.

In order for polyimide membranes to be used effectively in high pressure CO_2 separations, a better understanding of the CO_2/polyimide interactions is a must. Specifically, it is important to understand how the sorption, dilation, and diffusion processes are coupled in a polyimide gas separation membrane in the presence of high CO_2 concentrations. For more details on this aspect the willing reader is further referred to specific works[34].

§ 2.4 Polymeric thin films in CO_2

§ 2.4.1 Thin Film Properties

In recent years, nanometer scale polymer thin films have drawn tremendous interest due to their technological importance in particular in areas such as microelectronics, coatings, biomaterials, and membranes. There are many applications involving polymer thin films that are currently being developed using compressed CO_2, including coatings for buildings and electronics[3,4], stabilizers for colloidal dispersions[28], and membranes for high pressure CO_2 separations[29].

In order to fully optimize these applications, it is important to understand how CO_2 interacts with thin films and to this scope a brief outline of what will be the argument discussed in chapter VII is here introduced.

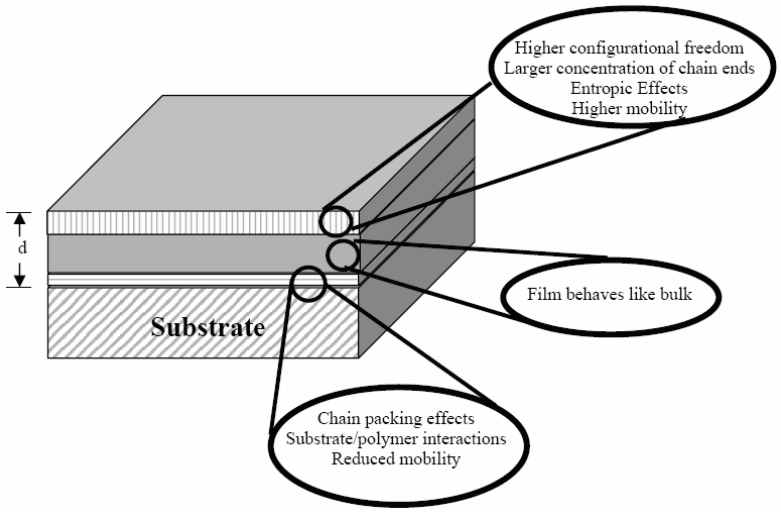

Figure 2.7 Supported polymeric thin film. Diagram illustrates the "layered mobility" model and the callouts highlights the important issues for the different regions of the thin film.

Polymer thin films, such as the one displayed in Figure 2.8, are interesting because they often exhibit properties that are different from the corresponding bulk

polymer due to entropic effects and energetic interactions arising at the interfaces. These interfacial effects lead to changes in chain conformation and mobility that affect the properties of the entire polymer film, especially when the length scales of the interfacial regions become comparable to the length scale of the bulk of the film[43].

There have been many interesting phenomena observed for confined polymer films. For example, the glass transition temperatures (T_g) of polymer thin films deviate from the bulk value and often show a strong thickness dependence for films less than ~40 nm[43]. Glass transition temperatures for supported thin films have been observed to either increase or decrease with decreasing film thickness, depending on the specific polymer/substrate system. Generally polymers that strongly interact with the substrate, such as PMMA on quartz, show an increase in T_g with decreasing film thickness.[33] However, films supported on non-interacting substrates usually show a decrease in T_g with decreasing film thickness[43]. Thus, the strength of the polymer/substrate interaction is very important. There are several explanations as to the origins of this behavior such as a layer of increased mobility near the free surface (see Figure 2.8) [43-44].

Several researchers offer evidence in support of this model[44], whereas others offer results that question this concept[45]. Currently, there is not a strong consensus on a detailed description for this observed behavior and this highlights the fact that probing these small length scales is experimentally challenging.

In addition to deviations in T_g for polymer thin films, other interesting phenomena have also been documented. McCaig et al. have observed that the rate of physical aging in thin polymer membranes is greater than in thicker films[46]. They concluded

that this was due in part to diffusion of free volume out of the polymer film. This increased aging results in significant changes in the permeation properties of the membrane that occur over experimental time scales.

§ 2.4.2 Thin Films in CO_2

Supercritical and liquid CO_2 are being investigated as replacements to harsh chlorofluorocarbon (CFC) solvents in the microelectronics industry. Work is ongoing to incorporate compressed CO_2 in almost all facets of the photolithography process. The continuously shrinking feature sizes are now requiring processing solvents that have low viscosities, high diffusivities, adjustable solvent quality, and low capillary forces. In addition, fluoropolymers are becoming more prominent as resists as the feature sizes decrease. In a single conventional fabricating line, over 1 million gallons of harsh solvents are used annually[3]. Thus, CO_2 could drastically reduce the use of these harsh solvents, while at the same time provide the demanding properties that are needed for future device processing.

Work has been undertaken to use compressed CO_2 as a solvent for spincoating resist films on silicon wafers[3]. In addition, CO_2 has also been used as a solvent for performing free-meniscus thin film coatings of perfluropolyethers (PFPEs). PFPEs are used to lubricate electronic hard disks and as protective coatings on stone structures[8]. Supercritical CO_2 is also being used as a solvent in developing and stripping photoresist films[8,9]. Futhermore, the cleaning and drying of high aspect ratio features is being successfully carried out using CO_2 in order to minimize capillary forces and prevent feature collapse[46-48]. However little work has been done to probe

on a nanometer scale how CO_2 influences the structures of these thin films. For example, it will be important to know how CO_2 swells and interacts with resist structures and porous low-k dielectrics as well as how these processes are affected by film confinement.

Intelligent design of these CO_2-thin film applications cannot be achieved without probing the *in-situ* structure of these systems. Chapter VII will contribute to understanding the interaction of CO_2 with polymer thin films as well as the structure of these systems.

§ 2.5 References

(1) Bruno, T. J.; Ely, J. F. *Supercritical Fluid Technology: Reviews in Modern Theory and Applications*, CRC Press: Boston, 1991.

(2) Kiran, E.; Brennecke, J. F. *Supercritical Fluid Engineering Science*, American Chemical Society: Washington D.C., 1991.

(3) Ely, J. F.; Magee, J. W.; Haynes, W. M., *Gas Processors Association* **1987**.

(4) Smith, J. M.; VanNess, H. C. *Introduction to Chemical Engineering Thermodynamics*, 4th; MacGraw Hill, Inc.: New York, 1987.

(5) Kikic, I., Vecchione, F., Alessi, P., Cortesi, A., Eva, F., and Elvassore, N. *Ind. Eng. Chem. Res.* **2003**, 42, *13*, 3022 - 3029.

(6) Canelas, D. A.; Betts, D. E.; DeSimone, J. M. *Macromolecules* **1996**, *29*, 2818-2821.

(7) Quadir, M. A.; Kipp, B. E.; Gilbert, R. G.; DeSimone, J. M. *Macromolecules* **1997**, *30*, 6015-6023.

(8) DeSimone, J. M.; Guan, Z.; Eisbernd, C. S. *Science* **1992** , *257*, 945-947.

(9) Magee, J. W. in *Supercritical Fluid Technology*, T. J. Bruno, J. F. Ely Eds; CRC Press: Boston, 1991, 325-334.

(10) Henon, F. E.; Camaiti, M.; Burke, A. L.; Carbonell, R. G.; DeSimone, J. M.; Piacenti, F. j*ournal of Supercritical Fluids* **1999**, *15*, 173-179.

(11) DeSimone, J. M.; Maury, E. E.; Menceloglu, Y. Z.; McClain, J. B.; Romack, T. J.; Combes, J. R. *Science* **1994**, *265*, 356-359.

(12) McClain, J. B.; Betts, D. E.; Canelas, D. A.; Samulski, E. T.; DeSimone, J. M.; Londono, J. D.; Cochran, H. D.; Wignall, G. D.; Chillura-Martino, D.; Triolo, R. *Science* **1996**, *285*, 426-429.

(13) Gerhardt, L. J.; Garg, A.; Bae, Y. C.; Manke, C. W.; Gulari, E. in *Theoretical and Applied Rheology*, P. Moldenaers, R. Keunings Eds; Elsevier Science Publishers: Brussels, Belgium, 1992, 348-350.

(14) Alessi, P., Cortesi, A., Kikic, I., Foster, N.R., Macnaughton, S.J., and Colombo, I. *Ind. Eng. Chem. Res.* **1996**, *35*, 4718-4726.

(15) Handa, Y. P.; Capowski, S.; O'Neill, M. *Thermochimica Acta* **1993**, 226, 177-185.

(16) Beckman, E.; Porter, R. S. *Journal of Polymer Science: Part B: Polymer Physics* **1987**, *27*, 1511-1517.

(17) Koros, W. J.; Paul, D. R. *Journal of Polymer Science: Part B Polymer Physics* **1978**, *16*, 1947-1963.

(18) Goel, S. K.; Beckman, E. J. *Polymer* **1993**, *34*, 1410-1417.

(19) Handa, Y. P.; Kruus, P.; O'Neill, M. *Journal of Polymer Science: Part B: Polymer Physics* **1996**, *34*, 2635-2639.

(20) Wang, W.-c. V.; Kramer, E. J.; Sachse, W. H. *Journal of Polymer Science : Polymer Physics Edition* **1982**, *20*, 1371-1384.

(21) Briscoe, B. J.; Kelly, C. T. *Polymer* **1995**, *36*, 3099-3102.

(22) Rodriguez, F. *Principles of Polymers Systems*, Hemisphere Publishing Corporation: New York, 1989.

(23) Johnston, K. P.; Penninger, J. M. L. *Supercritical Fluid Science and Technology*, American Chemical Society: Washington, D.C., 1989.

(24) McHugh, M.; Krukonis, V. J. *Supercritical Fluid Extraction*, 2nd; Butterworth-Heinemann: Boston, 1994.

(25) Combey, M. *Plasticisers, Stabilisers, and Fillers*, Iliffe Books Ltd: London, 1972.

(26) Billmeyer, F. W. *Textbook of Polymer Science*, 3rd; John Wiley & Sons: New York, 1984.

(27) Charrier, J.-M. *Polymeric Materials and Processing: Plastics,Elastomers and Composites*, Hanser Publishers: New York, 1991.

(28) Shine, A. D. in *Physical Properties of Polymers Handbook*, J. E. Mark Eds; AIP Press: New York, 1996, 249-256.

(29) Williams, M. L.; Landel, R. F.; Ferry, J. D. *J. of the Am. Chem. Soc.* **1955**, *77*, 3701-3707.

(30) Wissinger, R. G.; Paulaitis, M. E. *Journal of Polymer Science. Part B:* **1991**, *29*, 631-633.

(31) Handa, Y. P.; Lampron, S.; O'Neill, M. L. *Journal of Polymer Science: Part B:* **1994**, *32*, 2549-2553.

(32) Hachisuka, H.; Sato, T.; Imai, T.; Tsujita, Y.; Takizawa, A.; Kinoshita, T. *Polymer Journal* **1990**, *22*, 77-79.

(33) Chiou, J. S.; Maeda, Y.; Paul, D. R. *J. of Applied Polymer Science* **1985**, *30*, 4019-4029.

(34) Bae, Y. C.; Gulari, E. *Journal of Applied Polymer Science* **1997**, *63*, 459-466.

(35) Shieh, Y.-T.; Su, J.-H.; Manivannan, G.; Lee, P. H. C.; Sawan, S. P.; Spall, W. D. *J. of Applied Polymer Science* **1996**, *59*, 707-717.

(36) Shieh, Y.-T.; Su, J.-H.; Manivannan, G.; Lee, P. H. C.; Sawan, S. P.; Spall, W. D. *Journal of Applied Polymer Science* **1996**, *59*, 695-705.

(37) Zhou, S.; Stern, S. A. *Journal of Polymer Science: Part B: Polymer Physics* **1989**, 27, 205-222.

(38) Watkins, J. J.; Brown, G. D.; Pollard, M. A.; Ramachandra-Rao, V.; Russell, T. P. *Macromolecules* **1999**, *32*, 7737-7740.

(39) Walker, T. A.; Raghavan, S. R.; Royer, J. R.; Smith, S. D.; Wignall, G. W.; Melnichenko, Y.; Khan, S. A.; Spontak, R. J. *Journal of Physical Chemistry B* **1999**, *103*, 5472-5476.

(40) Bae, Y. C. *Polymer* **1996**, *37*, 3011-3017.

(41) StMartin, H. C.; Choi, K. Y. *Industrial and Engineering Chemistry* **1991**, *30*, 1712-1718.

(42). Deshpande, M. M.; Jadhav, A. S.; Gunari, A. A.; Sehra, J. C.; Sivaram, S. *Journal of Polymer Science: Part A. Polymer Chemistry* **1995**, *33*, 701-705.

(43) Gross, S. M.; Givens, R. D.; Jikei, M.; Royer, J. R.; Khan, S. A.; DeSimone, J. M.; Odell, P. G.; Hamer, G. K. *Macromolecules* **1998**, *31*, 9090-9092.

(44) Burke, A. L.; Givens, R. D.; Jikei, M.; DeSimone, J. M. *Polym. Prepr.* **1997**, *38*, 387.

(45) Odian, G. *Principles of Polymerization*, 3rd; John Wiley&Sons, Inc.: New York, 1991.

(46) Balsara, N. P. in *Physical Properties of Polymers Handbook*, J. E. Mark Eds; AIP Press: New York, 1996.

(47) Bates, F. S. *Science* **1991**, *251*, 898-905.

(48) Binder, K. *Adv. Polym. Sci.* **1994**, *138*, 1-89.

CHAPTER III

Experimental methods: High-Pressure Ellipsometry and Quartz Crystal Microbalance

In this chapter the experimental techniques to which we will refer throughout the thesis will be discussed in detail. Basic principles as well as underlying theoretical development, generic raw and analyzed data and description of system apparatus form the content of the following paragraphs. Specific details about sample preparations and measurement protocols adopted for the measurements will instead be given as needed, in the experimental section of chapters IV, VI and VII.

§ 3.1 Introduction to spectroscopic ellipsometry

Ellipsometry is a powerful optical analytical technique that has been used extensively over the past 30 years, primarily in the study of semiconductors but increasingly more in the analysis of polymer thin films and interfaces. There is an

extensive literature on ellipsometry, including a well-know textbook[1]. The present chapter is not meant to provide an exhaustive review of the literature, its main goal is to outline principles of the technique, describe its applicability and limitations, and then illustrate the range of problems in polymer science that it can tackle, in particular those relevant to the present dissertation.

Ellipsometry measurements are sensitive to steps or gradients in complex optical constants. For some applications, such as optical waveguides and antireflection coatings, the determination of the optical constants (*i.e.* the real $<n>$ and imaginary $<k>$ components of the refractive index) is the final objective of the measurement. Quite often though, refractive index profiles are used to determine the thickness of films and adsorbed layers, interfacial widths and surface roughness. Ellipsometry has the advantage of being a laboratory-based technique that is non-invasive (unless, of course, specimen is light-sensitive). Because the technique is relatively fast, processes may be studied in real-time. Moreover, the technique is applicable to any kind of matter, namely solid, liquid, liquid crystal, gas, plasma and even supercritical fluids. During analysis, the sample may be placed in a controlled atmosphere, such as in a reaction vessel or under high vacuum. Under good experimental conditions, ellipsometry can detect sub-monolayer coverage on a surface and determine refractive index to the nearest 0.001[1].

§ 3.2 Principles of ellipsometry

Ellipsometry relies on the reflection of light with a known state of polarization from a planar surface or parallel interfaces.

The state of polarization *after* reflection is determined experimentally. The beam of light, often described as a two dimensional structure in which the entire wave is contained in a single plane, actually travels as a three-dimensional wave, much like an elongated spring. If one were to look directly down the path of an individual photon, there are three general cases that properly describe the wave, shown schematically in Figure 3.1.

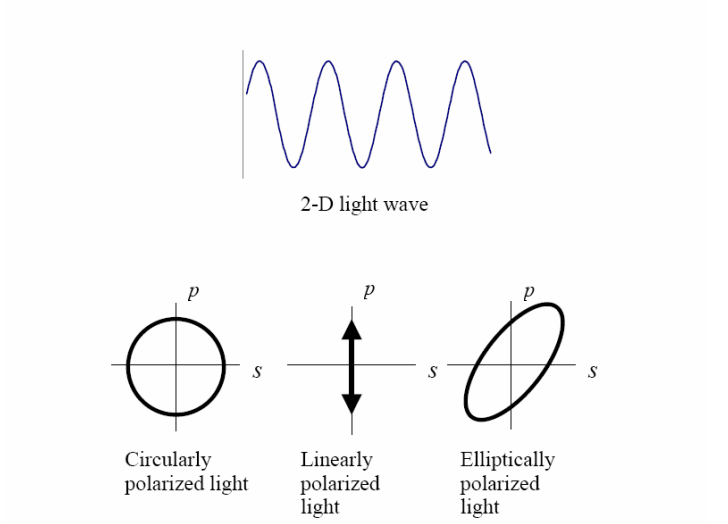

Figure 3.1 Schematic representations of a beam of light.

The light could be traveling as a perfectly cylindrical wave. That is, the magnitude of the electric vector in the plane normal to the direction of propagation is constant in any direction. In this case the light is said to be *circularly polarized*. The other extreme case is that the light could be traveling such that this vector oscillates in a single plane, and this case is termed *linearly polarized*. Intermediate cases are known as *elliptically* polarized light.

The theory behind ellipsometry is well established[1,2]. The effect of the reflection of light from a film depends on several variables such as the wavelength of probe

beam and the angle of incidence as well as the thickness and optical properties of all the layers in the film.

The change in amplitude and phase of the polarized light upon reflection is determined in two components, *i.e.* in the plane of the reflection (the '*p*'-plane) and perpendicular to this plane (the *'s'*-plane), as portrayed in Fig. 3.2.

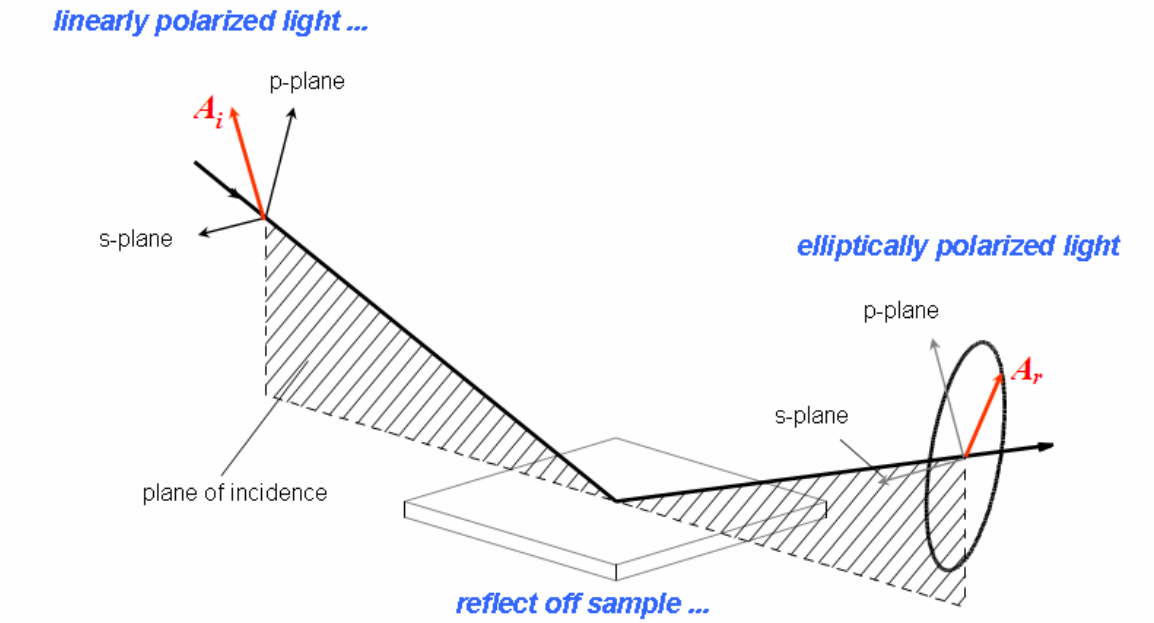

Figure 3.2 Schematic representation of ellipsometry principle.

In the case of a single interface, as shown in Figure 3.3a, the ratio of the amplitude of the reflected beam to the incoming beam is given by equations (3.1) and (3.2) for the *p*- and *s*-waves respectively[1]

$$r_{1,2}^{s} = \frac{A_s^r}{A_s^i} = \frac{N_2 \cos\phi_1 - N_1 \cos\phi_2}{N_2 \cos\phi_1 + N_1 \cos\phi_2} \qquad (3.1)$$

$$r_{1,2}^{p} = \frac{A_p^r}{A_p^i} = \frac{N_2 \cos\phi_1 - N_1 \cos\phi_2}{N_2 \cos\phi_1 + N_1 \cos\phi_2} \tag{3.2}$$

N_i is the complex refractive index of medium i and is given by

$$N_i = n_i - jk \tag{3.3}$$

where n_i is the real part of the refractive index, k is the extinction coefficient, and j is the imaginary number. In the special case of a single interface, r_p and r_s are more commonly referred to as the Fresnel reflection coefficients.

When a film is present on a substrate, *i.e.* when two interfaces are present, the equations describing the ratio of the amplitudes of the outgoing wave to the incoming wave are modified. This scenario is shown schematically in Figure 3.3b. The resultant equations for the ratios of the p and s-waves, respectively, are then:

$$R_p = \frac{A_p^r}{A_p^i} = \frac{r_{0,1}^{p} + r_{1,2}^{p} \exp(-j2\beta)}{1 + r_{0,1}^{p} r_{1,2}^{p} \exp(-j2\beta)} \tag{3.4}$$

$$R_s = \frac{A_s^r}{A_s^i} = \frac{r_{0,1}^{s} + r_{1,2}^{s} \exp(-j2\beta)}{1 + r_{0,1}^{s} r_{1,2}^{s} \exp(-j2\beta)} \tag{3.5}$$

where R_p and R_s are the total reflection coefficients, $r_{x,y}$ are the Fresnel reflection coefficients between interfaces x and y, and β is the optical thickness that describes

the phase change of the wave as it moves from the top to the bottom of the film (it will be further discussed later) [1].

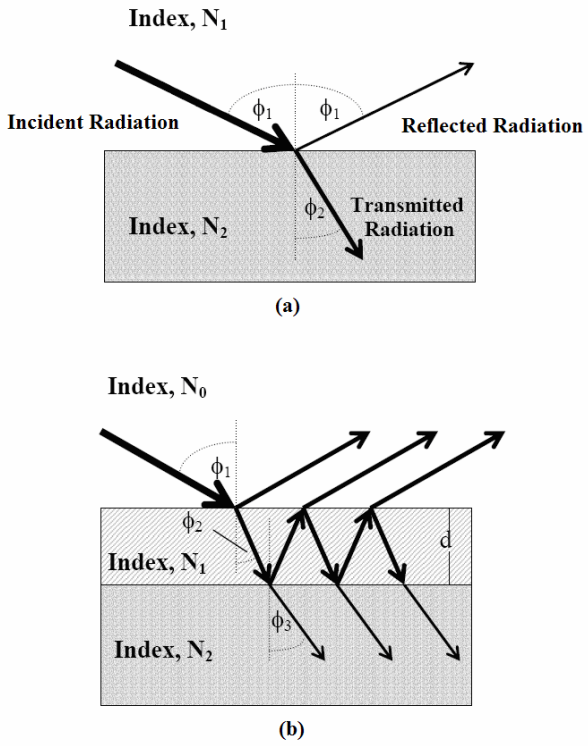

Figure 3.3 (a) Radiation interacting with a single plane parallel interface between material 1, with refractive index N_1 and material 2, with refractive index N_2. (b) Diagram of the beam path in a sample comprised of a film of thickness d and refractive index N_1, between material 0, with refractive index N_0, and material 2, with refractive index N_2

Physically, two ellipsometric angles, known as ψ and Δ, can be defined as follows[2]. Prior to reflection, the polarization of the light is characterized by an amplitude ratio A_p / A_s, and a phase difference (dp – ds), of the two components, p and s. Upon reflection, both the amplitude ratio and phase difference change. The angle Δ is the change in phase difference caused by the reflection:

$$\Delta = \left(d_p^r - d_s^r\right) - \left(d_p^i - d_s^i\right) \tag{3.6}$$

where the superscripts *r* and *i* refer to the reflected and incident light, respectively. The angle ψ is defined by the ratio of the amplitude ratios before and after the reflection:

$$\tan\psi = \frac{A_p^r / A_s^r}{A_p^i / A_s^i} \tag{3.7}$$

By using the Fresnel reflection coefficients, the ellipsometric angles can also be related to the optical constants and to the dimensions of the sample and the experimental set-up. The ratio of total Fresnel reflection coefficients, R_p and R_s (corresponding to the *p*- and *s*- planes, respectively) defines the ellipticity ρ (a complex number). This ratio is mathematically related to the two ellipsometric angles, ψ and Δ by the following relationship:

$$\rho = \frac{R_p}{R_s} = \tan\psi \cdot e^{i\Delta} \tag{3.8}$$

Note that this definition relates the ellipsometric parameters, which are measured in a particular experiment, to the Fresnel coefficients, which are dependent on the actual sample. Ellipsometry derives its name from the fact that it analyses the polarization state of elliptically polarized light in order to find the ellipticity[1].

Contrary to common perception, ellipsometry *does not* measure the absolute reflectivity of a surface or interface.

For a single interface, the ellipsometric angles, ψ and Δ, are function of the refractive index of the two media at that interface and the angle of the incident light from the normal to the sample surface, ϕ_1. The refractive index of a material is also dependent on the wavelength of light, λ, as a result of optical dispersion. Consequently, ψ and Δ also vary with λ. In most samples of experimental interest, there are one or more thin layers on the sample surface. In this case, Fresnel coefficients, and hence ψ and Δ, also vary with the layer thickness and its optical constants.

In any experiment, one or more pairs of the angle ψ and Δ are determined. The experiment may be performed in any one of several modes, depending on the apparatus being used and on the purpose of the experiment.

Measurements are obtained as a function of ϕ_1 in a multi-angle scan, as a function of λ (or photon energy) in a spectroscopic scan, and as a function of both of these parameters in a multi-angle spectroscopic scan. In dynamic sample systems, it is often beneficial to determine ψ and Δ as a function of time. In figures 3.4a and 3.4b examples of such measured angles taken in our study are shown.

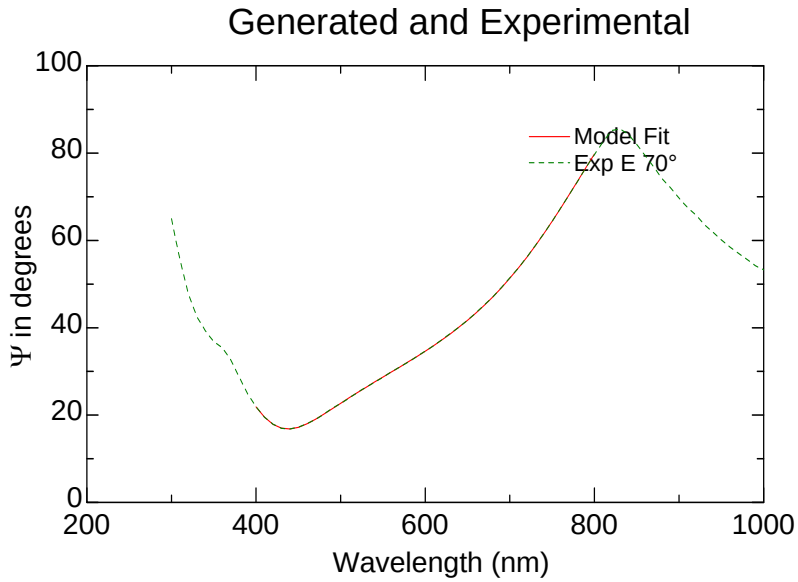

Figure 3.4a Ψ measured in a typical multiwavelength experiment vs. data generated by a model.

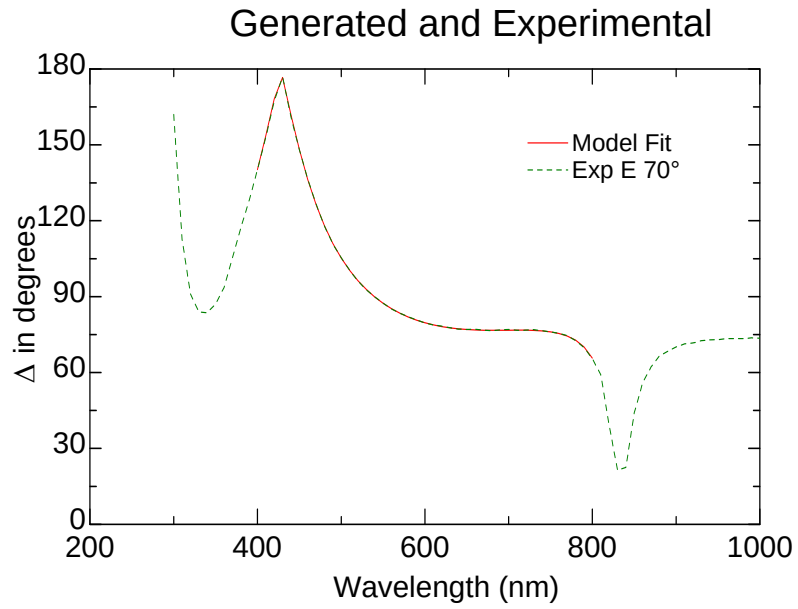

Figure 3.4b Ψ measured in another typical multiwavelength experiment vs. data generated by a model.

Spectroscopic scans can, in principle, provide more independent data points to use in constructing a model of a sample than can be obtained with a single wavelength of

light. At the same time, they create more unknown values of refractive index as a result of optical dispersion. As a specific example, imagine a transparent polymer thin film on a substrate.

The aim of an ellipsometry measurement might be to determine the thickness of this film. At one wavelength and angle incidence, one will obtain a value of ψ and Δ and then need to determine the thickness and the refractive index of the film. Using X different wavelengths, one would need to determine X values of the refractive index. As a means of minimizing the number of parameters in a model, the optical dispersion of a glassy polymer can be described by a dispersion model. In an optically transparent (k=0) material, the Cauchy equation is often used[1,2]:

$$n(\lambda) = A + \frac{B}{\lambda^2} + \frac{C}{\lambda^4} + \ldots \tag{3.9}$$

where A, B and C are constants. Higher-order terms can usually be neglected, and so only a few constants are needed to describe the material over a wide range of wavelengths. A parametric equation can likewise be used to describe the imaginary component of the index in an optically absorbing polymer in order to reduce the number of unknown parameters.

For a single, *sharp* interface between two transparent media (such as a glassy polymer and carbon dioxide), ψ goes to 0^o and Δ passes through an abrupt step between 0 and 180^o at a certain angle, known as the Brewster angle. In such a case, the Brewster angle, ϕ_B, is determined by the refractive indices of the two media:

$$\frac{n_1}{n_0} = \tan^{-1}\left(\phi_B\right) \tag{3.10}$$

where n_0 is the refractive index of the ambient medium and n_1 is the refractive index of the material at the interface. As seen in the equation, the determination of the Brewster angle can be used to find the index of a material if the index of the ambient is known (which is usually the case). If the refractive index of the ambient varied between successive ellipsometry measurements on the same sample, then additional data are obtained for precise determination of the unknown refractive index[3]. A common way of varying the ambient refractive index is to use a variety of solvents or, as in the case of this specific endeavor, different pressures.

Often in interpreting ellipsometry data, there is a need to predict the refractive index of a composite consisting of a mixture of known volume fraction of two different media. There are other instances in which the inverse problem is of interest, *i.e.* one may wish to calculate the mixture composition, given the refractive index of the mixture, an example of this procedure is given in Chapter IV.

The most common way of calculating the index of a composite material, such as a polymer-solvent mixture, is to use a mathematical model known as an effective medium approximation (EMA). Several EMA models exist, with each making slightly different assumptions[4]. For instance the simplest one, Maxwell-Garnett EMA model, assumes spherical inclusions of one or more materials (denoted as B or C) in a host matrix of material A. The dielectric constant of the composite, ε (where $\varepsilon = n^2$),

is related to the dielectric constant of each of the components (denoted by subscripts A, B and C) by the expression:

$$\frac{\varepsilon - \varepsilon_A}{\varepsilon + 2\varepsilon_A} = f_B \frac{\varepsilon_B - \varepsilon_A}{\varepsilon_B + 2\varepsilon_A} + f_C \frac{\varepsilon_C - \varepsilon_A}{\varepsilon_C + 2\varepsilon_A} \tag{3.11}$$

where f_B and f_C represent the volume fraction of material B and C, respectively. The dielectric constant can be a complex number, but it is real in an optically transparent material. An EMA model is a convenient and effective way in which to relate polymer density to refractive index by considering the material to be a mixture of fully-dense polymer and voids with $\varepsilon = n^2 = 1$.

However, for most cases in interest, a sharp interface does not exist. For an optically transparent dielectric, the values of ψ and Δ near the Brewster angle are particularly sensitive to any broadening or step in index at the interface. The presence of even a monolayer of a second material at the interface will change the ellipsometric angles significantly. Likewise, roughness at the surface in the *z*-direction and optical absorption will cause ψ to increase from 0, and Δ will broaden from a step function.

In the situation in which ψ does not fall to a minimum of 0^o, an operational definition of the Brewster angle is when $\mathrm{Re}(\rho)=0$ (*i.e.* when ρ is entirely imaginary)[5]. Note that by making use of the Euler equation, the ellipticity can be expressed in terms of strictly real and imaginary components:

$$\rho = \tan\psi \cos\Delta + i \tan\psi \sin\Delta = \mathrm{Re}(\rho) + \mathrm{Im}(\rho) \qquad (3.12)$$

It can be easily seen from the above equation that when Δ has a value of 90 or 270°, the ellipticity is completely imaginary, while when Δ is 0, 180 or 360°, the ellipticity is completely real.

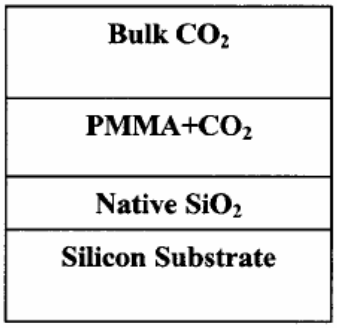

Figure 3.5 Example of ellipsometric model used for data analysis in the case of PMMA-CO_2 on silicon[6].

A typical measurement is performed as follows. The ellipsometric angles of ψ and Δ are determined as a function of the wavelength, angle of incidence and time, or various combination of these parameters. A suitable model, as shown in figure 3.5, is constructed of the optical system, and from this model the ellipsometric angles are predicted.

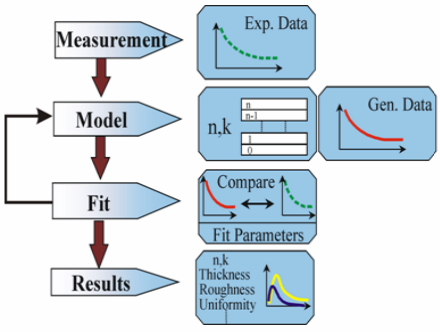

Figure 3.6 Schematic of ellipsometry as model-dependent technique.

The predicted and experimental results are compared, and then the model is adjusted until the difference between the two is minimized, as illustrated by the flow chart in Figure 3.6. By using this approach to data analysis, ellipsometry is a model-dependent technique. Consequently, great care and skill must be used in data and error analysis to ensure that it is not misleading or incorrect[7].

§ 3.3 Strengths and limitations of ellipsometry

From a single measurement of ψ and Δ, a maximum of two unknown parameters can be determined. If a transparent (k=0) film is deposited on a substrate with known optical constants, then the thickness and real component of the refractive index of the film can be determined. In a multi-layer system, such as that considered in figure 3.4, more unknown parameters will require more data points, which are collected at different λ or ϕ_1 values, or both. Thus, there is often need for multi-angle or spectroscopic scans. Of course, with an increasing number of parameters, it becomes increasingly difficult to obtain a unique solution. An increased amount of data does not always result in the capability of determining more experimental parameters.

Nevertheless, spectroscopic or multi-angle analysis of polymer/polymer interfaces is more reliable than single-wavelength measurements. The analysis is less affected by errors in a measurement for a given fixed wavelength and angle of incidence when the solution is 'over-determined' (*i.e.* there are more measured parameters than required to find the number of unknowns). Furthermore, adjusting λ and ϕ_1 allows the experimentalist to maximize the sensitivity of the ellipsometric angles to such factors as the film thickness or refractive index.

As already pointed out, for example, the sensitivity is at a maximum around the Brewster angle for a transparent thin film on a transparent substrate. Some types of ellipsometer do not provide reliable values of ψ and Δ, over certain ranges. For instance, phase-modulated ellipsometers fail when ψ approaches 45^{o}. Having multi-angular and spectroscopic capabilities allows experiments to be performed over ranges in which the data are most reliable.

Unlike many inorganic interfaces, polymer/polymer interfaces, especially in the presence of low molecular weight solvent, might extend over several tens of nanometers. Ellipsometry is a good technique for studying sharp interfaces (in the order of 20nm at most) but is less sensitive to broad interfaces, where other techniques like Neutron reflectivity are to be preferred[1,7].

It is worthwhile to anticipate at this point that this limitation is the reason why in chapter VII a series of cunning tests using Quartz Crystal Microbalance had to be devised in order to obtain information about a submerged broad polymer/substrate interface, where the resolution capacity of our ellipsometry could not provide any insight about the physical structure of such interface.

Furthermore the sensitivity of ellipsometry is enhanced when the refractive indices of the two media at the interface differ by a large amount. Unfortunately, most organic materials have a refractive index in the range 1.4 to 1.6, and so the contrast at interfaces between these materials is not very high, and the sensitivity of ellipsometry is therefore decreased[1].

Ellipsometry is in theory capable of studying profiles in refractive index normal to the sample surface (*i.e.* in the *z*-direction). However, as the reader shall see in

chapter VII, in this case further assumptions must be made about the nature of such profiles, which in turns introduce another degree of uncertainty in the measure (either average density or average packing volume).

§ 3.4 Rotating-Analyzer Spectroscopic ellipsometer

In order to measure the polarization of the light, ellipsometers must consist of several optical elements. There are many ellipsometer schemes but all of them have the same functional elements[1]:

Source of light → *Polarization generator* → *Surface of the sample* →

→ *Analyzer* → *Detector*

The *source of light* can be either a laser or a stable output lamp (typically a *Xe* lamp for the UV/vis spectral range). The *polarization generator* is usually just a polarizer with a fast axis that can rotate normal to the beam path. The generator can optionally also contain a compensator and a polarization modulator. The compensator (or retarder) is normally a quarter-wave plate which shifts the phase of the incoming light, while the polarization modulator is a piezoelectric device which slightly changes the light's polarization state in response to an applied high-frequency electric field.

The *analyzer* is an optical element (usually a second polarizer) which allows the measurement of the angle between the transmitted polarized light and the plane of incidence. The ellipsometric angles, ψ and Δ, are more sensitive to imperfections in

the polarizer than in the analyzer. Therefore, the quality requirements for a polarizer must be stricter than for the analyzer[1].

The *detector* can be either a photomultiplier or a photodiode, or for simultaneous detection of the whole spectrum, a multi-channel photodiode array.

From the calculation of ψ and Δ for a given model of a materials system, it is possible to predict high sensitivity in ellipsometric experiments. In practice, sensitivity requires that a noise level in determining ψ and Δ is below the expected signal change from the feature or phenomenon under investigation. Therefore, it is important to know what will be studied in order to make the right choice in choosing an ellipsometer and usually a trade-off between speed and precision is needed. Stated differently, given a certain type of setup only a certain type of experiments can be carried out in a reliable fashion.

There are three main categories of ellipsometer design, namely *null*, *rotating-element* and *phase-modulated*, but only the setup of a *rotating-analyzer spectroscopic ellipsometer*, considered for the aims of the present dissertation, will be briefly described.

The polarization state is determined by an analyzer rotating at a stabilized frequency of *ca* 50-100 Hz. For 7s of averaging time, the precision of such ellipsometer is *ca* 0.001^{o} in ψ and Δ. At this precision level, the ellipsometer can, *in theory*, detect the presence of a surface layer of *ca* 0.01Å^4. For a 0.1s acquisition time, the accuracy in ψ and Δ is reduced to *ca* 0.01^{o}. Figure 3.6 is a picture of our ellipsometry setup.

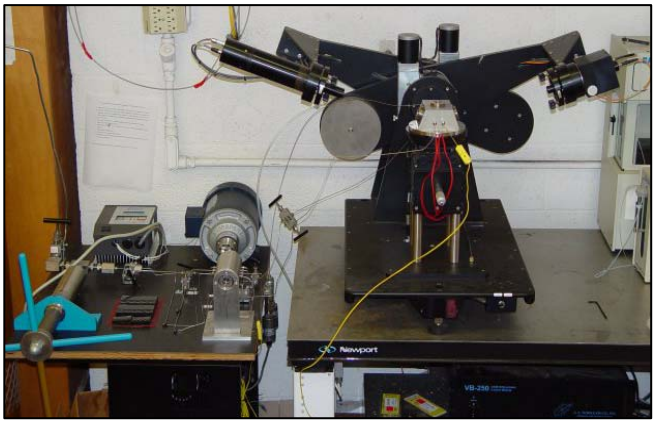

Figure 3.7 Picture of the ellipsometry setup used in this study

§ 3.5 Application of ellipsometry to polymer studies

§ 3.5.1 Range of thicknesses accessible to ellipsometry

Ellipsometry is routinely used to determine the thickness of films and coatings with sub-nanometer accuracy. The so-called 'slab' model (fig. 3.3b) is often used to analyze thin film data. This model assumes a layer of thickness d and a refractive index n on a substrate, with the ambient/film and film/substrate interfaces being parallel. The Fresnel coefficients describing this optical system are then modified with an exponential term containing the parameter β (optical thickness), defined as:

$$\beta = 2\pi n_1 \frac{d}{\lambda} \cos\phi_1 \qquad (3.13)$$

Note that both n_1 and d influence the value of β. By taking measurements at more than one value of λ or ϕ_1, it is straightforward to determine both n and d in films thicker than *ca* 20 nm. Below this thickness, they become highly correlated. A higher

value of the index and a lower value of the thickness yield comparable fits to the experimental data, as do a lower index and a higher thickness. At the other extreme, in very thick films, of the order of 2 μm and above, there will almost always be variations in the thickness, of the order of tens of nanometers (or more), that will invalidate a simple slab model, *i.e.* there is not a unique solution for film thickness, and so analysis becomes troublesome.

During the developments of this dissertation only specimens with thickness well within the above discussed threshold values will be considered. In the following two sections the main utilization of ellipsometry discussed in details in chapter IV through VII will be briefly outlined.

§ 3.5.2 The glass transition in polymer thin films via ellipsometry

The glass transition temperature, T_g, of a polymer is an important parameter for use in modeling and prediction of diffusion properties and viscosity behavior. In bulk materials, thermal analysis (such as differential scanning calorimetry or DSC) and mechanical analysis (such as creep compliance) are often used to determine T_g. In thin films, most types of analysis are very difficult to perform, or sometimes even impossible, because of the small sample volume.

Measurements of thermal expansivity have long been employed to determine T_g in bulk polymers. The thermal expansivity of the glass is usually lower than that of the melt, with the former changing at T_g. A plot of specific volume as a function of temperature will therefore have an inflection point that indicates the glass transition[7,8]. When studying thin films, ellipsometry can monitor the linear thermal

expansion. The technique thus provides a sensitive probe of the polymer dynamic properties in small volumes.

In Chapter IV a slight variant will be presented when the inflection point will be obtained as function of carbon dioxide pressure at fixed temperature.

§ 3.5.3 Cells used for polymer swelling with HPE

Finally, let us consider how ellipsometry can actually be applied to measuring the swelling percentage (and sometimes even rate) of polymer thin films in a high-pressure environment. For the *in-situ* studies conducted throughout this dissertation a cell, shown in figure 3.7 (schematic) and 3.8 (actual cell), equipped with thin, amorphous silica windows at a fixed-angle has been used.

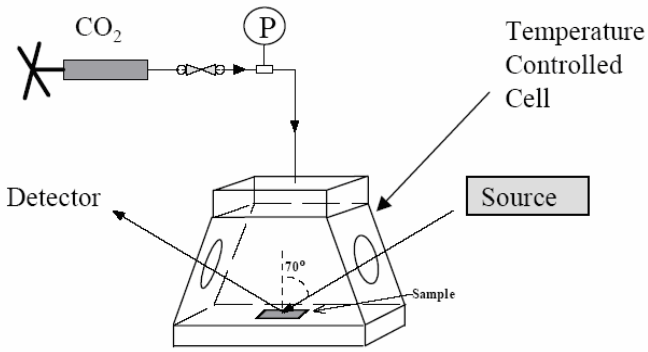

Figure 3.8 Schematic of in-situ cell for spectroscopic ellipsometer

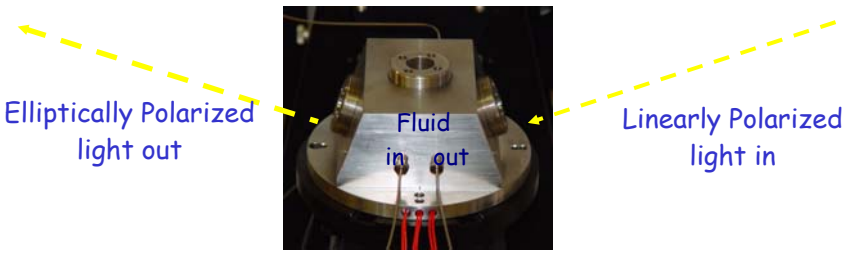

Figure 3.9 Actual cell equipped with quartz windows used for high-pressure swelling experiments.

Windows with a variety of angles allow one to work close to the Brewster angle of the system of interest. For the study of PMMA on silicon, swelling in carbon dioxide, an angle of 70^{o} gives best result. In this case fit must include a correction for the phase shift introduced by the windows in the sample cell (windows birefringence). Errors of up to *ca* 30% can occur if such window effects are not taken into account[9]. This will be further discussed in the experimental section of chapters IV and VII.

§ 3.6 Concluding remarks about ellipsometry

To conclude it is worth stressing that ellipsometry has great potential in the study of polymer surfaces and interfaces, and many important results have already been reported in the literature for T_g measurements and thin polymeric film swelling. At the same time, it must not be forgotten that, as with any model-dependent analytical technique, the quality of a result hinges on the appropriateness of the model considered and the property of the fitting procedure so that great care must be used in data analysis.

Fortunately, several software packages exist that are capable of performing regression fitting the model data to experimental data. The WVASE32 software package available from J.A. Wollam was used for the data analysis in this work.

Finally, all results obtained applying HPE technique throughout this work to film ranging from 88nm up to 1.2μm has yielded high quality outcomes, always in good agreement with already reported literature values.

§ 3.7 Introduction to quartz crystal microbalance (QCM)

Quartz is one of the ionic crystalline materials with structure lacking a center of inversion[10]. Therefore, a single crystal will possess a polar axis associated with the orientation of atoms in the crystalline lattice[11]. As a consequence, if the crystal is deformed due to a mechanical pressure, an electrical current will be generated. This is the well-known phenomenon of *piezoelectricity*. Similarly, if an electrical field is applied across the crystal, the polar dipoles will be displaced in a specific direction causing an elastic deformation in the crystal. This phenomenon is known as *reverse piezoelectricity*.

If a certain potential is applied across two parallel surfaces of a quartz slab, the crystal will deform in a certain direction. If the applied potential polarity is inversed, the crystal will deform in the opposite direction. Hence, an applied AC voltage will cause a periodic deformation in the crystal. The direction of the deformation depends on the angle at which the crystal is cut giving raise to several oscillatory modes such as the thickness shear, the surface acoustic wave, the flexural mode, and the shear horizontal acoustic plate modes as shown in Figure 3.10[12]. The frequency at which the crystal is made to oscillate is directly related to the applied voltage frequency. By selecting a proper frequency, resonance can be achieved. This frequency is usually called resonance or natural frequency. The sensitivity of the resonance frequency to the surrounding environment is the operation principle of a family of analytical tools called the piezoelectric oscillators.

Quartz Crystal Microbalance (QCM) is probably the most commonly used member of the piezoelectric oscillator family. The QCM operates under thickness

shear mode (TSM) where resonance is achieved when the wavelength is half the thickness of the quartz. The TSM mode is achieved through cutting the quartz crystal at a range of cuts known as the Y-cut family, which includes the AT-cut (at 35° 25') and BT-cut (at 49° 0') as shown in Figure 3.11[13].

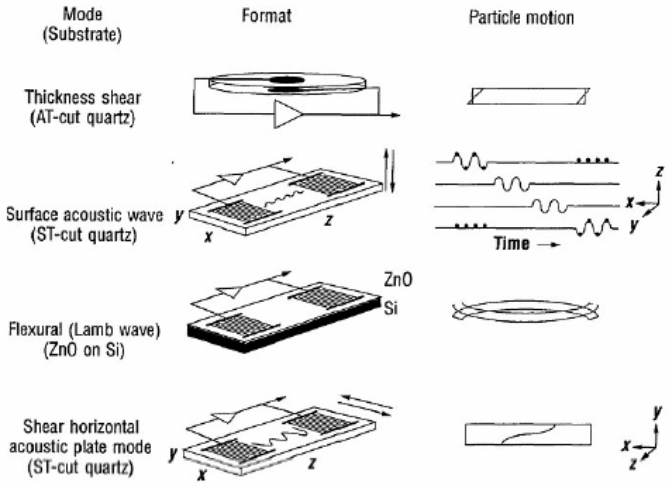

Figure 3.10 Representations of typical formats for different piezoelectric devices and their corresponding particle motions. For the SAW and shear horizontal mode, the direction of particle motion is indicated by the arrows[13].

Due to mechanical losses in quartz, the crystal will oscillate at a spectrum of frequencies instead of one discrete value. The quality factor, Q, is used to describe these mechanical losses. Q can be defined as the ratio of the resonant frequency to the full width of frequency at half the maximum amplitude of conductance[14].

§ 3.8 The Sauerbrey equation

The resonance frequency of a crystal occurs when the shear wave has a length equal to half the crystal thickness or its odd multipliers. The wave for this case will

have zero amplitude at the crystal's center, known as the wave's node, and a maximum at the crystal boundaries, know as the anti-nodes. This can be written as:

$$F_0 = \frac{u_q}{2t_q} \tag{3.14}$$

where F_0 is the resonance frequency, u_q is the acoustic wave velocity in quartz, and t_q is the quartz thickness.

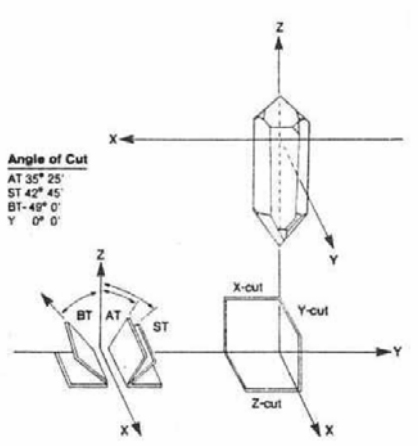

Figure 3.11 The assignment of axes to a quartz crystal, and different common axes of cut.

By simple manipulations, Eq. (3.14) can be used to derive a relation between the change in frequency to the change in thickness (or, in other words, mass if the density is known) as follows:

$$\Delta F = -\frac{2F_0^2}{\sqrt{\rho_q \mu_q}} \Delta m \tag{3.15}$$

Here, ΔF is the change in frequency due to a mass change of Δm, ρ_q and μ_q are the quartz density and elastic shear modulus, respectively. This equation is the well-known relation derived by Sauerbrey in 1959 and named after him[15]. The main assumptions behind Eq. (3.15) are that the applied mass has negligible thickness with respect to the crystal (below 1%) and that the film has similar acoustic properties to quartz[14]. While such assumptions hold true to many metallic films up to a relatively high thicknesses, non-metallic materials, especially polymers, can show significant deviations. These assumptions and others are discussed in several references[10,12,16].

§ 3.9 Electrical Circuit Analogy

In QCM studies, a useful analogy is made between the vibrating quartz crystal and an equivalent electrical circuit. If an ideal crystal, i.e., crystal with no internal friction, is excited by applying a DC voltage for a short time, upon removal of this voltage the crystal will continue to oscillate by virtue of its inertial and elastic energies[11]. This is similar to a swinging pendulum in frictionless surroundings, where the oscillation continues by cyclic transformation of potential and kinetic energies. In electrical circuits, the so called tank circuit shows an identical “swinging" behavior in terms of current and voltage. The tank circuit is composed of an ideal capacitor and an ideal inductor in series. For such circuit, if a voltage is applied for a short period of time, the energy will keep oscillating between the inductor, which stores the energy in the form of magnetic field, and the capacitor, which stores the energy in the from of electrical potential. For a non-ideal crystal, friction imposes a resistance that will

cause dissipation of the stored energy. Similarly, in the tank circuit, a resistance can be added in series to the inductor and capacitor, which will cause energy dissipation.

The resulting aforementioned circuit does not represent the QCM system completely; one more component needs to be added. This is due to the piezoelectric nature of quartz, which couples the mechanical and electrical energies through the piezoelectric constant. A brief description of commonly used commercial QCM crystals follows to help explaining this point.

Commercially available QCM crystals are usually made of thin quartz desk with metal electrodes deposited on both sides, as portrayed in Figure 3.12.

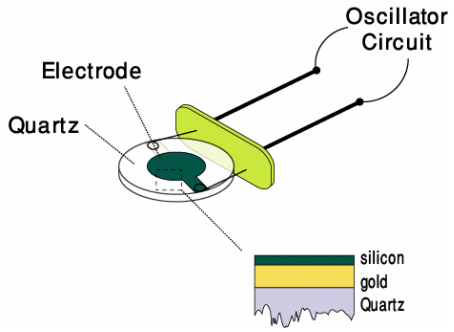

Figure 3.12 Schematic representation of a QCM.

The disk is usually half an inch in diameter with portion of the central region fully plated on both sides[17]. Going back to the equivalent circuit representation, the two metal electrodes deposited on both sides of the crystal with the quartz sandwiched between them will act as a capacitor. Taking into consideration the fact that this is an electromechanical process, it becomes necessary to include this last component, the capacitance, although it does not directly interfere with the motional crystal.

Because this capacitance does not depend on the quartz deformation, it should be added to the circuit in parallel. For this reason, the first group of components (the inductor, capacitor, and resistor in series) is called the motional arm, and the second component (the capacitor) is called the static arm. Figure 3.13 is a representation of this circuit, which is also known as Butterworth-Van Dyke (BVD) equivalent circuit for unperturbed quarts microbalance[18].

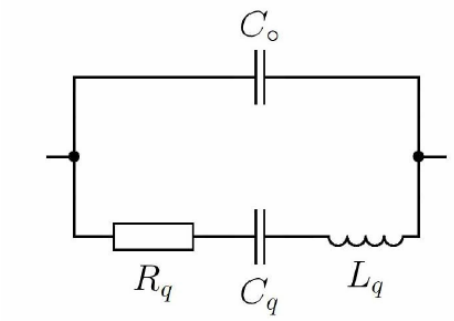

Figure 3.13 Butterworth-Van Dyke equivalent circuit for an unperturbed QCM.

This analogy has several advantages[18]. One advantage is that, with only few lumped elements, this model simulates the electrical characteristics of the QCM over a range of frequencies near resonance. Ideally, the model should explicitly relate the circuit elements to physical properties of the QCM as well as surface mass layer and contacting liquid. This allows easier prediction of the QCM behavior. As an example, if the mechanical model for an unloaded QCM is solved and compared to the corresponding circuit model, the following relations are obtained:

$$\begin{cases} C_0 = \dfrac{\varepsilon_{22} A}{h} \\ C_q = \dfrac{8K_0^2 C_0}{(N\pi)^2} \end{cases} \qquad \begin{cases} L_q = \dfrac{1}{(2\pi F_0)^2 C_q} \\ R_q = \dfrac{\eta_q}{\bar{c}_{66} C_q}\left(\dfrac{F}{F_0}\right) \end{cases} \qquad \text{(3.16-a, b, c, d)}$$

where ε_{22} is the quartz permittivity, A is the active area of quartz (the area of the smallest electrode), h is the crystal thickness, K_0 is a quartz constant related to the electromechanical coupling constant, N is the harmonic number (1, 3, 5,…), and η_q is a effective quartz viscosity used to take into account any mechanical losses, and $\bar{c}_{66}$ is the piezo-electrically stiffened quartz elastic modulus[18]. These relations are useful when performing impedance analysis (see next section) on the QCM. Another advantage of the analogy is that standard circuit analysis software can be used to extract information from electrical measurements made on the QCM. This analogy is also useful when the crystal is under external load, *i.e.* film deposition or liquid medium[11].

§ 3.10 Impedance analysis

The similarity between the QCM and the BVD circuit suggests that electrical circuit measurements can be applied to the QCM. Specifically, the so called impedance (or network) analysis can be used to determine the values of the circuit components[11]. Impedance analysis involves measuring the current resulting from a certain system at known applied voltage over a specified range of frequencies. In the QCM, this can be done because of the piezoelectric nature. Such analysis can

elucidate the properties of the quartz as well as the interaction of the crystal with the contacting medium[11].

The way impedance analysis is performed on QCM is analogous to that for electrical circuits. A certain voltage, having known frequency, is applied to the crystal, the piezoelectric effect will cause the crystal to oscillate and generate an electric current, which is measured. Resonance can be found when the current reaches its maximum, or the impedance reaches its minimum. Beside resonance frequency, the magnitude and phase shift of the current are also measured. Knowing the current's magnitude and phase allows the impedance (or admittance) of the quartz crystal to be calculated.

§ 3.11 Factors affecting QCM behavior

While the high sensitivity of the QCM makes it a unique analytical technique, it imposes a substantial challenge due to the large number of factors that can perturb the QCM operation. Therefore, it is important to comprehensively study the different factors that can affect the QCM operation in order to separate their effects and make correct conclusions. These factors are the subject of this section.

§ 3.11.1 Mass change

Equation (3.15) is the well known Sauerbrey relation that has been applied extensively for mass calculations from frequency data. This equation is usually written as:

$$\Delta F_m = -C_m \Delta m \qquad (3.17)$$

where C_m is the mass sensitivity constant and is equal to 56.6 Hz·μg^{-1}·cm^2 for a 5 MHz crystal. The advantage of this equation is that it is independent of the deposited mass properties, i.e., C_m is only a function of quartz properties.

However, due to the implied assumptions in this equation, its applicability is limited to frequency changes about 2% of F_0 for rigid films, e.g., metal films. Lu and Lewis[16] presented a more accurate relation, based on the work of Miller and Bolef[19] which can be written as[20]:

$$\frac{m_f}{m_q} = -\frac{z_f F_0}{z_q \pi F} \tan^{-1}\frac{z_q}{z_f} \tan\frac{\pi F}{F_0} \qquad (3.18)$$

where $z_i = c_i v_i$, and c_i and v_i are the shear stiffness constant and the wave velocity in the quartz (q) and film (f). The validity of this equation has been experimentally justified up to mass loads of 70%, however, it requires the film properties to be known a priori[20].

§ 3.11.2 Environment effects

The nature of the medium surrounding the QCM greatly affects its behavior. In fact, it was initially believed that the mechanical losses of the oscillating quartz if immersed in a viscous medium will be very high that the oscillation will cease [110].

Therefore, it is expected that the use of the QCM will be more difficult in viscous media than under vacuum because[21]:

1. *The high damping caused by the medium in contact with the quartz surface resulting in a large loss in the quality factor and a decrease in the phase gradient;*
2. *The observed frequency shift is not only due to mass loading, but also to the viscous coupling with the surrounding medium.*

In representing the additional effect of viscous media on the quartz crystal using the analogous electrical components, several analyses were made[22]. Commonly, the viscous medium is assumed to increase the mechanical losses and to introduce an additional mass loading on the crystal surface (*entrained fluid mass)*. This is equivalent to adding a resistor and an inductor in series with the motional arm in the BVD equivalent circuit[11]. Another effect arises from the parasitic capacitance from the test fixture, which, *i.e.*, the capacitance, arises from the external fields surrounding the QCM. This was accounted for by an additional capacitor in parallel with the motional arm[18].

The effect of viscous coupling on the frequency was quantified by Kanazawa and Gordon[23]. The change in frequency was found to be:

$$\Delta F_{\eta} = -\frac{1}{2} C_m \left(\pi F_0\right)^{1/2} \left(\rho_f \eta_f\right)^{1/2} \tag{3.19}$$

where ρ_f and η_f are the density and shear viscosity of the fluid medium surrounding the crystal, respectively. This equation was derived for Newtonian fluids. The same relation was also obtained using a transmission-line model for immersed QCM by Filiâtre et al.[24]. Using this equation, the density-viscosity product for a mixture of ethanol and water was estimated and found to be in good agreement with the tabulated values[23,24]. When studying polymer films with the QCM, another source of viscous coupling is introduced due to the viscoelastic nature of polymers. This effect from the polymer film must be added to that of the fluid to avoid its incorrect interpretation as mass change[25].

Since Eq. (3.19) was derived for viscous fluids, it cannot be used to account for the viscous contribution from polymer films. As a result, the situation becomes more complex, and large deviations from the ideal behavior may occur depending on the physical properties of the film[26].

An attempt to account for this non-gravimetric effect on the mass calculations was presented by Johannsmann and coworkers[27,28]. The following relation was proposed:

$$\frac{\Delta F^*}{F} \approx -\frac{2F_0}{\left(\rho_q \mu_q\right)^{1/2}} \Delta m \left[1 + J\frac{4\pi^2 \Delta m^2}{3\rho} F^2\right] \qquad (3.20)$$

where $J = J' - iJ'' = 1/G$ is the shear compliance of the polymer film and ρ is its density. The change in the complex frequency ΔF^* can be written as $\Delta F + i\Delta\Gamma$ where $\Delta\Gamma$ is the change in the bandwidth. From Eq. (3.20), a plot of $\Delta F^*/F$ versus F^2 should

give a straight line, the intercept of which can be used to determine the mass change. It is also possible, using the same plot, to determine the complex compliance of the film using the slope. Unfortunately, this method requires the use of a network analyzer to obtain the necessary frequency and bandwidth changes. It is not possible to obtain such information with the conventional oscillator circuit method[29] which is the technique used in this study.

However, a useful criterion to study viscous coupling is through measuring the QCM resistance. Since viscous coupling affects the mechanical losses experienced by the QCM, both the frequency and resistance will change as a result of this viscous loading. Mass loadings, on the other hand, will only affect the frequency and its effect on the resistance is negligible. The relation between crystal resistance and the product of viscosity and density for a QCM at its first harmonic resonance was determined, for a Newtonian fluid, to be[30]:

$$\Delta R = \frac{\pi}{8K^2 C_0}\left(\frac{\rho_f \eta_f}{\pi F_0 \rho_q \mu_q}\right)^{1/2} \tag{3.21}$$

where K^2 is the quartz electromechanical coupling coefficient (= $7.74 \cdot 10^{-3}$), C_0 is the static capacitance of the crystal (= 4.25 pF). From this relation, the change in the QCM resistance is expected to be linear with the density-viscosity product if the polymer film has no effect on the resistance. As will be seen in the following chapters, this is not always true.

§ 3.11.3 Temperature

The piezoelectric nature of quartz will be severely affected upon approaching phase transition temperature 573^{o}C where the quartz loses its piezoelectric nature[31]. Therefore, it is usually not recommended to use the QCM at temperatures above 300^{o}C.

The advantage of AT-cut quartz crystals is the fact that it has a very small temperature coefficient near room temperature[10]. If large temperature changes are experienced, it becomes necessary to account for this contribution. Rahtu and Ritala[31] present a method to compensate for such effect using a reference crystal and a modeled baseline. More on the temperature effect can be found in the reference by Wang et al.[32]. It should also be kept in mind that changes in temperature may have an effect on the surrounding medium properties, especially liquids, which will affect the QCM response.

§ 3.11.4 Pressure

Pressure has a compression effect on the QCM, which causes the frequency to increase linearly with increasing pressure. For the case of liquids, where one side of the crystal is exposed to the liquid medium and the other to air, the difference in hydrostatic pressure causes surface stresses, and the relation between the change in frequency and pressure difference is believed to be parabolic[11]. This effect, however, seems not to be very important, since the pressure generally will be constant during the experiment.

For gases, original studies by Stockbridge reported the following relation between the frequency and pressure:

$$\frac{1}{F_0}\frac{dF}{dp} = 15 \cdot 10^{-10}\left(1 - \sqrt{\frac{M}{165}}\right) \tag{3.22}$$

where F is in Hertz, p in torr and M is the gas molecular weight. This relation was proposed for pressures between 100 and 1000 torr. However, Park et al.[33] showed experimentally that a similar relation can still be used for pressures well above 1000 torr. The relation given by Park et al. is written as:

$$\alpha = \frac{1}{F_0}\frac{dF}{dp} \rightarrow \Delta F_p = \alpha F_0 \Delta p \tag{3.23}$$

where the constant α depends on temperature according to:

$$\alpha = 1.095 \cdot 10^{-5} - 2 \cdot 10^{-8} T \tag{3.24}$$

In the above two relations p is given in MPa and T in ^{o}C Wu et al.[34], using the same system as the one used in this work, confirmed that such relations are valid by measuring the change in frequency for adsorbing and non-adsorbing gases.

§ 3.11.5 Surface roughness

The issue of surface roughness effect on the frequency response and its interaction with other parameters in the system has been considered for the case of bare[35] and coated[36] QCM crystals in solution. The non- uniform morphology of the surface can affect the frequency in two ways. First, it can result in the entrapment of the fluid within the surface crevices.

This factor increases the mass load but will have small effect on energy dissipation. The second factor is the non-shear coupling generated by the movement of the surface asperities in the fluid which will contribute to the energy dissipation[37].

Frequency change due to surface roughness is a function of the fluid properties and surface morphology[35,38]. The general form of the relation for the change in frequency contributed to the surface roughness was written as[38]:

$$\Delta F_r = \Psi \Delta F_\eta \tag{3.25}$$

where ΔF_η is defined by Eq. (3.19) and Ψ is a function that depends on the surface morphology. The difficulty in determining an analytical expression for Ψ highly limits the use of Eq. (3.25). An attempt to simplify this relation was made by experimentally analyzing the response of QCM crystals with different surface morphologies. Park et al.[33] proposed the following relation:

$$\Delta F_r = -H \rho_f \tag{3.26}$$

where H is a constant that depends on the surface roughness. A similar approach was taken by Wu et al.[34] who proposed the following relation:

$$\Delta F_r = -\frac{1}{2} C_m C_r \rho_f \tag{3.27}$$

where C_m is the constant from Eq. (3.27) and C_r is defined as:

$$C_r = \left(a + b\delta\right)\frac{\xi}{\xi_0} \tag{3.28}$$

The constants a, b, and ξ_0 depend only on the crystal morphology, while ξ depends on the surface morphology and the adsorbed material. δ is the decay length of the fluid near the QCM surface given by

$$\delta = \left(\frac{\eta_f}{\pi F_0 \rho_f}\right)^{1/2} \tag{3.29}$$

While Eqs. (3.26) and (3.27) greatly simplify the expression for ΔF_r, the parameters used within these equations must be experimentally determined.

§ 3.12 General Applications of the QCM

QCM is a very powerful sensor: it responds to extremely small changes in mass, as low as ~1 pg/cm^2; it can be coated, theoretically, with any material to make it sensitive to specific reagent of interest; it has a very high response time in the order of microseconds; it occupies a small volume and can be used for in-situ measurements; and it is inexpensive. These merits are reflected on the wide range of applications where the QCM has been utilized.

Commercially, QCM has been used as thickness monitors for vacuum deposition systems. This kind of gravimetric measurements comprises the major section of QCM applications. Examples of such applications are: monitoring the detergency process[39], removal of solid organic soils from hard surfaces[40], surfactant adsorption[41], sub-monolayer deposition[42], biological species adsorption[43-45], and electrochemical processes monitoring[46,47]. Figure 3.14 shows a picture of a QCM cut-through.

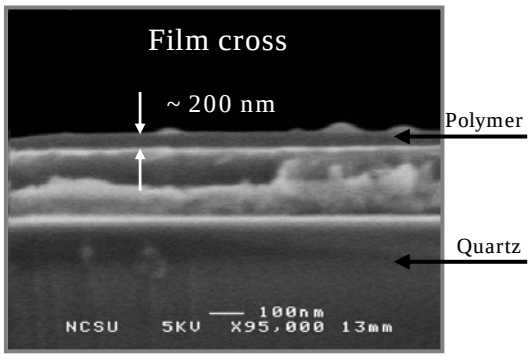

Figure 3.14 QCM cut-through seen with SEM. The different layers are indicated by the arrows.

While the main use of the QCM is in gravimetric measurements, other non-gravimetric applications have been performed. For example, Wang et al. used a QCM

crystal for pH measurements by coating the crystal with a polymer film that exhibits large changes in frequency upon changing the pH[48]. Another example includes measuring polymers shear modulus. This was done by measuring the change in the QCM current amplitude and phase. These changes indicate a change in the physical properties of the film on top of the crystal[49]. QCM was also used as a scanning electrode to determine the surface topography of metal coatings. In this case, a quartz crystal coated with a metal film was actuated using a thin gold wire that scans over the crystal surface. The change in frequency from one point to another is then used to determine the local thickness at the scanning point[50].

§ 3.13 QCM for High Pressure Systems

A similar discussion to that in Section 3.11 can be applied for high pressure systems. In general, for an isothermal system, the overall frequency change can be written as:

$$\Delta F = F - F_0 = \Delta F_m + \Delta F_\eta + \Delta F_p + \Delta F_r \qquad (3.30)$$

The different terms on the RHS of this equation can be estimated using the appropriate equations from Section 3.11. It is, however, commonly accepted that surface roughness contribution (ΔF_r) is usually small compared to the other terms. Because of this, and due to the difficulty of its estimation, it has been a common practice to omit the roughness term from the equation.

Indeed, for most of the studies reviewed in the next chapters the roughness effect is neglected. A previous study on the system used in the work presented in this thesis[34] has shown that when a smooth crystal (with rms less than 5 nm) is used, the surface roughness effect can be reduced significantly.

Generally speaking, two main challenges largely limit the use of QCM. First, the ability to obtain quantitative information from the QCM is still limited. Second, the reproducibility with this technique is poor due to its high sensitivity and to the large number of variables that can interfere with its operation.

When polymer films are considered, some questions are raised concerning the accuracy of the QCM results. The two main concerns are whether the viscoelastic nature of the film and the stresses due to the sorption-induced swelling will affect the frequency change.

The viscoelastic effect can be caused by polymers with low glass transition or by the plasticization induced by sorption of small molecules. While these issues are applicable to other systems, the following discussion is focused on high pressure studies only.

Due to the above mentioned factors, some researchers were reluctant to apply the QCM for polymeric materials above the glass transition point[51, 52] or to use it at all[53].

Most notably, the report by Banda et al.[53] argued that such effects can cause frequency changes as great as or greater than the frequency change due to the mass uptake itself if the film thickness is large. It is, therefore, necessary to set a limit for the acceptable range of thickness in which the Sauerbrey equation is valid.

As discussed earlier, the Sauerbrey equation is expected to apply up to 2% change in frequency. For a 5 MHz crystal, this is translated into ~ 7.5 μm for a typical polymer film. Indeed, several analyses had shown that such thickness is still within the range of applicability for the Sauerbrey equation even for soft polymeric films[25, 54, 55]. However, when the absorption of a plasticizing agent is involved, this range becomes unacceptable. Some authors suggest that the film thickness should not exceed 100 nm[53].

However, it will be shown, in the following chapters, that films up to ~ 1 μm thick still give satisfactory results.

§ 3.14 Studies on uncoated QCM in CO_2

§ 3.14.1 Frequency components

To illustrate the use of Eq. (3.30), a sample of the QCM results for an uncoated crystal is shown in Figure 3.16. In this figure, the pressure contribution (ΔF_p) and the viscosity contribution (ΔF_η) were determined using Eqs. (3.23) and (3.19), respectively. The value of ΔF_m was calculated from Eq. (3.30). It can be seen from Figure 3.15 that ΔF_η has a considerably smaller contribution to the total frequency change compared to that of the pressure ΔF_p. This is especially evident in the low pressure regime, i.e., gas phase regime, but slightly increases as the more viscous supercritical phase is approached.

It must be noted that ΔF_p will have a positive value at all pressures, while ΔF_η is always negative. Therefore, as the pressure increases, the total frequency will increase due to the pressure effect while the viscosity will have an opposite effect. The large

difference between ΔF_T and ΔF_p highlights the tendency of CO_2 to adsorb on Si surfaces. For non-adsorbing gases, such as He, the total frequency change was almost identical to that predicted from ΔF_p and ΔF_η[34].

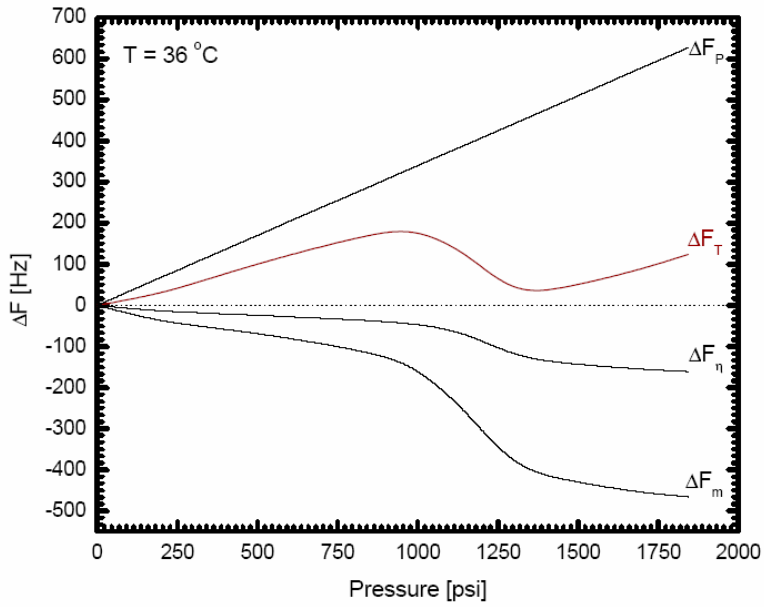

Figure 3.15 The frequency components of an uncoated Si QCM at 36°C. The experimentally measured ΔF_T represents the raw data. The values of ΔF_P, ΔF_η, and ΔF_m were calculated as discussed in the text.

§ 3.14.2 Resistance calibration

As mentioned earlier, the oscillator circuit used in this work can measure the resistance and the frequency of the QCM. While the resistance value is not used for quantitative measurements, it can be very useful if comparison with a reference state is made or if general trend is examined. Therefore, the change in resistance was recorded together with the frequency.

The circuit, as provided by the manufacturer, does not output the resistance values directly. Instead, it measures a DC voltage proportional to the crystal conductance

(conductance = 1/resistance). Therefore, in order to obtain the crystal's resistance, the voltage reading must be calibrated. The relation between the resistance and voltage given by the manufacturer is:

$$R = \frac{32}{V} - 20 \tag{3.31}$$

where the constant 32 is a scaling factor and 20 represents the circuit internal resistance. This relation was tested by recording the voltage of an uncoated crystal in CO_2.

Equation (3.21) gives a theoretical expression for the change in the QCM resistance as a function of the density-viscosity product for a Newtonian fluid.

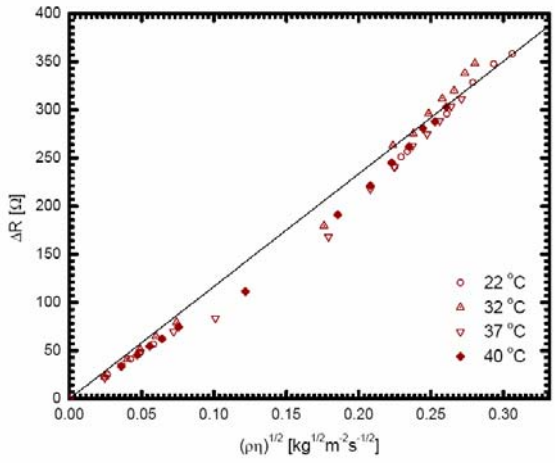

Figure 3.16 Change in resistance (ΔR) as a function of CO_2 properties at different temperatures. The straight line represents Eq. (3.21).

The above calibration was tested against a different set of experiments. In Figure 3.16, ΔR was calculated from the measured voltage using Eq. (3.31) and plotted

against the square root of the CO_2 density-viscosity product. Good agreement was found for temperatures below and above the critical temperature.

§ 3.15 QCM Setup

§ 3.15.1 QCM system

The quartz crystals used in this study were 5.00 MHz AT-cut. The crystals, as obtained from International Crystal Manufacturing (Oklahoma City, OK), had a blank diameter of 8.5 mm and a thickness of 0.25 mm. An Si film (6 mm diameter and 0.1 μm thickness) was vacuum sputtered over an Au electrode; the gold provides the necessary electrical actuation to the quartz. The rms surface roughness for the crystals is less than 10 nm (analyzed using Atomic Force Microscopy[34]).

The crystal is connected to an oscillator circuit (Maxtek model PLO-10). This oscillator provides two outputs, frequency and voltage; the voltage reading is inversely proportional to the crystal's resistance. The oscillator is connected to an Agilent 225 MHz Universal Frequency Counter (model 53131A) to read the frequency of the vibrating crystal. Temperature, pressure, voltage, and frequency readings are acquired using LabView.

§ 3.15.2 Pressure cell and apparatus

The custom built pressure cell was a thick-walled cylinder (I.D. 63.5×200 mm), with a high-pressure electrical feedthrough (Conax Buffalo Technologies) at the top end to drive the QCM. The cell had an inside volume of 25 cm^3 and a maximum

working pressure of 7500 psi. During an experiment, the crystal was placed into the cell and connected to the oscillator through the electrical feedthrough. A high-pressure thermocouple (Omega) was placed in the cell to indicate any variation in the temperature of CO2 fluid. The pressure inside the cell was monitored using a pressure transducer (Omega) with an accuracy of 0.02% of the reading. The whole assembly was then placed in a water bath and controlled to 0.1°C. The required pressure was achieved via an ISCO pump (model 260D, ISCO, Inc.) which can provide pressures up to 7500 psi. A sketch of the apparatus is displayed in Figure 3.17.

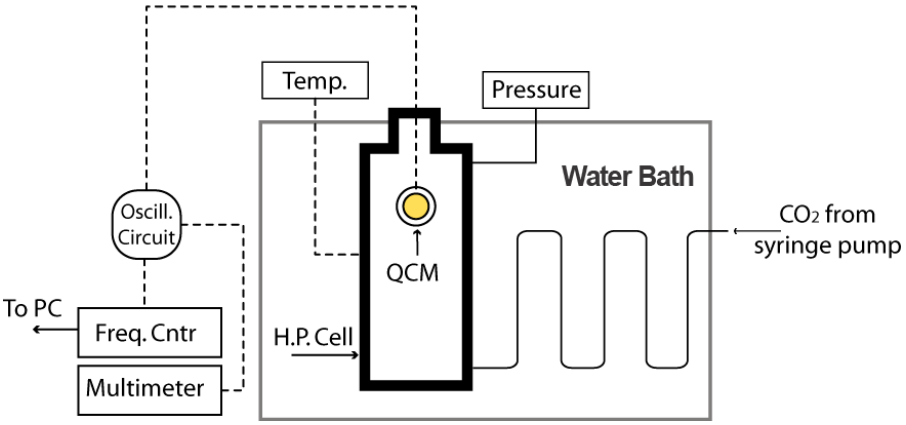

Figure 3.17 QCM apparatus.

§ 3.16 Concluding remarks on QCM

The quartz crystal microbalance (QCM) is a highly sensitive technique that can be used in a wide range of applications. While mass measurement is the most common, the QCM can be used, for example, in chemical analysis, determination of the shear modulus of polymers, and detection of phase transition. Several factors affect the

QCM response. Contribution from changes in mass is usually the main factor. Pressure and viscous coupling contributions can be significant and are reasonably estimated with specific analytical expressions. Other factors, such as surface roughness, cannot be estimated readily. For polymer films, the viscoelastic nature of the polymer can contribute to the total frequency change; impedance analysis is required in order to quantify such contribution.

A limited number of studies exist that utilize the QCM in high pressure systems. The majority of these studies examined the sorption of small molecules into polymers. In all of these sorption studies, the relations used to estimate the mass change were those mentioned in Eq.(3.30). Objections on the accuracy of such calculations have been reported. These objections are mainly concerned with the viscoelastic effects of polymers and the swelling induced stresses which might affect the total frequency change. If such factors are significant, the estimated apparent mass uptake can be higher than the actual uptake. This issue is discussed in more details in the next chapter.

The relation between the measured QCM resistance and the density-viscosity product was tested. Excellent agreement between the theoretical values and the measured ones where obtained.

§ 3.17 References

(1) Azzam, R. M. A.; Bashara, N. M. *Ellipsometry and Polarized Light*; North-Holland Publishing Co.: Elshevier, 1977.

(2) Tompkins, H. G.; McGahan, W. A. *Spectroscopic Ellipsometry and Reflectometry*; John Wiley & Sons, Inc.: New York, 1999.

(3) Styrkas, D.; Doran, S. J.; Gilchrist, V.; Keddie, J. L.; Lu, J. R.; Murphy, E.; Sackin, R.; Su, T.-J.; Tzitzinou, A. In *Polymer surfaces and interfaces III*; Richards, R. W.; Peace, S. K., Eds.; New York: Johe Wiley & Sons Ltd: Chichester, 1999.

(4) Woollam, J. A.; Johs, B.; Herzinger, C. M.; Hilfiker, J.; Synowicki, R.; Bungay, C. L. *SPIE Proc.* **1999**, *CR72*, 3-28.

(5) Guide to using WVASE®32. J. A. Woollam Co., Inc., 2001.

(6) Sirard, S. M.; Green, P. F.; Johnston, K. P. *J. Phys. Chem. B* **2001**, *105*, 766-772.

(7) Lipson, S. G.; Lipson, H.; Tannhauser, D. S. *Optical physics*, 3rd ed.; Cambridge ; New York, NY, USA : Cambridge University Press: New York, 1998.

(8) Keddie, J. L.; Jones, R. A. L.; Cory, R. A. *Europhys. Lett.* **1994**, *27*, 59-64.

(9) Keddie, J. L.; Jones, R. A. L.; Cory, R. A. *Faraday Discuss* **1994**, *98*, 219-230.

(10) Lu, C. and Czanderna, A.W. *Applications of piezoelectric quartz crystal microbalances, volume 7 of Methods and phenomena, their applications in science and technology*. Elsevier, Amsterdam, 1984.

(11) Buttry, D. A. and Ward, M. D. *Chemical Reviews* **1992**, *92*, 1355–1379.

(12) Ward, M. D. and Buttry, D. A. *Science* **1990**, *249*, 1000–1007.

(13) O'Sullivan, C. K. and Guilbault, G. G. *Biosensors & Bioelectronics* **1999**, *14*, 663–670.

(14) Kanazawa, K. K. and Gordon II, J. G.. *Proceedings - Electrochemical Society* **1993**, *93*, 725–731.

(15) Sauerbrey, G. *Zeitschrift Fur Physik* **1959**, *155*, 206–222.

(16) Lu, C.S. and Lewis, O. *Journal of Applied Physics* **1972**, *43*, 4385–4390.

(17) Glocker, D. and Shah, S. I. *Handbook of Thin Film Process Technology*. Institute of Physics Publishing, Bristol, UK, 1995.

(18) Martin, S. J. ;Granstaff, V. E. and Frye, G. C. *Analytical Chemistry*, **1991**, *63*, 2272–2281.

(19) Miller, J. G. and Bolef, D. I. *Journal of Applied Physics* **1968**, *39*, 4589–4593.

(20) Benes E. *Journal of Applied Physics* **1984**, *56*, 608–626.

(21) Auge, J.; Hauptmann, P.; Eichelbaum, F. and Roesler S. *Sensors and Actuators, B: Chemical* **1994**, *19*, 518–522.

(22) Kanazawa, K. K. and Hildebrand, C. *Proceedings - Electrochemical Society* **1997**, *19,* 212–217.

(23) Kanazawa, K. K. and Gordon II, J. G. *Analytica Chimica Acta* **1985**, *175*, 99–105.

(24) Filiatre, C.; Bardeche, G. and Valentin, M. *Sensors and Actuators A: Physical* **1994**, *44*, 137–144.

(25) Lucklum, R. and Hauptmann, P. *Sensors and Actuators, B: Chemical* **2000**, *70*, 30–36.

(26) White, C. C. and Schrag, J. L. *Journal of Chemical Physics* **1999**, *111*, 11192–11206.

(27) Wolff, O.; Seydel, E. and Johannsmann, D. *Faraday Discussions* **1997**, *107*, 91–104.

(28) Johannsmann, D. *Macromolecular Chemistry & Physics* **1999**, *200*, 501–516.

(29) Kanazawa, K. K. *Analyst* **2005**, *130*, 1459–1464.

(30) Klavetter, E. A.; Martin, S. J. and Wessendorf, K. O. *Energy & Fuels* **1993**, *7*, 582–588.

(31) Rahtu, A. and Ritala M. *Applied Physics Letters* **2002**, *80*, 521–523.

(32) Wang, D.; Mousavi, P.; Hauser, P. J.; Oxenham, W. and Grant C. S. *Colloids and Surfaces A: Physicochemical and Engineering Aspects* **2005**, *268*, 30–39.

(33) Park, K.; Koh, M.; Yoon, C.; and Kim H. *Journal of Supercritical Fluids* **2004**, *29*, 203–212.

(34) Wu, Y. T.; Akoto-Ampaw, P. J.; Elbaccouch, M.; Hurrey, M. L.; Wallen, S. L. and Grant C. S. *Langmuir* **2004**, *20*, 3665–3673.

(35) Daikhin, L.; Gileadi, E.; Katz, G.; Tsionsky, V.; Urbakh, M.; and Zagidulin D. *Analytical Chemistry* **2002**, *74*, 554–561.

(36) Daikhin, L. and M. Urbakh *Langmuir* **1996**, *12*, 6354–6360.

(37) Yang, M. and Thompson, M. *Langmuir* **1993**, *9*, 1990–1994.

(38) Urbakh, M. and Daikhin, L. *Physical Review B* **1994**, *49*, 4866–4870.

(39) Weerawardena, A.; Drummond, C. J.; Caruso, F.; and McCormick M. *Langmuir* **1998**, *14*, 575–577.

(40) Weerawardena, A.; Drummond, C. J.; Caruso, F. and McCormick M. *Colloids and Surfaces a-Physicochemical and Engineering Aspects* **1999**, *146*, 185–197.

(41) Caruso, F.; Serizawa, T.; Furlong, D. N. and Okahata Y. *Langmuir* **1995**, *11*, 1546–1552.

(42) Narine, S. S. and Slavin, A. J. *Journal of Vacuum Science & Technology a-Vacuum Surfaces and Films* **1998**, *16*, 1857–1862.

(43) Caruso, F.; Rodda, E.; Furlong, D. N.; Niikura, K. and Okahata Y. *Analytical Chemistry* **1997**, *69*, 2043–2049.

(44) Ha, T. H. and Kim, K. *Langmuir* **2001**, *17*, 1999–2007.

(45) Murray, B. S. and Cros, L. *Colloids and Surfaces, B: Biointerfaces* **1998**, *10*, 227–241.

(46) Kanazawa, K. K. and Melroy, O. R. *IBM Journal of Research and Development* **1993**, *37*, 157–171.

(47) Ostrom, G. S. and Buttry, D. A. *Journal of Electroanalytical Chemistry and Interfacial Electrochemistry* **1988**, *256*, 411–431.

(48) Wang, J.; Ward, M. D.; Ebersole, R. C. and Foss, R. P. *Analytical Chemistry* **1993**, *65*, 2553–2562.

(49) Lucklum, R. and Hauptmann, P. *Faraday Discussions* **1997**, *107*, 123–140.

(50) Schumacher, R.; Borges, G. and Kanazawa, K. K. *Surface Science* **1985**, *163*, L621–L626.

(51) Hussain, Y.; Krim, J. and Grant, C. S. *Colloids and Surfaces, A: Physicochemical and Engineering Aspects* **2005**, *262*, 81–86.

(52) French, R. N. and Koplos, G. J. *Fluid Phase Equilibria* **1999**, *160*, 879–892.

(53) Banda, L.; Alcoutlabi, M. and McKenna, G. B. *Journal of Polymer Science Part B: Polymer Physics* **2006**, *44*, 801–814.

(54) Granstaff, V. E. and Martin, S. J. *Journal of Applied Physics* **1994**, *75*, 1319–1329.

(55) Behling, C.; Lucklum, R. and Hauptmann, P. *Sensors and Actuators A: Physical* **1997**, *61*, 260–266.

PART II

Results

"It is in the worst conditions that
the most extraordinary things are accomplished"

CHAPTER IV

Non-equilibrium model for sorption and swelling of bulk glassy polymeric films in supercritical carbon dioxide

A new procedure is introduced for the calculation of solubility isotherms of plasticizing agents in glassy polymer matrices with particular application to the case of absorption of supercritical gases in bulk glassy polymer films. The model presented is an extension of the non-equilibrium thermodynamics for glassy polymers (NET-GP) approach, modified to allow for the calculation of the effects of pressure, temperature, and gas concentration on the glass transition.

Mass sorption and one-dimensional swelling behavior are analyzed for the carbon dioxide (CO2)-poly(methyl methacrylate) (PMMA) system at high pressure. A quantitative comparison is presented between the model performance and experimental data measured using quartz crystal microbalance (QCM) and high-pressure ellipsometry (HPE)

Chapter IV is essentially a reprint (with slight modifications) of Carla, V., et al. "Non-Equilibrium Model for Sorption and Swelling of Bulk Glassy Polymeric Films in Supercritical Carbon Dioxide" *Macromolecules* **2005,** *38,* 10299-10313.

§ 4.1 Introduction

As extensively discussed in the second chapter, carbon dioxide in its liquid and supercritical state is an attractive replacement for aqueous and organic solvents in industry primarily because of its tunable solvent properties, low cost, low toxicity, non-flammability, and its ease of recycle[1-6]. In addition, carbon dioxide is an excellent plasticizer for polymeric materials[7-10]; it is inert as a reaction solvent, and it has very low surface energy and viscosity, making it ideal for producing thin uniform coatings[11-13]. For these reasons, carbon dioxide has been used in several processes, such as, polymerization reactions[14], dry cleaning[15], drug formulations[16], foam production[17], metal deposition onto substrates[18], polymer surface modification[19], and microelectronics fabrication[20] and many applications, including polymeric membrane conditioning[21], removal of residual solvents and contaminants from polymeric films[22-24], solute impregnation[25, 26], and photoresist development[27-29].

In most of the aforementioned industrial applications the key factor that influences the quality of the final product is the ability to predict sorption and consequent swelling behavior of the polymer matrix at different operating conditions. Indeed, a reliable thermodynamic model, capable of describing the swelling of glassy polymer systems starting from dry polymeric matrices up to fully plasticized materials, is an essential pre-requisite of any good transport model aimed at predicting sorption, desorption, and dissolution kinetics in polymeric films. Because glassy polymers are non-equilibrium systems, the usual thermodynamic models for fluids and amorphous polymers, such as the Sanchez-Lacombe (SL) or the Statistical Associated Fluid Theory (SAFT) equation of state, are not directly applicable to these systems.

In order to fill this knowledge gap, a great deal of work has been done over the years to obtain useful and reliable models for sorption and dilation in glassy polymers.

Figure 4.1 is a brief and not comprehensive summary of some of the models developed.

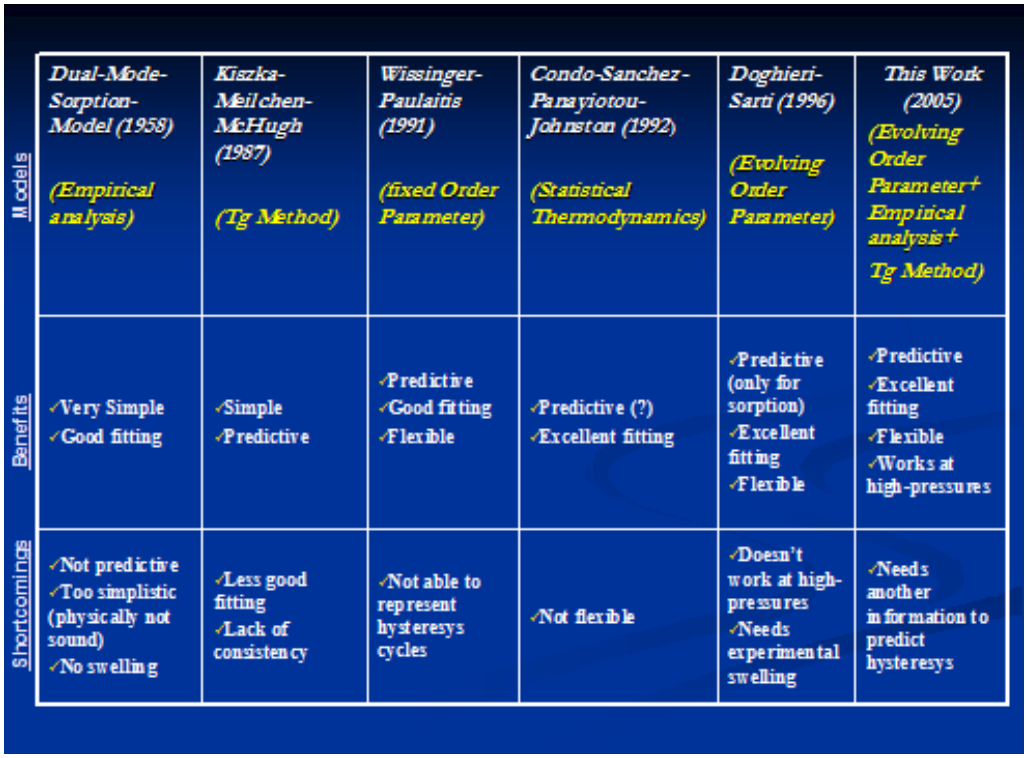

Figure 4.1 A brief summary of the different attempts of dealing with glassy polymers.

Wissinger and Paulaitis (WP model) were the first to apply successfully the non-equilibrium thermodynamics concept of an order parameter to an equilibrium lattice model[30]. Although their results were in good agreement with their experimental data, they used a constant order parameter with its value fixed at the glass transition conditions so that their model was unable to represent the significant solubility variations and hysteresis behavior associated with sorption-desorption cycles.

Soon after their work, several models appeared in the literature based on the same approach but with a different choice of the order parameter[31, 32].

The Gibbs-DiMarzio criterion, which postulates a loss of configurational entropy at the glass transition temperature, was used by Condo et al. (CSPJ model) to develop a complete consistent theory for glassy systems through an extension of the classical Sanchez-Lacombe model[33]. Because this theory is a direct extension of the Sanchez-Lacombe lattice fluid theory, its predictive power is restricted to systems for which the Sanchez-Lacombe equation of state (EoS) is able to reproduce correctly the mixture behavior in the equilibrium region. However, there exist many real systems of importance for which this is not the case.

The main aim of this chapter is to introduce a new flexible model for mass uptake and swelling of glassy polymer films induced by the sorption of plasticizing agents, with special attention to the case of CO_2-polymer systems, over a wide range of pressures. This new model is an extension, to the case of plasticizing solutes, of the Non-Equilibrium Thermodynamic model for solubility in Glassy Polymers (NET-GP), introduced by Doghieri and Sarti[34] and named NELF in its first version[35-37].

The NET-GP model extends the free energy mapping for the equilibrium state, which can be obtained from any equations of state, to the non-equilibrium domain of the glassy region using a thermodynamically consistent procedure. The NET-GP approach requires that independent information be available for the mass density of the polymer in the glassy state since this is used as an order parameter. Therefore, the first assumption of the NET-GP model is that the value of the order parameter, the out of equilibrium polymer density, determines the behavior of the system, regardless of

the sample history through which this polymer density is achieved. Thus, the NET-GP approach cannot be used as a pure predictive tool because a value of the out-of-equilibrium polymer mass density must be available. It should also be stressed that the latter, being a non-equilibrium property, depends, in the most general case, on the thermal, mechanical, and sorption history of the glassy sample.

This contribution enhances the predictive capability of the NET-GP model by coupling it with a simple theory[38] capable of estimating the amount of swelling agent necessary to result in a transition from the glassy to the rubbery state based solely on the physical properties of the pure components. As the gas is absorbed, the polymer starts to swell and eventually, as result of the augmented free volume, the glass transition temperature is lowered until the system crosses the transition point from glass to rubber. While the model obtained this way still requires independent information about the non-equilibrium dry polymer density, it does not make use of any specific adjustable parameter and only equilibrium binary interaction coefficients need to be determined in order to perform the calculations.

In this chapter, the predictions of the new model are compared with mass sorption data collected using a quartz crystal microbalance (QCM) and one-dimensional swelling data recorded using high-pressure ellipsometry (HPE) for PMMA/CO_2 films supported on silicon at two different temperatures and over a wide range of pressures. We also compare the modeling results with other literature data.

An additional significant finding of the present effort is the experimental verification of the basic assumption of the NET-GP approach, never done before, which states that two different glassy polymer samples should exhibit the same

behavior provided that their initial densities are the same, whatever their thermal, mechanical and sorption histories.

This was achieved by preparing PMMA films with the same density using two completely different coating and curing techniques. These samples were used to collect sorption and swelling data as a function of pressure at two different temperatures using high-pressure ellipsometry (HPE) and quartz crystal microbalance (QCM) methods. HPE measurements yield data on the film thickness, which can be related to the film dilation through the expression,

$$\%\ \ Swelling = \left(\frac{h - h_0}{h_0} \right) \cdot 100 \qquad (4.1)$$

HPE also provides information on the average refractive index of the swollen film, which can be converted into total carbon dioxide mass uptake[39, 40] using the index of refraction of the pure components. In this work, the mass sorption measurements from HPE were compared to the more direct mass sorption data measured with QCM.

In the first part of this chapter we describe the experimental procedures utilized in film preparation, swelling, and sorption measurements. This is followed by a description of the NET-GP model, the model used to predict the glass transition point, and the numerical procedure used for carrying out the sorption and swelling calculations. The last section presents the model results of the simulations along with the experimental results. The model performance has been tested at two different temperature, 35^{o}C and 50^{o}C, with pressures ranging from 0 to 1800 psi.

§ 4.2 Experimental Methods

§ 4.2.1 High Pressure Ellipsometry (HPE)

§ 4.2.1.1 Materials and Sample Preparation

PMMA (Mw: 72kDa, Mw/Mn = 1.06) was purchased from Polymer Source, Inc. Dorval (Montreal, Canada). Toluene (Fisher) was used as solvent to dissolve PMMA. Silicon wafers (100 mm diameter, a <100> orientation) having ≈1.7 nm thick native oxide films (SiO_x) were purchased from International Wafer Services (Portola Valley, CA). The wafers were cleaned by soaking in a mixture of JTB-111 alkaline-surfactant, hydrogen peroxide and DI water with a 4.6:1:22.8 volume ratio for 10 minutes and subsequently rinsed with copious amounts of DI water, and dried with nitrogen. PMMA/Toluene solutions were spin-coated onto silicon wafers using a Headway Research (Model 131-024, Indianapolis, IN) spin coater. The concentrations of the PMMA/Toluene solutions and spin rates were varied to obtain films of different thickness. The coated wafers were annealed at 120^{o}C under vacuum for 3-6 h to remove any residual solvent. After spin coating and annealing, the film thickness at room pressure was measured by ellipsometry (see below) and the initial mass was measured using a precision lab balance (Mettler Toledo, model AB204, Switzerland). Films of thickness ≈1.2 and ≈1.5 μm were formed with a resulting density of 1.187 g/cm^3. The densities of films used for HPE were matched as closely as possible to those used for QCM measurements. As described in detail below, the PMMA films for QCM experiments were formed by dip coating QCM substrates into PMMA/toluene solution, followed by annealing in vacuum at 80-90^{o}C for 1-2 hrs. The difference in density between the films used in QCM (1.189 g/cm^3) and those

used in ellipsometry (1.187 g/cm^3) was less than 0.2%. The polymer mass per unit area on the QCM substrates was determined by measuring the fundamental frequency difference between the bare crystal and the coated crystal. SEM was used to measure the film thickness.

§ 4.2.1.2 Ellipsometry Equipment

A Variable Angle Spectroscopic Ellipsometer (J.A. Woollam, Inc., Lincoln, NE) with rotating analyzer equipped with a custom-built high pressure CO_2 cell was used in the HPE experiments. The angle of incidence (with respect to the sample normal) was fixed at 70^o and the wavelength was varied from 500 to 800 nm. The high-pressure cell, constructed of stainless steel was equipped with 3 fused silica windows (2.54 cm in diameter and 1.5 cm in thickness, Rubicon Technology Franklin Park, IL). The two side windows were fixed at an angle of 110^o from vertical in order to obtain normal incidence of the beam with the window to avoid any deviations that can cause a change in polarization of the light and to minimize the uncertainties in the incident angle of the beam on the sample. A custom-made copper sample holder with a spring clip was used to hold the wafer and it was placed on the bottom of the cell. A torque wrench was used to put an equivalent and minimal amount of force to seal the windows to minimize the window birefringence induced by strain under high pressure. High purity CO_2 gas (Matheson Gas Product, Montgomeryville, PA, Purity > 99.999%) was charged to the cell to the desired pressure using an ISCO pump (Model 260D, Isco, Inc., Lincoln, NE).

The pressure in the cell was measured using a pressure transducer (Omegadyne, Model PX01C1-1KG10T, OMEGA Engineering, Inc. Stamford, Connecticut) controlled to an accuracy of ±2 psi (0.14 bar). A heating tape was wrapped around the cell and was connected to a variable autotransformer (Model 3PN1010, Staco, Hayward, CA) for temperature control. An insulation cap was used to cover the entire cell and heating tapes, except the windows, to obtain a uniform thermal equilibration that was found to be crucial in these experiments, especially near the critical point of CO_2. A custom-built metal heating plate was placed beneath the supporting stage to prevent heat losses. An ISCO pump (Model 260D, Isco Inc., Lincoln, NE) was connected to a heated water bath (Model 9110, Poly Science, Niles, IL) to preheat CO_2 to the desired temperature. The temperature inside the cell was measured by using a thermocouple (Omegadyne Model HGKQSS-116G-12-OMEGA Engineering, Inc., Stamford, CT) and was controlled to within ±0.1^{o}C. The cell was allowed to reach thermal equilibration at each desired temperature for at least 1 hour.

Birefringence of the windows can corrupt the polarization state of the light, and even non-birefringent windows can become birefringent due to pressure-induced window strain[41]. This, in turn, can cause large errors in the calculated properties of the samples. An experimental procedure developed by J.A. Woollam Co., Inc. was used in this work to account for the effect of the window birefringence[42, 43].

§ 4.2.1.3 Calibration at High Pressures

In order to test the effectiveness of the procedure for correcting induced window birefringence in the ellipsometric data, a calibration wafer (made at Triangle National

Lithography Center) with a thick thermal oxide layer (≈85nm) was used for scans at different pressures and temperatures. A four-layer model was used to fit the data. The refractive indices of the silicon substrate, the Si-SiO_2 interface layer, and SiO_2 were fixed using literature values[44]. The refractive index of the bulk CO_2 atmosphere at a given pressure and temperature was also obtained from literature values[45, 46]. The ellipsometry data were fitted to determine the thickness of the thermal oxide layer and the angle of incidence using WVASE32 software (J.A. Woollam, Co. Inc.). Excellent fits to the experimental data were obtained when the effects of window birefringence were measured and accounted for in the model calculations. The maximum deviation of the measured thermal oxide thickness under pressure from the thickness of the oxide layer measured in ambient air without windows was found to range between –1 and + 4% over a range of pressures from 0 to 1800 psi.

§ 4.2.1.4 Swelling Measurements

The PMMA films on the silicon wafer substrates were introduced into the chamber and scanned using the ellipsometer described above. The experimental ellipsometric data were fitted using a four-layer model, as the one discussed in the previous chapter, comprising the silicon substrate, a native oxide layer, a mixed polymer/CO_2 layer, and a bulk CO_2 medium. The refractive indices at different wavelengths were adopted from literature values[45, 46] for silicon substrate, the native oxide, and the CO_2 atmosphere. The fitted parameters for the swelling experiments were the same as those in the calibration scan, with the additional fitting of the refractive index of the swollen PMMA/CO_2 layer. The refractive index of the swollen

PMMA/CO_2 layer was modeled as a function of wavelength by assuming a Cauchy dispersion relationship[47].

§ 4.2.1.5 Mass Sorption Calculations Using Ellipsometry Data

Ellipsometry measurements provide values of the thickness and average refractive index of the swollen film. From this information it is possible to estimate the mass of gas absorbed given refractive index information for the pure components. Sirard et al.[40] showed that the mass concentration of CO_2 in a PMMA film can be estimated by applying the Clausius-Masotti equation[48, 49] to each component in the swollen film,

$$\frac{\langle n_j \rangle^2 - 1}{\langle n_j \rangle^2 + 2} = \frac{R_j}{M_{wj}} \rho_j = q_j \rho_j ; \qquad j = CO_2; \text{ PMMA} \qquad (4.2)$$

where $< n_j >$ represents the average refractive index for CO_2 and for PMMA in the swollen layer over the wavelength range from 500 to 800 nm, R_j is the mole refraction, M_{wj} is the molecular weight, and ρ_j is the mass density of the component j. Eq. (4.2) can be used to calculate values of the ratio R_j/M_{wj} for each component in the film, given literature values of the refractive indices of CO_2 and PMMA at the pressure and temperature in which the measurement is taken. The mass concentration of CO_2 and PMMA in the swollen PMMA film can be calculated from the measured refractive index $<n_f>$ of the swollen film layer through the following mixing rule[39, 40]

$$\frac{\langle n_f \rangle^2 - 1}{\langle n_f \rangle^2 + 2} = q_{CO_2}\rho_{CO_2} + q_{PMMA}\rho_{PMMA} \tag{4.3}$$

where q_{CO_2} and q_{PMMA} are determined from the pure component refractive index data.

In their analysis of sorption in glassy polymers using simple interferometry, Fleming and Koros have shown that the linear mixing rule in Eq. (4.3) may fail when the polymer is in the glassy state because of the difficulty of independently decoupling the thickness and the refractive index from optical data[50]. However, in our case, with the use of multiwavelength spectroscopic ellipsometry, it is possible to independently determine the thickness and the refractive index of a thin film, thus avoiding the aforementioned complications. Using this technique, HPE has been shown to be able to provide reasonably accurate estimates of sorption levels in rigid glassy polymers[39].

A mass balance on the polymer may be used to relate the mass concentration of the polymer in the swollen film to the measured thickness change of the film upon swelling and the original polymer density,

$$\rho_{PMMA} = \rho^0_{PMMA}\frac{h_0}{h} \tag{4.4}$$

Using Eqs. (4.2) - (4.4), the sorption of CO_2 can be estimated from knowing the quantities h, h_0, and $<n_f>$ (mixture refractive index). The densities of PMMA were calculated, for temperature higher than the room temperature, using a thermal expansion coefficient[51] of 5.6×10^{-4} K^{-1} and the refractive index of pure PMMA was

measured by ellipsometry at 1 atm. The densities of CO_2 were taken[24] to be 0.94 at and 0.93 g/cm^3 at 35 and 50^{o}C, respectively. The refractive index of the CO_2 dissolved in the polymer was taken[45] to be 1.225 and 1.221 at 35 and 50^{o}C, respectively. Over the range of pressure of these experiments, the effect of pressure on the refractive index of both PMMA and CO_2 was negligible.

§ 4.2.2 QCM Measurements

§ 4.2.2.1 Materials and Sample Preparation

5.00 MHz AT-cut Si quartz crystals (a blank diameter of 8.5 mm and a thickness of 0.25 mm) were obtained from International Crystal Manufacturing (Oklahoma City, OK). The Si film was vacuum sputtered over an Au electrode that provided the necessary electrical actuation to the quartz. The RMS surface roughness of the crystals used was less than 10 nm (analyzed using AFM). The crystal was connected to a voltage-controlled oscillator (Maxtek model PLO-10, Santa Fe Springs, CA). This oscillator provides two outputs: frequency and voltage. The voltage reading is inversely proportional to the resistance of the crystal. The oscillator is further connected to an Agilent 225 MHz Universal Frequency Counter (Model 53131A, Palo Alto, CA) that records the frequency of the vibrating crystal. The time-dependent frequency readings were stored on a computer using Agilent Intuilink Connectivity software.

PMMA films for the QCM experiments were cast onto the surface of the crystal by dip-coating. The crystal was dipped vertically into a 2.4 wt% PMMA/toluene solution, allowed to equilibrate for a specific time and then was withdrawn from the

solution at a controlled rate using a motorized device. The coated crystal was dried under vacuum at 90-100^{o}C for 1-2 hours. The clean crystal was then placed in the cell under vacuum (0.01 psia), using precision DD-20 (Inxs Inc. Delray Beach, FL) vacuum pump, and the fundamental frequency F_o of the coated crystal was recorded. The stable frequency level is indicative of complete evaporation of the solvent from the polymer during curing. The value of the stabilized frequency of the coated QCM in vacuum was utilized to calculate the mass of coated polymer by comparing to fundamental frequency of the quartz crystal without polymer. The annealing conditions were chosen so that the density of the films formed for the QCM samples were as close as possible to the density of the films made for the ellipsometry experiments (final measured value 1.187 g/cm^3 for the ellipsometry sample and 1.189 g/cm^3 for the QCM sample).

§ 4.2.2.2 High Pressure QCM Cell

The custom-built pressure cell consists of a thick-wall stainless steel cylinder (63.5 mm I.D. × 200 mm height), with a high-pressure electrical feedthrough (Conax Buffalo Techno-logies, NY) at the top end to drive the QCM. The cell has an inside volume of 25 cm^3 and a maximum working pressure of 7500 psi. The crystal was placed in the cell and connected to the oscillator through the electrical feedthrough during an experiment. A high-pressure thermocouple (Omega, Stamfortd, CT) was placed in the cell to monitor the temperature of the CO_2 fluid. Data acquisition was accomplished via a National Instrument DAQ interface using Labwiew software. The

whole assembly was then placed in a custom-built water bath and controlled to within ±0.1 °C.

§ 4.2.2.3 Mass Sorption Measurements

QCM crystals coated with polymer films were placed in the pressure cell and the fundamental F_o frequency of the QCM was measured in vacuum. After a stable signal was achieved, CO_2 was slowly introduced into the chamber to increase the pressure. The frequency was then allowed to reach a new stable level and recorded. This procedure was repeated for the third pressure level, and so on. A pressure range from 0 up to 1800 psi was examined in steps of 150 psi. After the time-dependent frequency readings were recorded for each pressure, an analysis was performed in order to obtain the correspondent mass of CO_2 uptake versus time behavior.

§ 4.3. Theory

§ 4.3.1 The NET-GP Model

This section summarizes the NET-GP model for sorption of gases into glassy polymers for the case of homogeneous, amorphous, and isotropic materials[34-37]. The model makes use of the well-known concept of order parameter for the description of the non-equilibrium state of the glassy phase at a given temperature, pressure, and composition. This idea provides a useful framework for describing systems that are not at equilibrium and avoids the introduction of mathematically cumbersome memory functions otherwise necessary for dealing with sample histories. The model then assumes that an unambiguous description of the thermodynamic properties of the

glassy polymer-gas mixture can be based on a set of state variables in which, along with temperature T, pressure P and gas content ω_1, the polymer mass density ρ_2 is included as independent variable which measures the volume deformation of the polymer network,

$$\Sigma = \Sigma(T, P, \omega_1, \rho_2) \tag{4.5}$$

thus, any specific non-equilibrium function F^{NE} of the state of the system can be described by an expression of the form

$$F^{NE} = F^{NE}(T, P, \omega_1, \rho_2) \tag{4.6}$$

With this assumption, polymeric samples below the glass transition temperature have identical thermodynamic properties at given T, P, and ω_1, provided the order parameter ρ_2 is the same, regardless of their thermal, mechanical or and sorption histories. Indeed, while the use of a single order parameter may not be sufficient to describe all the non-equilibrium characteristics of the structure of a glassy polymer mixture[61, 62], the first order approximation used in NET-GP addresses the major effect of volume deformation on the properties of the glassy polymeric mixture and it allows for a quantitative representation of sorption behavior which is satisfactory for most technical purposes.

The thermodynamic analysis of NET-GP model relies on the additional assumption that the order parameter ρ_2 is an internal state variable for the system, i.e. its rate of change in time depends strictly on the state of the system:

$$\frac{d\rho_2}{dt} = f\left(T, P, \omega_1, \rho_2\right) \tag{4.7}$$

While different order parameters can be used to describe the same thermodynamic properties of a glassy gas-polymer mixture, the assumption of different internal state variables definitely leads to different expressions for the properties in the non-equilibrium states. In this sense, results of the NET-GP model are unique with regard to earlier attempts to describe properties of glassy phases by means of different order parameters.[30-32]

Given the assumptions of Eqs. (4.6) and (4.7), through the use of well established tools of thermodynamics of systems endowed with internal state variables, the following conditions hold for the non-equilibrium Helmholtz free energy density a^{NE} and penetrant chemical potential μ_1^{NE} in the mixture[35-37]:

$$a = a^{NE}\left(T, P, \omega_1, \rho_2\right) = a^{EQ}\left(T, \omega_1, \rho_2\right) \tag{4.8}$$

$$\mu_1^{NE} = \left(\frac{\partial a^{NE}}{\partial n_1}\right)_{T, n_2, \rho_2} \tag{4.9}$$

Eqs. (4.8) – (4.9) constitute the key results of the thermodynamic analysis of non-equilibrium states for penetrant-polymer mixtures below the glass transition temperature. They allow for the derivation of expressions for the free energy and solute chemical potential of any non-equilibrium state of a glassy gas-polymer mixture, once reliable expressions for the corresponding equilibrium conditions are known. It is thus possible to calculate the solute solubility in the system, knowing the polymer mass per unit volume, through the classical phase equilibrium condition

$$\mu_1^{(S)}\left(T,P,\omega_1,\rho_2^{\infty}\right)=\mu_1^{0}\left(T,P\right) \tag{4.10}$$

or equivalently, in terms of fugacities,

$$f_1^{(S)}\left(T,P,\omega_1,\rho_2^{\infty}\right)=f_1^{0}\left(T,P\right) \tag{4.11}$$

in the expressions above, μ_1^0 and f_1^0 are the equilibrium chemical potential and fugacity of a pure penetrant phase, at temperature T and pressure P, respectively, and ρ_2^{∞} is the pseudo-equilibrium polymer density the system reaches under sorption conditions. It is important to stress that ρ_2^{∞} must be known without using equilibrium arguments in order to solve either one of Eqs. (4.10)-(4.11) for the pseudo-equilibrium gas content ω_1.

In a low-pressure sorption experiment, the swelling induced by the penetrant is negligible and the pseudo-equilibrium value of the density, ρ_2^{∞}, can be approximated

by the initial density of the pure polymer ρ_2^0. It is useful to remember that ρ_2^0 is a non-equilibrium property, which depends on the history of the polymeric material and as such it should be specifically calculated for the case of interest. The problem of representation of solubility isotherms in the low-pressure range has been addressed in previous papers, where numerous examples have been discussed[35-37, 63]. However, in the more general case, the polymer density ρ_2^∞ changes with penetrant pressure P in the external phase and its variation must be considered in order to correctly describe sorption isotherms at moderate and high pressures.

Careful analysis of experimental dilation data for a wide variety of systems indicates that at constant temperature the pseudo-equilibrium polymer density varies linearly with pressure[64], so that it can be adequately represented by an equation of the form,

$$\rho_2^\infty(P) = \rho_2^0 \cdot (1 - k_s P) \tag{4.12}$$

where the parameter k_s is the dilation coefficient of the polymeric material in the gaseous atmosphere. This is also a non-equilibrium variable, which may change according to the thermal and sorption history of the polymeric material, as well as depending on sorption/desorption runs. Fig. 4.2 shows a schematic representation of the density behavior with pressure at constant temperature.

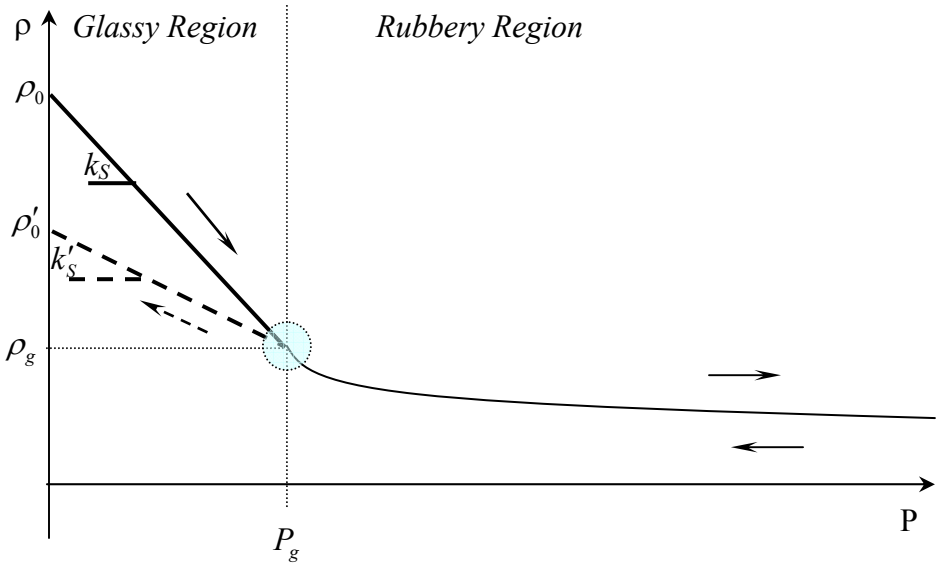

Figure 4.2 Schematic linear behavior of the polymer density with pressure at constant temperature in the glassy region.

An increase in pressure results in a linear decrease in density until a certain pressure P_g is reached at which the amount of solvent absorbed is sufficient to reach the glass transition concentration ω_1^g at which the equilibrium behavior is recovered. The point $\left(P_g, \rho_2^g\right)$ is the glass transition point and for a given mixture it depends only on temperature.

The case of representing sorption isotherms in glassy polymers up to moderate pressures, in which the swelling effect of the penetrant component must be taken into account, has been considered in a previous work through the discussion of several examples[64]. However, while the dilation coefficient k_s has a precise physical meaning, it has been treated in this previous work as an adjustable parameter that needed to be fitted using high pressure non-equilibrium solubility data. In the following section, an approach is presented that eliminates this shortcoming present in earlier NET-GP theories.

§ 4.3.2 Model for Plasticization

Using classical and statistical mechanical arguments, Chow[38] derived a relationship expressing the depression of the glass transition temperature of a polymer-solvent mixture (T_g^{mix}) by means of liquid plasticizers at low pressures, in terms of the glass transition temperature (T_g^0) of the pure polymer, the excess heat capacity, and the mass fraction of solvent inside the polymer. The derivation was based on the application of the Gibbs-DiMarzio criterion, which states that at the glass transition temperature the entropy is zero, to a lattice model.

The resulting expression for the glass transition temperature of the polymer-solvent mixture is given by,

$$\ln\left(\frac{T_g^{mix}}{T_g^0}\right) = \Psi\left[(1-\theta)\ln(1-\theta) + \theta\ln\theta\right] \tag{4.13}$$

with

$$\Psi = \frac{zR}{M_p \Delta C_p} \tag{4.14}$$

and

$$\theta = \frac{M_p}{zM_d}\frac{\omega_1}{1-\omega_1} \tag{4.15}$$

In the equations above, T_g^0 is the glass transition temperature of the dry polymer, and M_p and M_d are the molecular weights of the monomer and solvent respectively.

The quantity ΔC_p represents the difference in heat capacity between the supercooled liquid and glass, z is the lattice coordination number, R is the ideal gas constant, and ω_1 is the mass fraction of solvent in the polymer. In Table I these parameters, obtained from the literature[65, 66], are listed for PMMA.

PMMA PARAMETERS
$z = 2$
$M_p = 100.12 \quad Kg/mol$
$M_d = 44 \quad Kg/Kmol$
$\Delta C_p = 32.72 \quad J/mol \cdot K$
$T_g = 105°C$

Table I. Physical properties of un-crosslinked and non-branched PMMA[65, 66].

Chow's theory requires that the dimensionless parameter θ in Eq. (4.15) be always less than 0.25 (small concentration limit) [38, 67]. In the present work, the most extreme case has been represented by the lower temperature, where a carbon dioxide mass fraction of 0.146 is needed to lower the glass transition temperature to 35°C. This, in turn, corresponds to a value of $\theta = 0.194$, well within the window of applicability of Eq. (4.13) [38, 67].

Since Eq. (4.13) was developed for calculating the glass transition point in the presence of a liquid plasticizer, it does not have any dependence on pressure. In our case the plasticizer is a high-pressure gas and increases in pressure beyond the critical point may compress the polymer sample, reducing the free volume and increasing its glass transition temperature. However, the effect of pressure on most polymers only

becomes important at pressures far above 500 bars[33], significantly above the pressures being considered in this work. As a result, it is reasonable to neglect pressure effects on the glass transition temperature and to use Eq. (4.13) in the calculations of the depression of the glass transition temperature for the PMMA/CO_2 system.

A version of the Sanchez-Lacombe equation of state has been developed recently to address the problem of sorption in glassy polymers that also provides a method for estimating the glass transition depression due to sorption[33]. Condo et al. have shown that the Chow theory provides a better quantitative agreement with experimental data[67] than this new Sanchez-Lacombe theory. Our own calculations (not shown here) have also confirmed the results of Condo et al., showing that the Chow theory led to a much better fit to T_g data, especially at high solute concentrations. Because of its simplicity and better predictive capability, the Chow model was used here to make all predictions of T_g values. Just as the NET-GP theory can be used with any equilibrium equation of state, the Chow theory can be readily implemented with any equilibrium thermodynamic model to predict glass transition temperatures.

In next chapter a revised equation will be presented that substantially improves upon Chow's theory.

§ 4.3.3 Calculation of Solubility Isotherms in Glassy Polymers

Eqs. (4.13) – (4.15) make it possible to find the value of the penetrant composition that causes the glass transition temperature to drop down to the experimental temperature. Knowing this value, it is possible to calculate, using the equilibrium equation of state, the value of pressure and polymer density at the glass/rubber

transition point (P_g, ρ_2^g). The assumption that the density variation with pressure is approximately linear up the glass transition point leads to the expression,

$$\rho_2^{\infty}(P) = \rho_2^0 + {P}/{P_g}\left(\rho_2^g - \rho_2^0\right) \tag{4.16}$$

where ρ_2^g can be evaluated using the equilibrium EoS at T, P_g and ω_1^g. Knowing the density at the glass-rubber transition, it is possible to calculate the swelling parameter combining Eqs. (4.12) and (4.16)

$$k_S = \frac{1}{P_g}\left(1 - \frac{\rho_2^g}{\rho_2^0}\right) \tag{4.17}$$

The knowledge of the initial polymer density is crucial for the present model, however, in many cases in the literature this information is not provided, either because it is not deemed to be relevant or because it is difficult to measure the given size or shape of the sample. For those cases in which it is not directly available, we figured out a simple procedure to estimate its value from swelling data. Taking as example swelling data from the works of Wissinger et al.[68] and Zhang et al.[32], Fig. 4.3 presents the swelling information as a density ratio $\left(\rho_2/\rho_2^0\right)$ depicting the variation of PMMA density with CO_2 pressure at two different temperatures, 32.7 and 35°C.

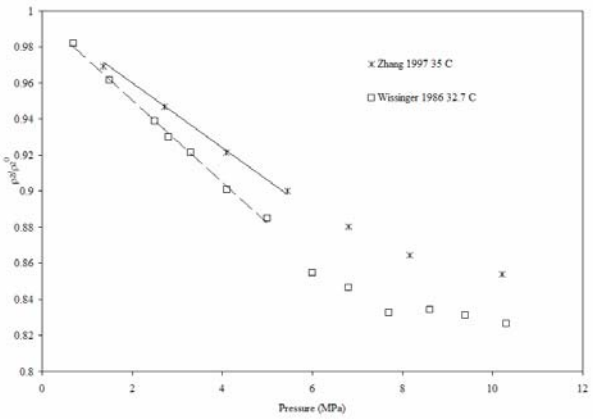

Figure 4.3 Linear behavior of PMMA density with CO_2 pressure in the glassy state[32, 61].

From the slope of the line it is possible to evaluate the value of k_s and then by using Eq. (4.17) and knowledge about the glass transition point $\left(P_g, \rho_2^g\right)$ one can estimate to a good approximation the initial polymer density ρ_2^0.

A general procedure for the calculation of the pseudo-equilibrium penetrant fraction for vapor or gas sorption in glassy polymers at an assigned temperature and pressure can now be stated as follows:

- Choose a suitable Equation of State (EoS) for the penetrant/polymer pair that provides a successful description of system properties in the melt or rubber phase;
- Choose a model for calculating either the chemical potential or the fugacity of penetrant in the gaseous phase. In most cases the same model could be conveniently used to represent thermodynamic properties in both the polymeric and gaseous phases;
- If not available, estimate the mass density of the pure polymer at the initial *T* and pressure of interest.
- Evaluate the glassy/rubbery transition point $\left(T, \omega_1^g\right)$ by taking $T_g^{mix} = T$ in Eq. (4.13) and by solving iteratively for ω_1^g. By using the

equilibrium equation of state at constant T, the mixture density and the mass fraction of the penetrant at a given P, $\omega_1(P)$, can be calculated. The glass transition pressure is defined at the pressure at which the mass fraction of penetrant becomes equal to ω_1^g; this fixes the point (P_g, ρ_2^g). Finally, evaluate the polymer density in the penetrant polymer mixture according to whether the pressure is above or below the glass transition pressure,

$$\rho_2 = \begin{cases} \rho_2^{\infty} \quad from \quad Eq.(19) \quad for \quad P < P_g \\ \rho_2^{eq} \quad from \quad EoS \quad for \quad P \geq P_g \end{cases} \tag{4.18}$$

- For each pressure value solve either Eq. (4.10) or (4.11) for the penetrant density in the polymeric mixture.

§ 4.3.4 Equilibrium Equations of State

According to the general procedure described above, different thermodynamic models can be derived for sorption and swelling in glassy polymers using different expressions for the description of polymer/penetrant mixture properties in the melt phase. This makes the NET-GP approach highly flexible since it can be used with any equilibrium EoS capable of describing accurately the melt or rubbery phase.

This work focuses on one of the most successful and frequently used equation of state for polymer solutions, the Sanchez-Lacombe equation of state (SL)[69-71]. The SL EoS is a lattice-fluid model, in which each component is divided into parts (or "mers") that are placed into a lattice and are allowed to interact with a mean-field intermolecular potential.

In the SL EoS, the reduced density is related to the reduced pressure and temperature according to,

$$\widetilde{\rho}^2 + \widetilde{P} + \widetilde{T}\left[\ln(1-\widetilde{\rho}) - \left(1-\frac{1}{r}\right)\widetilde{\rho}\right] = 0 \tag{4.19}$$

The compressibility of the system and the expressions for the fugacity coefficient, derived from the residual Helmholtz free energy[71, 72], are shown below:

$$Z = \frac{\widetilde{P}\widetilde{v}}{\widetilde{T}} r \tag{4.20}$$

$$\ln \varphi_i = -\ln Z + (Z-1) + \left(\frac{\partial a^{res}(T,V,n)}{\partial n_i}\right)_{T,V,n_j} \tag{4.21}$$

$$\ln \varphi_i(T,P,\omega_i) = -\ln Z + (Z-1) +$$

$$+ r_i\left[-\frac{\widetilde{\rho}}{\widetilde{T}} + \left(\frac{1}{\widetilde{\rho}} - 1\right)\ln(1-\widetilde{\rho}) + 1\right] + \left(\frac{Z-1}{r}\right)\left[\frac{nr}{v^*}\left(\frac{\partial v^*}{\partial n_1}\right)_{n_j}\right] - \frac{\widetilde{\rho}}{\widetilde{T}}\left[\frac{nr}{\varepsilon^*}\left(\frac{\partial \varepsilon^*}{\partial n_1}\right)_{n_j}\right] \tag{4.22}$$

Alternatively the NET-GP chemical potential can be obtained directly from the expression of the free energy as follows:

$$\mu_1^{NE} = \frac{\partial}{\partial n_1}\left\{rN\varepsilon^*\left[-\tilde{\rho} + \frac{\tilde{P}}{\tilde{\rho}} + \tilde{T}\left(\left(\frac{1-\tilde{\rho}}{\tilde{\rho}}\right)\ln(1-\tilde{\rho}) + \frac{1}{r}\ln\tilde{\rho} + \frac{\phi_1}{r_1}\ln\phi_1 + \frac{\phi_2}{r_2}\ln\phi_2\right)\right]\right\} \tag{4.23}$$

It is useful to divide the free energy as:

$$G = (rN)\cdot\left(\varepsilon^{*}\tilde{G}\right) = (rN)\cdot g \tag{4.24}$$

So that

$$\mu_1^{NE} = g\frac{\partial}{\partial n_1}(rN) + rN\frac{\partial g}{\partial n_1} = r_1 g + r_1\phi_2\frac{\partial g}{\partial \phi_1} \tag{4.25}$$

Since

$$\frac{\partial \phi_1}{\partial n_1} = \frac{\partial}{\partial n_1}\left(\frac{r_1 N_1}{r_1 N_1 + r_2 N_2}\right) = \frac{r_1\phi_2}{rN} \tag{4.26}$$

So that in the end we must evaluate

$$\left.\frac{\partial g}{\partial \phi_1}\right|_{T,P,N_2} = -\frac{\partial\tilde{\rho}}{\partial\phi_1}\varepsilon^{*} - \tilde{\rho}\frac{\partial\varepsilon^{*}}{\partial\phi_1} + Pv^{*}\frac{\partial}{\partial\phi_1}\left(\frac{1}{\tilde{\rho}}\right) + \frac{P}{\tilde{\rho}}\frac{\partial v^{*}}{\partial\phi_1} + kT\left[\frac{\partial}{\partial\phi_1}\left(\frac{1}{\tilde{\rho}}\right)\ln(1-\tilde{\rho}) + \right.$$

$$\left. -\frac{1}{\tilde{\rho}}\frac{\partial\tilde{\rho}}{\partial\phi_1} + \frac{\partial}{\partial\phi_1}\left(\frac{1}{r}\right)\ln\tilde{\rho} + \frac{1}{r\tilde{\rho}}\frac{\partial\tilde{\rho}}{\partial\phi_1} + \frac{1}{r_1}\ln\phi_1 + \frac{1}{r_1} + \frac{\partial\phi_2}{\partial\phi_1}\frac{1}{r_2}\ln\phi_2\right] \tag{4.27}$$

With clear meaning of the symbols

$$\begin{cases} \dfrac{\partial\tilde{\rho}}{\partial\phi_1} = \dfrac{(1-\tilde{\rho})\tilde{\rho}}{\phi_2} \\ \dfrac{\partial}{\partial\phi_1}\left(\dfrac{1}{\tilde{\rho}}\right) = -\dfrac{(1-\tilde{\rho})}{\tilde{\rho}\phi_2} \\ \dfrac{\partial}{\partial\phi_1}\left(\dfrac{1}{r}\right) = \left(\dfrac{1}{r_1} - \dfrac{1}{r_2}\right) \end{cases} \tag{4.28}$$

$$\begin{cases} \dfrac{\partial\varepsilon^*}{\partial\phi_1} = \left(\varepsilon_{11}^* - \varepsilon_{22}^*\right) + \left(\phi_1 - \phi_2\right) kT\chi_{12} \\ \dfrac{\partial v^*}{\partial\phi_1} = \left(v_{11}^* - v_{22}^*\right) \\ \dfrac{\partial\phi_2}{\partial\phi_1} = -1 \end{cases} \tag{4.29}$$

So that with a little algebra:

$$\frac{\mu_1^{NE}}{kT} = -r_1\tilde{\rho}\frac{\varepsilon^*}{kT} - r_1(1-\tilde{\rho})\tilde{\rho}\frac{\varepsilon^*}{kT} + r_1\phi_2\tilde{\rho}\left[\frac{\left(\varepsilon_{11}^* - \varepsilon_{22}^*\right)}{kT} + \left(\phi_1 - \phi_2\right)\chi_{12}\right] + \frac{r_1}{\tilde{\rho}}\frac{Pv^*}{kT} - \frac{r_1}{\tilde{\rho}}\frac{(1-\tilde{\rho})Pv^*}{kT} +$$

$$+\phi_2\frac{r_1}{\tilde{\rho}}\frac{P\left(v_{11}^* - v_{22}^*\right)}{kT} + \frac{r_1}{\tilde{\rho}}(1-\tilde{\rho})\ln(1-\tilde{\rho}) - \frac{r_1}{\tilde{\rho}}(1-\tilde{\rho})\ln(1-\tilde{\rho}) + \frac{r_1}{r}\ln\tilde{\rho} - r_1(1-\tilde{\rho}) +$$

$$+\left(1-\frac{r_1}{r_2}\right)\phi_2\ln\tilde{\rho} + \frac{r_1}{r}(1-\tilde{\rho}) + \phi_1\ln\phi_1 + \frac{r_1}{r_2}\phi_2\ln\phi_2 + \phi_2\ln\phi_1 + \phi_2 - \phi_2\ln\phi_2 - r_1 \tag{4.30}$$

The terms circled in the above equation prove that the effort of calculating the chemical potential has not been carried out in vane. In fact all the terms circled are not present in the traditional expression for the Sanchez-Lacombe chemical potential. The

reason of this and its importance for our purposes will be clearer to the reader in a moment.

Re-arranging the above expression into a more common form:

$$\frac{\mu_1^{NE}}{kT} = \ln\phi_1 + \left(1-\frac{r_1}{r_2}\right)\phi_2 + r_1\phi_2^2\tilde{\rho}\chi_{12} +$$

$$+ r_1\left[-\frac{\tilde{\rho}}{\tilde{T}_1} + \frac{\tilde{P}_1}{\tilde{\rho}\tilde{T}_1} + \frac{(1-\tilde{\rho})}{\tilde{\rho}}\ln(1-\tilde{\rho}) + \frac{1}{r_1}\ln\tilde{\rho}\right] + \frac{\mu_1^{extra}}{kT} \qquad (4.31)$$

where

$$\frac{\mu_1^{extra}}{kT} = -r_1\tilde{\rho}(1-\tilde{\rho})\frac{\varepsilon^*}{kT} - r_1\frac{P v^*(1-\tilde{\rho})}{\tilde{\rho}kT} - r_1\frac{(1-\tilde{\rho})}{\tilde{\rho}}\ln(1-\tilde{\rho}) - r_1(1-\tilde{\rho})\left(1-\frac{1}{r}\right) =$$

$$= -r_1(1-\tilde{\rho})\frac{\varepsilon^*}{\tilde{\rho}kT}\left\{\tilde{\rho}^2 + \tilde{P} + \tilde{T}\left[\ln(1-\tilde{\rho}) + \left(1-\frac{1}{r}\right)\tilde{\rho}\right]\right\} \qquad (4.32)$$

Clearly the term in parenthesis represents the equation of state which in equilibrium conditions is always zero. This explains the reason for the extra circled terms in Eq.(4.29) as well as indicates precisely the difference between equilibrium S-L and non-equilibrium S-L. In the non-equilibrium conditions in fact the equation of state does not hold any more and the extra chemical potential must be evaluated according to Eq.(4.31).

In this work two versions of the SL equation of state have been used. The first version (SL-I) [69-71] is the classical version with one adjustable binary parameter in the

mixing rules, as expressed by Eqs. (4.32) – (4.34). The second version (SL-II) has two adjustable binary parameters in the mixing rules as proposed more recently by McHugh and Krunokis[1, 71-73], as represented by Eqs. (4.34) – (4.37).

$$v^* = \sum \phi_i v_{ii}^* \tag{4.33}$$

$$\varepsilon^* = \sum\sum \phi_i \phi_j \varepsilon_{ij}^* \tag{4.34}$$

$$\varepsilon_{ij}^* = \sqrt{\varepsilon_{ii}^* \varepsilon_{jj}^*}\left(1 - k_{ij}\right) \tag{4.35}$$

$$\varepsilon^* = \frac{1}{v^*}\sum\sum \phi_i \phi_j \left(v\varepsilon\right)_{ij}^* \tag{4.36}$$

$$v_{ij}^* = \frac{1}{2}\left(v_{ii}^* + v_{jj}^*\right)\left(1 - \eta_{ij}\right) \tag{4.37}$$

$$v^* = \sum\sum \phi_i \phi_j v_{ij}^* \tag{4.38}$$

For a complete description of the symbols used above the reader is referred to the original manuscript[ref]. In the following section, results from the correlation of experimental sorption and swelling data for the PMMA/CO_2 system through use of NET-GP model will be shown in detail, using both the SL-I and SL-II equations of state. The pure component parameters for CO_2 and PMMA for use in the SL-I and

SL-II equations of state were obtained from the literature and are tabulated in Table II.

Pure parameter[33-72]	CO_2	PMMA
T^* [K]	283	696
P^* [MPa]	659	503
ρ^* [g/cm^3]	1.62	1.269

Table II. Pure component parameters[33, 72].

The critical point for carbon dioxide predicted using these parameters is (42°C, 75 bar), which means that the model overestimates the critical temperature by about 11°C and overestimates the critical pressure by only 20 psi. In the case of the lowest temperature considered in this study, the CO_2 model will predict a phase change from gas to liquid instead of the real transition from gas to supercritical CO_2.

The binary interaction parameters, k_{ij} for SL-I and the pair (k_{ij}, η_{ij}) for the SL-II model, were determined by fitting the EoS to sorption data at pressures above 100 bars. In this region the PMMA/CO_2 mixture is rubbery and the SL equation of state is able to do an excellent job of correlating the thermodynamic properties.

Table III lists values of the binary interaction parameters for SL-I and SL-II taken from high-pressure data at 35 and 50°C. The values of these parameters are in general agreement with previous literature results[73]. The data used to make these parameter fits are presented Figures 7–9, to be discussed in detail in the following section.

Binary Parameters	SL-II	SL-I
k_{ij}^{35}	0.1246	-0.044
η_{ij}^{35}	0.033	//
k_{ij}^{50}	0.1161	-0.040
η_{ij}^{50}	-0.015	//

Table III. Interaction parameters for both versions of the SL equation of state. Parameters fit to sorption data above 100 bars at two temperatures, 35°C and 50°C.

Once the binary interaction parameters were estimated, the model was used to compute sorption and swelling behavior over the entire range of pressure including the glassy region using the NET-GP approach described above.

§ 4.4. Results and Discussion

In order to provide good estimates of the effect of the penetrant concentration on the glass transition pressure, the modified NET-GP procedure described above must result in good estimates of the dilation parameter. Table IV compares experimental[64] and predicted values for the swelling coefficient k_s for a series of polymer-gas pairs. All the reported values were calculated at 35°C.

The predicted values of k_s were obtained using the procedure described above, using Eq. (4.17) coupled with the SL-II equation of state with pure component and binary interaction parameters fitted in this work for the PMMA-CO_2 pair and taken from the literature for the other pairs[64, 65].

	k_s [Mpa^{-1}] experimental	k_s[Mpa^{-1}] calculated	Error %
PMMA-CO_2	$1.85 \cdot 10^{-2}$	$1.80 \cdot 10^{-2}$	2.78
PC-CO_2	$1.14 \cdot 10^{-2}$	$1.18 \cdot 10^{-2}$	3.51
PC-C_2H_4	$1.20 \cdot 10^{-2}$	$1.21 \cdot 10^{-2}$	1.67
PS-CO_2	$1.21 \cdot 10^{-2}$	$1.23 \cdot 10^{-2}$	1.65

Table IV. Comparison of experimental[64] and calculated swelling coefficients for several polymer- gas pairs at 35°C. The data needed for the calculations have been taken from the literature[64, 65].

The predicted swelling coefficients are all within 1-4% of the experimental values, indicating that the procedure is indeed capable of making reasonable extrapolations of the density variations with pressure at constant temperature. Solubility data obtained for CO_2 in PMMA at 50°C as measured by both the HPE and QCM techniques in sorption/desorption experiments are compared in Fig. 4.4, where the quantity Ω_{CO_2} represents the ratio of grams of CO_2 absorbed per gram of polymer $\left(g_{CO_2} / g_{Polymer}\right)$.

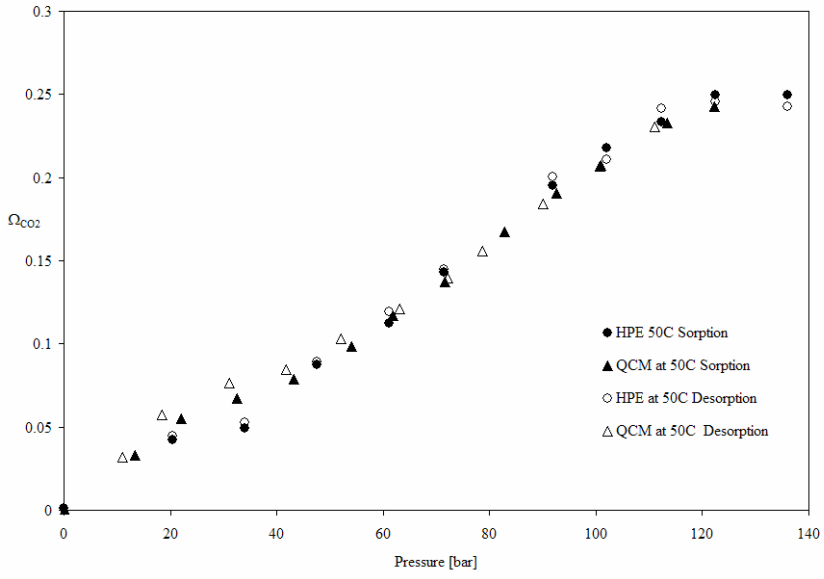

Figure 4.4 Solubility isotherm for CO_2 in PMMA at 35°C from sorption and desorption experiments as measured by QCM and high-pressure ellipsometry.

The two series of measurements are in very good agreement with each other, except for a few scattered points at low pressures. At this relatively high temperature there is very little hysteresis in the CO_2 isotherm as the pressure is decreased. As discussed in the experimental description, films prepared for QCM and HPE followed two completely different preparation histories, but have nearly identical densities. The excellent agreement between the sorption data for both samples shown in Fig. 4.4 indicates not only that the two measurement techniques are highly consistent, but also that glassy polymer films prepared according to two completely different protocols exhibit similar sorption behaviors, provided they are characterized by the same polymer mass density. This result provides experimental verification of one of the basic assumptions in the development of NET-GP models, namely, that the glass polymer density can be used as a single order parameter to determine swelling and sorption, and as a consequence, samples with the same initial density are expected to exhibit similar sorption and swelling behavior regardless of their past histories. This is the first experimental verification of the suitability of this assumption.

HPE can provide a prompt measurement for the glass transition pressure, i.e. the pressure required to have sufficient amount of CO_2 absorbed into the polymer matrix necessary to lower the glass transition temperature to the experimental temperature[39, 74]. To determine the glass transition pressure, we measured the ellipsometric angle ψ as a function of CO_2 pressure at different wavelengths (from 500 to 800 nm) for both sorption and desorption isotherms. Fig. 4.5 shows a plot of the average ψ values as a function of pressure along with straight line fits to point out the difference in slopes before and after the critical pressure.

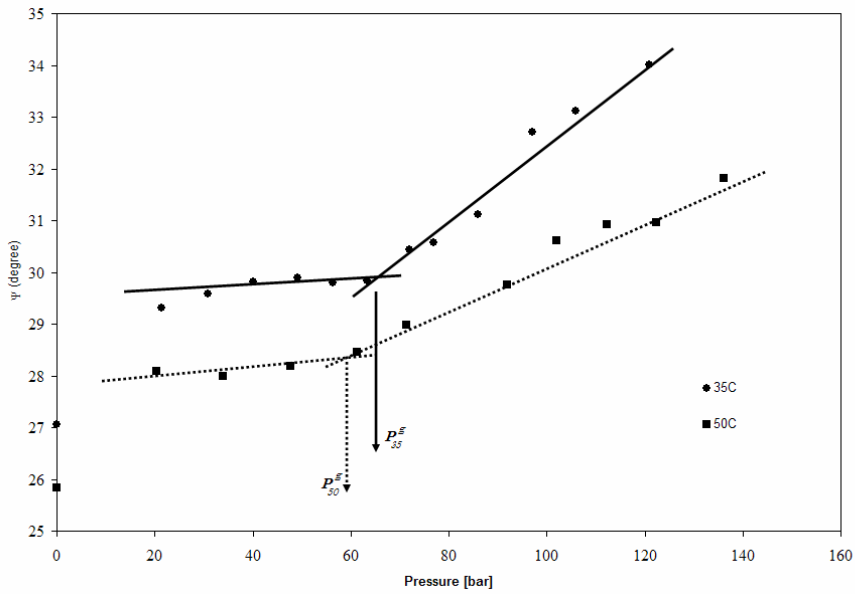

Figure 4.5 Ellipsometric angle ψ as a function of CO_2 pressure at 35°C and 50°C. The CO_2-induced glass transition pressure, P_g, is identified as the pressure at which the slope of the ψ–*Pressure* curve changes.

The pressure at which the change in curvature occurs is identified as the P_g[74], *i.e.* $P_g^{35} \cong 64$ bar and $P_g^{50} \cong 58$ bar, which are in very good agreement with previous measurements[74, 75]. The beginning of the hysteresis in the dilation data upon sorption and desorption cycles has been often associated with the glass transition location of the glass transition pressure[39, 40]. The data in Figures 4.4 and 4.5 indicate that the P_g values estimated from the change in slope of the ellipsometric angle agree quite well with P_g values estimated from the presence of hysteresis in dilation during the sorption and desorption cycles.

Fig. 4.6 shows experimental data for CO_2 solubility in PMMA at 50°C measured from QCM sorption experiments. Superimposed on the data in the same figure are the predictions of the NET-GP model using the SL-I and SL-II equations of state.

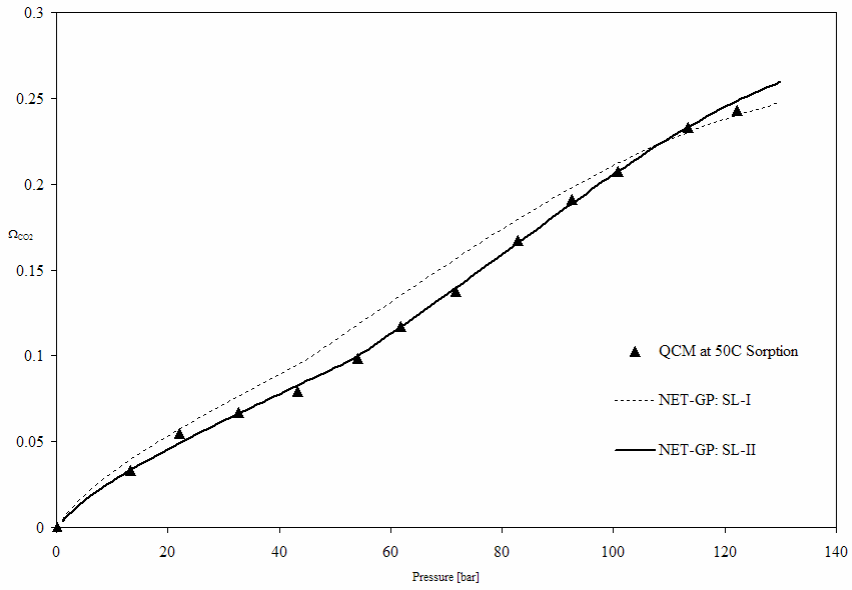

Figure 4.6 Solubility isotherm for sorption of CO_2 in PMMA at 50°C: comparison between experimental data and fitting results using NET-GP SL-I [thin solid line] and NET-GP SL-II [thick solid line]

The interaction parameters used in the SL-I and SL-II models fitted to the sorption data for pressures greater than 100 bars are listed in Table III. According to the Chow theory in Eq. (4.13), the CO_2 concentration at the glass transition point should correspond to a value of $\Omega_{CO_2}^{50} = 0.096$.

At this penetrant concentration, the glass transition pressure P_g^{50} was estimated as 46 bar and 54 bar using the SL-I and SL-II models respectively, within a few bars from the measured experimental value. Model predictions below P_g shown in Fig. 4.6 were obtained from solubility calculations using the non-equilibrium NET-GP approach with the SL-I and SL-II equations of state.

Solubility results obtained with NET-GP and the SL-II equation of state exhibit a clear representation of all features shown by experimental data over the entire

pressure range, including a slight change in the slope at the glass transition pressure. A less accurate picture of solubility and pseudo-solubility data is obtained by means of NET-GP with the SL-I equation of state, although the qualitative variation of the solubility isotherm with pressure range are correctly represented.

Figure 4.7 shows % swelling or dilatation data using HPE during sorption at 50°C for PMMA at CO_2 pressures corresponding to the sorption data shown in Fig. 4.6. The predicted % swelling results from the NET-GP model using SL-I and SL-II parameters shown in Table III are superimposed on the experimental results.

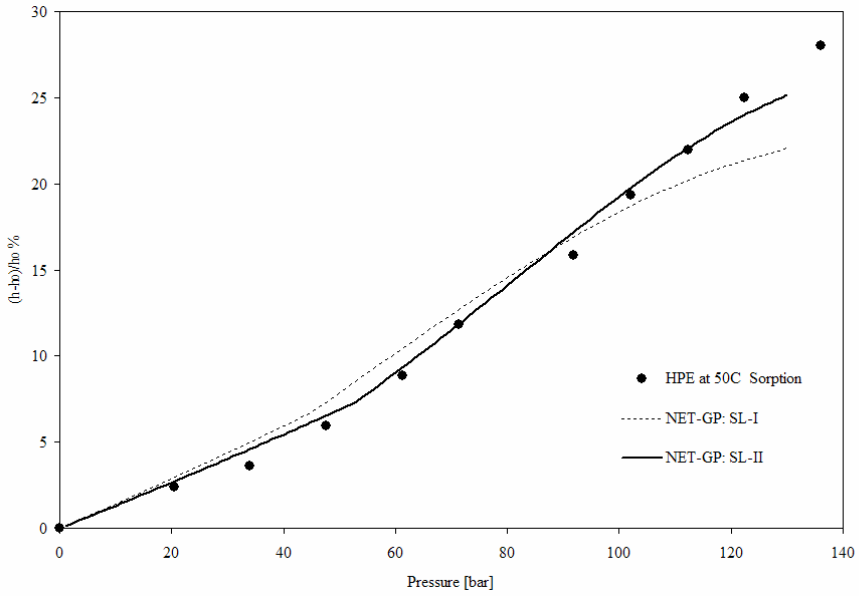

Figure 4.7 Volume swelling isotherm for sorption of CO_2 in PMMA at 35°C: comparison between experimental data and predicted results using NET-GP SL-I [thin solid line] and NET-GP SL-II [thick solid line].

The swelling calculations shown in this figure did not require any additional fits of parameters, only a direct application of the parameters fitted in the high-pressure regime with sorption data shown in Fig. 4.6. As was the case with the sorption data,

the results from the NET-GP approach with the SL-II model provide a more accurate representation of the swelling experimental data. Considering that all the model results in Fig. 4.7 were complete predictions, even the less accurate NET-GP SL-I model resulted in an impressively good comparison with the % swelling experimental results. The linear behavior assumed for volume swelling below P_g^{50} in Eq. (4.13) is clearly visible in the model predictions, and it is substantially confirmed by the experimental data.

Having established that the NET-GP SL-II model clearly offers a more accurate representation of the experimental results for the PMMA/CO_2 system, only the results of this model will be presented in subsequent discussions.

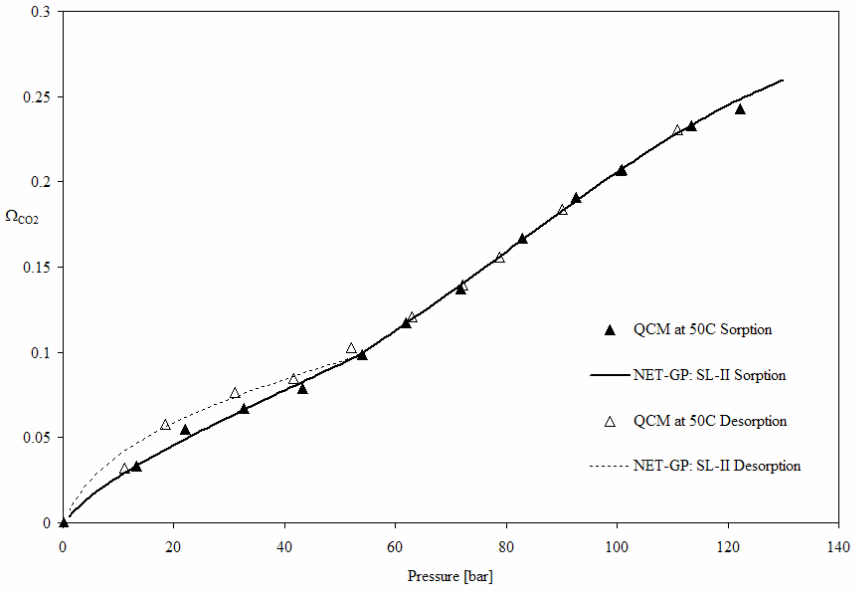

Figure 4.8 Solubility isotherm for sorption-desorption cycle of CO_2 in PMMA at 50°C: comparison between experimental data and fitting results using the NET-GP SL-II theory.

Figure 4.8 shows QCM sorption data measured at 50°C during both sorption and desorption cycles as the pressure is increased to 135 bars and then decreased to the atmospheric pressure. The results are compared to the predicted gas solubility calculated using NET-GP SL-II. Even though the hysteresis in CO_2 solubility for sorption-desorption cycles in this system is not very large, the model is able to represent it through the use of a different swelling coefficient (k'_S) for the desorption leg. The extra information needed for the calculation of the desorption curve in the glassy region has been retrieved here through the use of a fitting procedure for the swelling coefficient.

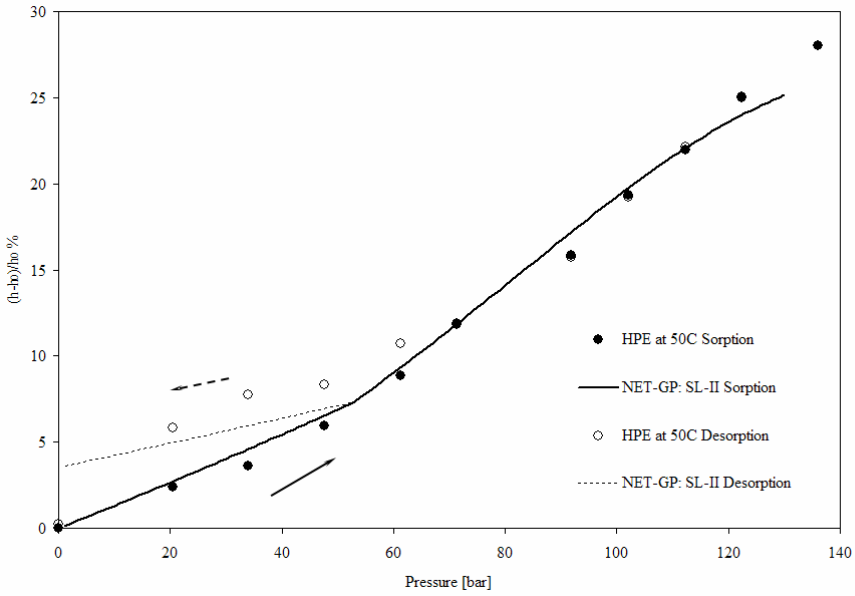

Figure 4.9 Volume swelling isotherms for sorption - desorption cycle of CO_2 in PMMA at 50°C: prediction using the NET-GP SL-II theory.

The corresponding HPE swelling data during the sorption and desorption cycle at 50°C are shown in Fig. 4.9. For comparison, Fig. 4.9 also shows the % swelling

predictions using the NET-GP SL-II. The hysteresis in the measured system volume between sorption and desorption below P_g^{50} is clearly evident in the experimental data. The model is able to obtain a fairly accurate quantitative comparison on the magnitude of the % swelling hysteresis, at least close to the glass transition, but it is not able to predict very well the values at lower pressure.

This large disparity between the model and the experimental data at low pressures is probably due to the assumption of linearity of polymer density with pressure in desorption as well as sorption. Whereas this assumption, based on experimental evidence, has been useful for modeling sorption, apparently it does not hold true in desorption for the entire pressure range. It seems to be a reasonable approximation near the glass transition point, but it does not carry forward as the pressure goes to atmospheric. This assumption is also responsible for the predicted non-zero value of the swelling at zero pressure.

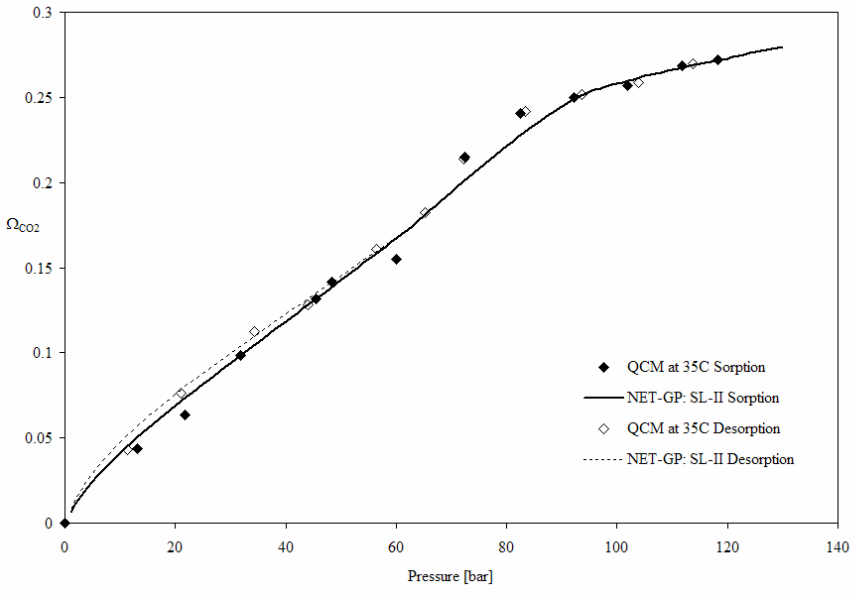

Figure 4.10 Solubility isotherm for sorption-desorption cycle of CO_2 in PMMA at 35°C: comparison between experimental data and fitted results using the NET-GP SL-II theory.

Figure 4.10 shows the measured solubility of carbon dioxide by QCM in terms of grams of CO_2 absorbed per gram of polymer (Ω_{CO_2}) during a sorption-desorption cycle at 35°C, a temperature just above the critical temperature for CO_2. Also shown are the comparisons to calculated values using the NET-GP SL-II model with parameters fit with solubility data during the sorption step above 100 bars at 35°C.

The binary interaction parameters for both the SL-I and SL-II models at this temperature are also shown in Table III. Chow's theory in Eq. (4.13) predicts that the CO_2 mass density at the glass transition point corresponds to a value of $\Omega_{CO_2} = 0.171$. Using the NET-GP SL II model, the value of the glass transition pressure at 35°C was estimated to be P_g^{35}= 62 bars, very close to the measured value. In the figure the sorption isotherm for CO_2 in PMMA at 35°C has been predicted by means of the equilibrium SL-II equation of state above P_g^{35} and the NET-GP SL-II model below that limit. A comparison of the experimental and predicted results reveals that the model provides an accurate representation throughout the whole pressure range, as the polymer changes from glassy to rubbery and the penetrant transits from vapor to a supercritical fluid.

Figure 4.11 shows the corresponding % swelling of PMMA measured by HPE during the sorption-desorption cycle at 35°C, together with the NET-GP SL-II predictions. The linear volume dilation below the glass transition pressure is evident as well as the hysteresis in measured film thickness below P_g during sorption and desorption runs. The results from the NET-GP SL-II model provide a good representation of the complex swelling behavior of this system for sorption process in the whole pressure range and for desorption process as long as the pressure is above

20 bars, the point below which the linear density variation with pressure assumption during dilation apparently fails in reproducing the experimental results, as discussed above.

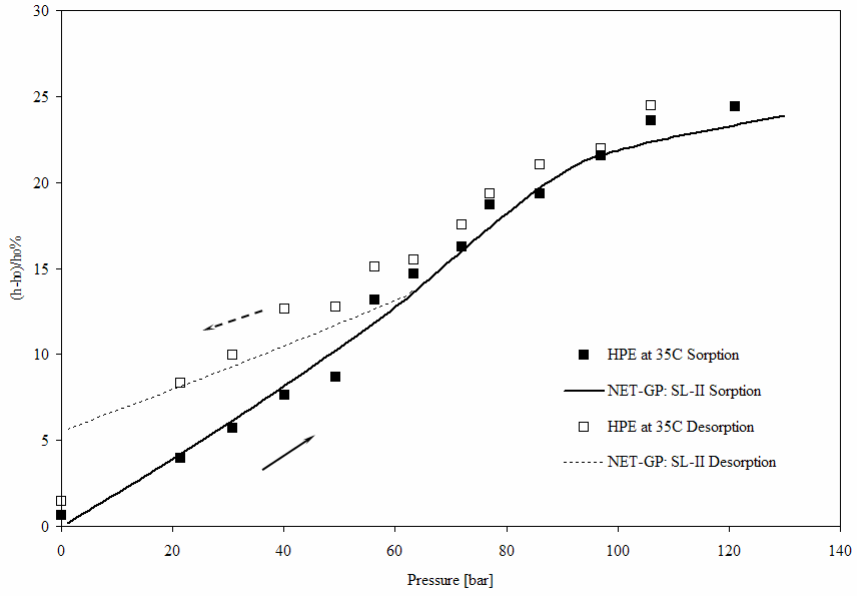

Figure 4.11 Volume swelling isotherm for sorption of CO_2 in PMMA at 35°C: comparison between experimental data and predicted results from NET-GP SL-II theory.

Finally, in Fig. 4.12 a comparison is shown between the predictions of the NET-GP SL-II model and swelling data for CO_2 sorption in PMMA measured by Wissinger and Paulaitis[30]. The binary interaction parameters for this calculation were estimated by fitting the swelling data at high pressure and the results are summarized in Table V. The initial density of the polymer samples used in the NET-GP SL-II calculations were not reported by Wissinger and Paulaitis[75], but they were estimated by the procedure described in the model development section of this work. Little squares in the figure mark the glass transition point as estimated here from Chow's theory. The

highest glass transition pressure is that at 42°C, because P_g experiences a maximum with temperature.

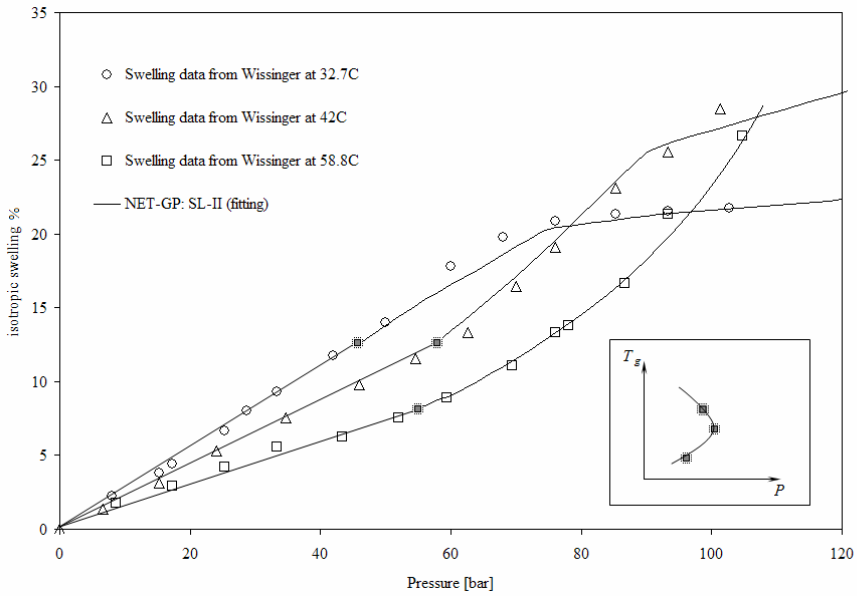

Figure 4.12 Volume swelling isotherm for sorption of CO_2 in PMMA at 32.7°C, 42°C, and 58.8°C: comparison between experimental data[61] and fitting results using the NET-GP SL-II theory [thin solid lines].

This feature, reported by Condo et al.[33], has been called "retrograde vitrification" and can be explained by considering the Chow's theory and the sorption behavior versus pressure at different temperatures.

As the temperature increases, the amount of carbon dioxide needed for the transition decreases but also the sorption isotherm decreases, as result of the two opposite effects there is a maximum of P_g versus temperature as shown in the little inbox of the figure. It is encouraging that our model coupled with Chow's equation is able to predict such a complex behavior.

Binary Parameters	SL-II
k_{ij}^{33}	0.099
η_{ij}^{33}	0.078
k_{ij}^{42}	0.091
η_{ij}^{42}	-0.080
k_{ij}^{59}	0.077
η_{ij}^{59}	-0.161

Table V. Interaction parameters for the SL-II model. Parameters fit to data above 80 bars for each temperature.

§ 4.5. Conclusions

This chapter describes an extension of the Non Equilibrium Thermodynamics of Glassy Polymer (NET-GP) model for swelling and sorption to the case of a high-pressure plasticizing penetrant. The theory of Chow is used to estimate the penetrant concentration at the glass transition point, which can then be used to estimate the pressure at the glass transition point using the equilibrium equation of state for the rubber phase. By assuming there is a linear relation between the glassy polymer density and the pressure below the glass transition pressure, it is possible to estimate the dilatation or swelling coefficient for the polymer-penetrant system. This facilitates the calculation of the sorption and swelling behavior by modeling the

system using NET-GP below the glass transition pressure and the equilibrium equation of state above the glass transition pressure. The NET-GP approach can be used with any equilibrium equation of state that is capable of predicting the behavior of the system in the rubbery state. As a result, this is a very flexible approach that can be used for any equation of state regardless of its complexity. Use of the theory relies on knowledge of the initial density of the glassy polymer prior to solvent penetration. For cases, in which the initial polymer density is not known or is not provided, a procedure is described that facilitates its estimation based on the magnitude of the swelling coefficient.

The new model was applied to the interpretation of experimental data collected for sorption/desorption processes of CO_2 in PMMA films at different temperatures and for a wide range of CO_2 pressures. Swelling of PMMA was measured using high-pressure ellipsometry (HPE) and mass absorption was measured directly by use of a quartz crystal microbalance (QCM). The mass of absorbed CO_2 was also determined indirectly from the measured refractive index of the swollen film resulting from the ellipsometric analysis.

One of the major experimental findings of this contribution is that the sorption and swelling behaviors of two samples of a polymer are the same as long as their densities are the same, even though their histories can be significantly different. To the best of our knowledge, this is the first experimental verification of the basic assumption of the NET-GP model, namely, that the glass polymer density can be used as order parameter to describe the non-equilibrium thermodynamic state of the system.

Through the use of a non-equilibrium version of the Sanchez-Lacombe lattice fluid model with two binary interaction parameters (NET-GP SL-II model), gas solubility and volume dilation were correctly represented at all experimental conditions. The model was able to provide a remarkably good agreement with the swelling hysteresis observed experimentally upon sorption and desorption of the gas, except for pressures close to atmospheric in desorption runs, where there is an apparent breakdown in the assumption of linearly of density with pressure.

The model also was able to provide an accurate description of the glass transition pressure variation with temperature as well as the amount of gas absorption in the glassy polymer region. The work presented in this chapter will serve as the basis for the development in the study of the dynamic and equilibrium properties of high-pressure gas-polymer systems presented in chapter VI.

§ 4.6 References

(1) McHugh, M. A.; Krukonis, V. J. *Supercritical Fluid Extraction: Principles and Practice;* Butterworths: Boston, 1986.

(2) McHugh, M. A.; Krukonis, V. J. *Encyclopedia of Polymer Science and Technology;* Mark, H. F., Bikales, N. M., Overberger, C. G., Menges, G., Eds.; Wiley-Interscience: New York, **1989**; Vol. 16, p 368.

(3) Daneshvar, M.; Gulari, E. *Supercritical Fluid Science and Technology;* Johnston K.P., Penninger, J. M.L.,Eds.; ACS Symposium Series 406; American Chemical Society: Washington, DC, **1989**.

(4) Canelas, D. A.; Betts, D. E.; DeSimone, J. M.; Yates, M. Z.; Johnston, K. P. *Macromolecules* **1998**, *31*, 6794.

(5) Yates, M. Z.; Li, G.; Shim, J.-J.; Johnston, K. P. Lim, K.T.; Webber, S. *Macromolecules* **1999**, *32*, 1018.

(6) Kiran, E.; Saraf,V. P.; Sen, Y.L. *Int. J. Thermophys.* **1989**, *10*, 437

(7) Wang, W.-C. V.; Kramer, E. J.; Sachse, W. H. *J. Polym. Sci., Polym. Phys. Ed.* **1982**, *20*, 1371.

(8) Chiou, J. S.; Barlow, J. W.; Paul, D. R. *J. Appl. Polym. Sci.* **1985**, 30, 2633.

(9) Hachisuka, H.; Sato, T.; Imai, T.; Tsujita, Y.; Takizawa, A.; Kinoshita, T. *Polym. J.* **1990**, *22*, 77.

(10) Wissinger, R. G.; Paulatis, M. E. *J. Polym. Sci., Part B: Polym. Phys.* **1991**, *29*, 879.

(11) Hoy, K. L., Donhue, M. D. *Polym. Prepr.* **1990**, *31*, 679.

(12) Cooper, A.I. *Mater. Chem.* **2000**, *10*, 207.

(13) Novick, B.J.; Carbonell, R. G; DeSimone, J. M. *Proceedings of the 5th International Symposium of Supercritical Fluids*, April **2000**.

(14) DeSimone, J. M.;Guan, Z; Eisbernd, C.S. *Science*, **1992**, *257*, 945.

(15) Flores, P. A. PCT Int. Appl. (2004)

(16) Kazarian, S. G. *Drugs and the Pharmaceutical Sciences* **2004**, *138*, 343.

(17) Dixon, D. J.; Johnston, K. P.; Bodmeier, M. A. *AIChE J.* **1993**, *39*, 127.

(18) Watkins, J. J.; Blackburn, J. M.; McCarthy, T. J. *Chem. Mater.* **1999**, *11*, 213.

(19) Howdle, S. M.; George, M. W.; Poliakoff, M. in *Chemical Synthesis Using Supercritical Fluids*; Jessop, P. G., Leiner, W. , Eds.; Wiley-Vch: Weinheim, 1999.

(20) Weibel, G.L.; Ober C.K *Microelectronic Engineering* **2003**, *65*, 145

(21) Pope, D. S.; Koros, W.J. *Macromolecules* **1992**, *25*, 1711.

(22) Shim, J.-J.; Johnston, K. P. *AIChE J.* **1989**, *35*, 1097.

(23) Shim, J.-J.; Johnston, K. P. *J.Phys. Chem.* **1991**, *95*, 353.

(24) Shim, J.-J.; Johnston, K. P. *AIChE J.* **1991**, *37*, 607.

(25) Sand, M. L. Method for Impregnating a Thermoplastic Polymer, US Patent #4,598,006 (**1986**).

(26) Kazarian, S. G.; Vincent, M. F.; West, B. L.; Eckert, C. A. *J. Supercritical Fluids* **1998**, *13*, 107.

(27) Gallacher-Wetmore, P.; Ober, C. K.; Gabor, A. H.; Allen, R. D. *Proc. SPIE-Int. Soc. Opt. Eng.* **1996**, *289*, 2725.

(28) Gabor, A. H.; Allen, R. D.; Gallacher-Wetmore, P.; Ober, C. K. *Proc. SPIE-Int. Soc. Opt. Eng.* **1996**, *410*, 2724.

(29) Sundararajan, N.; Yang, S.; Ogino, K.; Valiyaveettil, S.; Wang, J.; Zhou, X.; Ober, C. K.; Obendorf, S. K.; Allen, R. D. *Chem. Mater.* **2000**, *12*, 41.

(30) Wissinger, R. G.; Paulatis, M. E. *Ind. Eng. Chem. Res.* **1991**, *30*, 842.

(31) Barbari, T. A.; Conforti, R. M. *Polym. Adv. Technol.* **1994**, *5*, 698.

(32) Zhang, Y; Gangwani, K. K.; Lemert, R. M. *J. Supercritical Fluids* **1997**, *11*, 115.

(33) Condo, P. D.; Sanchez, I. C.; Panayiotou, C. G.; Johnston, K. P. *Macromolecules* **1992**, *25*, 6119.

(34) Doghieri, F., Ghedini, M., Quinzi, M., Rethwisch, D.G., and Sarti, G.C., *in Advanced Materials for Membrane*, Ed., I. Pinnau and B.D. Freeman, ACS Symposium Series, v. 876, 55-73, 2004.

(35) Doghieri, F.; Sarti, G. C. *Macromolecules*, **1996**, *29*, 7885.

(36) Sarti, G. C.; Doghieri, *F. Chem. Eng. Sci.* **1998**, *53*, 3435.

(37) Doghieri, F.; Sarti, G. C. *J. Membr. Sci.* **1998**, *147*, 73.

(38) Chow, T. S. *Macromolecules* **1980**, *13*, 362.

(39) Wind, J. D.; Sirard, S. M.; Paul, D. R.; Green, P. F.; Johnston, K. P.; Koros, W. J. *Macromolecules* **2003**, *36*, 6433.

(40) Sirard, S. M.; Green, P. F.; Johnston, K. P. *J. Phys. Chem. B* **2001**, *105*, 766.

(41) Scmidt, J. W.; Moldover, M. R. *J. Chem. Phys.* **1993**, *99*, 582-589.

(42) Johs, B., *Accurate Correction of Window Effects in Ellipsometric Data*. J. A. Woollam Co., Inc., 9/7/99.

(43) Johs, B. *Methods for uncorrelated evaluation of parameters in parameterized mathematical equations for window retardance, in ellipsometer and polarimeter systems* US Patent #6,034,777.

(44) Herzinger, C. M.; Johs, B.; McGahan, W. A.; Woollam, J. A.; Paulson, W. *J. Appl. Phys.* **1998**, *83*, 3323-3336.

(45) Michels, A.; Hamers, J. *Physica IV* **1937**, 995-1006.

(46) Obriot, J.; Ge, J.; Bose, T. K.; St-Arnaud, J. M. *Fluid Phase Equilib.* **1993**, *86*, 315-350.

(47) Tompkins, H. G.; McGahan, W. A. *Spectroscopic Ellipsometry and Reflectometry*; John Wiley & Sons: New York, 1999.

(48) Stamatialis, D. F.; Wessling, M.; Sanopoulou, M.; Strathmann, H.; Petropoulos, J. H. *J. Membr. Sci.* **1997**, *130*, 75.

(49) Bolton, B. A.; Kint, S.; Bailey, G. F.; Scherer, J. R. *J. Phys. Chem.* **1986**, *90*, 1207.

(50) Fleming, G.K.; Koros, W.J. *Journal of Polymer Science: Part B: Polymer Physics*, **1987**, *25*, 2033.

(51) Orwoll, R. A.; In *Physical Properties of Polymers Handbook*; Mark, J. E., Ed., American Institute of Physics: Woodbury, 1996.

(52) Wu, Y. T.; Akoto-Ampaw, P. J.; Elbaccouch, M.; Hurrey, M. L.; Wallen, S. L.; Grant, C. S., *Langmuir*, **2004**, *20*, 3665.

(53) Miura, K.-I.; Otakeb, K.; Kurosawab, S.; Sakob, T.; Sugetab, T.; Nakaneb, T.; Satob, M.; Tsujia,T.; Hiakia, T.; Hongoa, M. *Fluid Phase Equilibria*, **1998**, *144*, 181.

(54) Sauerbrey, G. *Zeitschrift fuer Physik* **1959**, *155*, 206

(55) C. S. Lu and O. Lewis, *Journal of Applied Physics*, **1972**, *43*, 4385.

(56) K. Kanazawa, *Faraday Discussions*, **1997**, *107*, 77.

(57) C. C. White and J. L. Schrag, *J. Chem. Phys*., **1999**, *111*, 24, 11192.

(58) R. Lucklum and P. Hauptmann, *Electrochimica Acta*, **2000**, *45*, 3907.

(59) Stockbridge, C. D.; Behrndt, K. H. (Eds.) in *Vacuum Microbalance Techniques*, Plenum, New York, 1966, Vol.5, pp. 147-191.

(60) Kanazawa, K. K.; Gordon, J. G., II *Analytical Chemistry Acta*, **1985**, *175*, 99.

(61) Astarita, G.; Paulatis, M. E.; Wissinger, R. G. *J. Polym. Sci., Part B: Polym. Phys.* **1989**, *27*, 2105.

(62) Roe, R.-J. *J. Appl. Phys.* **1977**, *48*, 4085.

(63) Doghieri. F; Ghedini, M.; Quinzi, M.; Rethwisch,D.; Sarti, G.C. *Desalination* **2002**, *144*,73

(64) Giacinti Baschetti M.; Doghieri, F.; Sarti, G. C. *Ind. Eng. Chem. Res.* **2001**, *40*, 3027.

(65) Varma-Nair, M.; Wunderbelich B. *J. Phys. Chem. Ref. Data* **1982**, *11,* 1985

(66) Royer, J.R.; DeSimone, J.M.; Khan, S.A. *Journal of Polymer Science: Part B: Polymer Physics*, **2001**, *39*, 3055.

(67) Condo, P.D.; Paul, D.R.; Johnston, K.P. *Macromolecules,* **1994**, 27, 365-371

(68) Wissinger, R. G.; Paulatis, M. E. *J. Polym. Sci., Part B: Polym. Phys.* **1987**, *25*, 2497.

(69) Sanchez, I. C.; Lacombe, R. H. *J. Phys. Chem.* **1976**, *80*, 2352.

(70) Lacombe, R. H. ; Sanchez, I. C. *J. Phys. Chem.* **1976**, *80*, 2568.

(71) Sanchez, I. C.; Lacombe, R. H. *Macromolecules* **1978**, *11*, 1145.

(72) Neau, E. *Fluid Phase Equil.* **2002**, *203*, 133

(73) Kirby, C. F.; McHugh, M. A. *Chem. Rev.* **1999**, *99*, 565.

(74) Pham, J.Q.; Sirard, S.M.; Johnston, K.P. and Green P.F. *Physical Review Letters*, **2003**, *91*, 17.

(75) Wissinger, R. G.; Paulatis, M. E. *J. Polym. Sci., Part B: Polym. Phys.* **1987**, *25*, 2497.

CHAPTER V

Glass Transition Temperature of Polymer-CO_2 system: Revisiting Chow's Theory

In the last chapter we have applied Chow's equation for the evaluation of the glass transition point shift with carbon dioxide pressure. In this chapter the Gibbs-DiMarzio criterion is re-applied to deriving new expression for correlating glass transition temperature with pressure and solvent content using classical and statistical thermodynamics. A modified Chow's equation is obtained as main result of the present analysis that overcomes the major drawbacks embedded in the original expression.

§ 5.1 Introduction to glass transition temperature T_g

Glass transition temperature is an important physical quantity when dealing with many different applications, ranging from rheology to studies of diffusion in polymers. Often, especially in engineering, there is the need for fast ways of getting

estimates or approximate results and equations readily available for this purpose are in short supply.

Over the past thirty years many different attempts at providing such expressions have appeared in the literature, utilizing rather different approaches, both equilibrium thermodynamics and kinetics, in order to answer the simple question: *how much does T_g drop with the sorption of a given amount of solvent?*

The most important contribution has been that of Gibbs and DiMarzio[1-4] who developed a consistent thermodynamic procedure showing how it is possible to conceive a temperature at which all the discontinuities of the experimental glass transition temperature can be located.

The Gibbs-DiMarzio criterion states that for temperatures equal or lower than T_g the configurational entropy of the system is zero, or in other words, the glass transition temperature is the highest temperature for which the entropy is still null[1-4], as illustrates the black line in Figure 5.1.

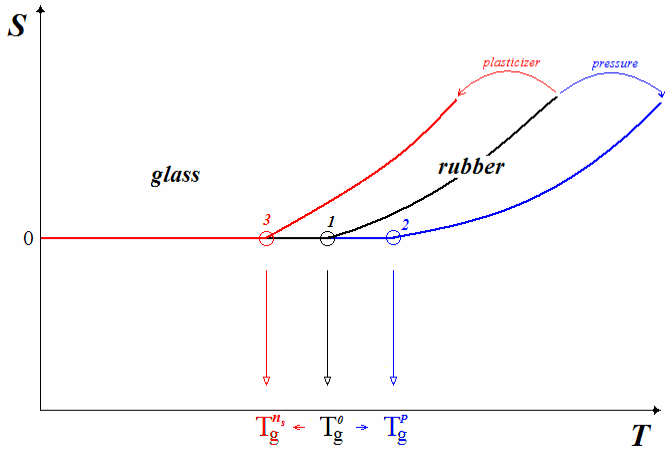

Figure 5.1 Schematic of the Gibbs-DiMarzio Criterion. Increasing the pressure makes T_g increase whereas increasing the content of plasticizer T_g decreases.

§ 5.2 Original Chow's theory for liquid plasticizer

Using Gibbs-DiMarzio approach Chow[5] has obtained a relationship between the configurational entropy of a polymer-diluent system and the change of glass transition temperature upon sorption based on a calculation of the configurational entropy according to Bragg-Williams approximation.

Even thought the final equation of the theory is rather simple it presents two major flaws that have prevented it from being more widely adopted by the polymer community. The main aim of the present effort is to revisit Chow's equation using different assumptions that allow solving the issues embedded in the original theory.

From classic thermodynamics arguments, the entropy of a two-component (polymer-solvent) mixture can be written as:

$$dS = \left(\frac{C_p}{T}\right)_{P,n_s} dT - \left(\frac{\partial V}{\partial T}\right)_{T,n_s} dP + \mu_s dn_s \qquad (5.1)$$

Moving from point (1) in figure 5.1 to point (2) according to Gibbs-DiMarzio the entropy is always zero thus:

$$0 = \int_{T_1}^{T_2}\left(\frac{C_p}{T}\right)_{P,n_s} dT - \int_{P_1}^{P_2}\left(\frac{\partial V}{\partial T}\right)_{T,n_s} dP + \int_{n_1}^{n_2} \mu_s dn_s \qquad (5.2)$$

Eq. (5.2) is the starting point for building equations aimed at predicting glass transition change upon sorption of plasticizers.

In the case of a non-adsorbing gas (such as helium or argon) by increasing the pressure an increase of the glass transition can be observed experimentally. This is usually interpreted in the light of a reduction in free volume upon compression of the sample by the static pressure.

We show here that this behavior can be easily explained with thermodynamic arguments descending from Gibbs-DiMarzio criterion.

Let us consider for the sake of simplicity constant C_p and thermal expansion coefficient $\alpha = \left(\partial V/\partial T\right)_T$ and no further adsorption upon a pressure step from P_1 to P_2 (n_1=n_2), from equation (5.2) one finds:

$$0 = C_p \int_{T_1}^{T_2} \frac{dT}{T} - \alpha \int_{P_1}^{P_2} dP \tag{5.3}$$

Which after integration yields:

$$\ln\left\{\frac{T_g(P)}{T_g^0}\right\} = \frac{\alpha}{C_p}\left(P - P_0\right) \tag{5.4}$$

Eq. (5.4) predicts that the glass transition temperature increases exponentially with the pressure step. However, since the coefficient is very small ($\alpha/C_p \ll 1$) very high pressures are required in order to increase T_g of an appreciable percentage. This is the reason why the pressure term in Eq. (5.2) is usually neglected even for gaseous plasticizers.

In general Eq. (5.2) can be integrated following the path, *(a),(b),(c),* indicated in figure 5.2, however for liquid plasticizers and for low pressures (below 500bars) the pressure term can be neglected leading to an expression that correlates change in glass transition temperature with the solvent content

$$0 = \int_{T_g^0}^{T_g} C_p\Big|_{P,n_s} d\ln T + \int_0^{n_s} \left(\frac{\partial S}{\partial n_s}\right)_{T,P} dn_s \qquad (5.5)$$

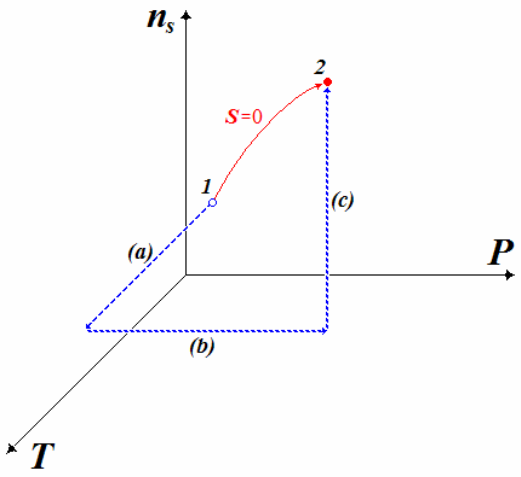

Figure 5.2 Three dimensional path followed for the integration of equation (5.2)

Which assuming a constant heat capacity can be re-arranged into

$$\ln\left(\frac{T_g(n_s)}{T_g^0}\right) = \frac{1}{C_p\Big|_{P,n_s}}\left[S(0) - S(n_s)\right] \qquad (5.6)$$

At this point in order to evaluate the change in entropy of combination due to the change in composition that appears in the left-hand side of Eq. (5.4) we must turn to

statistical mechanics. It is important to understand that the entropic change we are talking about does not depend upon the number of ways that the polymer chains have to rearrange on the lattice.

To keep the calculations as simple as possible Chow used Bragg-Williams lattice fluid approximation which gives:

$$\Omega(N) = \frac{(N+L)!}{N!L!} \tag{5.7}$$

with N number of sites occupied by solvent molecules (1 site for each molecule) and L number of sites occupied by polymer chains. The corresponding physical picture that one should bear in mind is rather simple, having a lattice of N+L sites, first place the number of solvent molecules N and then in the remaining L sites place the polymer chains. The figure 5.3 represents a sketch of the situation described. Of course this idea is questionable if the aim is that of obtaining a complete thermodynamic description of the system under study but perfectly legitimate for the purposes of the present analysis.

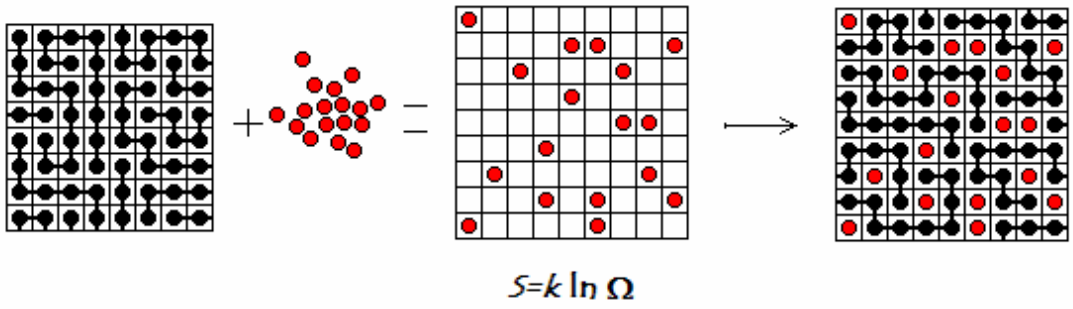

Figure 5.3 Schematic representation of the assumption behind the approximation made by Chow, the only relevant step is the distribution of solvent molecules on the lattice sites.

From Boltzmann law, $S = k \ln \Omega$, one has:

$$ln\left(\frac{T_g(n_s)}{T_g^0}\right) = -\frac{k}{C_p}\left[\ln\left(\Omega(N)\right)\right] \tag{5.8}$$

Where of course from (5.7), $\Omega(0) = 1$. Simplifying Eq.(5.7) by means of Stirling's approximation: $n! = \left(\frac{n}{e}\right)^n$ for n very high one gets

$$\Omega(N) \approx \frac{(N+L)^{(N+L)}}{N^N L^L} \cdot \mathrm{e}^{N+L-(N+L)} = \left(\frac{N+L}{N}\right)^N \cdot \left(\frac{N+L}{L}\right)^L \tag{5.9}$$

Combining Eq.(5.8) with Eq.(5.9) yields:

$$ln\left(\frac{T_g(n_s)}{T_g^0}\right) = \frac{k(N+L)}{C_p}\left\{\left(\frac{N}{N+L}\right)\ln\left(\frac{N}{N+L}\right) + \left(\frac{L}{N+L}\right)\ln\left(\frac{L}{N+L}\right)\right\} \tag{5.10}$$

Which now by defining two dimensionless quantities:

$$\begin{cases} \beta = \dfrac{k(N+L)}{\Delta C_p} \\ \theta = \dfrac{N}{N+L} \end{cases} \tag{5.11-1-2}$$

returns the final result of Chow's analysis:

$$\boxed{ln\left(\frac{T_g(n_s)}{T_g^0}\right)=\beta\left\{\theta\ln\theta+(1-\theta)\ln(1-\theta)\right\}} \qquad (5.12)$$

after evaluating θ and β, or else N and L, from macroscopic quantities Eq. (5.12) allows to calculate the T_g change upon sorption.

§ 5.3 New assumptions for *L*

Chow assumes then

$$\begin{cases} N = m_d N_A / M_d \\ (N+L) = z\, m_P N_A / M_p \end{cases} \qquad (5.13\text{-}1,2)$$

It is clear from the second equation in (5.13) that this can be true only for $N<<L$ since the solvent moles are assumed to not change the total number of lattice sites.

According to the Bragg-Williams lattice fluid model there is no free volume (no empty lattice sites) so at the beginning (dry polymer) the only species present is the polymer and it occupies all the lattice sites. As the solvent comes into the matrix, more lattice sites are added to the system (the ones occupied by the solvent).

While it is correct to assume N according to Chow's definition, a new definition is in order for equation (5.13.2) since the total initial number of lattice sites $(N+L)$ should in general depend upon N.

Indeed, it is assumed that each solvent molecule occupies a single lattice site whereas the polymer repeating unit might be (it usually is) bigger than the solvent molecule. Calling z now the ratio of the number of lattice sites occupied by one monomer unit to the ration of lattice sites occupied by each solvent molecule (one site) a more rigorous definition for L would be:

$$\begin{cases} N = m_d N_A / M_d \\ L = z\, m_P N_A / M_p \end{cases} \qquad (5.14\text{-}1,2)$$

So that by evaluating θ and β from their definitions Eqs.(5.11-1,2) we obtain

$$\theta_{new} = \left(\frac{N}{N+L} \right) = \frac{m_d / M_d}{m_d / M_d + z m_p / M_p} = \frac{1}{1 + z M_d \left(1-\omega\right) / M_p\, \omega} =$$

$$= \frac{1}{1 + 1/\theta_{chow}} = \frac{\theta_{chow}}{1+\theta_{chow}} \qquad (5.15)$$

And

$$\beta_{new} = \frac{k}{\Delta C_p}\left(N+L\right) = \frac{k N_A}{\Delta C_p}\left(\frac{m_d}{M_d} + \frac{z m_p}{M_p} \right) = \frac{R}{m_p \Delta C_{pp}}\left(\frac{m_d}{M_d} + \frac{z m_p}{M_p} \right) =$$

$$= \frac{zR}{M_p \Delta C_{pp}}\left(\frac{M_p}{z M_d} \frac{\omega}{1-\omega} + 1 \right) = \beta_{chow}\left(1+\theta_{chow}\right) \qquad (5.16)$$

Where the subscript *new* means according to assumption (5.14-1,2) and the subscript *chow* means according to assumptions (5.13-1,2).

It is possible then to rewrite the final result Eq.(5.12) in terms of Chow's own dimensionless quantities:

$$ln\left(\frac{T_g(N)}{T_g^0}\right)=\beta_{new}\left\{\theta_{new}\ln\theta_{new}+(1-\theta_{new})\ln(1-\theta_{new})\right\} \tag{5.17}$$

$$ln\left(\frac{T_g(N)}{T_g^0}\right)=\beta_{chow}(1+\theta_{chow})\left\{\left(\frac{\theta_{chow}}{1+\theta_{chow}}\right)\ln\left(\frac{\theta_{chow}}{1+\theta_{chow}}\right)+\right.$$
$$\left.+\left(1-\left(\frac{\theta_{chow}}{1+\theta_{chow}}\right)\right)\ln\left(1-\left(\frac{\theta_{chow}}{1+\theta_{chow}}\right)\right)\right\} \tag{5.18}$$

which simplifying and regrouping becomes:

$$\boxed{\begin{aligned} &ln\left(\frac{T_g(N)}{T_g^0}\right)=\beta_{chow}\left\{\theta_{chow}\ln\theta_{chow}-(1+\theta_{chow})\ln(1+\theta_{chow})\right\} \\ &\begin{cases}\theta_{chow}=\dfrac{M_p}{zM_d}\dfrac{\omega}{1-\omega}\\ \beta_{chow}=\dfrac{zR}{M_p\Delta C_{pp}}\end{cases}\end{aligned}} \tag{5.19}$$

The above expression is the main result of the present chapter.

§ 5.4 Discussion

In this section we briefly discuss the advantages embedded in Eq.(5.19) by comparing its performance with Chow's original expression Eq.(5.12) as well as with another model recently appeared in the literature[4,6-8] that applies the Gibbs-DiMarzio criterion to Guggenheim's partition function and utilizes the Sanchez-Lacombe equation of state for the properties of the mixture. A different expression obtained utilizing Guggenheim's solution will also be introduced and discussed.

First of all it is easy to show that the new equation does not predict a minimum in T_g versus composition. Taking the derivative with composition from Eq.(5.12) (original equation) results:

$$\frac{T_g(N)}{T_g^0} = \exp\left\{\beta\left[\theta\ln\theta + (1-\theta)\ln(1-\theta)\right]\right\}$$
$$\frac{\partial T_g(N)}{\partial\omega} = 0 \Rightarrow \frac{\partial\left[\theta\ln\theta + (1-\theta)\ln(1-\theta)\right]}{\partial\theta}\left(\frac{\partial\theta}{\partial\omega}\right) = 0 \qquad (5.20.1\text{-}2)$$

$$\left\{\ln\theta + 1 - \ln(1-\theta) - 1\right\}\left(\frac{\partial\theta}{\partial\omega}\right) = 0 \Rightarrow \ln\left(\frac{\theta}{1-\theta}\right) = 0 \Rightarrow \theta = \frac{1}{2} \qquad (5.21)$$

There exists a singularity (minimum) in the original version which corresponds to a physically unrealistic situation, it is worth to mention that this shortcoming is a direct consequence of having assumed that the solvent molecules do not increase the number of lattice sites.

Taking the derivative from the revisited theory, Eq. (5.19), yields:

$$\frac{T_g(N)}{T_g^0} = \exp\left\{\beta\left[\theta\ln\theta-(1+\theta)\ln(1+\theta)\right]\right\}$$
$$\frac{\partial T_g(N)}{\partial\omega}=0\Rightarrow\frac{\partial\left[\theta\ln\theta-(1+\theta)\ln(1+\theta)\right]}{\partial\theta}\left(\frac{\partial\theta}{\partial\omega}\right)=0 \qquad (5.22\text{-}1\text{-}2)$$

$$\left\{\ln\theta+1-\ln(1+\theta)-1\right\}\left(\frac{\partial\theta}{\partial\omega}\right)=0\Rightarrow$$

$$\ln\left(\frac{\theta}{1+\theta}\right)=0\Rightarrow \textit{impossible} \qquad (5.23)$$

A second advantage embedded in the new form over the original theory is that *z* does not represent the lattice coordination number but it is meant to be the number of unit sites occupied by a single monomer if the solvent occupies only one site. Being a physical parameter it can be a real number and does not need to be an integer!

Furthermore, it is possible to devise ways of getting an estimate of *z* which then is no longer treated as adjustable parameter of the theory. The following figures 5.4 and 5.5 serve as comparison of performances between the original expression and our new expression. Figure 5.4 portrays data from ref. 5 of polystyrene and many different solvents. Clearly up to a concentration around 0.10 the two expressions match each other because in the low concentration limit, assumption 5.13.2 is not a bad approximation.

However there exist many cases of importance where the aforementioned assumptions does not hold true anymore.

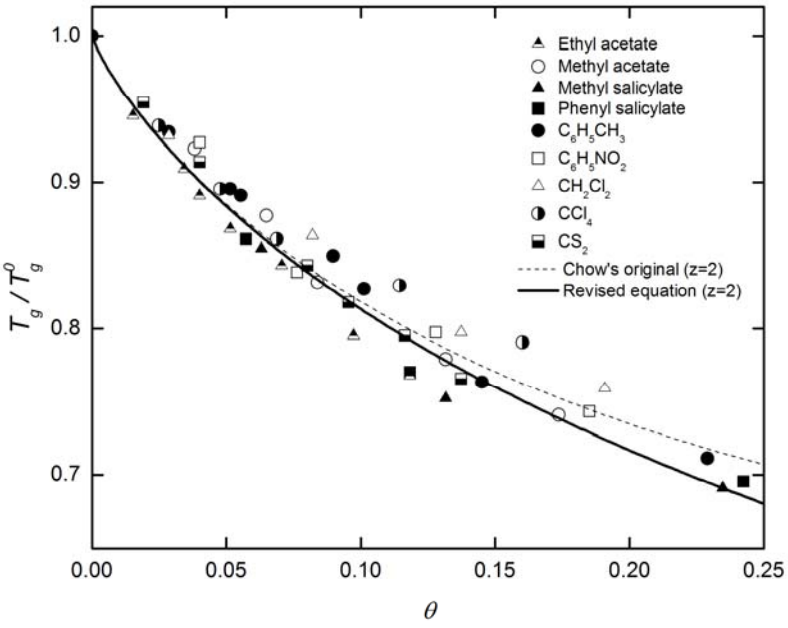

Figure 5.4 Data are replotted from ref.5.

Figure 5.5 depicts another comparison of performance between the original expression and the new revised theory. Data are re-plotted from ref. 10. This time there is only one solvent, carbon dioxide, and many different polymers have been studied using DSC.

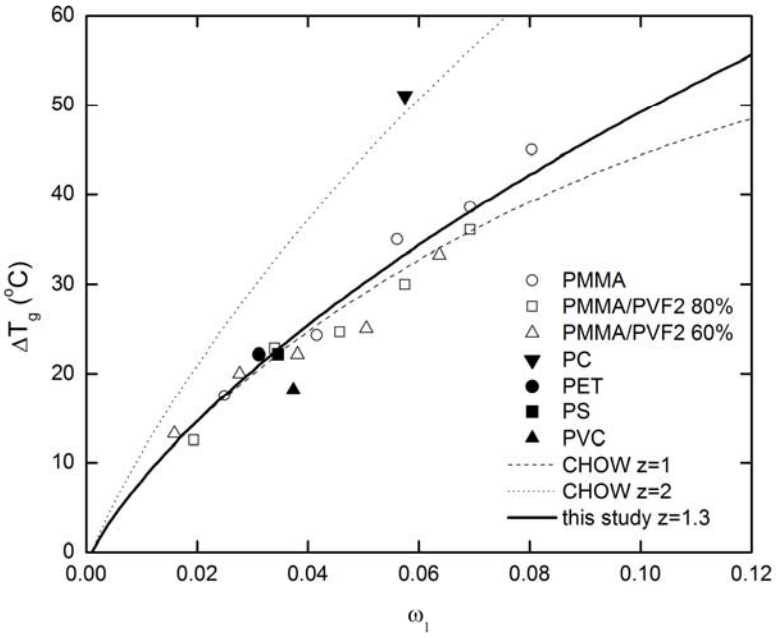

Figure 5.5 Carbon dioxide with different polymers. Data are from ref. 10

It is possible to conceive other expressions like Eq. (5.12), by choosing a different expression for the evaluation of the change in the entropy of configuration of the system.

Perhaps the simplest improvement would be to aim at calculating the entropy of mixing N molecules of solvent each occupying r_d lattice sites instead of just one. This introduces the need to define a surface effect (linked to the shape of molecules that are not spherical anymore) as well as a flexibility parameter. To describe the situation shown in figure 5.3 we consider here a simple expression obtained starting from Guggenheim's result for the partition function[4]

$$\Omega = \delta^N \frac{(r_d N + L)!}{N!L!}\left[\frac{(qN + L)!}{(r_d N + L)!}\right]^{z/2} \tag{5.24}$$

Where r_d is the number of sites occupied by one solvent molecule (>1), z is the real coordination number, δ is the flexibility of the solvent, usually assumed to be[4]

$$\delta \simeq z(z-1)^{(r_d-2)} \tag{5.25}$$

and q is a surface factor defined by:

$$q = r_d - \frac{2}{z} + \frac{2}{r_d z} \tag{5.26}$$

Going back to Eq. (5.6) and in complete analogy with what done to derive Eq. (5.12) the final expression, Eq. (5.27), is retrieved:

$$ln\left(\frac{T_g(N)}{T_g^0}\right) = \beta\left\{\theta \ln\theta - (r_d + \theta)\ln(1+\theta) - \theta \ln(r_d\delta) + \right.$$

$$\left. -\left(\frac{z}{2} r_d\right)(1+\psi\theta)\ln\left(\frac{1+\psi\theta}{1+\theta}\right)\right\} \tag{5.26}$$

with

$$\begin{cases} \psi = \dfrac{q}{r_d} \\ \theta = \dfrac{r_d}{r_p}\dfrac{M_p}{M_d}\dfrac{\omega}{1-\omega} \\ \beta = \dfrac{r_p}{r_d}\dfrac{R}{M_p \Delta C_{pp}} \end{cases} \tag{5.27}$$

Equation (5.26) is the natural extension of Eq.(5.19) into which it will transform when r_d=1. Figures 5.6-5.8 show the effect of parameters r_d, z and δ on the T_g predictions.

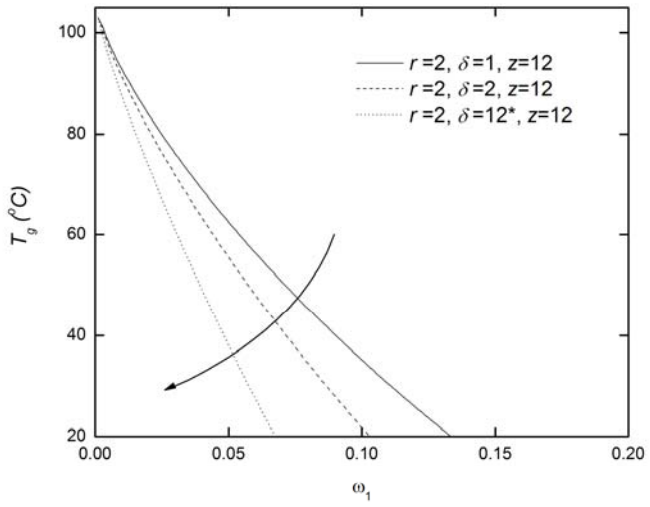

Figure 5.6 Results from Eq.(5.26) showing the effect of changing the flexibility parameter δ. Interestingly the more flexible is the solvent the higher is the impact on T_g reduction. δ=12 corresponds to the maximum value compatible with Eq.(5.25).

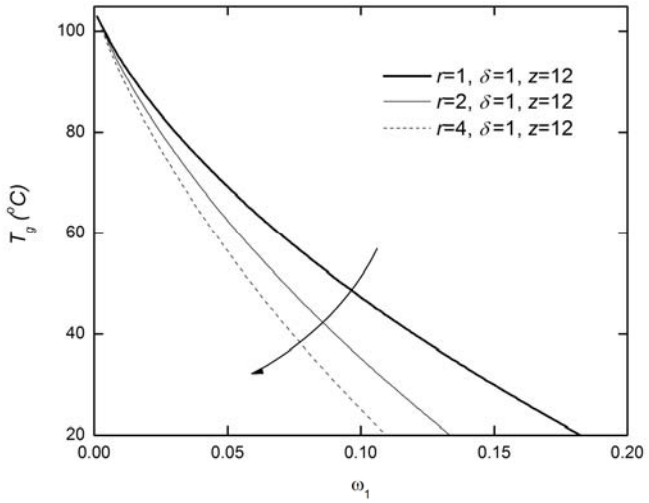

Figure 5.7 Results from Eq.(5.26) showing the effect of changing the extension parameter r. As expected, the bigger is the solvent the more T_g will decrease.

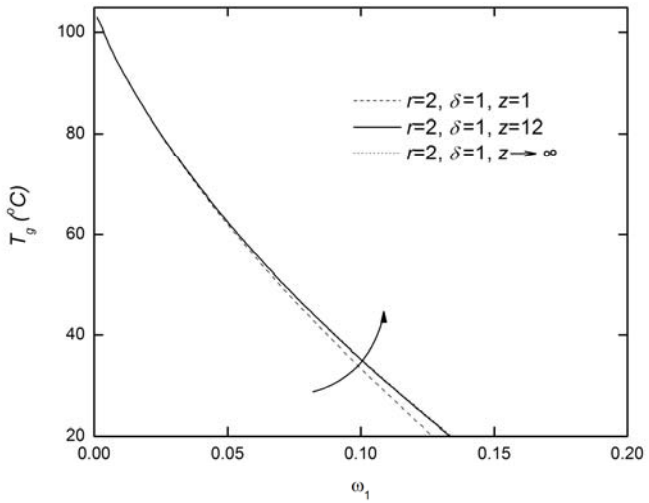

Figure 5.8 Results from Eq.(5.26) showing the effect of changing the lattice coordination number z. As expected, the impact of z on T_g is negligible.

Another feature worth considering is adding free volume to the mixture under study. This can be done in two ways, by applying Eq.(5.6) in combination with a theory able to study systems endowed with free volume, such as Sanchez-Lacombe

equation of state[9]. The other possibility is to follow the work by Condo et al. (referred as CSPJ model) who applied Gibbs-DiMarzio criterion to a modified version of the Sanchez-Lacombe equation endowed with internal flexibility energy for the polymeric species. In the last figure 5.9 we have compared these last two approaches with the original expression as well as with our revised version. All the models performed well at least from a qualitative point of view.

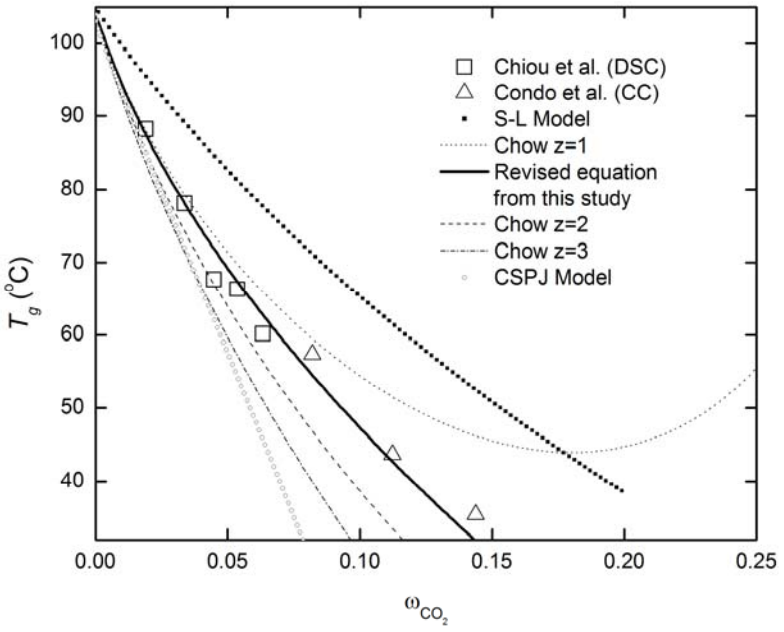

Figure 5.9 Comparing different models with experimental data on PMMA-CO2 taken from literature[6], Sanchez-Lacombe, CSPJ and original Chow's equation perform worse than Eq.(5.26).

§ 5.5 Conclusion

In conclusion it is safe to say that more complex does not always mean more effective.

This is the case of models aimed at describing the glass transition depression upon sorption of small molecules examined in this study. We have shown that following Gibbs-DiMarzio criterion for glass transition temperature it is possible to develop a whole family of expressions aimed at calculating the glass transition change with plasticizer content. The effect of static pressure in increasing T_g has also been explained in the light of Gibbs-DiMarzio analysis. As main result of the present effort a new revised equation has been established that enhances the results obtained with Chow's theory by overcoming the issues present in the original formulation.

§ 5.6 References

(1) Di Marzio, E. A. and Gibbs, J. H., *J. Polym. Sci., Part A-1*. **1963**, 1417.

(2) Di Marzio, E. A. and Gibbs, J. H., *J. Chem. Phys.* **1958**, *28*, 373.

(3) Di Marzio, E. A. and Gibbs, J. H., *J. Chem. Phys.* **1965**, *43*, 139.

(4) Di Marzio, E. A.; Gibbs, J. H.; Fleming III, P. D., and Sanchez, I. C. *Macromolecules* **1976**, *9*, 763.

(5) Chow, T. S. *Macromolecules* **1980**, *13*, 362.

(6) Condo, P. D.; Sanchez, I. C.; Panayiotou, C. G.; and Johnston, K. P. *Macromolecules* **1992**, *25*, 6119.

(7) Kikic, I., Vecchione, F., Alessi, P., Cortesi, A., Eva, F., and Elvassore, N. *Ind. Eng. Chem. Res.* **2003**, 42, *13*, 3022.

(8) Liu, D.; Li, H.; Noon, M. S. and Tomasko, D. L. *Macromolecules* **2005**, *38*, 4416.

(9) Sanchez, I. C. and Lacombe, R. H., *Macromolecules* **1978**, *11*, 1145.

CHAPTER VI

Modeling sorption kinetics of carbon dioxide in bulk polymeric films using the NET-GP approach

The Non-Equilibrium Thermodynamics of Glassy Polymers (NET-GP) approach is applied to the development of a one-dimensional transport model aimed at describing the kinetics of sorption and dilation of supported polymeric films in supercritical carbon dioxide. The NET-GP model has been combined with the free volume theory to estimate the diffusive flux, and with a simple rheological constitutive equation to model relaxation behavior, to build a sorption-diffusion-relaxation model to describe mass uptake and swelling kinetics of polymeric films in contact with carbon dioxide over a wide range of pressures and temperatures. The model calculations are compared to real-time mass sorption data of CO_2 in poly(methylmetacrylate) (PMMA) taken using a high-pressure Quartz Crystal Microbalance (QCM) in both rubbery and glassy polymer regimes.

Chapter VI is essentially a reprint (with slight modifications) of Hussain, Y., Carla, V., et al. "Modeling sorption kinetics of carbon dioxide in bulk polymeric films using the NET-GP approach" *Macromolecules* **(in Press)**

§ 6.1 Introduction

Carbon dioxide is gaining increasing interest as a solvent for industrial applications because of its unique characteristics, such as non-flammability, low toxicity, natural abundance, low cost, and environmental compatibility[1,2]. As a supercritical fluid, CO_2 has a gas-like viscosity, a low surface energy and a liquid-like density, which allows it to penetrate into small gaps and to exhibit enhanced solubility and transport properties. In addition, the solvent power of CO_2 can be easily tuned by small changes in temperature and pressure, as thoroughly discussed in the second chapter.

As a result, there is a wide range of applications in which CO_2 could replace traditional aqueous and organic solvents, from the food industry to coatings in the automotive and furniture industries, and polymer production and processing[3]. The latter is of particular interest due to the ability of carbon dioxide to easily swell and plasticize many polymers, making it ideal for manipulating polymer physical properties, enhance diffusion of small molecules and as foaming agent[4,5].

Modeling the transport of solvents, including CO_2 at high pressure, in polymeric materials is of paramount importance in processes such as drug impregnation and photolithography. Such models would eventually allow for process optimization and facilitate extension to other desired systems and applications. However, the mathematical description of solvent mass sorption in polymers is a difficult task in view of changes in polymer structure induced by the diffusion of penetrant molecules. Indeed, several different types of transport behaviors have been observed experimentally over the years for various polymer-solvent pairs at different operating

conditions[6-12]. In general the penetration of small molecules into polymer films enhances the free volume of the system and the mobility of the polymer chains, thus lowering the glass transition temperature and allowing the matrix to relax and swell[13]. In turn, these factors affect strongly the additional adsorption and diffusion of penetrant molecules.

The aim of the present chapter is to introduce a new sorption-diffusion-relaxation model for studying mass uptake and swelling kinetics of polymeric films brought in contact with good plasticizers, such as CO_2, over a wide range of pressures and temperatures. It is conceived as a direct application of the Non-Equilibrium Thermodynamics of Glassy Polymers (NET-GP) approach, initially developed by Doghieri and Sarti[14,15] for the study of sorption in glassy polymers at low pressures, and recently extended by Carla et al.[16] to high-pressure regions.

The NET-GP approach consists of extending any suitable equilibrium model for the Helmholtz free energy applicable in the rubbery region over into the non-equilibrium glassy region by means of an order parameter, the polymer density. This parameter is considered to be not only a function of thermodynamic variables, *i.e.*, temperature, pressure, and composition, but also of the thermal, mechanical, and sorption history of the sample, and it is taken as a measure of the out-of-equilibrium degree of the system.

In chapter IV, the pseudo-equilibrium density of the polymer was estimated by means of a linear relationship between the density and the pressure below the glass transition point. While this was sufficient for calculating the sorption isotherms, an evolution equation for the polymer density must be considered in order to describe

the kinetics of the relaxation process. This has been accomplished using a mechanical model that provides information on the polymer density change with time through a stress-strain relationship.

Although a review of modeling efforts to represent the coupling between diffusion and relaxation in glassy polymers is beyond the aim of this work, it is useful to remember that the concept of polymer relaxation induced by the stress exerted by diffusion of swelling agents dates back to the early works by Newns[17]. Several attempts followed in describing the driving force for the relaxation process in the polymer-solute mixture, which relied on different functional forms for the analysis of the mechanical response of the glassy polymeric materials to the swelling stress.

Sarti[18] used the difference in the chemical potential between the pure polymer and the swollen polymer as the driving force for polymer swelling. Sarti and Apicella revised this approach by considering the non-equilibrium state of the glassy polymer, adding an excess term to the equilibrium driving force[19]. A similar expression for the chemical potential was used by Bischops et al.[20] and its gradient was used as the driving force for swelling.

Instead, the mechanical model introduced here has been developed starting from a force balance on a volume element of the film and it is written in terms of isotropic pressures, so that the driving force for swelling ends up being the difference between the actual system pressure and the equilibrium pressure calculated for that particular volume element.

Several studies have been published over the years on modeling the diffusion of small molecules in polymers and some of the milestones achieved in the past will be

briefly discussed here to put our work in perspective. Much more complete summaries of this field have been recently published by Frisch[11] and by Vrentas and Duda[21].

Vrentas and Duda[12] studied the diffusion of small molecules in amorphous polymers through a re-examination of the free volume theory and were able to explain successfully the change in diffusion behavior with molecular size. Unfortunately, the quantitative comparison of their model with experiments gives good results only at low pressures. Durning and Tabor[22] investigated the problem of mutual diffusion of small molecules in concentrated polymeric solutions under small driving forces. Their analysis took into account the deformation of the polymer caused by the solvent and their work included a memory integral contribution from transient network theory and the reptation model. However, Durning and Tabor model is limited to incompressible systems with small deformation. Peppas and coworkers developed a more complete model for describing sorption and dissolution kinetics but their approach makes use of the Flory-Huggins theory for the chemical potential, thus neglecting the non-equilibrium nature of the glassy system[23,24].

In the aforementioned models, one of the major shortcomings arises from the absence of a reliable thermodynamic model valid over a wide range of pressures, from the glassy state up to fully plasticized rubbery state. In the previous chapter, a new procedure has been introduced to calculate solubility isotherms for gas absorption in bulk films; in the present chapter we utilize that procedure in conjunction with the free volume theory and a simple rheological model for polymer deformation to describe the mass transport of CO_2 in PMMA.

In the following sections, the various aspects of this new transport model are described. A finite element discretization procedure was used to obtain a numerical solution to the set of coupled partial differential equations describing solute transport and polymer deformation. The resulting concentration profiles of penetrant molecules inside the polymer under both glassy and rubber conditions were integrated to predict the kinetics of mass sorption and desorption of CO_2 in supported films of PMMA at two different temperatures and under a wide range of pressures. These theoretical results are compared to real-time mass sorption data taken with a high-pressure Quartz Crystal Microbalance (QCM). It is demonstrated that the model provides an excellent description of the mass sorption and desorption rates in both the glassy and rubbery polymer regimes.

§ 6.2 Theory

This section describes the formulation of a one-dimensional mass transport model for diffusion of a mobile solvent species into a polymeric film using the NET-GP approach. The continuity equations for the solvent (*s*) and polymer (*p*) species take the form,

$$\frac{\partial \rho_s}{\partial t} = \nabla \cdot \left(\rho_s \underline{v}_p + \underline{j}_s \right) \tag{6.1}$$

$$\frac{\partial \rho_p}{\partial t} = \nabla \cdot \left(\rho_p \underline{v}_p \right) \tag{6.2}$$

where $\underline{j}_s$ is the solvent diffusive flux,

$$\underline{j}_s = \rho_s(\underline{v}_s - \underline{v}_p) \tag{6.3}$$

Here $\underline{v}_s$ and $\underline{v}_p$ are the local mass velocities of the solvent and polymer respectively, and ρ_s and ρ_p are the corresponding mass densities. The mass diffusive flux for the mobile species can be calculated using a generalized Fickian constitutive equation where the driving force is the gradient in the chemical potential of the solvent in the polymer,

$$\underline{j}_s = -D^* \nabla \mu_s \tag{6.4}$$

The quantity D^* is a generalized diffusion coefficient for the solvent transport in the polymer which will be described in additional detail later.

The solvent chemical potential in the equation above can be determined using the NET-GP approach modified for high pressures[16], which provides an expression for the solvent chemical potential under non-equilibrium (glassy) conditions:

$$\mu_s^{NE} = \mu_s^{NE}\left(T, P, \omega_s, \rho_p\right) \tag{6.5}$$

The expression for the non-equilibrium equation of state is obtained through the proper extension of any well-established equilibrium equation of state (EoS) for fluid

systems, by assuming the polymer density is an order parameter for the system that can be treated as an internal state variable. The NET-GP approach requires an evolution equation for the mass density that describes the polymer volume relaxation to its final value,

$$\frac{d\rho_p}{dt} = f(T, P, \omega_s, \rho_p) \tag{6.6}$$

In this work, the evolution equation will take the form of a mechanical constitutive equation to determine the kinetics of this relaxation process.

For the case of one-dimensional transport along the x-axis, the continuity equation for the mobile species (CO_2) in *lab-fixed* coordinates reduces to the form,

$$\left(\frac{\partial \rho_s}{\partial t}\right)_x = -\left[\frac{\partial}{\partial x}\left(\rho_s v_{px} + j_{sx}\right)\right] \tag{6.7}$$

This coordinate system is illustrated in Fig. 6.1 for the case of a polymer film coated on a hard substrate. At the CO_2-polymer interface ($x = \delta$ at t = 0 and $x = \delta + \Delta\delta$ at t = Δt) it will be assumed that the chemical potential of the external fluid is the same as the chemical potential of the solvent in the polymer. It will also be assumed that the substrate is impervious to solvent transport so that at x=0 the flux of solvent is zero.

In *lab-fixed* coordinates, the swelling of the polymer during solvent diffusion gives rise to a mathematically difficult moving boundary problem since the polymer

film thickness δ will be time-dependent. In order to avoid this complication, it is useful to define a *polymer-fixed* coordinate ξ in which the spatial domain of the solvent continuity equation has fixed, time independent boundaries so that $0 \leq \xi \leq \delta$. Dependent variables expressed in polymer-fixed coordinates will be designated with the superscript P in the following development.

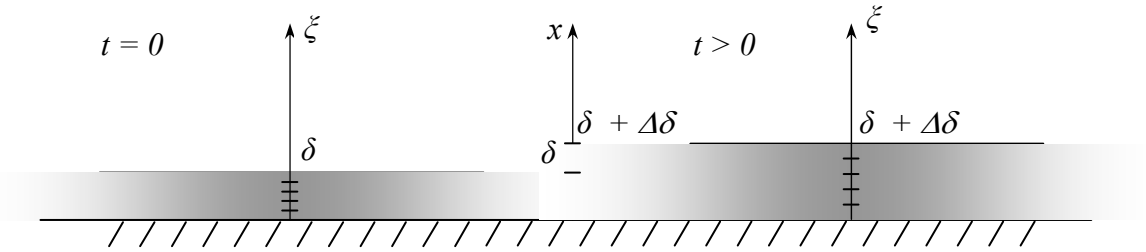

Figure 6.1 Schematic illustration of the relationship between the lab-fixed and polymer-fixed coordinate systems

It is possible to rewrite the solvent continuity equation, Eq. (6.7), in terms of these new coordinates by defining a quantity we shall call *elongation*, λ, which serves to relate the *lab-fixed* to the *polymer-fixed* coordinates,

$$\lambda = \left(\frac{\partial x}{\partial \xi} \right)_t \tag{6.8}$$

By definition, the velocity of the polymer at a given time along the x direction is equal to the time rate of change in the spatial position x for a fixed value of the polymer-fixed coordinate,

$$\left(\frac{\partial x}{\partial t}\right)_{\xi} = v_{px} \tag{6.9}$$

Chain differentiation of the terms in Eq. (6.7) results in the expressions,

$$\left(\frac{\partial \rho_s}{\partial t}\right)_x = \left(\frac{\partial \rho_s}{\partial t}\right)_{\xi} + \left(\frac{\partial \rho_s}{\partial \xi}\right)_t \left(\frac{\partial \xi}{\partial t}\right)_x = \left(\frac{\partial \rho_s}{\partial t}\right)_{\xi} - \frac{v_{px}}{\lambda}\left(\frac{\partial \rho_s}{\partial \xi}\right)_t \tag{6.10}$$

And

$$\frac{\partial}{\partial \xi}\left(\rho_s v_{px} + j_{sx}\right)\frac{1}{\lambda} = \left(v_{px}\frac{\partial \rho_s}{\partial \xi} + \rho_s \frac{\partial v_{px}}{\partial \xi} + \frac{\partial j_{sx}}{\partial \xi}\right)\frac{1}{\lambda} \tag{6.11}$$

A substitution of Eqs. (6.10) and (6.11) in Eq. (6.7) gives rise to an alternative form of the continuity equation for the solvent species,

$$\lambda \frac{\partial \rho_s}{\partial t} + \rho_s \frac{\partial \lambda}{\partial t} = -\frac{\partial j_{sx}}{\partial \xi} \tag{6.12}$$

that can be written in the simpler form,

$$\left[\frac{\partial}{\partial t}\left(\rho_s \lambda\right)\right]_{\xi} = -\left[\frac{\partial j_{sx}}{\partial \xi}\right]_t \tag{6.13}$$

The diffusive flux of solute in the equation above also needs to be expressed in the polymer-fixed system, in which, by definition, the polymer velocity is zero,

$$j_{s\xi}^{P} = \rho_s^{P}\left(v_{s\xi}^{P} - v_{p\xi}^{P}\right) = \rho_s^{P} v_{s\xi}^{P} \tag{6.14}$$

It is also necessary to recognize that the specific density of the polymer is coordinate dependent. In fact, the volume of the polymer sample changes in the lab-fixed system but it remains constant in the polymer-fixed coordinates. In order to express the solute density in the polymer-fixed coordinate system, it is useful to refer to the determinant of the *displacement gradient tensor*[24]

$$\det \underline{\underline{F}} = \frac{V}{V^0} = \frac{\rho_s^{P}}{\rho_s} \tag{6.15}$$

The displacement gradient tensor, $\underline{\underline{F}}$, can be easily obtained from the relationship between the two systems of coordinates, and, for the particular case of one dimensional diffusion in a polymer film in rectangular coordinates, is given by the expression,

$$\underline{\underline{F}} = \begin{pmatrix} \lambda & 0 & 0 \\ 0 & 1 & 0 \\ 0 & 0 & 1 \end{pmatrix} \tag{6.16}$$

From the definition of λ in Eq. (6.8) and the ratio of densities in Eq. (6.15) we have,

$$\rho_s^P = \lambda \rho_s \tag{6.17}$$

After accounting for the unit vector difference between the systems, *i.e.*, $\underline{e} = \lambda^{-1}\underline{e}^P$, it is clear that $v_{s\xi}^P = \lambda^{-1}\left(v_{sx} - v_{px}\right)$ and finally $j_{s\xi}^P = j_{sx}$. It is clear that the solute flux in the polymer fixed coordinate system is the same as that in fixed laboratory coordinates. As a result, the solvent continuity equation in the polymer-fixed coordinates, Eq. (6.13), takes the form,

$$\left[\frac{\partial}{\partial t}\left(\rho_s \lambda\right)\right]_\xi = -\left[\frac{\partial}{\partial \xi}\left(j_{s\xi}^P\right)\right]_t \tag{6.18}$$

In a completely analogous manner, it is possible to derive the continuity equation for the polymer in a polymer-fixed frame, which takes the form,

$$\left[\frac{\partial}{\partial t}\left(\rho_p \lambda\right)\right]_\xi = 0 \tag{6.19}$$

Eq. (6.19) implies that $\left(\rho_p \lambda\right)_\xi$ is constant in time. Since, by definition, at the beginning of the diffusion process the elongation is equal to unity, this equation also indicates that λ is equal to the ratio of the initial polymer density to the polymer density at a given time,

$$\lambda = \frac{\rho_p^0}{\rho_p} \tag{6.20}$$

Using the above equation, it is possible to evaluate the elongation once the *evolution expression* for the polymer density is provided. It should be noted that Eq. (6.20) could also have been derived from Eq. (6.15) and Eq. (6.16), thus validating the mathematical consistency of the present formulation.

Eqs. (6.18) and (6.20) can be used for calculating the penetrant and polymer density profiles inside the polymer matrix with time, resulting in a description of the kinetics of mass sorption and volume dilatation. In order to complete the model description, constitutive equations are needed for the diffusive flux in Eq. (6.18) and the evolution equation for the polymer density, Eq. (6.20). In addition, the initial and boundary conditions must be considered for the particular case chosen.

§ 6.3 Constitutive Equation for the Diffusive Flux

The generalized Fickian expression for the diffusive flux, Eq. (6.4), can be written in the form[25]

$$j_{sx} = -\left(\frac{L_s \rho_s \omega_p}{RT}\right)\frac{\partial \mu_s^{NE}}{\partial x} \tag{6.21}$$

where the driving force has been expressed as a chemical potential gradient and the diffusivity L_s has been taken from the free volume theory of Vrentas and Duda[21] in the form,

$$L_s = L_s^0 \cdot \exp\left[-\frac{\gamma\left(\omega_s \hat{V}_s^* + \omega_p \zeta \hat{V}_p^*\right)}{\hat{V}_f^{mix}} \right] \tag{6.22}$$

In the above and throughout this work, the free volume term has been calculated according to the expression[26],

$$\hat{V}_f^{mix} = \hat{V}_p - 1/\rho_{Mix}^* \tag{6.23}$$

where $\hat{V}_p$ is the polymer molar volume obtained from a force balance acting upon the sample, as shall be shown later, and ρ_{mix}^* is the *closed packed density* of the mixture, which can be evaluated from the thermodynamic model.

Writing Eq. (6.21) in the *polymer-fixed* system we have:

$$j_{s\xi}^P = -\left(\frac{L_s\left(\lambda \rho_s^P\right)\omega_p}{RT} \right) \frac{\partial \mu_s^{NE}}{\partial \xi} \left(\frac{\partial \xi}{\partial x} \right) = -\left(\frac{L_s \rho_s^P \omega_p}{RT} \right) \frac{\partial \mu_s^{NE}}{\partial \xi} \tag{6.24}$$

By considering the explicit functional form of the non-equilibrium chemical potential of the solute, the total differential change in chemical potential for a process takes the form,

$$d\mu_s^{NE} = \frac{\partial \mu_s^{NE}}{\partial T} dT + \frac{\partial \mu_s^{NE}}{\partial P} dP + \frac{\partial \mu_s^{NE}}{\partial \omega_s} d\omega_s + \frac{\partial \mu_s^{NE}}{\partial \rho_p} d\rho_p \tag{6.25}$$

In the case of uniform temperature and pressure fields, and when the composition, ω_s, is written in terms of solvent density, Eq. (6.25) becomes,

$$d\mu_s^{NE}\Big|_{T,P} = \frac{\partial \mu_s^{NE}}{\partial \rho_s} d\rho_s + \left(\frac{\partial \mu_s^{NE}}{\partial \rho_p} - \frac{\partial \mu_s^{NE}}{\partial \rho_s} \frac{\rho_s}{\rho_p} \right) d\rho_p \tag{6.26}$$

This equation can be more conveniently written in the form,

$$j_{s\xi} = -L_{ss} \frac{\partial \rho_s}{\partial \xi} - L_{sp} \frac{\partial \rho_p}{\partial \xi} \tag{6.27}$$

Where

$$L_{ss} = \left(\frac{L_s \rho_s \omega_p}{RT} \right) \frac{\partial \mu_s^{NE}}{\partial \rho_s} \tag{6.28}$$

and

$$L_{sp} = \left(\frac{L_s \rho_s \omega_p}{RT} \right) \left[\frac{\partial \mu_s^{NE}}{\partial \rho_p} - \frac{\partial \mu_s^{NE}}{\partial \rho_s} \frac{\rho_s}{\rho_p} \right] \tag{6.29}$$

The first terms in the parentheses in Eqs. (6.28) and (6.29) represent the *kinetic* contributions to the diffusion coefficient, while the terms involving gradients of the *non-equilibrium* chemical potential represent the *thermodynamic* contribution. The expression for the non-equilibrium chemical potential is derived in chapter IV, based on an expression for the non-equilibrium Helmholtz free energy of the system,

$$\frac{\mu_s^{NE}}{kT} = \ln \phi_s + \left(1 - \frac{r_s}{r_p} \right) \phi_p - r_s \left(1 - \tilde{\rho} \right) \left(1 - \frac{1}{r} \right) + \ln \tilde{\rho} +$$

$$+ \frac{r_s \tilde{\rho}}{\tilde{T}} \left[\left(\tilde{\rho} - 1 \right) + \tilde{T} \left(\phi_p^2 \chi_{sp} - \frac{1}{\tilde{T}_s} \right) \right] + r_s \left[\frac{\tilde{P}}{\tilde{T}} + \frac{\phi_p}{\tilde{\rho}} \left(\frac{\tilde{P}_s}{\tilde{T}_s} - \frac{\tilde{P}_p}{\tilde{T}_p} \right) \right] \tag{6.30}$$

where ϕ_s is the volume fraction of the penetrant species. The NET-GP model modified for high pressures[16] was used to estimate the solute chemical potential in the non-equilibrium glassy state for the solute-polymer mixture. The Sanchez-Lacombe (SL) two binary parameter equation of state (EoS) was used to represent the thermodynamic properties in the equilibrium (rubbery) states. The SL EoS was also used to model the thermodynamic properties of the pure polymer and pure CO_2.

§ 6.4 Evolution Equation for the Polymer Density

According to one of the assumptions of the NET-GP approach, the polymer density is treated as the order parameter that provides the out-of-equilibrium degree of the system, so that a non-equilibrium argument is required for calculating its value.

The development of an evolution equation for the density can be approached through the use of a rheological constitutive equation that provides the force balance acting upon each element of the sample, thus relating the stress resulting from solvent penetration and the resulting strains due to polymer relaxation.

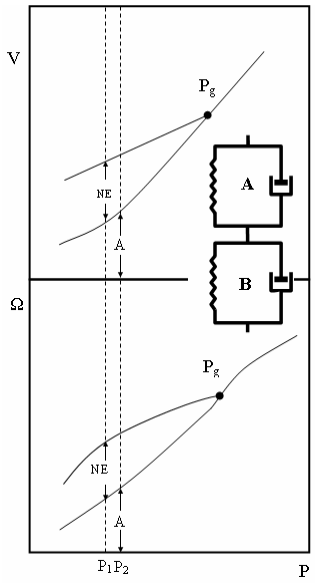

Figure 6.2 Two Voigt rheological model and physical interpretation of its components

It is clear from a careful analysis of the data available in the literature that an accurate description of the viscoelastic behavior of a polymer is only made possible by accounting for more than a single relaxation time for the material[27], due to the distribution of strengths of polymer chain entanglements, which ultimately are

strongly dependent upon the thermo-mechanical history of each sample. As a result, we adopt a simple rheological model, shown in Fig. 6.2 to describe the stress-strain relationship of the polymeric material.

The mechanical model involves two Voigt elements, each having its own stress-free equilibrium length, modulus and viscosity. The two Voigt elements share the same overall forces that can be written in the form of sum of elastic and viscous contributions, as follows,

$$F = k\left(\frac{x - x^0}{x^0}\right) + \vartheta\frac{d}{dt}\left(\frac{x - x^0}{x^0}\right) \tag{6.31}$$

where k represents the modulus, x^0 and x are the initial and final length, and ζ has the meaning of a viscosity.

For a given deformation, the resulting force acting upon each element at equilibrium is balanced only by the contribution of the spring (elastic contribution) and can be written as $F^{eq} = k\left(\frac{x - x^0}{x^0}\right)$. Eq. (6.31) can then be rewritten in the form,

$$F - F^{eq} = \vartheta\frac{d}{dt}\left(\frac{x - x^0}{x^0}\right) \tag{6.32}$$

in which the elastic term is incorporated in the equilibrium resulting force acting upon the element.

Eq. (6.32) can be written in terms of derivatives of the pressure and volume, by adopting the following formal equivalences:

$$\begin{cases} F - F^{eq} \Leftrightarrow p - p^{eq} \\ \dfrac{d}{dt}\left(\dfrac{x - x^0}{x^0}\right) \Leftrightarrow \dfrac{1}{V}\dfrac{dV}{dt} = -\dfrac{d\ln\rho}{dt} \\ \vartheta \Leftrightarrow \eta \end{cases} \tag{6.33}$$

Note that in this particular mechanical model, the driving force for evolution of the polymer density is the difference between the actual pressure exerted upon the polymeric sample and the corresponding pressure in the equilibrium system. The constitutive equation for the polymer density then takes the simple form,

$$\frac{\partial \rho_p}{\partial t} = -\rho_p \frac{\left(P^{eq} - P\right)}{\eta} \tag{6.34}$$

When the time rate of change of the polymer density goes to zero, the expression above gives rise to the equilibrium polymer density

$$\frac{\partial \rho_p}{\partial t} \to 0 \Rightarrow P \to P^{eq} \overset{def}{=} -\left(\frac{\partial A}{\partial V}\right)_T \tag{6.35}$$

Under these conditions the formalism is consistent with the equilibrium equation of state.

With this picture in mind, the volume deformation of the polymer can be thought as being made up of two contributions, one from each Voigt element, with a suitable weighting factor,

$$\hat{V}_p = \chi \hat{V}_P^A + (1-\chi)\hat{V}_P^B \tag{6.36}$$

Here χ represents the weight of Voigt element *A* in the set, and $\hat{V}_p^A$ and $\hat{V}_p^B$ are the two measures of volume deformation associated with each Voigt element which can be calculated using evolution equations analogous to Eq. (6.34),

$$\frac{1}{\hat{V}_p^A}\frac{\partial \hat{V}_p^A}{\partial t} = \frac{P^{eq}\left(T, \hat{V}_p^A, \mu_s\right) - P}{\eta_A} \tag{6.37}$$

and

$$\frac{1}{\hat{V}_p^B}\frac{\partial \hat{V}_p^B}{\partial t} = \frac{P^{eq}\left(T, \hat{V}_p^B, \mu_s\right) - P}{\eta_B} \tag{6.39}$$

In the equations above, μ_s is the CO_2 chemical potential in the external phase. Eqs. (6.36)- (6.38) represent the evolution law for the polymer volume, to be solved along with the pertinent initial conditions,

$$\hat{V}_p^A\left(t=0\right) = \hat{V}_p^{A0} = \hat{V}_{eq}\left(T, P, \omega_s\right) \tag{6.40}$$

$$\hat{V}_p^B\left(t=0\right) = \hat{V}_p^{B0} = \hat{V}_{eq}\left(T, P_g, \omega_{sg}\right) = \hat{V}_g \tag{6.41}$$

In the simplified picture of the polymer rheology considered here, the intent is to have Voigt element *A* represent short time relaxation phenomena, so that steady-state conditions can be reached, i.e. $P = P^{eq}\left(T, \hat{V}_P^A, \mu_s\right)$, in the pseudo-equilibrium state. On the other hand, element *B* is intended to represent the long time relaxation response of the polymer and it is supposed to reach the equilibrium state on an appreciable time scale only above the glass transition point.

According to the model assumption, the dried polymer specific volume must result from the sum of two contributions,

$$
\begin{aligned}
V_p^{\,0} &= \chi V_p^{A} + (1-\chi) V_p^{B} \\
&= \chi V_{p\,(T,\omega_s=0,P\to 0)}^{EQ} + (1-\chi) V_{p\,\left(T,\omega_{s_g},P_g\right)}^{EQ}
\end{aligned}
\tag{6.42}
$$

In Eq. (6.42) the volume per polymer mass of Voigt element A for the dried state of the polymeric sample is taken to be equal to the volume per polymer mass of the pure polymer at atmospheric pressure at the temperature of interest.

Solving for the parameter χ in Eq. (6.42) results in an expression for estimating its magnitude from known values of the polymer volume per unit mass,

$$
\chi = \frac{V_p^{0} - V_{p\,\left(T,\omega_{s_g},P_g\right)}^{EQ}}{V_{p\,(T,\omega_s=0,P\to 0)}^{EQ} - V_{p\,\left(T,\omega_{s_g},P_g\right)}^{EQ}}
\tag{6.43}
$$

It should be noted that in the estimation procedure in Eq. (6.43) the χ parameter is evaluated using the specific volume of dried polymer that can be affected by the history of the sample.

It is interesting to note that, from the assumption above, the polymer specific volume in pseudo equilibrium conditions is a function of the solute fugacity f_s, as represented in the following equation,

$$
\begin{aligned}
V_{p\,(T,f_s)}^{PE} &= \chi V_{p\,(T,f_s,P)}^{EQ} + (1-\chi) V_{p\,\left(T,\omega_{s_g},P_g\right)}^{EQ} \\
&= V_p^{\,0} + \left(V_{p\,(T,f_s,P)}^{EQ} - V_{p\,(T,\omega_s=0,P\to 0)}^{EQ} \right) \frac{V_p^{\,0} - V_{P\,\left(T,\omega_{s_g},P_g\right)}^{EQ}}{V_{p\,(T,\omega_s=0,P\to 0)}^{EQ} - V_{P\,\left(T,\omega_{s_g},P_g\right)}^{EQ}}
\end{aligned}
\tag{6.44}
$$

The latter expression accounts for a pseudo equilibrium polymer volume which is equal to the measured volume $V_p^{\,0}$ at negligible solute content and tends to V_g^{EQ} when the solute concentration approaches the glass transition value. The above limit conditions are basic assumptions of the analysis of the pseudo-equilibrium solubility isotherm proposed in chapter IV where a linear relation of V_p with solute gas pressure with the same limits was also assumed. The latter condition is also attained in Eq.(6.44) as long as the equilibrium thermodynamic model accounts for a constant value of solute partial molar volume and solubility coefficient in the fugacity range from 0 up to the glass transition value f_g.

Since the main interest in this work is in the representation of short time relaxation phenomena, the following assumptions will be made for the characteristic viscosities of the Voigt elements *A* and *B*,

$$\eta_A = \begin{cases} \eta_A\left(T, P, \omega_s\right) & T \le T_{gmix}\left(\omega_s\right) \\ \to 0 & T > T_{gmix}\left(\omega_s\right) \end{cases} \tag{6.45}$$

$$\eta_B = \begin{cases} \to \infty & T \le T_{gmix}\left(\omega_s\right) \\ \to 0 & T > T_{gmix}\left(\omega_s\right) \end{cases} \tag{6.46}$$

where $T_{gmix}\left(\omega_s\right)$ is the glass transition temperature of the mixture during sorption. In essence, Voigt element *A* has a finite viscosity below the glass transition temperature, while the volume of Voigt element *B* is thought to be 'frozen' at its initial volume evaluated through Eq. (6.41). Both Voigt elements *A* and *B* are assumed to have zero viscosity in the rubbery region, which implies that they are thought to react instantaneously to any force applied to them, thus behaving like an elastic solid. The overall polymer density, needed by the thermodynamic model, can be calculated from the expression

$$\rho_p = \frac{1}{\hat{V}_p} \tag{6.47}$$

where the partial mass volume of the polymer is calculated using Eqs. (6.36) – (6.38).

As for the bulk viscosity of element *A* below the glass transition that appears in Eq. (6.45), there is a simple treatment in the literature given by Royer et al.[28]. They have developed a correlation to take into account the effects of temperature, pressure and CO_2 concentration on the shear viscosity of polymers,

$$\ln\left(\frac{\eta_A\left(T,P,\omega_s\right)}{\eta_A^0}\right) = -\frac{C_1\cdot\left(T-T_g^{mix,\omega_s}\right)}{C_2+\left(T-T_g^{mix,\omega_s}\right)} - \frac{C_1\cdot\left(T-T_g^{mix,P}\right)}{C_2+\left(T-T_g^{mix,P}\right)} \tag{6.48}$$

This expression follows the Williams-Landel-Ferry (WLF) equation[28,29], in which the viscosity shifts are related to the change in the free volume of the mixture through the glass transition temperature change upon sorption, which in turn can be calculated using a simple model such as the Chow's theory of glass transition depression[13].

However, since the free volume of the mixture upon sorption can be retrieved through Eq. (6.23), we preferred to go utilize the fundamental Doolittle's equation[28],

$$\ln \eta_A = \ln A + \frac{B}{\hat{V}_f^{mix}} \tag{6.49}$$

The WLF equation can be derived from Eq. (6.49) once a simple expression for the free volume has been assumed. It is now assumed that the same functional relationship is valid through the glass transition point,

$$\ln \eta_A^0 = \ln A + \frac{B}{\hat{V}_f^0} \tag{6.50}$$

Subtracting Eq. (6.50) from Eq. (6.49) results in,

$$\ln \eta_A - \ln \eta_A^0 = B\left(\frac{1}{\hat{V}_f^{mix}} - \frac{1}{\hat{V}_f^0}\right) \tag{6.51}$$

where the constant B can be calculated either from *WLF* material parameters as $B = \alpha C_1 C_2$ [28] or from the Vrentas-Duda parameters as $B = \gamma \hat{V}_p^*$ [30]. Both approaches

are equivalent but the second approach has been chosen for these calculations, and with a little algebra it is possible to obtain the final shifting expression,

$$\ln\left(\frac{\eta_A}{\eta_A^0}\right)=\frac{\gamma\hat{V}_p^*\left(\hat{V}^0-\hat{V}_P\right)}{\left(\hat{V}^0-1/\rho_0^*\right)\left(\hat{V}_P-1/\rho_{mix}^*\right)} \tag{6.52}$$

In this way the only material parameter involved in the viscosity equation that needs to be estimated from the experimental data is the characteristic viscosity η_A^0 that is strongly dependent upon the thermo-mechanical history of the sample.

Whereas the initial bulk viscosity has a well-known physical meaning, and the values fit to the experimental data, as shall be shown later, are safely within the range of the literature reported values[27], a more detailed discussion is needed for χ. The value of χ represents the relative contributions of element A to the real system behavior. This parameter is used to account for the mechanical behavior of the out-of-equilibrium polymer density in the glassy state so that the magnitude of χ depends on the degree of deviation from the equilibrium (rubbery) state. For a rubbery material the value of χ is unity.

For the case of a glassy polymer, the values of χ are retrieved from experimental sorption data, whereas for the case of a rubbery polymer χ is simply set to be 1. However, it is possible to develop another, more simple, procedure that enables to achieve a rather good a-priori estimation of χ.

Taking the derivative with pressure of both sides of Eq. (6.36) results in the expression,

$$\frac{d\hat{V}_p}{dP} = \chi \frac{d\hat{V}_p^A}{dP} + (1-\chi)\frac{d\hat{V}_p^B}{dP} \tag{6.53}$$

By considering the assumption associated with Eq. (6.46), (i.e. $\tau_B \to \infty$) in the short time scale, at the glass transition temperature it is possible to make the approximation,

$$\left.\frac{d\hat{V}_p}{dP}\right|_{T_g^-} = \chi \left.\frac{d\hat{V}_p^A}{dP}\right|_{T_g} \tag{6.54}$$

The glass transition for the element *A* can be approached from above or below T_g, but the left hand side of the above equation can only be approached from below T_g. Eq. (6.54) can be divided on both sides by the specific volume,

$$\left.\left(\frac{1}{\hat{V}_p}\frac{d\hat{V}_p}{dP}\right)\right|_{T_g^-} = \chi \left.\left(\frac{1}{\hat{V}_p}\frac{d\hat{V}_p^A}{dP}\right)\right|_{T_g^+} \tag{6.55}$$

By noticing that the expression in parenthesis is nothing but the definition of the isothermal bulk compressibility, it can be seen that the value of χ can be related to the

ratio of the isothermal bulk compressibility above and below the glass transition temperature,

$$\chi = \frac{\left(\frac{1}{\hat{V}_p} \frac{d\hat{V}_p^A}{dP} \right)\Big|_{T_g^+}}{\left(\frac{1}{\hat{V}_p} \frac{d\hat{V}_p}{dP} \right)\Big|_{T_g^-}} = \frac{k_{T_g^-}}{k_{T_g^+}} \tag{6.56}$$

Using experimental values for the isothermal compressibility PMMA[31] in the rubber and glassy states yields an estimate of $\chi \simeq \frac{2.8 \cdot 10^{-4} MPa^{-1}}{4.4 \cdot 10^{-4} MPa^{-1}} \simeq 0.63$. This value agrees well result from Eq. (6.43).

§ 6.5 Initial and Boundary Conditions

The initial conditions can be written assuming a uniform distribution of concentration for both species at the beginning throughout the film thickness. The interfacial boundary condition derives from the phase relation and allows for the calculation of the solvent solubility, for a given temperature, pressure and polymer density. Finally, at the non-permeable substrate, the flux is taken equal to zero.

$$\begin{cases} t = 0, & \rho_s = \rho_s\left(\xi, 0\right) = \rho_s^0 \\ t = 0, & \rho_p = \rho_p\left(\xi, 0\right) = \rho_p^0 \\ \xi = \delta, & \mu_s^{NE}\left(\delta, t\right) = \mu_s^0 \\ \xi = 0, & j_{s\xi}\left(0, t\right) = 0 \end{cases} \tag{6.57}$$

The above set of equations was solved numerically through a procedure described in details in Appendix A and compared to real-time mass absorption data for CO_2 diffusion into PMMA films taken at two temperatures and over a wide range of pressures with a high-pressure Quartz Crystal Microbalance (QCM). The section that follows describes the details of these measurements.

§ 6.6 Experimental

Materials. Coleman Grade (purity > 99.999%) CO_2 was obtained from National Welders. Poly(methyl-methacrylate) having a molecular weight of 72kDa and PDI of 1.08 was obtained from Polymer Source Inc. (Montreal, Canada). A 5 wt% PMMA solution in Toluene (Fisher) was used for film preparation by dip coating. All materials were used as received.

QCM system. The quartz crystals, obtained from International Crystal Manufacturing and used in this study as received, were 5.00 MHz AT-cut Si with a blank diameter of 8.5 mm and a thickness of 0.25 mm. The rms surface roughness for the crystals used was less than 10 nm (analyzed using AFM). A voltage-controlled oscillator was used (Maxtek model PLO-10) to provide both frequency and voltage outputs. The voltage reading is inversely proportional to the resistance of the crystal. An Agilent 225 MHz Universal Frequency Counter (model 53131A) was used to read the frequency .

Pressure cell and apparatus. The custom-built pressure cell consisted of a thick-wall cylinder (63.5 mm I.D. x 200 mm height), with a high-pressure electrical

feedthrough for QCM connections. A high-pressure thermocouple (Omega) was used to measure the cell temperature, and a pressure transducer, (Omega, part. No. PX 302), was used to measure the pressure. The whole assembly was then placed in a water bath and controlled to ±0.1 ^{o}C. Data acquisition of the four readings was done using LabView.

Polymer film preparation. After measuring the fundamental frequency of the clean crystal in vacuum, F_o, the crystal was dipped vertically into the PMMA solution in toluene for 1 minute and withdrawn from the solution at a controlled rate. The coated crystal was then dried under vacuum at 76 ^{o}C for approximately 1 hour. The frequency was measured after drying; a constant stable frequency level was an indication of sufficient solvent removal. The value of the stabilized frequency of the coated QCM in vacuum was used to calculate the initial total mass of coated polymer, and this mass was in turn used with the bulk polymer density (chapter IV) to estimate the film thickness, which was found in all cases to be close to 1 μm. Cross-sectional SEM images of the coated QCM crystals support this estimation. The film roughness, as measured by AFM for samples before and after treatment with CO_2, was about 5 nm. After a stable signal was realized in vacuum, the pressure was increased to its initial value. The frequency was then allowed to reach the new stable level; the procedure was then repeated for the second pressure level, the third pressure level, and so on. The pressures studied in this work ranged from 0 up to 1800 psi. Runs during which sudden pressure changes were achieved at uniform temperature were used for comparison between theory and experiment.

§ 6.7 Results and Discussion

The sorption process resulting from a relatively small increase in the solute fugacity in the external phase is the combination of several elementary phenomena. The model developed above addresses the kinetics of two of these elementary phenomena, solute molecular diffusion and volume swelling of the polymer matrix. The Deborah number D_e, defined as the ratio of the characteristic time for polymer relaxation τ_R to the characteristic time for diffusion τ_D[32],

$$D_e = \frac{\tau_R}{\tau_D} = \frac{\eta / k}{\ell^2 / D} \tag{6.58}$$

Here k and η are the effective bulk modulus and the viscosity of the polymeric matrix respectively, D represents the mean diffusion coefficient of solute in the polymeric mixture and ℓ indicates the characteristic dimension of the polymer sample. For those cases in which $D_e << 1$ ($\tau_R << \tau_D$), the polymer relaxation phenomenon is fast when compared to solute molecular motion from the boundary to the core of the sample and diffusion process occurs in a fully relaxed matrix. These conditions give rise to the case of Fickian diffusion processes, typical of equilibrium fluid or solid phases.

On the other hand, for those cases in which $D_e \sim 1$ ($\tau_R \sim \tau_D$) the diffusion and relaxation occur on the same time scale and the resulting rate of overall mass uptake, which has very different features from those of classical Fickian processes, is often

referred to as *anomalous sorption* kinetics. Finally, when $D_e >> 1$ ($\tau_R >> \tau_D$) the relaxation is relatively slow and a first sorption stage, in which solute molecules diffuse in an unswollen matrix, is expected to be followed by a second relaxation-driven sorption step.

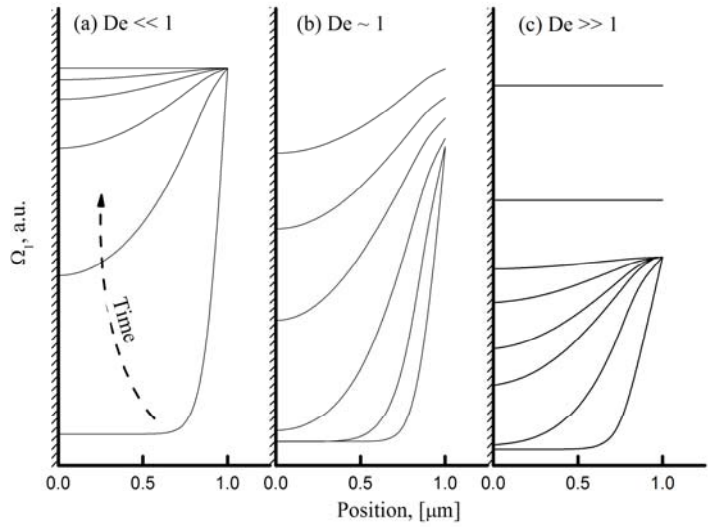

Figure 6.3 Concentration profiles of the penetrant species in the polymer at different times for De << 1 (a), De ~ 1 (b), and De >> 1 (c)

In these cases, at longer times, the volume relaxation phenomenon generates an enhanced diffusive flux caused by the increase in the polymer free volume without any change in the solute fugacity, as can be expected by the second term in the left-hand side of Eq. (6.27), which descends directly from the NET-GP approach. Higher solute mobility allows the sorption in this second step to occur without significant concentration gradients within the sample. The latter situation is known as *two-stage sorption* kinetics. Examples of typical solute concentration profiles for sorption processes in a polymeric sample are given in Figure 6.3 for the three different cases.

The experiments analyzed below are in the category of both small and large Deborah numbers, and the model developed is meant to test to what extent such complex diffusion phenomena can be modeled using relatively simple concepts of the polymer swelling mechanics and diffusive fluxes.

This section presents the analyses of several experimental results for sorption-desorption processes of CO_2 in PMMA films, using the sorption-diffusion-relaxation model described previously. By means of comparisons between model prediction/correlation and experimental results obtained for both rubbery and glassy polymeric phases, the capability of the model and the role of model parameters on determining the kinetics of sorption are discussed.

Pure component characteristic temperatures, pressures and densities for the SL EoS were obtained after analysis of experimental data for vapor pressure and saturated liquid density for CO_2, and of experimental data for specific volume as function of temperature and pressure for PMMA and they are shown in Table II and Table III. Temperature dependent binary parameters were fitted by analysis of high-pressure solubility and swelling data determined in chapter IV. Parameters for the free volume expression of solute mobility used in this work were obtained from the literature[26-31] and are listed in Table V.

Free Volume-parameters		
	Glass	Rubber
L_s^0 [cm^2/s]	6.7×10^{-11}	7.9×10^{-9}
γ	0.53	
$\zeta\hat{V}_p^*$ [cm^3/g]	0.1214	
$\hat{V}_s^*$ [cm^3/g]	0.77	

Table VI Parameters used in free volume model for mobility coefficient in rubbery states [26, 32]

Model results shown below were obtained through the numerical solution of a set of PDE's in the polymer fixed frame for the solute concentration and the volume swelling resulting from Eqs. (6.18), (6.20), (6.27) – (6.29). The equations were discretized by the application of a control volume formulation[33].

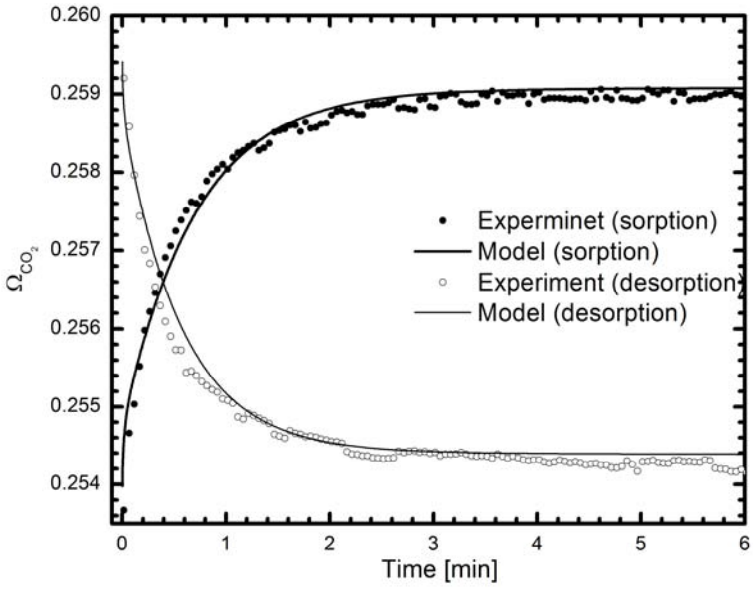

Figure 6.4 Solute content in PMMA film for CO_2 sorption from 1650 to 1750 psi and corresponding desorption at 35 ^oC, experimental data and model prediction

Figure 6.4 and Figure 6.5 show the experimentally measured mass of CO_2 in PMMA films as a function of time in terms of the mass ratio $\Omega_{CO_2} = \rho_s / \rho_p$ for sorption processes taking place at 35°C and 50°C.

Sorption measurements resulting from a step increase in CO_2 pressure from 1650 psi to 1750 psi are shown as full symbols while corresponding desorption results are shown as open symbols. In the same figures, model predictions (lines) are compared with experimental data.

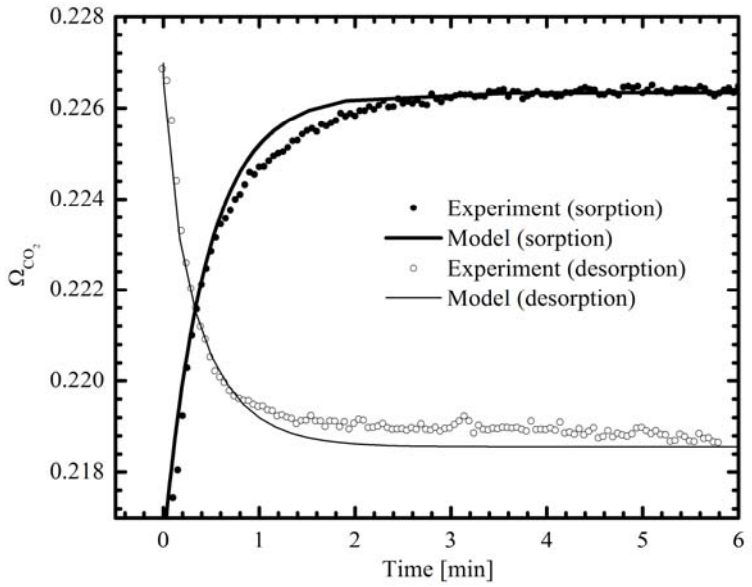

Figure 6.5 Solute content in PMMA film for CO_2 sorption from 1650 to 1750 *psi* and corresponding desorption at 50 °C, experimental data and model prediction

It should be noted that model results in Figure 6.4 and Figure 6.5 were obtained through pure predictive procedures, using parameters for thermodynamic and transport properties obtained from the literature, taking as initial values of CO_2 mass fraction those measured experimentally. There were no adjustable parameters used in

these computations. The rheological properties of the polymer discussed above do not play any role in the simulations in Figure 6.4 and Figure 6.5 since at these pressures and temperatures the solvent concentration keeps the material in the rubbery region, well above the critical value for glass transition. As expected, under such conditions the NET-GP simply becomes the SL EoS.

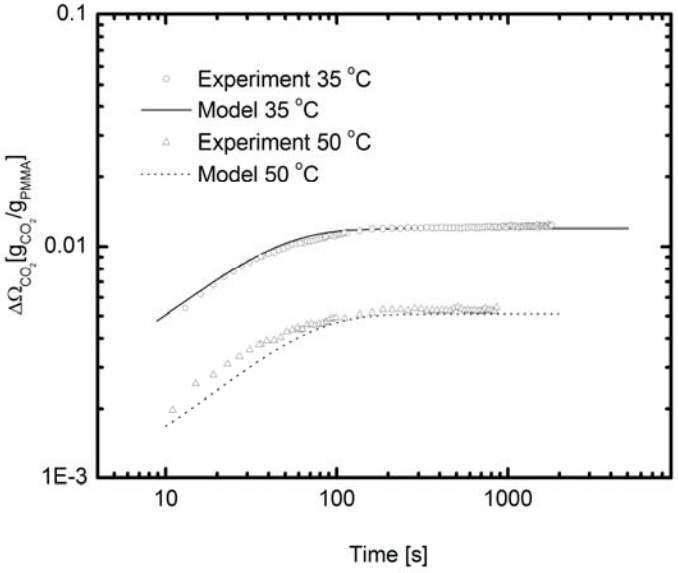

Figure 6.6 Solute mass uptake for CO_2 in PMMA film for sorption step from 1650 to 1750 psi at 35 and 50 °C, experimental data and model results

It is interesting to note that the long time concentrations predicted by the model in both sorption and desorption processes compare well with experimental data, as a result of the SL EoS ability to accurately represent the thermodynamic properties for the CO_2-PMMA system, with the binary interaction parameters indicated in Table VI. The agreement between experimental and predicted kinetics of both sorption and desorption processes is also remarkable, verifying the Fickian nature of the observed transport phenomenon and the validity of the pertinent free volume model parameters

obtained from the literature and listed in the rubber column in Table V. In Figure , the sorption data already shown in Figure 6.4 and Figure 6.5 are plotted on a logarithmic scale in terms of CO_2 mass uptake along with the model prediction illustrating the Fickian-like sorption behavior (slope ~ $1/2$) discussed above.

Figure 6.6 shows a comparison between experimental data and model calculations for CO_2 mass uptake in a PMMA film for the case of a sorption experiment run at 50°C for a jump in pressure from 370 to 450 psi. The solute content in this case is well below the critical value for glass transition so the material is always in the glassy state. As a result, the measured sorption data shows a *two-stage sorption* behavior that is commonly observed during diffusion processes in such systems. Two different steps in mass uptake, characterized by rather different time scales and kinetic orders are evident in the experimental data.

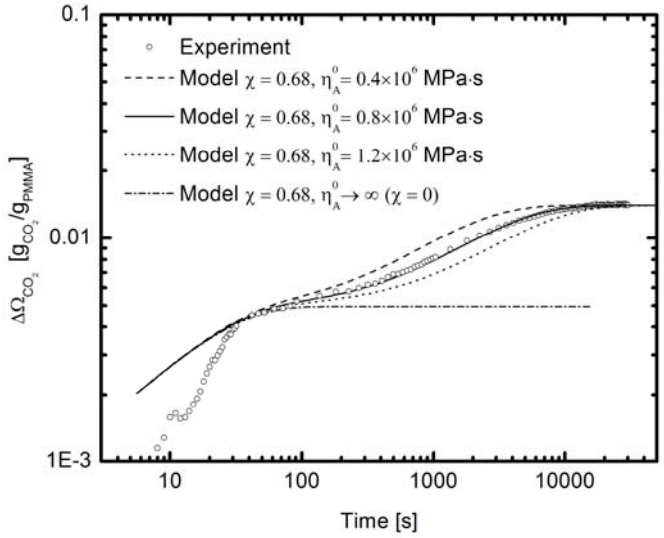

Figure 6.7 Solute mass uptake for CO_2 in PMMA film for sorption step from 370 to 450 *psi* at 50 °C, experimental data and model results

Model predictions for sorption kinetics are compared with experimental data in Figure 6.7, as obtained for different values of the characteristic initial viscosity η_A^0. Results for these model calculations were obtained in this case after accounting for measured values of the initial polymer density ($\rho_p^0 = 1.1344 \ \ g/cm^3$) and CO_2 content ($\rho_s^0 = 0.0598 \ \ g/cm^3$). While the same thermodynamic parameters listed in Table VI, and most of the free-volume parameters ($\gamma, \zeta\hat{V}_p^*, \hat{V}_s^*$), already considered in simulations above T_g, were used for model calculations shown in Figure , an exception has been made for the value of the characteristic penetrant mobility L_s^0. Given the glassy nature of the system, an adjustment of the mobility value was needed to obtain a correct time scale for the first sorption stage, as listed in the column labeled "Glass" in Table VII. It is evident from the comparison between the model and experiments in Figure 6.7 that the kinetic order of the experimental data (slope ~ 1) for the first sorption stage is definitely different from that obtained from the model calculation.

The non-Fickian nature of the experimental diffusion kinetics observed in this case for short times cannot be represented well with the model using the diffusive flux from of Eq. (6.27), which is always Fickian in nature. However, the model can account for the solute content reached in the polymeric sample at the end of the first short time step. This corresponds to the pseudo equilibrium conditions attained in the unswollen PMMA for the assigned value of CO_2 fugacity, and the result demonstrates the capability of the NET-GP model to describe this condition. The Voigt model parameters χ and η_A^0 were used to fit the observed kinetics of the second stage

sorption step. The pseudo equilibrium solute content predicted by the model at the end of the second stage only depends on the parameter χ and a value 0.68 was obtained from the best fit procedure, a value which is not too far from the theoretically predicted value of 0.63 discussed previously. The sensitivity of the predicted characteristic time for the relaxation stage to the value of η_A^0 is illustrated in Figure 6.7 in which several plots are shown. The best fit was obtained for a value of $\eta_A^0 = 0.8\times10^6$ MPa·s. For the sake of clarity, Figure 6.8 is a re-plot of the same experimental data shown in Fig. 6.7, this time on a linear scale, and compares it to the best fit of the parameters for the model.

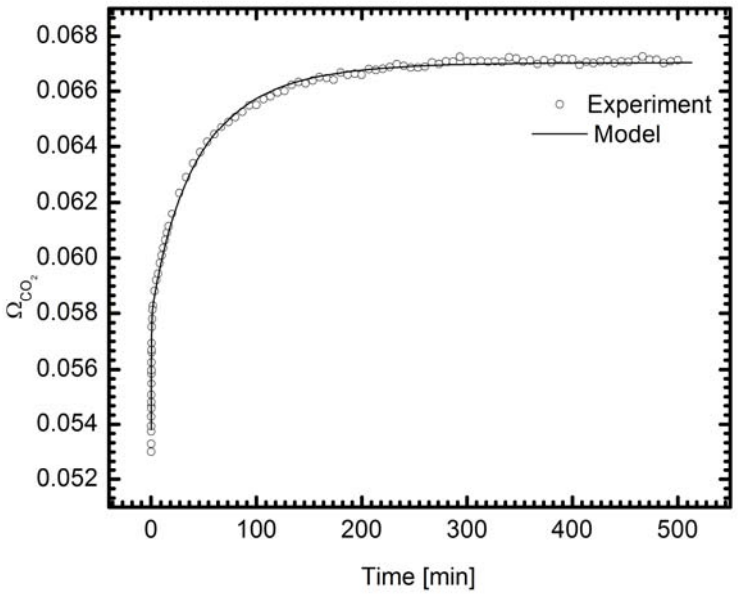

Figure 6.8 CO_2 content in PMMA film for sorption step from 370 to 450 psi at 50 ^oC, experimental data and best fit results from model

This figure makes it very clear that the first non-Fickian diffusion step lasts less than 60 sec, and the model does an excellent job of representing the CO_2 absorption data through most of the mass absorption process.

Using the parameters estimated through the fitting procedure, values for the characteristic diffusion and relaxation times in the sorption process analyzed above can be calculated and a Deborah number can be estimated, for the conditions of the experiments shown in Figure 6.7, as $D_e \cong 2 \cdot 10^3 \gg 1$. The large value of the Deborah number in this case indicates that relaxation is much slower than diffusion, which is consistent with the observed two-stage sorption behavior.

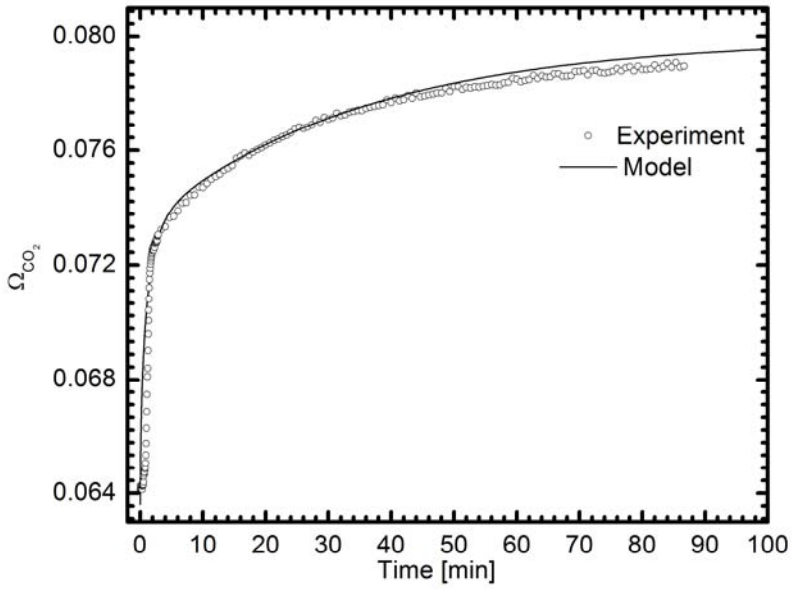

Figure 6.9 CO_2 content in PMMA film for sorption step from 370 to 450 psi at 35 ^oC, experimental data and best fit results from model

In Figure 6.9 and Figure 6.10 results are compared for solute content measured in a sorption experiment for CO_2 pressure jump from 370 to 450 *psi* at 35^oC and in a corresponding desorption step, together with the best fit from the model calculations.

Thermodynamic and transport parameters in Table III and values from the "Glass" column in Table VI were used in all calculations. The model results shown in

Figure 6.9 and Figure 6.10 were obtained with parameters χ and η_A^0 estimated from a fitting procedure and these are listed in Table VII.

Case	Temperature (^{o}C)	
	35	50
Bulk Viscosity[MPa s]		
η_A^0 (Sorption)	10^6	8×10^5
η_A^0 (Desorption)	2×10^5	$\rightarrow 0$
Voigt Fraction		
χ (Sorption)	0.60	0.68
χ (Desorption)	0.42	0.57

Table VII Mechanical model parameters (η_A^0 and χ) values for the glassy polymer case

It is interesting to observe that good estimates were obtained for the solute concentration level reached at the end of the first sorption or desorption step in both cases and that is remarkable, as the values at this time do not depend on fitting parameters. Reasonable representations of sorption levels attained at longer times and the kinetics of the second step in the sorption/desorption processes were obtained in these cases through the use of convenient values for model parameter χ and η_A^0, respectively.

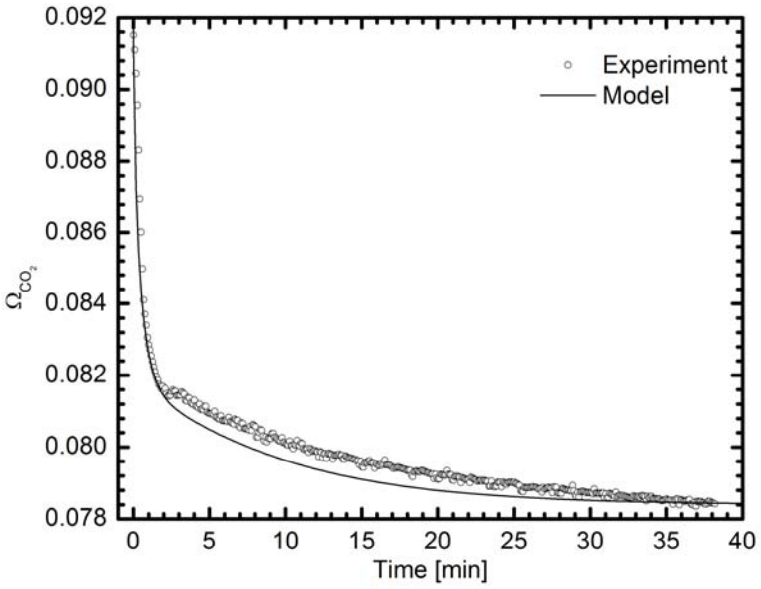

Figure 6.10 CO_2 content in PMMA film for desorption step from 450 to 370 psi at 35 ^oC, experimental data and best fit results from model

In Figure 6.11, data are shown for solute content measured during a desorption process of CO_2 in a PMMA film from 450 to 370 *psi* at 50^oC. The parameters used to fit this data with the model are shown in Table VIII. In this case a two-step desorption processes is not evident from the experimental observations, at least for the time interval examined. Analysis of the experimental data through the use of the model confirms that the volume relaxation process took place in the PMMA sample during the latter desorption experiment, as indicated by non negligible values of the χ parameter obtained from the fitting. On the other hand, the relaxation time is too short in this case, with respect to diffusion time, to allow the model to evaluate a characteristic viscosity and indeed the sorption results can be satisfactorily interpreted in terms of negligible η_A^0.

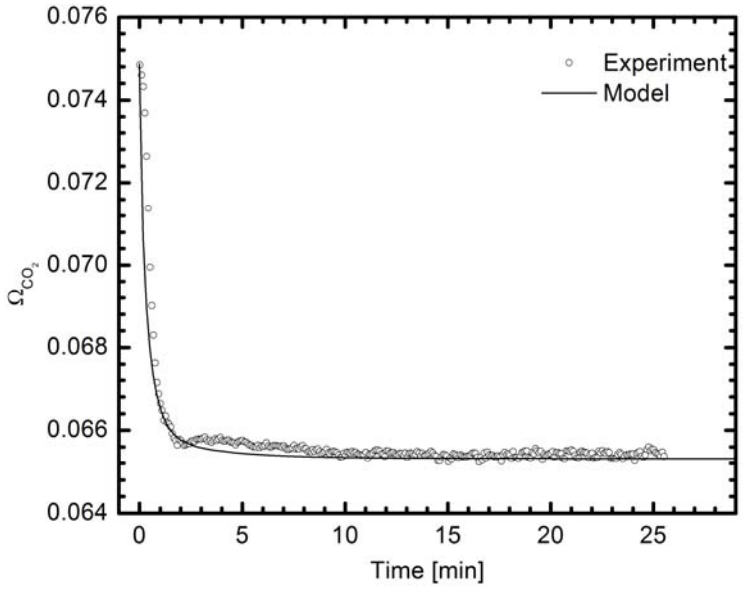

Figure 6.11 CO_2 content in PMMA film for desorption step from 450 to 370 *psi* at 50 ^oC, experimental data and best fit results from model

Figure 6.12 illustrates the viscosity shift upon sorption as a function of temperature and CO_2 concentration, as predicted by Eq. (6.52), our treatment of the viscosity does not require a different value of the C_2 parameter above and below the glass transition point, being this a must if one considers the linearity assumption between the specific volume and the temperature endowed in that theory[28].

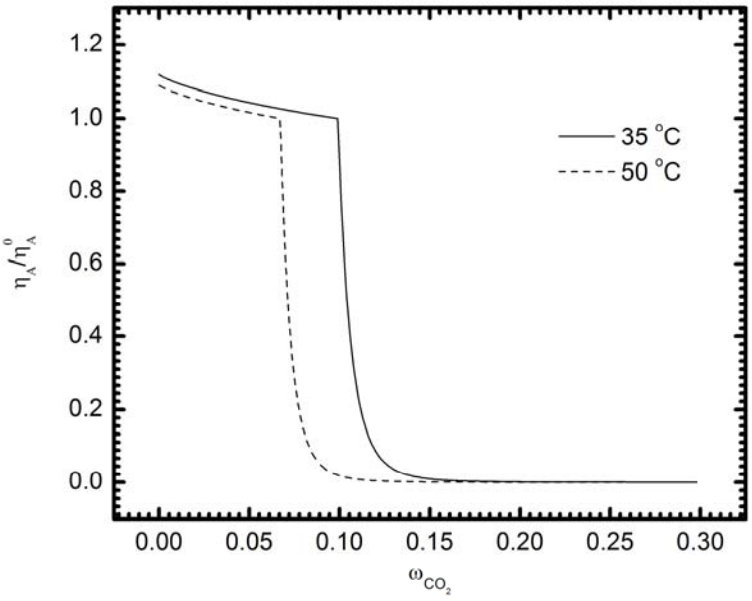

Figure 6.12 Viscosity shift upon sorption at 35 and 50 °C as predicted by model

The model introduced here interprets the relaxation process in solute sorption kinetics in terms of the volume dilation of the polymer matrix and it would be interesting to compare the time dependent swelling predicted by the model with experimental swelling rate data. Unfortunately, the experimental procedure used in these experiments did not allow for continuous measurements of film thickness to evaluate swelling kinetics. However, a few data points at relatively long sorption times could be retrieved from ellipsometry experiments performed in chapter IV and a comparison is possible for these data with the swelling values estimated by the model presented here.

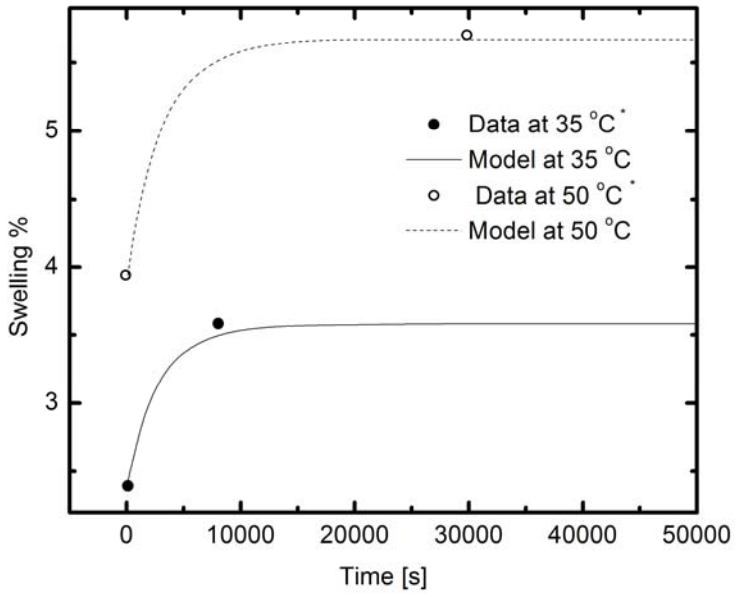

Figure 6.13 Swelling for CO_2 sorption experiment in PMMA from 370 to 450 psi, at 35 °C (a) and 50 °C (b)

Figure 6.13 compares time dependent swelling predicted in this case with measured data for sorption steps at 35 and 50°C in the glassy state. It is relevant to observe that the measured swelling values at long time are consistent with those described by the model used in the analysis of the solubility measurements.

§ 6.8 Conclusion

The NET-GP model has been shown to provide a good quantitative prediction of the isothermal sorption data in a wide range of pressures. By coupling this reliable model with the free volume theory for the diffusive part, and a simple rheological equation for the relaxation part, this work has proven the applicability of our

approach to represent the kinetics of differential sorption/desorption experiments in glassy as well as rubbery polymeric systems.

The model performance in different operating conditions, namely different temperatures and pressures for both sorption and desorption, was satisfactory and it allowed for a description of both Fickian and two-stage type sorption behavior and to account for transition from one to another in terms of temperature, and solute pressure.

Several examples of the application of model results to the analysis of differential sorption/desorption experiments for CO_2 in PMMA were considered. In all cases good results were obtained, confirming the validity of the approach used in representing thermodynamic properties, in both equilibrium and non-equilibrium conditions.

Relaxation steps during sorption/desorption cycles were described in this context in terms of volume relaxation of polymer samples with two adjustable model parameters: the characteristic bulk viscosity and the weight for Voigt elements in the rheological model. Characteristic viscosity values obtained from analysis of sorption data are in the expected order of magnitude[27], while weight values confirm the rough estimation performed on volumetric properties of pure polymeric species.

On the other hand, the rheological model parameters retrieved from sorption steps are different than those obtained through analysis of corresponding desorption runs. The latter is not surprising as the nonlinear character of bulk rheology of glassy polymers is well documented and a comprehensive representation of details in their volume swelling cannot be obtained in the simple terms discussed here.

The aim of this chapter was to provide a meaningful combination of mass transport and volume relaxation models that may prove or disprove the validity of the basic idea used to represent relaxation phenomena induced by solute sorption in glassy polymers. One major advantage of this approach consists in its simplicity and capability of being extendable, in a straightforward manner, to multi-component systems and multi-dimensional transport problems.

§ 6.9 References

(1) Taylor, D. K.; Carbonell, R. and DeSimone, J. M. *Annual Review of Energy and the Environment*, **2000**, *25*, 115-146.

(2) McHugh, M. A. and Krukonis, V. J. *Supercritical Fluid Extraction: Principles and Practice*, **1986**.

(3) DeSimone, J. M., *Science*, **2002**, *297(5582)*, 799-803.

(4) Berens, A. R., *Transport of Plasticizing Penetrants in Glassy-Polymers.* **1990**, *423*, 92-110.

(5) Wang, W. C. V.; Kramer, E. J. and Sachse, W. H. *Journal of Polymer Science, Polymer Physics Edition*, **1982**, *20(8)*, 1371-1384.

(6) Carbonell, R. G. and Sarti, G. C. *Industrial & Engineering Chemistry Research*, **1990**, *29(7)*, 1194-204.

(7) Petropoulos, J. H., *Journal of Polymer Science, Polymer Physics Edition*, **1984**, *22(11)*, 1885-900.

(8) Berens, A. R. and Hopfenberg, H. B. *Polymer*, **1978**, *19(5)*, 489-96.

(9) Crank, J., *The Mathematics of Diffusion*. 2nd ed. **1975**, London, England: Oxford University Press. 414.

(10) Enscore, D. J., Hopfenberg, H. B. and Stannett, V. T. *Polymer Engineering and Science*, **1980**, *20(1)*, 102-7.

(11) H. L. Frisch, *Polymer Engineering & Science*, **1980**, *20(1)*, 2-13.

(12) Vrentas, J. S. and Duda, J. L. *Macromolecules*, **1976**, *9(5)*, 785-790.

(13) Chow, T. S., *Polymer*, **1988**, *29(8)*, 1447-1451.

(14) Doghieri, F. and Sarti, G. C. *Macromolecules*, **1996**, *29(24)*, 7885-7896.

(15) Sarti, G. C. and Doghieri, F. *Chemical Engineering Science*, **1998**, *53(19)*, 3435-3447.

(16) Carla, V., et al., *Macromolecules*, **2005**, *38(24)*, 10299-10313.

(17) Sarti, G. C., *Polymer*, **1979**, ***20****(7)*, 827-832.

(18) Sarti, G. C. and Apicella, A. *Polymer*, **1980**, *21(9)*, 1031-1036.

(19) Bisschops, M. A. T.; Luyben, K. C. A. M. and van der Wielen, L.A.M. *Industrial & Engineering Chemistry Research*, **1998,** *37(8)*, 3312-3322.

(20) J. S. Vrentas, J. L. D., *Journal of Applied Polymer Science*, **1977,** *21(6)*, 1715-1728.

(21) Durning, C. J. and Tabor, M. *AIChE J.* **1986**, *19*, 2220-2232.

(22) Peppas, N. A.; Wu, J. C. and von Meerwall, E. D. *Macromolecules*, **1994**, *27(20)*, 5626-5638.

(23) Wu, J. C. and Peppas, N. A. *Journal of Polymer Science*, Part B: Polymer Physics, **1993**, *31(11)*, 1503-1518.

(24) Temam, R. and Miranville, A. *Mathematical Models in Continuum Mechanics*. 2nd ed. **2005**: Cambridge University Press. 342.

(25) Doghieri, F.; Roda, G. C. and Sarti, G. C. *AIChE Journal*, **1993**, *39(11)*, 1847-1858.

(26) Thran, A.; Kroll, G. and Faupel, F. *Journal of Polymer Science*, Part B: Polymer Physics, **1999**, *37(23)*, 3344-3358.

(27) Piccinini, E.; Gardini, D. and Doghieri, F. "Stress effects on mass transport in polymers: a model for volume relaxation." *Composites*: Part A. **in press**.

(28) Royer, J. R.; DeSimone, J. M. and Khan, S. A. *Journal of Polymer Science* Part B-Polymer Physics, **2001**, ***39****(23)*, 3055-3066.

(29) Williams, M. L.; Landel, R. F. and Ferry, J. D. *Journal of the American Chemical Society*, **1955**, ***77***, 3701-3707.

(30) Zielinski, J.M. and Duda, J.L. *AIChE Journal*, **1992**, *38*, 405-415.

(31) Brandup, J.; Immergut, E. H. and Grulke, E. A. eds. *Polymer handbook*. 4th ed. **1999**, Wiley: New York.

(32) Vrentas, J. S. and Duda, J. L. *AIChE Journal*, **1979**, *25(1)*, 1-24.

(33) Klenstremer, C., *Engineering Fluid Dynamics: An Interdisciplinary Systems Approach*. **1997**: Cambridge University Press.

CHAPTER VII

Interfacial effects and the anomalous swelling behavior of supported polymeric thin films in supercritical carbon dioxide

This chapter investigates the effects of temperature, initial thickness and material substrate on one-dimensional dilation of thin supported polymeric films in supercritical carbon dioxide. An excess Gibbs adsorption of carbon dioxide, strongly dependent upon temperature, pressure and surface forces involved, present at the submerged polymer/substrate interface was detected using High-Pressure Quartz Crystal Microbalance. This accumulation of carbon dioxide at the submerged surface could explain the so-called "anomalous swelling behavior" that has been reported in the literature, where a maximum in film thickness with pressure has been found. A thorough discussion of our ideas as well as those recently proposed by others in dealing with such phenomenon is also provided.

Chapter VII is essentially a reprint (with slight modifications) of Carla, V., et al. "Interfacial effects and the anomalous swelling behavior of supported polymeric thin films in supercritical carbon dioxide" *Langmuir* **(Submitted)**

§ 7.1 Introduction

There is a great interest in potential application of supercritical carbon dioxide ($scCO_2$) in many industrial processes as improved replacement for traditional aqueous and organic solvents[1-3]. Supercritical carbon dioxide is a very good plasticizer for a number of different polymers. It is inert as reaction solvent. It has a very low surface energy and viscosity, which make it ideal for thin uniform coatings particularly for microelectronics manufacturing and drug controlled-release devices[4,5]. In addition, $scCO_2$ may play a key role in the development of nanoscale high aspect ratio features in EUV photoresists[6-8]. Yet, as very recent studies have pointed out, much research is needed to better understand the physics of thin supported polymeric films/$scCO_2$ systems[9-18].

Studies on the dynamic properties of polymers at surfaces and interfaces have shown that constrained thin films behave quite differently from their bulk counterparts with respect to many features. Interfacial effects undoubtedly dominate the behavior of materials with small dimensions as a result of their high surface-to-volume ratio and the importance of chain mobility in the vicinity of surfaces and interfaces in understanding properties such as adhesion and friction has been extensively studied over the past decade[9, 10]. Moreover, surface effects have been shown to dramatically change the thickness dependence of the glass transition temperature of thin films coated onto different substrates[11-14].

Studies on mobility in thin films at the segment level by probing the glass transition behavior of ultra-thin films have brought many insights into the departure from bulk behavior. The experimental glass transition is a kinetic transition which

occurs when relaxation times associated with diffusive motion become long compared with experimental time and it is marked by discontinuities in quantities that are second derivatives of a free energy, such as heat capacity or isothermal expansion coefficient.

In thin films, the latter may be measured by following the thickness as a function of temperature using a technique like Ellipsometry or X-ray reflectivity; the glass transition is detectable as a sharp change in derivative of the thickness/temperature curve.

Keddie et al.[11], using Ellipsometry showed that polystyrene (PS) on silicon substrates experiences a measurable depression in glass transition temperature for films below 100 nm in thickness, the depression becoming substantial for thickness below 40 nm.

They also observed for poly(methyl methacrylate) (PMMA) on a gold substrate depression in T_g, while the same polymer on a silicon oxide substrate, with which a relatively strong interaction would be expected, showed an increment in glass transition temperature when decreasing the initial thickness[12]. Even stronger effects have been seen for poly(2-vinyl pyridine) on silicon oxide, where T_g increases of order 20K were observed for films thinner than 30 nm.

Grohens et al.[13, 14] have emphasized the role of specific interactions between polymer and substrate in determining whether the glass transition temperature increases or decreases. They showed that strong attractive interactions between the polymer and the substrate can lead to T_g increase with decreasing film thickness while weaker interactions (limiting case is the free standing film) lead to a decrease in T_g

with decreasing film thickness. It has also been reported by the same authors that polymer tacticity plays an important role where an increase of glass transition temperature with decreasing thickness for isotactic PMMA on silicon and aluminum with a decrease for syndiotactic PMMA. This aspect has been correlated with direct spectroscopic measurements of the density of polymer-substrate interactions showing a higher density in the former case.

Recent experimental results[15-18] have suggested that there is an interesting anomaly in the dilation behavior of thin polymeric films brought in contact with supercritical fluids. For very thin films, a maximum in the swelling percentage vs. CO_2 pressure has been observed around the critical pressure of the fluid for temperature close to the critical temperature.

However, while there is consistency among studies conducted by different groups about the experimental evidence of such phenomena, the picture that emerges is not yet clear and little in the way of proposing comprehensive theoretical basis has been done so far.

Sirard et al.[15] were the first to discover this interesting maximum studying the swelling behavior of thin silicon-supported poly(methyl methacrylate) (PMMA) films at pressures around the carbon dioxide critical pressure and temperature close to the critical temperature (35^{o}C) using High-Pressure Ellipsometry (HPE).

For the two thicknesses examined (88 and 321nm) it seemed that the higher the thickness the higher the extent of the deviation from bulk behavior, which is somehow unintuitive.

At the same pressure where the swelling maximum is located a drop in the corresponding mixture refractive index was detected. This feature would indicate a maximum in CO_2 content as well. In fact, the refractive index of a mixture can be related to mixture composition through a Lorentz-Lorentz equation[19, 20]. This would suggest an enhancement in carbon dioxide solubility in that particular range of pressures which could also explain the dilation anomaly in a straightforward way.

However the authors avoided this analysis and rather believed both phenomena to have a different cause to be found in a phase separation of CO_2-rich and PMMA-rich domains within the film. It was claimed that spinodal decomposition (micro-bubble formation) could take place under the driving force of carbon dioxide isothermal compressibility. In fact, the latter quantity experiences a maximum around the critical pressure as well and it is well-known that the compressibility of the system plays a key role when it comes to phase stability[19]. However their explanation is somehow questionable for two reasons: first, it fails to explain why the same behavior cannot be seen in bulk films.

Second, the compressibility of pure carbon dioxide (external phase) has been considered in their discussion instead of that of the whole polymer-CO_2 system, which has the exact opposite trend with temperature. Finally, no experimental evidence of such phase separation has been reported yet.

Using a rather different technique, Neutron Reflectivity, and exploring four different polymers, Koga et al.[16-18], found the same behavior for much thinner films (ranging from 20 to 120 nm).

They went a step further exploring the effect of many different parameters on the "anomalous peak" they had seen. It was discovered for instance, that elasticity plays an important role as well, since different materials experience a different relative peak size, apparently depending of their elastic modulus rather then their bulk solubility[16].

They also performed a series of studies aimed at providing insights about the size of the deviation with initial film thickness. It was found for polystyrene (PS) and poly-butadiene (PB) below 100nm that the higher the initial thickness the lower the size of the maximum, with their data showing an exponential decrease with initial thickness.

Unlike the previous investigators, Koga et al. believe that the phenomenon could be explained by an enhancement in carbon dioxide solubility, due to an enhancement in carbon dioxide density across the "ridge of density fluctuations". This critical fluid effect is related to the fact that when approaching critical conditions from either side of an isotherm, dynamic domains of different size and concentration can be found in the bulk fluid. There is a way of quantifying these domains measuring these fluctuations in the fluid density (via light scattering) and it can be shown that in the same range of pressure and temperatures these fluctuations show a maximum much like the swelling anomaly[16-18].

It has been suggested that the two facts must be somehow related to each other and this will bring to believe that the swelling isotherms are density dependent far from the ridge conditions and density fluctuations dependent otherwise.

However, their explanation fails to take into account the effect of thickness. Why would the polymer be sensitive to the ridge only below a given thickness and be ridge-independent above that threshold?

Moreover, it is well-known from fundamental thermodynamics of critical phenomena that solubility (hence sorption) depends on direct density enhancements, that is enhanced chemical interaction between solvent a solute, while the density fluctuations invoked would point to indirect density enhancement, or solvent-solvent interactions.

Furthermore, both groups seem to be focusing on the external phase, considering this anomaly solely a critical fluid phenomenon, thus overlooking the importance of confinement and surfaces effects in the polymeric phase.

The aim of this work is to provide a better understanding of the main factors affecting this anomaly, especially in terms of key variables such as temperature, initial film thickness and interfacial effects that could be important due to the small dimensions of the samples considered.

Since carbon dioxide can wet hard surfaces and a stable thin layer can be deposited at high pressures (Gibbs Excess Adsorption), we set out to investigate whether carbon dioxide could be adsorbed in excess at the submerged polymer/substrate interface as well, and if this accumulation could in turns be responsible for the anomalous swelling behavior of soft surfaces (polymer coated surfaces).

After a brief section on the experimental techniques and protocols adopted, we introduce and discuss our findings along with our physical interpretation, which is

based on the interactions between the supercritical phase dissolved in the polymer matrix and the polymer/substrate interface.

§ 7.2 Experimental Procedure

§7.2.1 High Pressure Ellipsometry (HPE)

§7.2.1.1 Materials and Sample Preparation

PMMA (Mw: 225700, Mw/Mn = 1.06) was purchased from Polymer Source, Inc. Dorval (Montreal, Canada). Toluene (Fisher) was used as solvent to dissolve PMMA. Silicon wafers (100 mm diameter, a <100> orientation) having ≈1.7 nm thick native oxide films (SiO_x), GaAs wafers (50 mm diameter, a <100> orientation) having ≈3.0 nm thick native oxide films ($GaAs\_O_x$) and Silicon wafers (50 mm diameter, a <100> orientation) covered with 300nm TiN_2 were purchased from International Wafer Services (Portola Valley, CA). The wafers were cleaned by soaking in a mixture of JTB-111 alkaline-surfactant, hydrogen peroxide and DI water with a 4.6:1:22.8 volume ratio for 10 minutes and subsequently rinsed with copious amounts of DI water, and dried with nitrogen. PMMA/Toluene solutions were spin-coated onto silicon wafers using a Headway Research (Model 131-024, Indianapolis, IN) spin coater. The concentrations of the PMMA/Toluene solutions and spin rates were varied to obtain films of different thickness. To etch away the oxide layer, GaAs wafers were immersed in HCl for 1 minute, then rinsed with copious amounts of DI water, and dried with nitrogen.

§7.2.1.2 Swelling Measurements

The PMMA films spun on the different substrates were introduced into the chamber and scanned using the ellipsometer described elsewhere[20]. The experimental ellipsometric data were fit using a different model for each kind of substrate. A four-layer model, shown in Figure 1-b, comprising the silicon substrate, a native oxide layer, a mixed polymer/CO_2 layer, and a bulk CO_2 medium was the standard model. Fig. 7.1-c shows the three layer model that has been considered instead for films cast on GaAs and TiN. The absence of the oxide layer is due to prior etching done on both substrates in order to avoid conflicting effects due to the presence of oxides.

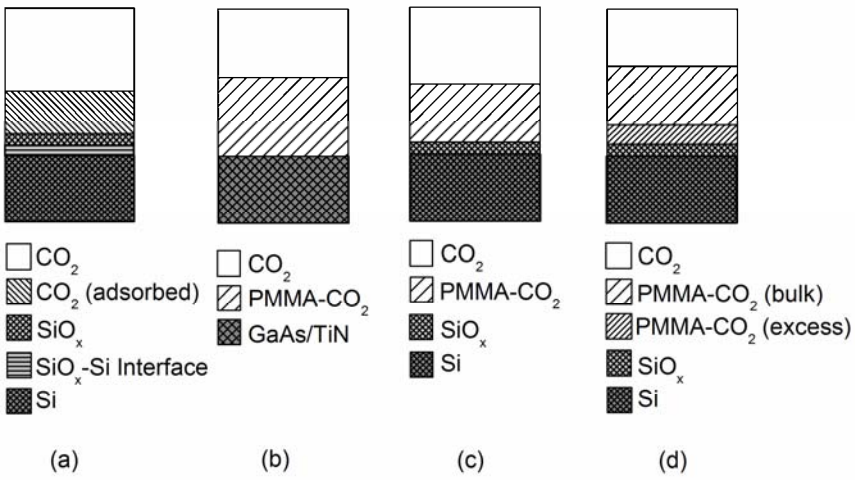

Figure 7.1 a-b-c-d Fitting models used for Ellipsometry data analysis: (a) CO_2 adsorption onto bare silicon, (b) PMMA-CO_2 adsorption and swelling onto silicon, (c) PMMA-CO_2 adsorption and swelling onto GaAs and TiN, (d) PMMA-CO_2 adsorption and swelling onto silicon, attempt to validate TLC

The refractive indices at different wavelengths were adopted from literature values[20] for all the substrates examined, the native silicon oxide, and the CO_2 atmosphere. The fitted parameters for the swelling experiments were the thickness

and refractive index of the swollen PMMA/CO_2 layer. The refractive index of the swollen PMMA/CO_2 layer was modeled as a function of wavelength by assuming a Cauchy dispersion relationship[20].

Fig. 7.1-d shows instead a five-layer model, in which besides the four standard layers a fifth one labeled "PMMA-CO_2 excess" has been added. In this case the fitting parameters were chosen to be the thickness and refractive index of this latter extra layer, while those of the "PMMA-CO_2 bulk" layer were retrieved using the information obtained for bulk films[20], as it will be discussed later.

§ 7.2.2 Quartz Crystal Microbalance Measurements (QCM)

§7.2.2.1 Materials and Sample Preparation

5.00 MHz AT-cut Si quartz crystals (a blank diameter of 8.5 mm and a thickness of 0.25 mm) were obtained from International Crystal Manufacturing (Oklahoma City, OK). The Si film was vacuum sputtered over an Au electrode that provided the necessary electrical actuation to the quartz. The RMS surface roughness of the crystals used was less than 10 nm (analyzed using AFM). The crystal was connected to a voltage-controlled oscillator (Maxtek model PLO-10, Santa Fe Springs, CA). This oscillator provides two outputs: frequency and voltage. The voltage reading is inversely proportional to the resistance of the crystal. The oscillator is further connected to an Agilent 225 MHz Universal Frequency Counter (Model 53131A, Palo Alto, CA) that records the frequency of the vibrating crystal. The time-dependent frequency readings were stored on a computer using Agilent Intuilink Connectivity software.

PMMA films for the QCM experiments were cast onto the surface of the crystal by dip-coating. The crystal was dipped vertically into a 2.4 w% PMMA/toluene solution, allowed to equilibrate for a specific time and then was withdrawn from the solution at a controlled rate using a motorized device. The coated crystal was dried under vacuum at 90-120^{o}C for 3-5 hours. The clean crystal was then placed in the cell under vacuum (0.01 psia), Precision DD-20 (Precision Scientific Inc., Chicago, IL) vacuum pump, and the fundamental frequency F_o of the coated crystal was recorded. The stable frequency level is indicative of complete evaporation of the solvent form the polymer during curing. The value of the stabilized frequency of the coated QCM in vacuum was utilized to calculate the mass of coated polymer by comparing to fundamental frequency of the quartz crystal without polymer.

§7.2.2.2 Surface Adsorption Measurements

To estimate the adsorption of CO_2 on the polymer-coated QCM surface the following experiments were performed. A QCM crystal was cleaned with the appropriate solvents until the initial frequency of the new crystal was recovered to within 5 Hz. The crystal was then coated with a certain amount of PMMA and a typical CO_2 uptake run was carried out, according to the procedures outline above, in pressures up to 1800 psi with 150 psi steps. This experiment was repeated using the same QCM crystal but each time coated with a different initial mass of PMMA. A total of 5 runs were performed where the PMMA mass ranged from 10 to 40 μg/cm^2.

The results obtained from this set of experiments provided the amount of CO_2 absorbed at different pressures for different initial PMMA masses. A linear

relationship between solvent solubility and polymer loading was established by plotting the mass of CO_2 uptake versus the coated PMMA mass. The adsorption on the surface was estimated by extrapolating the curves at different pressure to zero PMMA mass, as it will be further discussed in the next section.

§ 7.3 Adsorption on Hard and Soft Surfaces

§ 7.3.1 Absolute and Gibbs Excess Adsorption on bare substrates.

Previous studies have examined adsorption of supercritical fluids onto non-swelling hard surfaces. Findenegg[21] showed large surface excesses of ethylene on homogeneous graphitized carbon black surfaces near the critical pressure and critical temperature.

Others have seen large adsorption excesses of compressible fluids onto hard impenetrable surfaces when operating in the proximity of the critical pressure and temperature[22-24]. At supercritical temperatures, the excess adsorption of ethylene exhibited a pronounced maximum at a pressure slightly less than the pressure where the compressibility of ethylene displayed a maximum. The excess adsorption isotherms were very large and sharp at near critical pressures and at temperatures that were slightly higher than the critical temperature. At higher temperatures the excess adsorption maxima become smaller and much broader in nature, occurring at higher pressures.

Similar behaviors in the supercritical adsorption of CO_2 on both unmodified and chemically modified silica surfaces as well as on proteins and polysaccharides have

also been reported. Furthermore, da Rocha et al.[25] showed that the excess adsorption of CO_2 at the CO_2-water interface leads to a minimum in the interfacial tension vs. pressure at the near-critical temperatures and several theoretical studies successfully modeling the supercritical adsorption of fluids on various surfaces have appeared[26,27].

In all the abovementioned studies the only directly measurable property is the Gibbs Excess Adsorption (Γ^{ex}), also called surface excess by many authors. For the case of excess adsorption onto flat surfaces Γ^{ex} is defined in terms of density profiles as[21, 27]

$$\Gamma^{ex} = \int_0^{\infty} \left(\rho(z) - \rho_{bulk}\right) dz \approx \int_0^{\delta} \left(\rho(z) - \rho_{bulk}\right) dz = \delta\left(\langle \rho_{ads} \rangle - \rho_{bulk}\right) \qquad (7.1)$$

where $\rho(z)$ is the local density of CO_2 at a distance z from the substrate, ρ_{bulk} is the density of the bulk CO_2, $<\rho_{ads}>$ is the average over the entire adsorbed film thickness δ, and 0 represents the substrate surface. For many surfaces, the interaction between CO_2 and the surface may be expected to exceed the intermolecular attraction between pure CO_2 molecules, due to the low polarizability per volume of CO_2.

Since CO_2 is attracted preferentially to the surface, $\rho(z)$ will be larger than ρ_{bulk} (see Fig. 7.2). In highly CO_2 compressible regimes, the attraction of CO_2 to the surface produces $\rho(z)$ values with densities approaching those of liquid CO_2. The pronounced difference between $\rho(z)$ and ρ_{bulk} results in large excesses of CO_2 at the surface. As the pressure increases, the bulk density of CO_2 increases markedly, and the excess layer decreases since $\rho(z)$ becomes more equivalent to ρ_{bulk}.

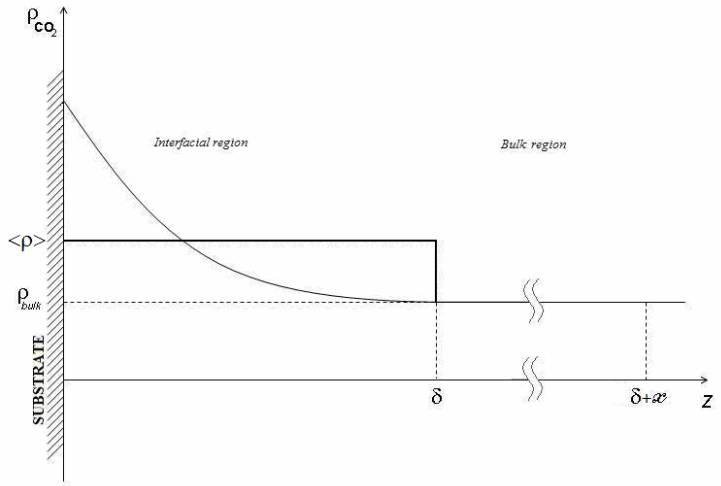

Figure 7.2 CO_2 concentration profile near the substrate. Shown are the thickness δ of the adsorbed layer as well as the average CO_2 density assumed stepwise over δ

Thus the qualitative behavior of Γ^{ex} should exhibit similar trends as that of the isothermal compressibility. For example, near the critical temperature large and sharp excess adsorption maxima are observed near the critical pressure. At higher temperatures, the maxima are smaller and broader and shift to higher pressures.

This excess accumulation on hard surfaces might be investigated experimentally using rather different techniques, both gravimetric and non-gravimetric. For instance, HPE, QCM[15, 28] (non-gravimetric) and Rubotherm[29] (gravimetric), have been used in the past and different outcomes of the same phenomenon have been reported, due to the intrinsic differences among the quantities measured. However, once referred to the same physical frame the results appear to be all consistent.

Among the gravimetric techniques, Rubotherm is one of the most largely employed. It yields rather accurate measurements but it suffers from the need to use a complex procedure to evaluate the volume of the adsorbent first (using a non-adsorbing gas like helium) which brings into the measurement a certain degree of uncertainty. Furthermore, when used to measure gas adsorption onto particles or gels

it does not account for potential packing effects which are then embedded into the measure.

HPE is an optical technique (non-gravimetric) that in theory should help overcome the aforementioned issues of gravimetric measurements. However, when utilized for bare sorption measurements it suffers of two important limitations. First, windows birefringence effects are not easily decoupled from surface adsorption. While this is not a crucial point when measuring thicknesses of polymeric samples where there is not a high physio-adsorption[15, 30] it becomes a crucial issue when dealing with adsorption onto hard surfaces.

The layer of carbon dioxide adsorbed onto silicon has a density gradient which slowly fades into the bulk carbon dioxide density, thus having a different refractive index as well (since the refractive index changes linearly with the density). HPE is sensitive enough to "see" an interface between the adsorbed layer and the bulk carbon dioxide and a thickness (δ) can be extracted from the measurements once a convenient choice has been made for the density, hence the refractive index, of the adsorbed phase.

Let us discuss this aspect a little further using a simple correlation[31]:

$$\Delta \simeq \frac{\delta}{\lambda_{opt}}\left(n_{ads} - n_{bulk}\right) \tag{7.2}$$

Where Δ is one of the two angles measured by HPE, λ_{opt} is the wavelength of the beam used to study the sample, δ is the thickness of the adsorbed film, and n_{ads} and

n_{bulk} are the refractive indices of the adsorbed phase (assumed as an average value) and the bulk phase respectively.

By comparing the trends of density and refractive index of carbon dioxide with pressure and temperature the following linear relationship between the two quantities can be successfully introduced:

$$n \simeq 1 + a(T)\rho(T,P) \tag{7.3}$$

With a(T) as only parameter, slightly dependent on temperature. At 35^{o}C, a(35)=0.2365 and we can conveniently rewrite Eq.(7.2) as

$$4.228 \cdot \left(\Delta\lambda_{opt}\right) \simeq \delta\left(\left\langle \rho_{ads} \right\rangle - \rho_{bulk}\right) = \Gamma^{ex}_{CO_2} \tag{7.4}$$

So for given T, P and λ_{opt} the left-hand side of the above expression is held constant and the effect of $<\rho_{ads}>$ on the measured δ can be better understood. Fig. 7.3 shows an example of such measurements taken in this study and compared with values re-plotted from the literature[15]. As stated before, the density of the adsorbed phase changes with distance from the substrate and an average value must be assumed in order to extract a reasonable film thickness.

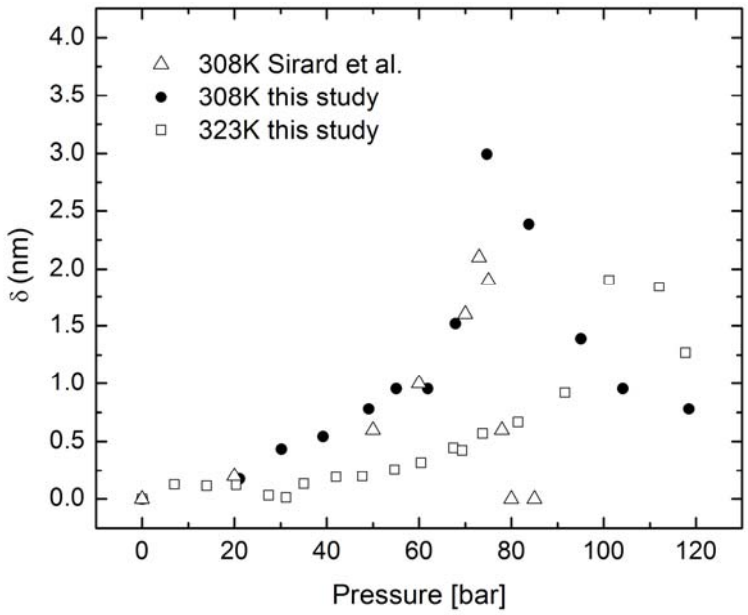

Figure 7.3 HPE measurement of CO_2 excess adsorption onto bare silicon. Full circle are data from this study taken at 35°C, open triangles are data at the same temperature from ref. [15], open squares are data from this study taken at 50°C

In order to avoid this degree of freedom and uncertainty in assuming an average density, we rather preferred to utilize a quartz crystal microbalance (QCM) which provides a direct non-gravimetric way of measuring absolute adsorption isotherms. Indeed, frequency shift due to carbon dioxide layers adsorbed on top of a quartz resonator enclosed within two electrodes can be directly translated into surface mass, as showed by Grant et al.[28], who successfully measured CO_2 adsorption isotherms in sub- and supercritical regimes for different electrode materials.

Once the contributions due to pressure, fluid environment and surface roughness are correctly accounted for and taken out from the actual measured change in frequency, the absolute sorption isotherms can be evaluated at different pressures and QCM measurements taken on bare silicon are shown in the Fig. 7.4 for 35°C and 50°C, as it can be seen there is a monotonic behavior with pressure (no maxima).

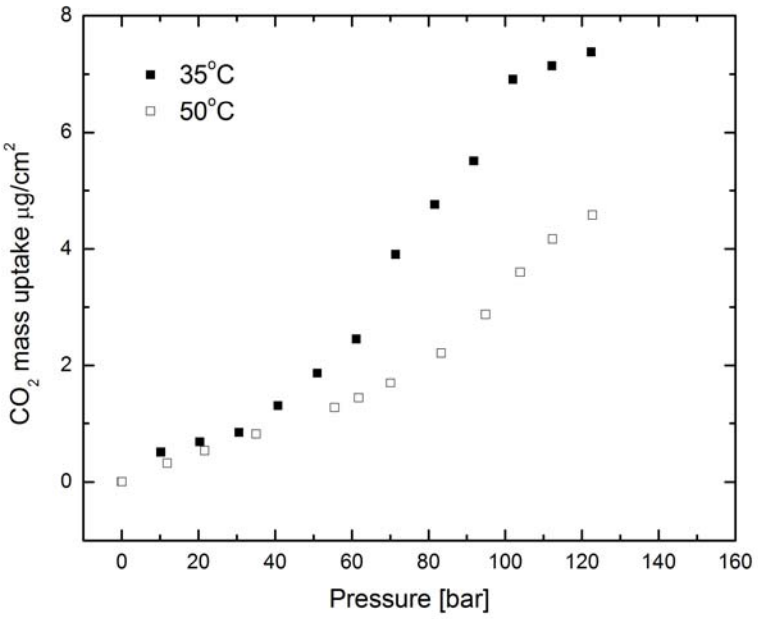

Figure 7.4 QCM measurement of CO_2 absolute adsorption onto bare silicon at 35 °C

§ 7.3.2 Gibbs excess adsorption at the buried polymer/substrate interface

We begin this section by asking ourselves if carbon dioxide could accumulate on a hard surface even when a polymer is coated on top of it. The question becomes a little clearer when picturing the film as a membrane separating two regions of different chemical potential.

Indeed, carbon dioxide chemical potential in the polymeric region close to the substrate is expected to be different from the CO_2 chemical potential throughout the rest of film. This is understandable in terms of van der Waals forces as well as hydrogen bonding (from the -OH groups of the silicon oxide) that could stabilize an excess amount of carbon dioxide with respect to the bulk isotherm[32,33].

The chemical potential of the system is broken down into two parts accordingly: the bulk system chemical potential (usual behavior) and the surface chemical potential due to the aforementioned stabilization offered by the substrate to CO_2 molecules already arrived near it[33]:

$$\mu_{CO_2} = \mu_{CO_2}^{bulk} + \mu_{CO_2}^{surface} \tag{7.5}$$

where μ_{CO_2} is the chemical potential of carbon dioxide and the subscripts stand for the two different contributions. The surface contribution can be evaluated from the usual expression of the Surface Gibbs Free Energy[32, 34]:

$$\mu_{CO_2}^{surface} = \left(\frac{\partial G^{Surface}}{\partial n_{CO_2}} \right)_{T,P} = \frac{\partial}{\partial n_{CO_2}} \left(-\frac{A_H}{12\pi\delta^2} \right)_{T,P} \tag{7.6}$$

In the above expression the Gibbs free energy has been written using the Hamaker coefficient for the system CO_2/adsorbed-CO_2/substrate, which can be evaluated using Lifshitz theory and once again assuming a packing density for the adsorbed phase. Since the Hamaker coefficient is constant for fixed T and P (fixed density, hence refractive index) the derivative involves only the thickness, as follows:

$$\mu_{CO_2}^{surface} = \frac{A_H}{6\pi\delta^3} \left(\frac{\partial \delta}{\partial n_{CO_2}} \right)_{T,P} \tag{7.7}$$

In order to solve the above expression some kind of assumption about the packing of carbon dioxide molecules in the adsorbed film must be made. Indeed, the film thickness and the number of CO_2 adsorbed molecules are related through the following:

$$\delta = N_{CO_2} \left\langle v''_{CO_2} \right\rangle \tag{7.8}$$

where the film thickness is given by the product of CO_2 adsorbed molecules times an average packing volume per unit of area. The lack of knowledge about the latter quantity is what limits the applicability of the above argument for predicting the thickness of an adsorbed film[33].

In order to experimentally detect this accumulation we devised a series of tests using QCM with four different initial polymeric mass coatings. In fact, if any accumulation (or any gradient in general) is present this should affect the region nearby the substrate and the total mass change upon sorption can be broken down as follows:

$$\Delta m''_{CO_2} = \int_0^h \rho_{CO_2}(z)\,dz = \int_0^\lambda \rho_{CO_2}(z)\,dz + \int_\lambda^h \rho_b\,dz \tag{7.9}$$

Where λ denotes the limiting point after which there is no more gradient in density and the bulk density (solubility) is recovered. Of course one should expect $\lambda \neq \delta$ due to the presence of the polymer. We further re-arrange the above expression into the following:

$$\Delta m''_{CO_2} = \int_0^{\lambda} \left(\rho_{CO_2}(z) - \rho_b \right) dz + h\rho_b \tag{7.10}$$

It is clear comparing the above with Eq.(1) that the integral term in the right-hand side is exactly the definition of Gibbs Excess adsorption within the polymeric film. The second term can be further modified by using the polymer mass balance:

$$h\rho_P = h_0\rho_P^0 = M''_P = const. \tag{7.11}$$

By combining Eq.(7.10) and Eq.(7.11) and introducing the bulk solubility[20] as ratio between the carbon dioxide and polymer densities, we finally obtain:

$$\Delta m''_{CO_2} = \Gamma_{\lambda}^{ex} + M''_P \left(\frac{\rho_b}{\rho_P} \right) = \Gamma_{\lambda}^{ex} + M''_P \theta_b \tag{7.12}$$

Eq. (7.12) will be the starting point of our analysis, since, according to it, by plotting at constant pressure and temperature the measured mass per unit area vs. h_0, or else M''_P, a linear behavior should be found as long as $h_0 >> \lambda$.

§ 7.3.3 Two Layers Correlation (TLC)

The extra amount of carbon dioxide could likely affect the swelling behavior of the chains nearer the substrate, which are strongly attached to it. In order to better comprehend this feature the system could be imagined, as depicted in Fig.7.5, as

made up by two parts: **A** of thickness (h_0-λ_0), which behaves like a simple bulk film (as long as it meets the requirement of being greater that a threshold thickness) and **B** of thickness λ_0, which swells up to λ upon sorption and it is formed by a layer of polymer chains strongly adhered to the substrate.

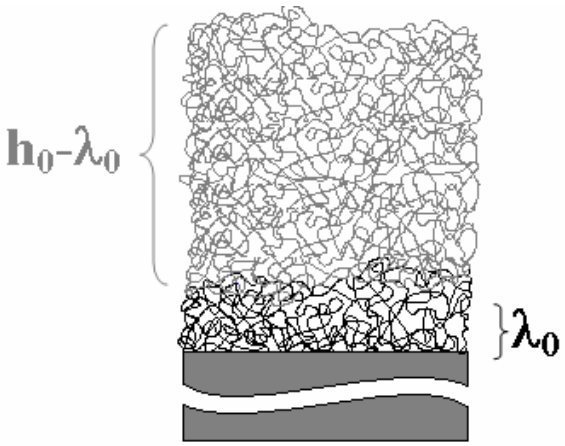

Figure 7.5 Film divided into two layers: **A** of thickness h_0- λ_0 and **B** of thickness λ_0

B should depend upon the sample preparation history and the polymer molecular weight. Using scaling arguments it could be assumed as[35, 36]:

$$\lambda_0 \sim R_g \tag{7.13}$$

With R_g radius of gyration of the polymer, which for ideal chains is $Rg = aN^{1/2}$ while including the excluded volume effect (concentrated solutions) becomes $Rg = aN^{3/(d+2)}$ with d number of dimensions. For d=3, $R_g = R_F$, Flory Radius[35, 36]. The film swelling will then be:

$$\frac{h-h_0}{h_0}=\underbrace{\frac{(h-\lambda)+(h_0-\lambda_0)}{(h_0-\lambda_0)}}_{A}\left(1-\frac{\lambda_0}{h_0}\right)+\underbrace{\left(\frac{\lambda-\lambda_0}{\lambda_0}\right)}_{B}\frac{\lambda_0}{h_0} \tag{7.14}$$

With the **A** piece which is affected by bulk carbon dioxide content and swells like a bulk film while the **B** piece should somehow swell more because of the excess CO_2. With a little algebra Eq. (7.14) becomes:

$$Sw(h_0)=Sw_{bulk}+\frac{\left(\lambda-\lambda_0\left(1+Sw_{bulk}\right)\right)}{h_0}=Sw_{bulk}+\frac{\left(\lambda-\lambda_B\right)}{h_0} \tag{7.15}$$

The last term in the above expression is the measure of the extra-swelling in the layer near the substrate. For a given polymer species, at a given temperature and pressure and for a given substrate materials the above combined with Eq.(7.13), returns:

$$Sw(h_0)=Sw_{bulk}+q\left(\frac{R_g}{h_0}\right) \tag{7.16}$$

Eq. (7.16) is a key result of the present chapter and its meaning will be further discussed in the next section. Let us now try to have a better look at the constant q that appears in the above expression. By definition results:

$$q=\frac{\left(\lambda-\lambda_B\right)}{R_g}=\frac{\left(\lambda_0\cdot(1+sw)-\lambda_0\cdot\left(1+sw_{bulk}\right)\right)}{R_g}=\frac{\lambda_0\Delta sw}{R_g} \tag{7.17}$$

Assuming that the extra swelling is coming from the excess of carbon dioxide accumulated at the buried polymer/substrate interface is not enough to explain why there is a maximum in the swelling behavior since as figure 7.4 shows, such surface accumulation does not have a maximum. There have been many attempts by the author to achieve a model able to predict all the fundamental features starting from a modified expression for the Gibbs free energy of the system, accounting for surface effects as well as confinement effects (entropy of frustration).

However, since only the swelling behavior is relevant, the situation can be explained in rather simple terms if we consider that this excess carbon dioxide does not behave like its bulk counterpart but shows *rod-like* nature.

Stated differently, according to this idea, carbon dioxide physically adsorbed at the surface can self-associate into rodwise ordered structures in the proximity of the critical point. Much like what happens in the pure fluid this 'islands' of CO_2 are stabilized by long-range forces and oblige the polymer chains nearby to re-arrange themselves accordingly.

As first approximation, we can assume that the length of these rods correspond to the characteristic length of CO_2 in the critical region, this length can be calculated from an equation of state able to describe well the critical region:

$$\xi_{CO_2} \approx \left(\frac{\sigma_{CO_2}}{1.5} \right) \sqrt{\frac{\rho_{CO_2} RT}{M_{CO_2}} \kappa_T} \tag{7.18}$$

The number of carbon dioxide molecules per rod will be simply given by:

$$\aleph = \frac{\ell_{rod}}{\ell_{CO_2}} = \left(\frac{\xi_{CO_2}}{\sigma_{CO_2}} \right)$$

The length of each rod in terms of lattice sites occupied is then given by:

$$r_{rod} = \aleph r_{CO_2} = \left(\frac{\xi_{CO_2}}{\sigma_{CO_2}} \right) r_{CO_2}$$

Finally the number of rods is given by the excess divided by the mass of a single rod:

$$N_{rod} = \frac{N_{CO_2}^{ex}}{\aleph} = \frac{A\Gamma_{\lambda}^{ex}}{m_{rod}} = \frac{A\Gamma_{\lambda}^{ex}}{m_{CO_2}} \left(\frac{\sigma_{CO_2}}{\xi_{CO_2}} \right) = N_A \frac{A\Gamma_{\lambda}^{ex}}{M_{CO_2}} \left(\frac{\sigma_{CO_2}}{\xi_{CO_2}} \right) \tag{7.19}$$

$$r_{rod} N_{rod} = N_A \frac{A\Gamma_{\lambda}^{ex}}{M_{CO_2}} r_{CO_2} = r_{CO_2} N_{CO_2}^{ex}$$

Given these definitions clearly results in:

$$\phi_{rod} = \frac{r_{rod} N_{rod}}{r_{rod} N_{rod} + r_{PMMA} N_{PMMA}^{\lambda}} = \phi_{CO_2}^{ex}$$

As for the polymer chains in the lambda layer we have:

$$N_{PMMA}^{\lambda} = N_A\left(\frac{m_{PMMA}^{\lambda}}{M_{PMMA}}\right) = N_A\left(\frac{m_{PMMA}^{\lambda_0}}{M_{PMMA}}\right) = N_A\left(\frac{\rho_p^0 A\lambda_0}{M_{PMMA}}\right)$$

$$\phi_{rod} = \phi_{CO_2}^{ex} = \frac{N_A\frac{A\Gamma_\lambda^{ex}}{M_{CO_2}}r_{CO_2}}{N_A\frac{A\Gamma_\lambda^{ex}}{M_{CO_2}}r_{CO_2} + r_{PMMA}N_A\left(\frac{\rho_p^0 A\lambda_0}{M_{PMMA}}\right)} = \frac{\Gamma_\lambda^{ex}r_{CO_2}}{\Gamma_\lambda^{ex}r_{CO_2} + \rho_p^0\lambda_0 r_{PMMA}\left(\frac{M_{CO_2}}{M_{PMMA}}\right)}$$

$$\frac{1}{r} = \frac{\phi_{rod}}{r_{rod}} + \frac{1-\phi_{rod}}{r_{PMMA}}$$

Evaluating the density, and thus λ, allows getting an estimate of q through the comparison with the empirical finding:

$$\Delta\lambda = qR_g$$

Qualitatively it is easy to understand that the volume of the mixture is expected to go through a maximum with pressure. However, these calculations will not be carried out here and are left as legacy for future theoretical developments.

§ 7.4 Results and Discussion

In this section, we introduce our experimental findings about the effects of temperature, initial thickness, and material substrate on the anomalous swelling

behavior along with a possible interpretation of the data and the physics behind the phenomenon.

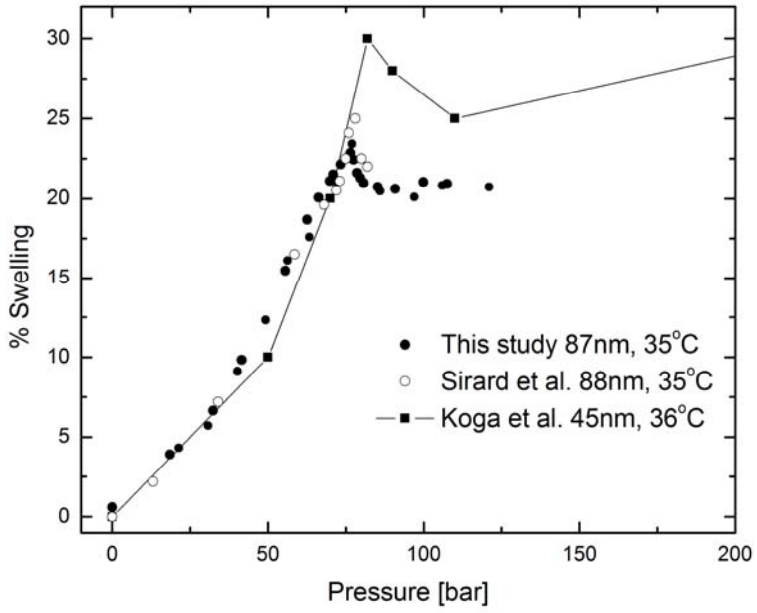

Figure 7.6 Validation of the swelling measurements: data at 35°C from this study, data from ref. [15], data at 36°C, initial thickness 45nm from ref.[16]

Fig. 7.6 shows three sets of one-dimensional dilation data for thin PMMA films coated onto silicon wafers plotted as swelling percentage vs. pressure, two sets are at 35°C while the third is at 36°C. Full circles represent isothermal measurements taken in this study using HPE for an 88nm film superimposed to literature values from the literature[15], where an 87nm film was studied under the same conditions with a similar apparatus. Data shown as full squares are from the literature[16], where a much thinner film (45 nm) was examined using Neutron Reflectivity. The good agreement between our data and the literature[15] can be used to validate our experimental setup and to confirm the existence of the anomalous behavior, while the discrepancy between these

two sets and the third could be ascribed to the different technique and initial thickness pointing to the importance of the film dimensions.

After having established good consistency with previous published data, three different variables will be discussed in details, namely temperature, substrate materials and initial film thickness. Experiments in which one of these variables was explored while keeping the other two constants have been carried out aiming at finding out the relevance of each one of them and at providing physically sound arguments for discussing our basic hypothesis concerning the importance of surface effects in explaining this complex phenomenon.

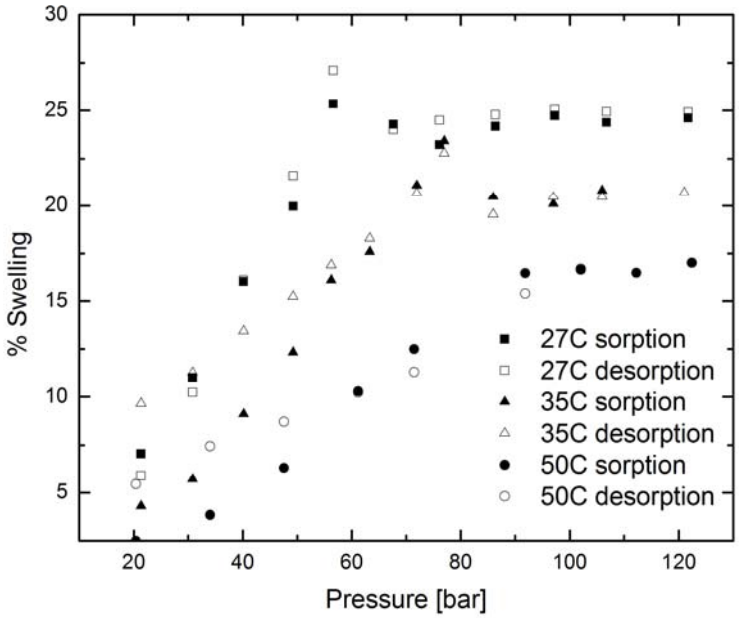

Figure 7.7 Temperature effect. Same thickness (88nm), same substrate (silicon), three temperatures: 27°C, 35°C and 50°C. The higher the temperature the smaller and broader the maximum

In Fig. 7.7, dilation isotherms are presented for an 88nm film spun onto silicon at three different temperatures: 27°C (sub critical), 35°C (near critical), and 50°C

(supercritical). Full symbols represent sorption runs whereas open symbols are the corresponding desorption runs. From this plot results that the operating temperature has a disrupting effect on the anomalous maximum, which becomes smaller and broader shifting at higher pressures for higher temperatures. Interestingly enough, these pressures can be located using the vapor-liquid pressure line at 27°C and the so-called "Ridge of density fluctuations" in the supercritical regions, as pointed out in the literature[16]. The same pattern can be found for carbon dioxide excess adsorption onto bare silicon shown previously in Fig. 7.3 and strongly points to a dramatic reduction of the stabilizing power of the substrate, typical of adsorption phenomena. Indeed, the higher the temperature the higher the system internal energy which competing with the stabilizing effect of the substrate leads to reduction of the amount of adsorbed carbon dioxide.

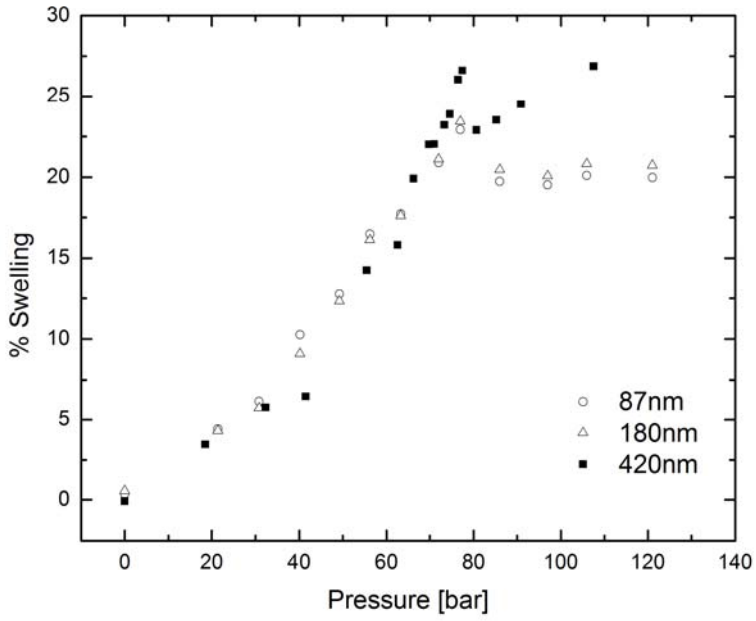

Figure 7.8 Thickness effect. Same temperature (35°C), same substrate (silicon), three initial thicknesses: 88nm, 180nm and 420nm. The higher the initial thickness the higher the deviation from bulk behavior

Initial thickness effects yield the most unclear results as shown in Fig. 7.8, where three different isotherms are displayed at 35^{o}C on silicon for three different thicknesses: 88nm, 180nm and 420nm respectively. What should strike most the attention of the reader is the size of the anomaly which apparently increases when passing from 88nm to 420nm. This trend, aside for being completely unintuitive, goes also against the experimental finding of Koga et al., who reported a detailed analysis of the incidence of initial thickness for polybutadine and polystyrene showing that the higher the initial thickness the smaller the extent of the maximum.

However it must be noticed that their experimental apparatus did not allow them to study films thicker than 100nm, restricting the validity of their results below that threshold value. On the other hand, Sirard et al. studied only two different thicknesses, 87nm and 321nm and their results seem to confirm our finding.

Fig.7.9 depicts a schematic representation of the aforementioned complex situation. Maximum swelling percentage data are plotted vs. initial thickness for PMMA films onto silicon at 35^{o}C. All points but two (circled) are from this study. The point at 45nm is from the literature[16] and it has been discussed already in Fig.7.7, while the point at 321nm is form the literature[15] and seems to fit well with the other points in the trend in the thin region, as mentioned earlier. Three regimes can then be extracted: ULTRATHIN behavior for thicknesses below about 100nm, where the higher the initial thickness the smaller the extent of the maximum. Below this threshold confinement effects as well as reduction in the configurational entropy are known to affect the glass transition temperature behavior with film thickness. Above 100nm these effects related to the size of the sample should be over but surface

effects, especially across the critical pressure where ordering could take place, related to the presence of the substrate/polymer and polymer/ambient interfaces could still be non-negligible. This could explain why the opposite trend with initial thickness is found in this region labeled THIN in Fig. 7.9. Somewhere above 1μm both size and surface effects are negligible and classic bulk behavior is recovered, where the swelling percentage does not change with the film thickness.

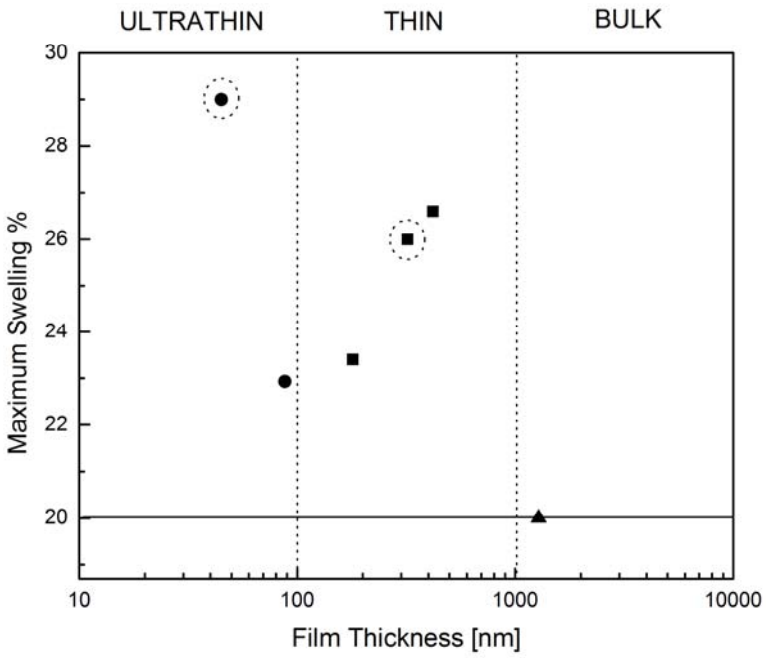

Figure 7.9 Three possible different regimes, PMMA-CO_2 at 35°C on silicon: ULTRATHIN below 100nm, THIN between 100 and 1000nm, and BULK above 1000nm. Circled points are from refs.[15] and [16]

In Fig. 7.10 for the sake of completeness sorption isotherms at 35°C and 50°C are reported for 88nm and 1.2μm films[20] coated on silicon. This plot clearly illustrates how the maximum goes away for thicknesses above 1μm as stated before and reported in the literature, but it also shows how the anomalous behavior is not restricted only to the region across the critical pressure. The trend at high pressures is

in fact rather different and in particular the classic cross-over which occurs for bulk films at high pressures is not present in the case of the thin film.

Finally, the effect of three different substrates is elucidated in Fig. 7.11 where a 87nm film at 35^{o}C has been spun onto SiOx, GaAs, and TiN. Clearly the size of the maximum is strongly affected by the different materials and the film coated on TiN shows the highest deviation from bulk value as could be expected by assuming that the anomaly is related to carbon dioxide adsorption at the buried substrate and by comparing the Hamaker coefficients, which give the extent of van der Waals forces, for the three different substrates.

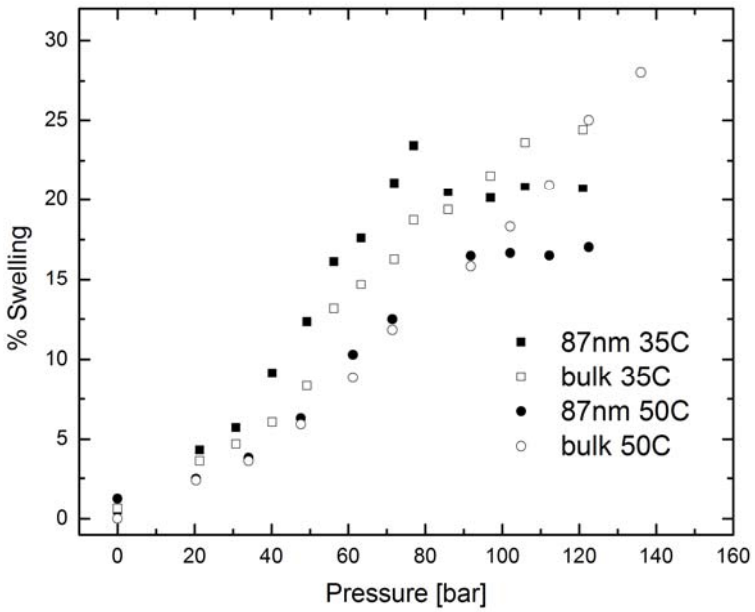

Figure 7.10 Thin (88nm) vs. Bulk (1280nm), 35^{o}C and 50^{o}C on silicon. As evident from the data at 50^{o}C the anomalous behavior does not consist only in the maximum but also in the slope right after it. Bulk data are re-plotted from ref. [20]

The above is the strongest evidence we found pointing at the need for a different interpretation of the anomaly from those proposed so far in the literature. If the

anomalous behavior were due to mixture isothermal compressibility or density fluctuations in the supercritical fluid the isotherms in Fig. 7.11 would have matched each other. On the other hand, Γ^{ex}, a key quantity in our treatment, being strongly related to the solvent-substrate interaction allows explaining such behavior.

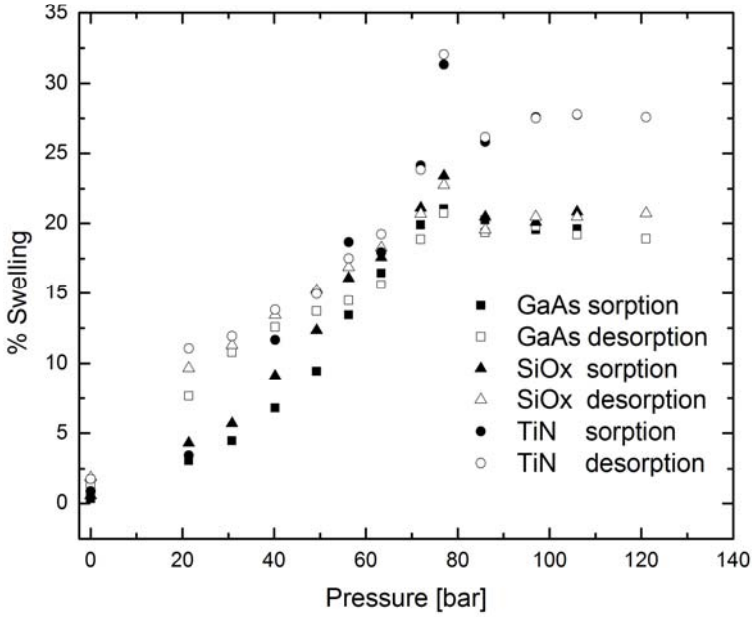

Figure 7.11 Substrate interaction effect. Same temperature (35°C), same thickness (88nm), three different substrates: silicon, GaAs, TiN. Silicon is the only one having a stable oxide layer

Using HPE and the five-layer model in Fig. 7.1-d all the data have been re-analyzed looking for a way of measuring directly the extra-swelling as depicted in Fig. 7.5 and described in sec. 7.3. The results obtained however did not provide much insights being affected by large statistical errors and showing a fitting always worse than the four-layer model used before, indicating that HPE was not able to detect the smooth surface between layers **A** and **B** at least with our setup.

A different approach based on the use of QCM was then pursued, testing the idea described in details in section 7.3.2 and expressed by Eq. (7.12). By making four films with four different initial mass loadings (and thicknesses ranging from 160nm to 440nm) and by processing them at thirteen different pressures (from 0psi to 1800psi) we were able to test the linear behavior of Eq.(7.12) and extract a non-zero intercept for each pressure as shown in Fig. 7.12. The fact that Γ^{ex} is non-zero is the main finding of the present work. It indicates beyond doubt that carbon dioxide indeed accumulates at the buried surface between the polymeric chains and the substrate. The slopes of the straight lines have been successfully compared with bulk solubilities obtained from the literature[20] (not shown here).

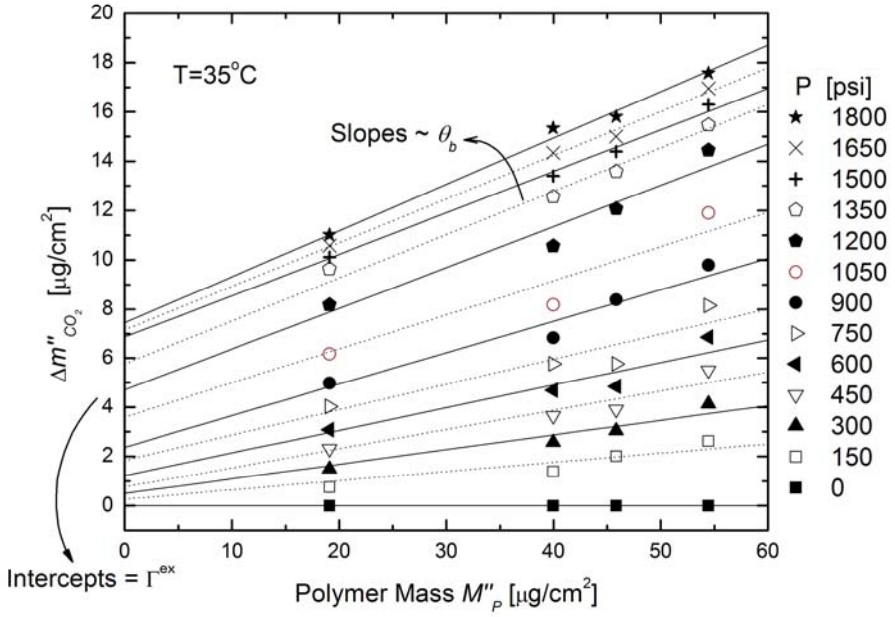

Figure 7.12 QCM Linear Regression, at 35°C on silicon. Four different initial loadings of PMMA have been processed at various pressures (from 0psi to 1800psi at steps of 150psi each). The linear behavior with non-zero intercept reflects the presence of a concentration gradient within the sample as stated in the text. The slopes of the straight lines compare favorably with bulk solubilities retrieved from ref. [20]

Even more interestingly, these extracted values are in very good agreement with carbon dioxide loadings on bare silicon (Fig. 7.5) as shown in Fig. 7.13. This indicates that during a sorption process carbon dioxide is adsorbed within the polymer sample (bulk solubility) and at the buried substrate as if there was no polymer at all. For samples above a certain thickness or mass (in the bulk region) the contribution coming from the Gibbs Excess Adsorption at the buried substrate is completely negligible while for the films discussed in the present study it represents an important percentage of the whole amount of carbon dioxide measured. This finding is currently under study with other substrates for confirmation.

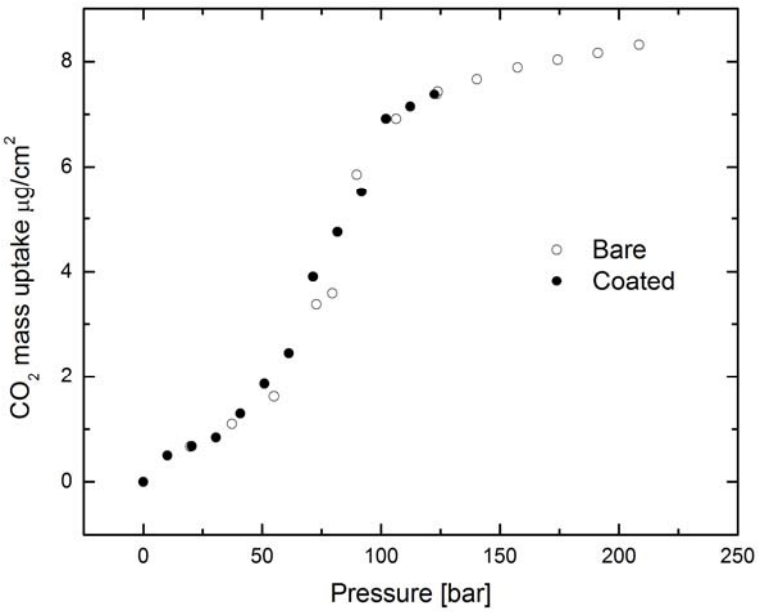

Figure 7.13 QCM, 35°C, silicon. Comparison of bare data with linear regression intercepts

In conclusion, the results embedded in Eq.(7.16) have been tested at constant pressure and temperature as shown in Fig. 7.14 where data for three polymers (PMMA, PB and PS) from the literature[16-18] and this study (circled) have been re-

plotted according to the simple linear behavior obtained from the TLC idea as discussed in section 7.3.4. The straight line seems to represent fairly well data taken for these three very different polymers indicating that the anomaly is actually coming from the excess swelling of the chains nearby the substrate that are in contact with more CO_2 than the rest of the sample.

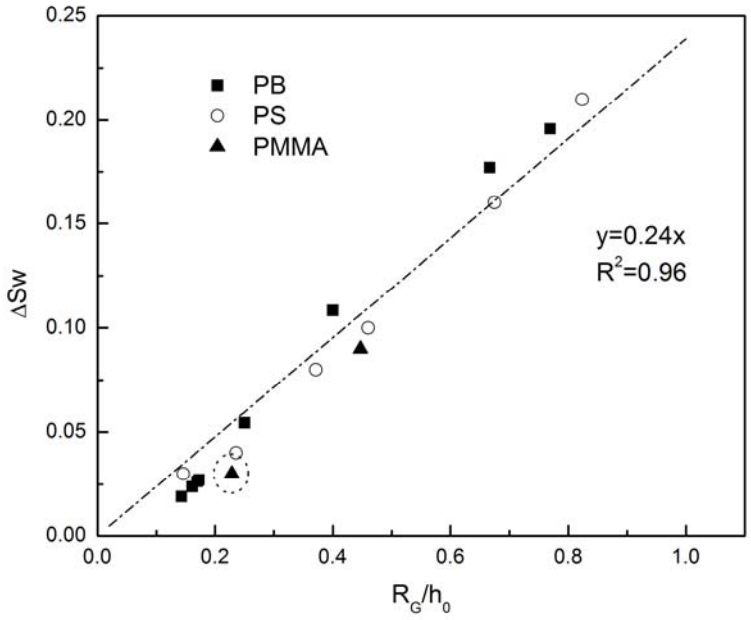

Figure 7.14 Validation of eq.(16), ΔSw vs. Rg/h_0, 35°C,on silicon wafer, three different polymers (PS, PB and PMMA). Circled point from this study, the others are from ref. [16]-[18] as discussed in the text

However since only one point comes form this study, this result could be a fortuitous case and a more extensive investigation is needed to confirm this important finding, which points to general effect regardless of polymer specific properties.

§ 7.5 Conclusions

The role of surfaces in the anomalous swelling behavior of thin polymeric films brought in contact with supercritical carbon dioxide has been investigated through the use of High-Pressure Ellipsometry technique applied to the PMMA-CO_2 system. The importance of substrate-CO_2 interactions in explaining the complex phenomenon has been found by using three very different substrates: GaAs, SiOx, and TiN as shown in the manuscript. None of the existing theories could explain such a behavior.

The author believes that the same principles responsible for the wetting of bare substrates by carbon dioxide could be invoked as explanation for such phenomena even for buried surfaces.

Stated differently, an accumulation of carbon dioxide, known as Gibbs Excess Adsorption, normally present in the case of hard surfaces has been detected using a series of cunning tests with QCM even when a polymeric film was coated on top of the hard surface.

This accumulation confronted with measurements taken on the bare substrate has yielded an outstanding match for the temperature (35^oC) and the substrate (silicon) studied. More experimental efforts are needed to seal these evidence.

A simple two-layer correlation model has been developed to try and understand how the anomalous swelling behavior could be related to this new discovered phenomenon. As a result a straight line is predicted for the extra-swelling versus the ratio of the polymer radius of gyration to the initial film thickness. The correlation has been verified using data from the literature for many different polymers with different molecular weights.

§ 7.6 References

(1) McHugh, M. A.; Krukonis, V. J. *Supercritical fluid extraction: principles and practice*, 2nd ed.; Butterworth-Heinemann: Stoneham, U.K. 1993

(2) McCoy, M. *Chem. Eng. News* **1999**, *77* (24), 11-13.

(3) DeSimone, J. M. *Science* **2002**, *297* (5582), 799-803

(4) Novick, B. J.; Carbonell, R. G.; DeSimone, J. M. *Pol. Mat. Sci. Eng.* **2001**, *84*, 51

(5) Kompella, U. B.; Koushik, K. *Crit. Rev. Ther. Drug Carrier Syst.* **2001**, *18*, 173-199.

(6) Zweber, A. E.; Carbonell, R. G. in Press

(7) DeYoung, J.; Wagner, M.; Harbinson, C.; Miles, M.; Zweber, A. E.; Carbonell, R. G. in Press

(8) Ober, C. K.; Weibel G. L. *Macroelectronic Engineering* **2003**, *65*, 145-152

(9) Reiter, G. *Europhys. Lett.* **1993,** *23***,** 579

(10) Krausch, G. *J. Phys: Conden. Matt.* **1997**, *9*, 7741-7752.

(11) Keddie, J. L.; Jones, R. A. L.; Cory, R. A. *Farady Discuss.* **1994**, *98*, 219-230.

(12) Keddie, J. L.; Jones, R. A. L.; Cory, R. A. *Europhys. Lett.* **1994**, *27*, 59-67.

(13) Grohens, Y.; Hamon, L.; Spevacek, J.; Holl, Y. *Macromol. Symp.* **2003**, *203*, 155-164.

(14) Grohens, Y.; Brogly, M.; Labbe, C.; David, M.-O.; Schultz, J. *Langmuir. Lett.* **1998**, *14* (11).

(15) Sirard, S. M.; Ziegler, K. J.; Sanchez, I. C. ; Green, P. F. ; Johnston, K. P. *Macromolecules* **2002**, *35*, 1928-1935.

(16) Koga, T.; Seo, Y.-S.; Shin, K.; Zhang, Y.; Rafailovich, M. H.; Sokolov, J. C.; Chu, B.; Satija, S. K. *Macromolecules* **2003**, *36*, 5236-5247.

(17) Koga, T.; Seo, Y.-S.; Zhang, Y.; Shin, K.; Kusano, K.; Nishikawa, K.; Rafailovich, M. H.; Sokolov, J. C.; Chu, B.; Peiffer, D.; Occhiogrosso, R.; Satija, S. K. *Phys. Rev. Lett.* **2002**, *89*.

(18) Koga, T.; Akashige, E.; Bronner, M.; Seo, Y.-S.; Shin, K.; Zhang, Y.; Rafailovich, M. H.; Sokolov, J. C.; Chu, B.; Satija, S. K. *Physica B* **2005**, *357*, 73-79.

(19) Sanchez, I. C.; Stone, M. T. In *Polymer Blends;* Paul, D. R.; Bucknall, C. B., Eds.; John Wiley & Sons: New York, 2000; Vol. 1

(20) Carla, V.; Wang, K.; Hussain, Y.; Efimenko, K.; Genzer, J.; Grant, C.; Sarti, G. C.; Carbonell, R.G.; Doghieri, F. *Macromolecules*, **2005**, *38* (24), 10299-10313.

(21) Findenegg, G. H. In *Fundamentals of Adsorption*; Myers, A. L.; Belfort, G., Eds.; Engineering Foundation: New York, 1984.

(22) Strubinger, J. R.; Parcher, J. F. *Anal. Chem.* **1989**, *61*, 951-955.

(23) Strubinger, J. R.; Song, H.; Parcher, J. F. *Anal. Chem.* **1991**, *63*, 98-103

(24) Nakamura, K.; Hoshino, T.; Ariyama, H. *Agric. Biol. Chem.* **1993**, *55*, 2341-2347.

(25) da Rocha, S. R. P.; Harrison, K. L.; Johnston, K. P. *Langmuir* **1999**, *15*,419-428.

(26) Subramanian, R.; Pyada, H.; Lira, C. T. *Ind. Eng. Chem. Res.* **1995**, *34*, 3830-3837.

(27) Tan, Z.; Gubbins, K. E. *J. Phys. Chem.* **1990**,*94*,6061-6069.

(28) Wu, Y.-T.; Akoto-Ampaw, P.-J.; Elbaccouch, M.; Hurrey, M. L.; Wallen, S. L.; Grant, C. S. *Langmuir*, **2004**, *20*, 3665-3673.

(29) DiGiovanni, O.; Dorfler, W.; Mazzotti, M.; Morbidelli, M. *Langmuir* **2001**, *17*, 4316-4321.

(30) Sirard, S. M.; Green, P. F. ; Johnston, K. P. *J. Phys. Chem. B* **2001**, *105*, 766.

(31) de Gennes, P. G. *Rep. Prog. Phys.* **1969**, *32*, 187-205.

(32) Israelachvili, J. *Intermolecular and surfaces forces* Academic Press, London, 1992.

(33) Vogt, B. D.; Soles, C. L.; Jones, R. L.; Wang, C.-Y.; Lin, E. K.; Wu, W-L.; Satija, S. K. *Langmuir*, **2004**, *20*, 5285-5290.

(34) Meli, L.; Pham, J. Q.; Johnston, K. P.; Green, P. F. *Phys. Rev.* E **2004**, *69*, 051601-8.

(35) deGennes P. G. *Scaling Concepts in Polymer Physics* Cornell University Press: Ithaca, NY 1979.

(36) deGennes, P. G. *Adv. Coll. Int. Science* **1987**, *27*, 189-209.

PART III

Conclusion

"The end of one thing
is only the beginning of another"

Conclusions

This journey, both figuratively and literally, started and ended in the United States, with a question. It started on January 2004 in Raleigh, North Carolina, when Prof. Ruben G. Carbonell asked me if I thought we could indeed use CO_2 as only solvent for microelectronic applications and it ended in November 2006 in San Francisco, California, at the AIChE meeting when, during my final oral presentation of the results introduced here in Chapter VII, somebody from the audience asked me what I thought was the meaning of the results embedded in figure 7.14.

More often than not, in life things like to go in circle, and to both questions my answer has been the same. 'I can't really say right now... there's a lot of work to do!'.

Aside from the above anecdote, what can be concluded after all the pages presented in this manuscript is that although much has been accomplished so far, even more is yet to be done.

In chapter IV we have described an extension of the Non Equilibrium Thermodynamics of Glassy Polymer (NET-GP) model for swelling and sorption to the case of a high-pressure plasticizing penetrant. The theory of Chow has been used to estimate the penetrant concentration at the glass transition point, which can then be used to estimate the pressure at the glass transition point using the equilibrium equation of state for the rubber phase. By assuming there is a linear relation between the glassy polymer density and the pressure below the glass transition pressure, it is possible to estimate the dilatation or swelling coefficient for the polymer-penetrant

system. This facilitates the calculation of the sorption and swelling behavior by modeling the system using NET-GP below the glass transition pressure and the equilibrium equation of state above the glass transition pressure. The NET-GP approach can be used with any equilibrium equation of state that is capable of predicting the behavior of the system in the rubbery state. As a result, this is a very flexible approach that can be used for any equation of state regardless of its complexity. Use of the theory relies on knowledge of the initial density of the glassy polymer prior to solvent penetration. For cases in which the initial polymer density is not known or is not provided, a procedure is described that facilitates its estimation based on the magnitude of the swelling coefficient.

The new model was then applied to the interpretation of experimental data collected for sorption/desorption processes of CO_2 in PMMA films at different temperatures and for a wide range of CO_2 pressures. Swelling of PMMA was measured using high-pressure ellipsometry (HPE) and mass absorption was measured directly by use of a quartz crystal microbalance (QCM). The mass of absorbed CO_2 was also determined indirectly from the measured refractive index of the swollen film resulting from the ellipsometric analysis.

One of the major experimental findings of chapter IV was that the sorption and swelling behaviors of two samples of a polymer are the same as long as their densities are the same, even though their histories can be significantly different. To the best of our knowledge, this is the first experimental verification of the basic assumption of the NET-GP model, namely, that the glass polymer density can be used as order parameter to describe the non-equilibrium thermodynamic state of the system.

Through the use of non-equilibrium version of the Sanchez-Lacombe lattice fluid model with two binary interaction parameters (NET-GP SL-II model), gas solubility and volume dilation were correctly represented at all experimental conditions. The model was able to provide a remarkably good agreement with the swelling hysteresis observed experimentally upon sorption and desorption of the gas, except for pressures close to atmospheric in desorption runs, where there is an apparent breakdown in the assumption of linearity of density with pressure.

The model was also able to provide an accurate description of the glass transition pressure variation with temperature as well as the amount of gas absorption in the glassy polymer region. The work presented in chapter IV served as the basis for the development in the study of the dynamic and equilibrium properties of high-pressure gas-polymer systems presented in chapter VI.

In chapter V, we have shown that following Gibbs-DiMarzio criterion for glass transition temperature, it is possible to develop a whole family of expressions aimed at calculating the glass transition change with plasticizer content. The effect of static pressure in increasing T_g has also been explained in the light of Gibbs-DiMarzio analysis. As main result of the present effort it has been established a new revised equation that enhances the results obtained with Chow's theory by overcoming the issues present in the original formulation.

In chapter VI, the NET-GP model has been coupled with the free volume theory for the diffusive coefficients and a simple rheological equation for the relaxation phenomena. The obtained model has proven the applicability of our approach to

represent the kinetics of differential sorption/desorption experiments in glassy as well as rubbery polymeric systems.

The model performance in different operating conditions, namely different temperatures and pressures for both sorption and desorption, was satisfactory and it allowed for a description of both Fickian and two-stage type sorption behavior and for a transition from one to another in terms of temperature and solute pressure.

Several examples of the application of model results to the analysis of differential sorption/desorption experiments for CO_2 in PMMA were considered. In all cases good results were obtained, confirming the validity of the approach used in representing thermodynamic properties, in both equilibrium and non-equilibrium conditions.

Relaxation steps during sorption/desorption cycles were described in this context in terms of volume relaxation of polymer samples with two adjustable model parameters: the characteristic bulk viscosity and the weight for Voigt elements in the rheological model. Characteristic viscosity values obtained from analysis of sorption data are in the expected order of magnitude, while weight values confirm the rough estimation performed on volumetric properties of pure polymeric species.

On the other hand, the rheological model parameters retrieved from sorption steps are different than those obtained through analysis of corresponding desorption runs. The latter is not surprising as the nonlinear character of bulk rheology of glassy polymers is well documented and a comprehensive representation of details in their volume swelling cannot be obtained in the simple terms discussed here.

The main aim of chapter VI was to provide a meaningful combination of mass transport and volume relaxation models that may prove or disprove the validity of the basic idea used to represent relaxation phenomena induced by solute sorption in glassy polymers. One major advantage of this approach consists in its simplicity and capability of being extendable, in a straightforward manner, to multi-component systems and multi-dimensional transport problems.

Finally, in chapter VII, the role of surfaces in the anomalous swelling behavior of thin polymeric films, brought in contact with supercritical carbon dioxide, has been investigated through the use of High-Pressure Ellipsometry technique applied to the PMMA-CO_2 system. The importance of substrate-CO_2 interactions in explaining the complex phenomenon has been found by using three very different substrates: GaAs, SiOx, and TiN as shown in the manuscript. None of the existing theories could explain such a behavior.

An accumulation of carbon dioxide, known as Gibbs Excess Adsorption and normally present in the case of hard surfaces, has been detected using a series of cunning tests with QCM, even when a polymeric film was coated on top of the hard surface.

This accumulation, compared with measurements taken on the bare substrate, has yielded an outstanding match for the temperature (35^oC) and the substrate (silicon) studied. More experimental efforts are needed to seal these evidence.

A simple two-layer correlation model has been developed to try and understand how the anomalous swelling behavior could be related to this new discovered phenomenon. As a result, a straight line is predicted for the extra-swelling versus the

ratio of the polymer radius of gyration to the initial film thickness. The correlation has been verified using data from the literature for many different polymers with different molecular weights.

Due to the outstanding findings about the physics of thin films in supercritical carbon dioxide, this work took a little detour from its initial purpose of developing a fundamental understanding of the process of microphotolithography. While we believe that to be a good sign of healthy research, this thesis should not be a cathedral in the desert.

An important legacy has been given and future developments would be highly desirable, in particular extensions to three-component systems and dissolution model for entangled network.

On the other hand, both the glass transition depression equations and the theory for thin films represent new starting point for developments. In particular, it is advised to pursue the road of free volume distribution recently opened by Isaac Sanchez, a real pioneer of thermodynamics, which could lead to unified expressions for glass transition, viscosity and diffusivity model developments.

As for the thin film studies, many are the potential applications ranging from inclusion of nanoparticles (which behave as substrate in short scales!) in polymeric matrices to thin film blends on a surface, and there is a strong need for further investigation, both experimental and theoretical.

I wish all the best to the ones who will take over these interesting topics and I hope that this thesis might be an important learning instrument as well as an

inspiring lecture. Finally I would like to thank the patient reader who has reached this point with relentless determination. I know that there have been many troublesome and unclear passages, but I sincerely hope that, as whole, this thesis has been a pleasant experience for you to read as it has been for me to write.

Vito Carla'

APPENDIX – NUMERICAL DISCRETIZATION

Once the set of differential equations governing the transport problem has been determined and appropriate initial and boundary conditions established, a numerical analysis must be performed aimed at transforming the equations into algebraic expressions that can be easily implemented in a computer language.

Among many possible choices of the discretization algorithm we have adopted the *finite volumes approach*, by Patankar (1980). As for the evolution equation for the polymer density, given its simple nature, a simple point-to-point integration is possible.

Grid and assumptions

An important point of the discretization method chosen is the construction of a suitable grid that should divide the sample thickness into small dominions into which all the properties can be assumed constant. The best approach is to build two distinct grids, one for delimiting the boundaries and the other to localize the centers of such small dominions.

Let us imagine the first grid to be made of $n+1$ points, which we name Q-points, this grid will be laid onto the film thickness having care that the first point is coincident with the interface between polymer and substrate. The second grid, of n points which we name P-points, will be laid in such a way that each P-point will be at the middle of each interval enclosed within two successive Q-points, so that the

last Q-point, Q_n is at a distance $\frac{\Delta\xi}{2}$ from the last P-point, P_n. Calling h the thickness of the polymeric film it is possible to evaluate the length of an interval between to successive Q-points (or P-points) as:

(A.1) $$\sum_{i=1}^{n-1}\Delta\xi+\frac{\Delta\xi}{2}=h\,,$$

so that

(A.2) $$\Delta\xi=\frac{2h}{2n-1}$$

In the application of Patankar algorithm the *fully implicit scheme* will be followed, which consists in assuming as average value of a given quantity in the time interval Δt the value that the same quantity has at the next instant, *i.e.* at the time $t+\Delta t$, when of course its value is unknown.

Set of equations

We start with the mass balance for the solvent species, Eq. (6.18), in the time interval $\left[t\ ,\ t+\Delta t\right]$ and on the *i-th* elemenar volume (with *i*=1,…,*n*-1), corresponding to $\left[\xi_{Q_i},\xi_{Q_{i+1}}\right]$ and having as middle point P_i:

(A.3) $$\int_t^{t+\Delta t}\int_{\xi_{Q_i}}^{\xi_{Q_{i+1}}}\frac{\partial}{\partial t}\left(\rho_s\lambda\right)d\xi\cdot dt=-\int_t^{t+\Delta t}\int_{\xi_{Q_i}}^{\xi_{Q_{i+1}}}\frac{\partial}{\partial \xi}\left(j_{s\xi}^{p}\right)d\xi\cdot dt\,,$$

Since in the coordinate system *polymer-fixed* the thickness is not changing in time it is allowed to switch the integration in the right-hand side of Eq. (A.3). After integration the above yields:

(A.4) $$\int_{\xi_{Q_i}}^{\xi_{Q_{i+1}}}\left[\left(\rho_s\lambda\right)^{t+\Delta t}-\left(\rho_s\lambda\right)^{t}\right]d\xi=-\int_t^{t+\Delta t}\left[\left(j_{s\xi}^{p}\right)_{\xi_{Q_{i+1}}}-\left(j_{s\xi}^{p}\right)_{\xi_{Q_i}}\right]dt$$

Given the assumption previously discussed the value of $\left(\rho_s\lambda\right)$ in the interval $\left[\xi_{Q_i},\xi_{Q_{i+1}}\right]$ is assumed constant and equal to the value in the middle point P_i, $\left(\rho_s\lambda\right)_{\xi_{P_i}}$. On the other hand, the value at time $\left(t+\Delta t\right)$ is assumed for the quantity $\left(j_{s\xi}^{p}\right)$ in the interval $\left[t\,,\,t+\Delta t\right]$:

(A.5) $$\left[\left(\rho_s\lambda\right)_{\xi_{P_i}}^{t+\Delta t}-\left(\rho_s\lambda\right)_{\xi_{P_i}}^{t}\right]\Delta\xi=-\left[\left(j_{s\xi}^{p}\right)_{\xi_{Q_{i+1}}}^{t+\Delta t}-\left(j_{s\xi}^{p}\right)_{\xi_{Q_i}}^{t+\Delta t}\right]\Delta t$$

We can write (*n*-1) equations of this kind, as many as the number of Q-volumes, thus one for each P-point but the last one, P_n, for which the phase equilibrium condition must be used in order to calculate the solvent density.

In a similar fashion, we apply this procedure to Eq.(6.27), which we integrate in the time interval $\left[t\ ,\ t+\Delta t\right]$ on the generic *i-th* volume element on the P-grid corresponding to the interval $\left\lfloor \xi_{P_{i-1}}, \xi_{P_i} \right\rfloor$, with *i=2…n*:

$$\text{(A.6)} \qquad \int_t^{t+\Delta t}\int_{\xi_{P_{i-1}}}^{\xi_{P_i}} j_{s\xi}^{p} d\xi \cdot dt = -\int_t^{t+\Delta t}\int_{\xi_{P_{i-1}}}^{\xi_{P_i}} \left(L_{ss}\frac{\partial \rho_s}{\partial \xi} + L_{sp}\frac{\partial \rho_p}{\partial \xi} \right) d\xi \cdot dt$$

Switching the integration as before, assuming the *fully implicit scheme for* $\left(j_{s\xi}^{p}\right)$ and assuming that $\left(L_{ss}\right)_{\xi_{Q_i}}$ and $\left(L_{sp}\right)_{\xi_{Q_i}}$ in Q_i are representative of the whole interval $\left[\xi_{P_{i-1}}, \xi_{P_i}\right]$ in the whole time interval $\left[t\ ,\ t+\Delta t\right]$ we have:

$$\text{(A.7)} \int_{\xi_{P_{-1i}}}^{\xi_{P_i}} \left[j_{s\xi}^{p\ t+\Delta t}\Delta t \right] d\xi = \int_t^{t+\Delta t} \left[\left(L_{ss}\right)_{\xi_{Q_i}} \left(\rho_s\big|_{\xi_{P_i}} - \rho_s\big|_{\xi_{P_i-1}} \right) + \left(L_{sp}\right)_{\xi_{Q_i}} \left(\rho_p\big|_{\xi_{P_i}} - \rho_p\big|_{\xi_{P_i-1}} \right) \right] dt$$

Assuming now that $\left(j_{s\xi}^{p}\right)_{\xi_{Q_i}}$ is representative of the whole interval $\left[\xi_{P_{i-1}}, \xi_{P_i}\right]$ in the whole time interval $\left[t\ ,\ t+\Delta t\right]$ and applying the fully implit scheme for $\left(L_{ss}\right)_{\xi_{Q_i}}$ and $\left(L_{sp}\right)_{\xi_{Q_i}}$ as well as for ρ_s and ρ_p in the interval $\left[\xi_{P_{i-1}}, \xi_{P_i}\right]$ we obtain:

$$\text{(A.8)} \qquad \left(j_{s\xi}^{p}\right)_{\xi_{Q_i}}^{t+\Delta t} \Delta t \Delta \xi =$$

$$-\left[\left(L_{ss}\right)_{\xi_{Q_i}}^{t+\Delta t}\left(\rho_s\Big|_{\xi_{P_i}}^{t+\Delta t}-\rho_s\Big|_{\xi_{P_i-1}}^{t+\Delta t}\right)+\left(L_{sp}\right)_{\xi_{Q_i}}^{t+\Delta t}\left(\rho_p\Big|_{\xi_{P_i}}^{t+\Delta t}-\rho_p\Big|_{\xi_{P_i-1}}^{t+\Delta t}\right)\right]\Delta t$$

By combining (A.5) and (A.8):

(A.9) $$\left[\left(\rho_s\lambda\right)_{\xi_{P_i}}^{t+\Delta t}-\left(\rho_s\lambda\right)_{\xi_{P_i}}^{t}\right]=$$

$$\frac{\Delta t}{\Delta\xi^2}\left\{\left[\left(L_{ss}\right)_{\xi_{Q_{i+1}}}^{t+\Delta t}\left(\rho_s\Big|_{\xi_{P_{i+1}}}^{t+\Delta t}-\rho_s\Big|_{\xi_{P_i}}^{t+\Delta t}\right)+\left(L_{sp}\right)_{\xi_{Q_{i+1}}}^{t+\Delta t}\left(\rho_p\Big|_{\xi_{P_{i+1}}}^{t+\Delta t}-\rho_p\Big|_{\xi_{P_i}}^{t+\Delta t}\right)\right]+\right.$$

$$\left.-\left[\left(L_{ss}\right)_{\xi_{Q_i}}^{t+\Delta t}\left(\rho_s\Big|_{\xi_{P_i}}^{t+\Delta t}-\rho_s\Big|_{\xi_{P_{i-1}}}^{t+\Delta t}\right)+\left(L_{sp}\right)_{\xi_{Q_i}}^{t+\Delta t}\left(\rho_p\Big|_{\xi_{P_i}}^{t+\Delta t}-\rho_p\Big|_{\xi_{P_{i-1}}}^{t+\Delta t}\right)\right]\right\}$$

This can be conveniently written as:

(A.10) $$\left(\rho_s\lambda\right)_{\xi_{P_i}}^{t+\Delta t}+\gamma_i=\left[\alpha_{i+1}\left(\rho_s\Big|_{\xi_{P_{i+1}}}^{t+\Delta t}-\rho_s\Big|_{\xi_{P_i}}^{t+\Delta t}\right)+\beta_{i+1}-\alpha_i\left(\rho_s\Big|_{\xi_{P_i}}^{t+\Delta t}-\rho_s\Big|_{\xi_{P_{i-1}}}^{t+\Delta t}\right)-\beta_i\right]$$

Where:

(A.11)
$$\begin{cases} \alpha_i = \left(\dfrac{\Delta t}{\Delta \xi^2} \right) L_{ss} \Big|_{\xi_{Q_i}}^{t+\Delta t} \\ \beta_i = \left(\dfrac{\Delta t}{\Delta \xi^2} \right) L_{sp} \Big|_{\xi_{Q_i}}^{t+\Delta t} \left(\rho_p \Big|_{\xi_{P_i}}^{t+\Delta t} - \rho_p \Big|_{\xi_{P_{i-1}}}^{t+\Delta t} \right) \\ \gamma_i = -\left(\rho_s \lambda \right)_{\xi_{P_i}}^{t} \end{cases}$$

Eq.(A.10) can be re-arranged then in the final form:

(A.12)
$$\boxed{a_i \, \rho_s \Big|_{\xi_{P_{i-1}}}^{t+\Delta t} + b_i \, \rho_s \Big|_{\xi_{P_i}}^{t+\Delta t} + c_i \, \rho_s \Big|_{\xi_{P_{i+1}}}^{t+\Delta t} = d_i} \qquad \forall \quad i = 1, \ldots, n-1$$

Having defined:

(A.13)
$$\begin{cases} a_i = \alpha_i \\ b_i = -\lambda_{\xi_{P_i}}^{t+\Delta t} - \alpha_{i+1} - \alpha_i \\ c_i = \alpha_{i+1} \\ d_i = \beta_i - \beta_{i+1} + \gamma_i \end{cases}$$

The set of (n – 1) equations like (A.12) forms a tridiagonal matrix that can be solved with the usual methods for matrices.

Evolution equation for the order parameter

Integrating the equation for the specific volume of Voigt element *A* between $[t\ ,\ t+\Delta t]$ assuming the *fully implicit scheme*:

(A.14) $$\ln\left(\frac{\hat{V}_p^A\Big|^{t+\Delta t}}{\hat{V}_p^A\Big|^{t}}\right)=\frac{P^{eq}\Big|^{t+\Delta t}-P}{\eta_A}\Delta t$$

(A.15) $$\hat{V}_p^A\Big|^{t+\Delta t}=\hat{V}_p^A\Big|^{t}\cdot e^{\left\{\left(P^{eq}\Big|^{t+\Delta t}-P\right)\Delta t\,/\,\eta_A\right\}}$$

The equation is implicit since P^{eq} is a function of $\hat{V}_p^A\Big|^{t+\Delta t}$ and an iterative procedure (guess → error) must be implemented in order to solve it.

Bibliography

Alessi, P., Cortesi, A., Kikic, I., Foster, N.R., Macnaughton, S.J., and Colombo, I. *Ind. Eng. Chem. Res.* **1996**, *35*, 4718-4726.

Allen, R. D.; Wallraff, G. M.; Hinsberg, W. D.; Conley, W. E.; Kunz, R. R. *J. Photopolymer Sci. Tech.* **1993**, *6*, 575.

Allen, R. D.; Wallraff, G. M.; Hofer, D. C.; Kunz, R. R. *IBM J. Res. Dev.***1997**, *41*, 95.

Astarita, G.; Paulatis, M. E.; Wissinger, R. G. *J. Polym. Sci., Part B: Polym. Phys.* **1989**, *27*, 2105.

Auge, J.; Hauptmann, P.; Eichelbaum, F. and Roesler S. *Sensors and Actuators, B: Chemical* **1994**, *19*, 518–522.

Azzam, R. M. A.; Bashara, N. M. *Ellipsometry and Polarized Light*; North-Holland Publishing Co.: Elshevier, 1977.

Bae, Y. C. *Polymer* **1996**, *37*, 3011-3017.

Bae, Y. C.; Gulari, E. *Journal of Applied Polymer Science* **1997**, *63*, 459-466.

Balsara, N. P. in *Physical Properties of Polymers Handbook*, J. E. Mark Eds; AIP Press: New York, 1996.

Banda, L.; Alcoutlabi, M. and McKenna, G. B. *Journal of Polymer Science Part B: Polymer Physics* **2006**, *44*, 801–814.

Barbari, T. A.; Conforti, R. M. *Polym. Adv. Technol.* **1994**, *5*, 698.

Bates, F. S. *Science* **1991**, *251*, 898-905.

Beckman, E.; Porter, R. S. *Journal of Polymer Science: Part B: Polymer Physics* **1987**, *27*, 1511-1517.

Behling, C.; Lucklum, R. and Hauptmann, P. *Sensors and Actuators A: Physical* **1997**, *61*, 260–266.

Benes E. *Journal of Applied Physics* **1984**, *56*, 608–626.

Berens, A. R., *Transport of Plasticizing Penetrants in Glassy-Polymers.* **1990**, *423*, 92-110

Berens, A. R. and Hopfenberg, H. B. *Polymer*, **1978**, *19(5)*, 489-96

Billmeyer, F. W. *Textbook of Polymer Science*, 3rd; John Wiley & Sons: New York, 1984.

Binder, K. *Adv. Polym. Sci.* **1994**, *138*, 1-89.

Bisschops, M. A. T.; Luyben, K. C. A. M. and van der Wielen, L.A.M. *Industrial & Engineering Chemistry Research*, **1998,** *37(8)*, 3312-3322

Bolton, B. A.; Kint, S.; Bailey, G. F.; Scherer, J. R. *J. Phys. Chem.* **1986**, *90*, 1207.

Brandup, J.; Immergut, E. H. and Grulke, E. A. eds. *Polymer handbook*. 4th ed. **1999**, Wiley: New York.

Briscoe, B. J.; Kelly, C. T. *Polymer* **1995**, *36*, 3099-3102.

Bruno, T. J.; Ely, J. F. *Supercritical Fluid Technology: Reviews in Modern Theory and Applications*, CRC Press: Boston, 1991.

Burke, A. L.; Givens, R. D.; Jikei, M.; DeSimone, J. M. *Polym. Prepr.* **1997**, *38*, 387.

Burns, S. D.; Gardiner, A.; Krukonis, V.; Wetmore, P.; Schmid, G. M.; Lutkenhaus, J.; Flanagin, L. W.; Willson, C. G. *Proc. SPIE* **2001**, *4345*,37-49.

Burns, S. D.; Stewart, M. D.; Hilfiker, J. N.; Synowicki, R. A.; Schmid, G.M.; Brodsky, C.; Willson, C. G. *Forefront of Lithographic Materials Research, Proc. of the 12th International Conference on Photopolymers* **2000**, 232-334.

Buttry, D. A. and Ward, M. D. *Chemical Reviews* **1992**, *92*, 1355–1379.

Campbell, S. A. *The Science and Engineering of Microelectronic Fabrication*; Oxford University Press: New York, 2001.

Canelas, D. A.; Betts, D. E.; DeSimone, J. M. *Macromolecules* **1996**, *29*, 2818-2821.

Canelas, D. A.; Betts, D. E.; DeSimone, J. M.; Yates, M. Z.; Johnston, K. P. *Macromolecules* **1998**, *31*, 6794.

Carbonell, R. G. and Sarti, G. C. *Industrial & Engineering Chemistry Research*, **1990**, *29(7)*, 1194-204

Carla, V., et al., *Macromolecules*, **2005**, *38(24)*, 10299-10313

Caruso, F.; Serizawa, T.; Furlong, D. N. and Okahata Y. *Langmuir* **1995**, *11*, 1546–1552.

Caruso, F.; Rodda, E.; Furlong, D. N.; Niikura, K. and Okahata Y. *Analytical Chemistry* **1997**, *69*, 2043–2049.

Charrier, J.-M. *Polymeric Materials and Processing: Plastics,Elastomers and Composites*, Hanser Publishers: New York, 1991.

Chiou, J. S.; Maeda, Y.; Paul, D. R. *J. of Applied Polymer Science* **1985**, *30*, 4019-4029.

Chiou, J. S.; Barlow, J. W.; Paul, D. R. *J. Appl. Polym. Sci.* **1985**, 30, 2633.

Chow, T. S. *Macromolecules* **1980**, *13*, 362.

Chow, T. S., *Polymer*, **1988**, *29(8)*, 1447-1451.

Combey, M. *Plasticisers, Stabilisers, and Fillers*, Iliffe Books Ltd: London, 1972.

Condo, P.D.; Paul, D.R.; Johnston, K.P. *Macromolecules*, **1994**, 27, 365-371

Condo, P. D.; Sanchez, I. C.; Panayiotou, C. G.; and Johnston, K. P. *Macromolecules* **1992**, *25*, 6119.

Cooper, A.I. *Mater. Chem.* **2000**, *10*, 207.

Crank, J., *The Mathematics of Diffusion*. 2nd ed. **1975**, London, England: Oxford University Press. 414.

Da Rocha, S. R. P.; Harrison, K. L.; Johnston, K. P. *Langmuir* **1999**, *15*,419-428.

Daikhin, L.; Gileadi, E.; Katz, G.; Tsionsky, V.; Urbakh, M.; and Zagidulin D. *Analytical Chemistry* **2002**, *74*, 554–561.

Daikhin, L. and M. Urbakh *Langmuir* **1996**, *12*, 6354–6360.

Dammel, R. *Diazonapthoquinone-based Resists*; SPIE Optical Engineering Press: Bellingham, Washington, 1993.

Daneshvar, M.; Gulari, E. *Supercritical Fluid Science and Technology;* Johnston K.P., Penninger, J. M.L.,Eds.; ACS Symposium Series 406; American Chemical Society: Washington, DC, 1989.

DeGennes, P. G. *Rep. Prog. Phys.* **1969**, *32*, 187-205.

DeGennes P. G. *Scaling Concepts in Polymer Physics* Cornell University Press: Ithaca, NY 1979.

DeGennes, P. G. *Adv. Coll. Int. Science* **1987**, *27*, 189-209.

Deshpande, M. M.; Jadhav, A. S.; Gunari, A. A.; Sehra, J. C.; Sivaram, S. *Journal of Polymer Science: Part A. Polymer Chemistry* **1995**, *33*, 701-705.

DeSimone, J. M., *Science*, **2002**, *297(5582)*, 799-803

DeSimone, J. M.; Guan, Z.; Eisbernd, C. S. *Science* **1992** , *257*, 945-947.

DeSimone, J. M.; Maury, E. E.; Menceloglu, Y. Z.; McClain, J. B.; Romack, T. J.; Combes, J. R. *Science* **1994**, *265*, 356-359.

DeYoung, J.; Wagner, M.; Harbinson, C.; Miles, M.; Zweber, A. E.; Carbonell, R. G. in Press

DiGiovanni, O.; Dorfler, W.; Mazzotti, M.; Morbidelli, M. *Langmuir* **2001**, *17*, 4316-4321.

Di Marzio, E. A. and Gibbs, J. H., *J. Polym. Sci., Part A-1*. **1963**, 1417.

Di Marzio, E. A. and Gibbs, J. H., *J. Chem. Phys.* **1958**, *28*, 373.

Di Marzio, E. A. and Gibbs, J. H., *J. Chem. Phys.* **1965**, *43*, 139.

Di Marzio, E. A.; Gibbs, J. H.; Fleming III, P. D., and Sanchez, I. C. *Macromolecules* **1976**, *9*, 763.

Dixon, D. J.; Johnston, K. P.; Bodmeier, M. A. *AIChE J.* **1993**, *39*, 127.

Doghieri, F.; Roda, G. C. and Sarti, G. C. *AIChE Journal*, **1993**, *39(11)*, 1847-1858.

Doghieri, F., Ghedini, M., Quinzi, M., Rethwisch, D.G., and Sarti, G.C., *in Advanced Materials for Membrane*, Ed., I. Pinnau and B.D. Freeman, ACS Symposium Series, v. 876, 55-73, 2004.

Doghieri. F; Ghedini, M.; Quinzi, M.; Rethwisch,D.; Sarti, G.C. *Desalination* **2002**, *144*,73

Doghieri, F.; Sarti, G. C. *J. Membr. Sci.* **1998**, *147*, 73.

Doghieri, F. and Sarti, G. C. *Macromolecules*, **1996**, *29(24)*, 7885-7896

Durning, C. J. and Tabor, M. *Macromolecules* 1986. **19**(8): p. 2220-2232

Ely, J. F.; Magee, J. W.; Haynes, W. M., *Gas Processors Association* **1987**.

Enscore, D. J., Hopfenberg, H. B. and Stannett, V. T. *Polymer Engineering and Science*, **1980**, *20(1)*, 102-7.

Findenegg, G. H. In *Fundamentals of Adsorption*; Myers, A. L.; Belfort, G., Eds.; Engineering Foundation: New York, 1984.

Fleming, G.K.; Koros, W.J. *Journal of Polymer Science: Part B: Polymer Physics*, **1987**, *25*, 2033.

Flores, P. A. PCT Int. Appl. (2004)

Frechet, J. M. J.; Eichler, E.; Ito, H.; Willson, C. G. *Polymer* **1983**, *24*,995-1000.

French, R. N. and Koplos, G. J. *Fluid Phase Equilibria* **1999**, *160*, 879–892.

Frisch, H. L. *Polymer Engineering & Science* **1980**, *20(1)*, 2-13.

Gabor, A. H.; Allen, R. D.; Gallacher-Wetmore, P.; Ober, C. K. *Proc. SPIE-Int. Soc. Opt. Eng.* **1996**, *410*, 2724.

Gallacher-Wetmore, P.; Ober, C. K.; Gabor, A. H.; Allen, R. D. *Proc. SPIE-Int. Soc. Opt. Eng.* **1996**, *289*, 2725.

Gerhardt, L. J.; Garg, A.; Bae, Y. C.; Manke, C. W.; Gulari, E. in *Theoretical and Applied Rheology*, P. Moldenaers, R. Keunings Eds; Elsevier Science Publishers: Brussels, Belgium, 1992, 348-350.

Giacinti Baschetti M.; Doghieri, F.; Sarti, G. C. *Ind. Eng. Chem. Res.* **2001**, *40*, 3027.

Goel, S. K.; Beckman, E. J. *Polymer* **1993**, *34*, 1410-1417.

Goken, H.; Esho, S.; Ohnishi, Y. *J. Electrochem. Soc.* **1983**, *130*, 143.

Granstaff, V. E. and Martin, S. J. *Journal of Applied Physics* **1994**, *75*, 1319–1329.

Grohens, Y.; Hamon, L.; Spevacek, J.; Holl, Y. *Macromol. Symp.* **2003**, *203*, 155-164.

Grohens, Y.; Brogly, M.; Labbe, C.; David, M.-O.; Schultz, J. *Langmuir. Lett.* **1998**, *14* (11).

Gross, S. M.; Givens, R. D.; Jikei, M.; Royer, J. R.; Khan, S. A.; DeSimone, J. M.; Odell, P. G.; Hamer, G. K. *Macromolecules* **1998**, *31*, 9090-9092.

Ha, T. H. and Kim, K. *Langmuir* **2001**, *17*, 1999–2007.

Hachisuka, H.; Sato, T.; Imai, T.; Tsujita, Y.; Takizawa, A.; Kinoshita, T. *Polym. J.* **1990**, *22*, 77.

Handa, Y. P.; Capowski, S.; O'Neill, M. *Thermochimica Acta* **1993**, 226, 177-185.

Handa, Y. P.; Lampron, S.; O'Neill, M. L. *Journal of Polymer Science: Part B:* **1994**, *32*, 2549-2553.

Handa, Y. P.; Kruus, P.; O'Neill, M. *Journal of Polymer Science: Part B: Polymer Physics* **1996**, *34*, 2635-2639.

Hachisuka, H.; Sato, T.; Imai, T.; Tsujita, Y.; Takizawa, A.; Kinoshita, T. *Polymer Journal* **1990**, *22*, 77-79.

Henon, F. E.; Camaiti, M.; Burke, A. L.; Carbonell, R. G.; DeSimone, J. M.; Piacenti, F. j*ournal of Supercritical Fluids* **1999**, *15*, 173-179.

Herzinger, C. M.; Johs, B.; McGahan, W. A.; Woollam, J. A.; Paulson, W. *J. Appl. Phys.* **1998**, *83*, 3323-3336.

Hinsberg, W. D.; Houle, F. A.; Poliskie, G. M.; Pearson, D.; Sanchez, M. I.; Ito, H. *Journal of Physical Chemistry A* **2002**, *106*, 9776-9787.

Hinsberg, W. D.; Houle, F. A.; Sanchez, M. I.; Wallraff, G. M. *Ibm Journal of Research and Development* **2001**, *45*, 667-682.

Houle, F. A.; Hinsberg, W. D.; Morrison, M.; Sanchez, M. I.; Wallraff, G. M.; Larson, C. E.; Hoffnagle, J. *J. Vac. Sci. & Tech. B* **2000**, *18*, 1874.

Houlihan, F. M. J.; TI, W.; Nalamasu, O.; Reichmanis, E. *Macromolecules* **1997**, *30*, 6517.

Howdle, S. M.; George, M. W.; Poliakoff, M. in *Chemical Synthesis Using Supercritical Fluids*; Jessop, P. G., Leiner, W. , Eds.; Wiley-Vch: Weinheim, 1999.

Hoy, K. L., Donhue, M. D. *Polym. Prepr.* **1990**, *31*, 679

Hussain, Y.; Krim, J. and Grant, C. S. *Colloids and Surfaces, A: Physicochemical and Engineering Aspects* **2005**, *262*, 81–86.

Israelachvili, J. *Intermolecular and surfaces forces* Academic Press, London, 1992.

Ito, H.; Willson, C. G. *Polym. Eng. Sci.* **1983**, *23*, 1012-1018.

Johannsmann, D. *Macromolecular Chemistry & Physics* **1999**, *200*, 501–516.

Johnston, K. P.; Penninger, J. M. L. *Supercritical Fluid Science and Technology*, American Chemical Society: Washington, D.C., 1989.

Johs, B., *Accurate Correction of Window Effects in Ellipsometric Data*. J. A. Woollam Co., Inc., 9/7/99.

Johs, B. *Methods for uncorrelated evaluation of parameters in parameterized mathematical equations for window retardance, in ellipsometer and polarimeter systems* US Patent #6,034,777.

Kaimoto, Y.; Nozaki, K.; Takechi, S.; Abe, N. *Proc. SPIE* **1992**, *1672*.

Kanazawa, K. K. *Analyst* **2005**, *130*, 1459–1464.

Kanazawa, K. K. and Hildebrand, C. *Proceedings - Electrochemical Society* **1997**, *19*, 212–217.

Kanazawa, K. K. and Gordon II, J. G.. *Proceedings - Electrochemical Society* **1993**, *93*, 725–731.

Kanazawa, K. K. and Gordon II, J. G. *Analytica Chimica Acta* **1985**, *175*, 99–105.

Kanazawa, K. K. and Melroy, O. R. *IBM Journal of Research and Development* **1993**, *37*, 157–171.

Kazarian, S. G. *Drugs and the Pharmaceutical Sciences* **2004**, *138*, 343.

Kazarian, S. G.; Vincent, M. F.; West, B. L.; Eckert, C. A. *J. Supercritical Fluids* **1998**, *13*, 107.

Keddie, J. L.; Jones, R. A. L.; Cory, R. A. *Europhys. Lett.* **1994**, *27*, 59-64.

Keddie, J. L.; Jones, R. A. L.; Cory, R. A. *Faraday Discuss* **1994**, *98*, 219-230.

Kikic, I., Vecchione, F., Alessi, P., Cortesi, A., Eva, F., and Elvassore, N. *Ind. Eng. Chem. Res.* **2003**, 42, *13*, 3022 - 3029.

Kiran, E.; Brennecke, J. F. *Supercritical Fluid Engineering Science*, American Chemical Society: Washington D.C., 1991.

Kiran, E.; Saraf,V. P.; Sen, Y.L. *Int. J. Thermophys.* **1989**, *10*, 437

Kirby, C. F.; McHugh, M. A. *Chem. Rev.* **1999**, *99*, 565.

Klavetter, E. A.; Martin, S. J. and Wessendorf, K. O. *Energy & Fuels* **1993**, *7*, 582–588.

Klenstremer, C., *Engineering Fluid Dynamics: An Interdisciplinary Systems Approach*. **1997**: Cambridge University Press.

Koga, T.; Seo, Y.-S.; Shin, K.; Zhang, Y.; Rafailovich, M. H.; Sokolov, J. C.; Chu, B.; Satija, S. K. *Macromolecules* **2003**, *36*, 5236-5247.

Koga, T.; Seo, Y.-S.; Zhang, Y.; Shin, K.; Kusano, K.; Nishikawa, K.; Rafailovich, M. H.; Sokolov, J. C.; Chu, B.; Peiffer, D.; Occhiogrosso, R.; Satija, S. K. *Phys. Rev. Lett.* **2002**, *89*.

Koga, T.; Akashige, E.; Bronner, M.; Seo, Y.-S.; Shin, K.; Zhang, Y.; Rafailovich, M. H.; Sokolov, J. C.; Chu, B.; Satija, S. K. *Physica B* **2005**, *357*, 73-79.

Kompella, U. B.; Koushik, K. *Crit. Rev. Ther. Drug Carrier Syst.* **2001**, *18*, 173-199.

Koros, W. J.; Paul, D. R. *Journal of Polymer Science: Part B Polymer Physics* **1978**, *16*, 1947-1963.

Krausch, G. *J. Phys: Conden. Matt.* **1997**, *9*, 7741-7752.

Kunz, R. R.; Allen, R. D.; Hinsberg, W. D.; Wallraff, G. M. *Proc. SPIE* **1993**, *1672*, 66.

Filiatre, C.; Bardeche, G. and Valentin, M. *Sensors and Actuators A: Physical* **1994**, *44*, 137–144.

Glocker, D. and Shah, S. I. *Handbook of Thin Film Process Technology*. Institute of Physics Publishing, Bristol, UK, 1995.

Lin, E. K.; Soles, C. L.; Goldfarb, D. L.; Trinque, B.; Burns, S. D.; Jones, R. L.; Lenhart, J. L.; Angelopoulos, M.; Willson, C. G.; Satija, S. K.; Wu, W.-l. *Science* **2002**, *297*, 372.

Lipson, S. G.; Lipson, H.; Tannhauser, D. S. *Optical physics*, 3rd ed.; Cambridge ; New York, NY, USA : Cambridge University Press: New York, 1998.

Liu, D.; Li, H.; Noon, M. S. and Tomasko, D. L. *Macromolecules* **2005**, *38*, 4416.

Lu, C. and Czanderna, A.W. *Applications of piezoelectric quartz crystal microbalances, volume 7 of Methods and phenomena, their applications in science and technology*. Elsevier, Amsterdam, 1984.

Lu, C.S. and Lewis, O. *Journal of Applied Physics* **1972**, *43*, 4385–4390.

Lucklum, R. and Hauptmann, P. *Sensors and Actuators, B: Chemical* **2000**, *70*, 30–36.

Lucklum, R. and Hauptmann, P. *Faraday Discussions* **1997**, *107*, 123–140.

McClain, J. B.; Betts, D. E.; Canelas, D. A.; Samulski, E. T.; DeSimone, J. M.; Londono, J. D.; Cochran, H. D.; Wignall, G. D.; Chillura-Martino, D.; Triolo, R. *Science* **1996**, *285*, 426-429.

McCoy, M. *Chem. Eng. News* **1999**, *77* (24), 11-13.

McHugh, M. A.; Krukonis, V. J. *Encyclopedia of Polymer Science and Technology;* Mark, H. F., Bikales, N. M., Overberger, C. G., Menges, G., Eds.; Wiley-Interscience: New York, 1989; Vol. 16, p 368.

McHugh, M.; Krukonis, V. J. *Supercritical Fluid Extraction*, 2nd; Butterworth-Heinemann: Boston, 1994.

McHugh, M. A.; Krukonis, V. J. *Supercritical fluid extraction: principles and practice*, 2nd ed.; Butterworth-Heinemann: Stoneham, U.K. 1993

Mack, C. A. *Inside Prolith: A Comprehensive Guide to Optical Lithography simulation*; FINLE Technologies: Austin, TX, 1997.

Magee, J. W. in *Supercritical Fluid Technology*, T. J. Bruno, J. F. Ely Eds; CRC Press: Boston, 1991, 325-334.

Martin, S. J. ;Granstaff, V. E. and Frye, G. C. *Analytical Chemistry*, **1991**, *63*, 2272–2281.

Meli, L.; Pham, J. Q.; Johnston, K. P.; Green, P. F. *Phys. Rev.* E **2004**, *69*, 051601-8.

Michels, A.; Hamers, J. *Physica IV* **1937**, 995-1006.

Miller, J. G. and Bolef, D. I. *Journal of Applied Physics* **1968**, *39*, 4589–4593.

Miura, K.-I.; Otakeb, K.; Kurosawab, S.; Sakob, T.; Sugetab, T.; Nakaneb, T.; Satob, M.; Tsujia,T.; Hiakia, T.; Hongoa, M. *Fluid Phase Equilibria*, **1998**, *144*, 181.

Moreau, W. M. *Semiconductor Lithography: Principles, Practices, andMaterials*; Plenum Publishing: New York, 1988.

Murray, B. S. and Cros, L. *Colloids and Surfaces, B: Biointerfaces* **1998**, *10*, 227–241.

Nakamura, K.; Hoshino, T.; Ariyama, H. *Agric. Biol. Chem.* **1993**, *55*, 2341-2347.

Narine, S. S. and Slavin, A. J. *Journal of Vacuum Science & Technology a-Vacuum Surfaces and Films* **1998**, *16*, 1857–1862.

Neau, E. *Fluid Phase Equil.* **2002**, *203*, 133

Novick, B. J.; Carbonell, R. G.; DeSimone, J. M. *Pol. Mat. Sci. Eng.* **2001**, *84*, 51

Novick, B.J.; Carbonell, R. G; DeSimone, J. M. *Proceedings of the 5th International Symposium of Supercritical Fluids*, April **2000**.

Ober, C. K.; Weibel G. L. *Macroelectronic Engineering* **2003**, *65*, 145-152

Obriot, J.; Ge, J.; Bose, T. K.; St-Arnaud, J. M. *Fluid Phase Equilib.* **1993**, *86*, 315-350.

Odian, G. *Principles of Polymerization*, 3rd; John Wiley&Sons, Inc.: New York, 1991.

Okoroanyanwu, U.; Shimokawa, T.; Medeiros, D.; Willson, C. G.; Frechet, J. M. J.; J.Q., N.; Byers, J.; Allen, R. D. *Proc. SPIE* **1997**, *3049*.

Orwoll, R. A.; In *Physical Properties of Polymers Handbook*; Mark, J. E., Ed., American Institute of Physics: Woodbury, 1996.

Ostrom, G. S. and Buttry, D. A. *Journal of Electroanalytical Chemistry and Interfacial Electrochemistry* **1988**, *256*, 411–431.

O'Sullivan, C. K. and Guilbault, G. G. *Biosensors & Bioelectronics* **1999**, *14*, 663–670.

Pham, J.Q.; Sirard, S.M.; Johnston, K.P. and Green P.F. *Physical Review Letters*, **2003**, *91*, 1Ober, C. K.; Obendorf, S. K.; Allen, R. D. *Chem. Mater.* **2000**, *12*, 41.

Park, K.; Koh, M.; Yoon, C.; and Kim H. *Journal of Supercritical Fluids* **2004**, *29*, 203–212.

Peppas, N. A.; Wu, J. C. and von Meerwall, E. D. *Macromolecules*, **1994**, *27(20)*, 5626-5638.

Piccinini, E.; Gardini, D. and Doghieri, F. "Stress effects on mass transport in polymers: a model for volume relaxation." *Composites*: Part A. **in press**.

Pope, D. S.; Koros, W.J. *Macromolecules* **1992**, *25*, 1711

Postnikov, S.; Stewart, M. D.; Tran, H. V.; Nierode, M.; Medeiros, D.; Cao, T.; Byers, J.; Webber, S.; Willson, C. G. *J. Vac. Sci. & Tech. B* **1999**, *17*, 2965-2969.

Patterson, K.; Somervell, M.; Willson, C. G. *Solid State Technol.* **2000**, *43*, 41.

Petropoulos, J. H., *Journal of Polymer Science, Polymer Physics Edition*, **1984**, *22(11)*, 1885-900

Pol, V.; Bennewitz, J. H.; Escher, G. C.; Feldman, M.; Firtion, V.; Jewell, T. E.; Wilcomb, B. E.; Clemens, J. T. *Proc. SPIE* **1986**, *633*, 6.

Quadir, M. A.; Kipp, B. E.; Gilbert, R. G.; DeSimone, J. M. *Macromolecules* **1997**, *30*, 6015-6023.

Rahtu, A. and Ritala M. *Applied Physics Letters* **2002**, *80*, 521–523.

Reiser, A. *Photoreactive Polymers*; John Wiley & Sons: New York, 1989.

Reiter, G. *Europhys. Lett.* **1993,** *23***,** 579

Rodriguez, F. *Principles of Polymers Systems*, Hemisphere Publishing Corporation: New York, 1989.

Roe, R.-J. *J. Appl. Phys.* **1977**, *48*, 4085.

Royer, J. R.; DeSimone, J. M. and Khan, S. A. *Journal of Polymer Science* Part B-Polymer Physics, **2001**, ***39****(23)*, 3055-3066.

Sanchez, I. C.; Lacombe, R. H. *J. Phys. Chem.* **1976**, *80*, 2352.

Sanchez, I. C. and Lacombe, R. H., *Macromolecules* **1978**, *11*, 1145.

Sanchez, I. C.; Stone, M. T. In *Polymer Blends;* Paul, D. R.; Bucknall, C. B., Eds.; John Wiley & Sons: New York, 2000; Vol. 1

Sand, M. L. Method for Impregnating a Thermoplastic Polymer, US Patent #4,598,006 (**1986**).

Sarti, G. C. and Doghieri, F. *Chemical Engineering Science*, **1998**, *53(19)*, 3435-3447.

Sarti, G. C., *Polymer*, **1979**, ***20****(7)*, 827-832.

Sarti, G. C. and Apicella, A. *Polymer*, **1980**, *21(9)*, 1031-1036.

Sauerbrey, G. *Zeitschrift Fur Physik* **1959**, *155*, 206–222.

Schumacher, R.; Borges, G. and Kanazawa, K. K. *Surface Science* **1985**, *163*, L621–L626.

Scmidt, J. W.; Moldover, M. R. *J. Chem. Phys.* **1993**, *99*, 582-589.

Shieh, Y.-T.; Su, J.-H.; Manivannan, G.; Lee, P. H. C.; Sawan, S. P.; Spall, W. D. *Journal of Applied Polymer Science* **1996**, *59*, 695-705.

Shieh, Y.-T.; Su, J.-H.; Manivannan, G.; Lee, P. H. C.; Sawan, S. P.; Spall, W. D. *J. of Applied Polymer Science* **1996**, *59*, 707-717.

Shim, J.-J.; Johnston, K. P. *AIChE J.* **1989**, *35*, 1097.

Shim, J.-J.; Johnston, K. P. *J.Phys. Chem.* **1991**, *95*, 353.

Shim, J.-J.; Johnston, K. P. *AIChE J.* **1991**, *37*, 607.

Shine, A. D. in *Physical Properties of Polymers Handbook*, J. E. Mark Eds; AIP Press: New York, 1996, 249-256.

Sirard, S. M.; Ziegler, K. J.; Sanchez, I. C. ; Green, P. F. ; Johnston, K. P. *Macromolecules* **2002**, *35*, 1928-1935.

Sirard, S. M.; Green, P. F.; Johnston, K. P. *J. Phys. Chem. B* **2001**, *105*, 766-772.

Smith, J. M.; VanNess, H. C. *Introduction to Chemical Engineering Thermodynamics*, 4th; MacGraw Hill, Inc.: New York, 1987.

Stamatialis, D. F.; Wessling, M.; Sanopoulou, M.; Strathmann, H.; Petropoulos, J. H. *J. Membr. Sci.* **1997**, *130*, 75.

Stewart, M. D.; Patterson, K.; Somervell, M.; Willson, C. G. *J. PhysicalOrganic Chemistry* **2000**, *13*, 767-764.

Stewart, M. D.; Schmid, G. M.; Postnikov, S.; Willson, C. G. *Proc. SPIE* **2001**, *4345*, 10-18.

Stewart, M. D.; Tran, H. V.; Schmid, G. M.; Stachowiak, T.; Becker, D. J.; Willson, C. G. *J. Vac. Sci. & Tech. B* **2002**, *20*, 2946.

StMartin, H. C.; Choi, K. Y. *Industrial and Engineering Chemistry* **1991**, *30*, 1712-1718.

Stockbridge, C. D.; Behrndt, K. H. (Eds.) in *Vacuum Microbalance Techniques*, Plenum, New York, 1966, Vol.5, pp. 147-191.

Strubinger, J. R.; Parcher, J. F. *Anal. Chem.* **1989**, *61*, 951-955.

Strubinger, J. R.; Song, H.; Parcher, J. F. *Anal. Chem.* **1991**, *63*, 98-103

Styrkas, D.; Doran, S. J.; Gilchrist, V.; Keddie, J. L.; Lu, J. R.; Murphy, E.; Sackin, R.; Su, T.-J.; Tzitzinou, A. In *Polymer surfaces and interfaces III*; Richards, R. W.; Peace, S. K., Eds.; New York: Johe Wiley & Sons Ltd: Chichester, 1999.

Subramanian, R.; Pyada, H.; Lira, C. T. *Ind. Eng. Chem. Res.* **1995**, *34*, 3830-3837.

Sundararajan, N.; Yang, S.; Ogino, K.; Valiyaveettil, S.; Wang, J.; Zhou, X.;

Tan, Z.; Gubbins, K. E. *J. Phys. Chem.* **1990**,*94*,6061-6069.

Taylor, D. K.; Carbonell, R. and DeSimone, J. M. *Annual Review of Energy and the Environment*, **2000**, *25*, 115-146

Temam, R. and Miranville, A. *Mathematical Models in Continuum Mechanics*. 2nd ed. **2005**: Cambridge University Press. 342.

Thompson, L. F.; Willson, C. G.; Bowden, M. J. *Introduction to Microlithography*; 2nd ed.; American Chemical Society: Washington D.C., 1994.

Thran, A.; Kroll, G. and Faupel, F. *Journal of Polymer Science*, Part B: Polymer Physics, **1999**, *37(23)*, 3344-3358.

Tompkins, H. G.; McGahan, W. A. *Spectroscopic Ellipsometry and Reflectometry*; John Wiley & Sons, Inc.: New York, 1999.

Umbach, C. P.; Broers, A. N.; Willson, C. G.; Koch, R.; Laibowitz, R. B. *J. Vac. Sci. Technol. B* **1988**, *6*, 319-322.

Urbakh, M. and Daikhin, L. *Physical Review B* **1994**, *49*, 4866–4870.

Varma-Nair, M.; Wunderbelich B. *J. Phys. Chem. Ref. Data* **1982**, *11*, 1985

Vogt, B. D.; Soles, C. L.; Jones, R. L.; Wang, C.-Y.; Lin, E. K.; Wu, W-L.; Satija, S. K. *Langmuir*, **2004**, *20*, 5285-5290.

Vrentas, J. S. and Duda, J. L. *Macromolecules*, **1976**, *9(5)*, 785-790.

Vrentas, J. S. and Duda, J. L. *Journal of Applied Polymer Science*, **1977,** *21(6)*, 1715-1728.

Vrentas, J. S. and Duda, J. L. *AIChE Journal*, **1979**, *25(1)*, 1-24.

Walker, T. A.; Raghavan, S. R.; Royer, J. R.; Smith, S. D.; Wignall, G. W.; Melnichenko, Y.; Khan, S. A.; Spontak, R. J. *Journal of Physical Chemistry B* **1999**, *103*, 5472-5476.

Wang, D.; Mousavi, P.; Hauser, P. J.; Oxenham, W. and Grant C. S. *Colloids and Surfaces A: Physicochemical and Engineering Aspects* **2005**, *268*, 30–39.

Wang, J.; Ward, M. D.; Ebersole, R. C. and Foss, R. P. *Analytical Chemistry* **1993**, *65*, 2553–2562.

Wang, W.-C. V.; Kramer, E. J.; Sachse, W. H. *Journal of Polymer Science : Polymer Physics Edition* **1982**, *20*, 1371-1384.

Ward, M. D. and Buttry, D. A. *Science* **1990**, *249*, 1000–1007.

Watkins, J. J.; Brown, G. D.; Pollard, M. A.; Ramachandra-Rao, V.; Russell, T. P. *Macromolecules* **1999**, *32*, 7737-7740.

Watkins, J. J.; Blackburn, J. M.; McCarthy, T. J. *Chem. Mater.* **1999**, *11*, 213.

Weerawardena, A.; Drummond, C. J.; Caruso, F.; and McCormick M. *Langmuir* **1998**, *14*, 575–577.

Weerawardena, A.; Drummond, C. J.; Caruso, F. and McCormick M. *Colloids and Surfaces a-Physicochemical and Engineering Aspects* **1999**, *146*, 185–197.

Weibel, G.L.; Ober C.K *Microelectronic Engineering* **2003**, *65*, 145

White, C. C. and Schrag, J. L. *Journal of Chemical Physics* **1999**, *111*, 11192–11206.

Williams, M. L.; Landel, R. F.; Ferry, J. D. *J. of the Am. Chem. Soc.* **1955**, *77*, 3701-3707.

Willson, C. G. *Acs Symposium Series* **1983**, *219*, 87-159.

Wind, J. D.; Sirard, S. M.; Paul, D. R.; Green, P. F.; Johnston, K. P.; Koros, W. J. *Macromolecules* **2003**, *36*, 6433.

Wissinger, R. G.; Paulatis, M. E. *Ind. Eng. Chem. Res.* **1991**, *30*, 842.

Wissinger, R. G.; Paulatis, M. E. *J. Polym. Sci., Part B: Polym. Phys.* **1991**, *29*, 879.

Wissinger, R. G.; Paulaitis, M. E. *Journal of Polymer Science. Part B:* **1991**, *29*, 631-633.

Wolff, O.; Seydel, E. and Johannsmann, D. *Faraday Discussions* **1997**, *107*, 91–104.

Woollam, J. A.; Johs, B.; Herzinger, C. M.; Hilfiker, J.; Synowicki, R.; Bungay, C. L. *SPIE Proc.* **1999**, *CR72*, 3-28.

Wu, J. C. and Peppas, N. A. *Journal of Polymer Science*, Part B: Polymer Physics, **1993**, *31(11)*, 1503-1518.

Wu, Y. T.; Akoto-Ampaw, P. J.; Elbaccouch, M.; Hurrey, M. L.; Wallen, S. L. and Grant C. S. *Langmuir* **2004**, *20*, 3665–3673.

Yang, M. and Thompson, M. *Langmuir* **1993**, *9*, 1990–1994.

Yates, M. Z.; Li, G.; Shim, J.-J.; Johnston, K. P. Lim, K.T.; Webber, S. *Macromolecules* **1999**, *32*, 1018.

Zhang, Y; Gangwani, K. K.; Lemert, R. M. *J. Supercritical Fluids* **1997**, *11*, 115.

Zhou, S.; Stern, S. A. *Journal of Polymer Science: Part B: Polymer Physics* **1989**, 27, 205-222.

Zielinski, J. M. and Duda, J.L., *AIChE Journal*, **1992**, ***38****(3)*, 405-415.

<http://www.intel.com/pressroom/kits/quickrefyr.htm>; 2003-05-International Technology Roadmap for Semiconductors, available at <http://public.itrs.net/Files/2000/UpdateFinal/ORTC2000final.pdf>. **2002**.

Guide to using WVASE®32. J. A. Woollam Co., Inc., 2001.